

Numerical methods for multi-scale cell migration models

Applied to glioma invasion

Gregor Corbin

Vom Fachbereich Mathematik der
Technischen Universität Kaiserslautern
zur Verleihung des akademischen Grades
Doktor der Naturwissenschaften (Doctor rerum naturalium)
genehmigte Dissertation

Gutachter:

Prof. Dr. Axel Klar, Technische Universität Kaiserslautern

Prof. Dr. Martin Frank, Karlsruher Institut für Technologie



28. September 2020

D386

Acknowledgements

The outward appearance of this thesis as a fixed collection of results is misleading. From every tangible concept, a hundred diffuse thoughts have infiltrated my mind, shaped by interactions with the excellent people in my environment.

First of all, thank you to my supervisor Prof. Dr. Axel Klar, for leaving me the freedom to experiment and learn, but always having an open door. Thank you, Florian Schneider, for all the hours you spent staring at a whiteboard with me and thinking about my questions, especially in my first year. Thanks to everyone in the technomathematics group for providing such a relaxed atmosphere to work in. I will miss those slightly extended coffee breaks.

Thank you to my colleague from WWU Münster, Michael Wenske. It was a pleasure working with you on the GlioMaTh project, especially because our research topics are somewhat different. I am grateful to the DUNE community for patiently answering many novice questions on how to abuse the software.

To all of you who offered to review the manuscript without hesitation and provided valuable input, I am extremely thankful. Thank you to Anne Dietrich, Maximilian Klaeren, and my sister Dagmar for your different perspective on Chapter 2; Merlin Schaufel for checking every hat in Chapter 3; Matthias Andres for your constructive criticism on Chapter 4; and my brother Armin for wading through the index-swamp of Chapter 5.

Thank you Nura and Max, you have become my second family over the years. And finally, very special thanks belong to Matthias. I don't know if I could have pulled it off without you.

This thesis was financially supported by the German Federal Ministry of Education and Research (BMBF) under funding code 05M16UKB as part of the project "Verbundprojekt 05M2016 - GlioMaTh: Gliomen, Mathematische Modelle und Therapieansätze".

Publications

The following articles, which were published in peer-reviewed journals, were used in this thesis:

- [36] G. Corbin, A. Hunt, A. Klar, F. Schneider, and C. Surulescu. *Higher-order models for glioma invasion: from a two-scale description to effective equations for mass density and momentum. Mathematical Models and Methods in Applied Sciences*, 2018. (see pp. 36, 52, 67, 68, 70, 72, 138, 146, 156)

Furthermore, the following preprints have been submitted:

- [32] G. Corbin *Asymptotic preserving P_N methods for haptotaxis equations* 2019 arXiv: [1909.08514](https://arxiv.org/abs/1909.08514) [[math.NA](https://arxiv.org/archive/math)] (see p. 99)
- [35] G. Corbin, C. Engwer, A. Klar, J. Nieto, J. Soler, C. Surulescu, and M. Wenske *Modeling glioma invasion with anisotropy- and hypoxia-triggered motility enhancement: from subcellular dynamics to macroscopic PDEs with multiple taxis* 2020 arXiv: [2006.12322](https://arxiv.org/abs/2006.12322) [[q-bio.T0](https://arxiv.org/archive/q-bio)] (see pp. 30, 90, 138)

Results from this thesis have been presented at these workshops and conferences:

- Numerical Aspects of Hyperbolic Balance Laws and Related Problems, **Ferrara**, April 16th-20th, 2018: *Model hierarchies for glioma migration (poster)*.
- Dune User and Developer Meeting 2018, **Stuttgart**, November 5th - 6th, 2018: *Making numerical experiments in Dune reproducible*.
- International Workshop on Simulating Interacting Particles, **Bordeaux**, May 9th - 10th, 2019: *Asymptotic preserving moment methods for haptotaxis equations in general space dimension*.
- Numerical Methods for Hyperbolic Problems 2019, **Málaga**, June 17th - 21st, 2019: *Asymptotic preserving moment methods for haptotaxis equations in general space dimension (poster)*.
- Workshop on Mathematical Modeling of Cell Migration, **Kaiserslautern**, January 8th - 9th, 2020: *Asymptotic preserving spectral methods for haptotaxis equations*.

The complete source code and data for this thesis is publicly available online:

- [34] G. Corbin *Numerical methods for multi-scale cell migration models: source code and data* 2020 doi: <https://doi.org/10.26204/data/2> (see p. 161)

Abstract

We study a multi-scale model for growth of malignant gliomas in the human brain. Interactions of individual glioma cells with their environment determine the gross tumor shape. We connect models on different time and length scales to derive a practical description of tumor growth that takes these microscopic interactions into account. From a simple subcellular model for haptotactic interactions of glioma cells with the white matter we derive a microscopic particle system, which leads to a meso-scale model for the distribution of particles, and finally to a macroscopic description of the cell density. The main body of this work is dedicated to the development and study of numerical methods adequate for the meso-scale transport model and its transition to the macroscopic limit.

Zusammenfassung

Wir betrachten ein Modell für das Wachstum bösartiger Gliome im menschlichen Gehirn. Die Form des gesamten Tumors ist eine direkte Folge von Interaktionen einzelner Krebszellen mit ihrer Umgebung. Indem wir Modelle auf verschiedenen Zeit und Längenskalen miteinander verknüpfen erhalten wir eine praktische Beschreibung des Tumorwachstums, die diese mikroskopischen Interaktionen berücksichtigt. Ausgehend von einem einfachen Modell für die Interaktionen zwischen Gliomenzellen mit der weißen Materie stellen wir zuerst ein mikroskopisches Partikelsystem auf, aus dem wir eine Transportgleichung für die Zellverteilung auf der Mesoskala, und schließlich eine makroskopische Beschreibung der Zelldichte herleiten. Im Hauptteil der Arbeit entwickeln und analysieren wir geeignete numerische Methoden für das Transportmodell für Gliomenausbreitung und den Übergang zu dessen makroskopischen Grenzwert.

Contents

1	Introduction	1
1.1	A toy example for multi-scale models	4
1.1.1	The micro-scale: A model for individual particles	4
1.1.2	The meso-scale: A kinetic equation for the collective behavior	5
1.1.3	The macro-scale: Scaling and diffusion limit	9
1.2	A summary of moment models	11
1.2.1	Monomial bases	14
1.2.2	Realizability	15
1.2.3	Minimum entropy closures	15
1.2.4	Kershaw closures	19
1.2.5	The diffusion limit of the first-order moment system	19
2	Biological and medical aspects of glioma	25
2.1	Aspects of glioma growth	25
2.1.1	Macroscopic characteristics	25
2.1.2	Microscopic processes	27
2.2	Mathematical models for tumor growth	28
2.2.1	The cell's perspective	28
2.2.2	The doctor's perspective	28
2.2.3	Multi-scale descriptions	29
2.3	Diffusion tensor imaging	30
2.3.1	Scalar diffusion quantities	31
2.3.2	Estimates for the fiber distribution	31
3	A multi-scale haptotaxis model	35
3.1	A particle model with subcellular receptor dynamics	36
3.1.1	Subcellular receptor dynamics	36
3.1.2	Model assumptions	37
3.1.3	The particle model	38

3.2	A meso-scale kinetic description	40
3.3	An activity-averaged kinetic model	43
3.3.1	The decay of moments	44
3.3.2	A zeroth-order approximation	45
3.4	The generalized haptotaxis equation	48
3.4.1	Properties of turning operators	49
3.4.2	The glioma model in this setting	51
3.4.3	Stroock's E.Coli model	51
3.5	Macroscopic population dynamics	52
3.5.1	The non-dimensional equation and its characteristic numbers	52
3.5.2	A parabolic scaling and the diffusion limit	53
3.5.3	A hyperbolic scaling and the hyperbolic limit	55
3.5.4	The transition between parabolic and hyperbolic scalings	57
3.5.5	The sub-characteristic condition	57
4	Moment methods for the haptotaxis equation	61
4.1	Modified entropy closures	61
4.1.1	Relative entropy	61
4.1.2	The modified minimum-entropy method	64
4.2	First-order monomial systems	65
4.2.1	The diffusion limit of the first-order moment system	66
4.2.2	Some examples for closures	67
4.3	Numerical experiments	72
4.3.1	The space and time discretization	72
4.3.2	The basic setup	75
4.3.3	A homogeneous setting	76
4.3.4	Flux functions and heterogeneous media	88
4.3.5	A proteolysis model	90
4.3.6	Direct methods in the diffusion limit	96
5	An asymptotic preserving method for the haptotaxis equation	99
5.1	A review of asymptotic preserving schemes	100
5.2	The micro-macro decomposition and the diffusion limit	101
5.3	The asymptotic preserving method	102
5.3.1	Primal-dual mesh pairs	103
5.3.2	The space discretization	105
5.3.3	The resulting scheme on a square grid	107
5.3.4	The time discretization	108
5.3.5	The asymptotic limit of the scheme	109
5.3.6	An improved diffusion stencil in the limit	111
5.3.7	An upwind discretization of the drift in the limit	115

5.3.8	The treatment of boundary conditions	116
5.3.9	The discretization of the velocity space by a linear spectral method	117
5.4	Numerical experiments	120
5.4.1	The fundamental solution of the limit equation	120
5.4.2	Convergence analysis with manufactured solutions	125
5.4.3	Stencil improvements	128
5.4.4	Strong discontinuities in the diffusion coefficients	128
5.4.5	The Fisher-KPP equation	131
5.4.6	Stroock's model	135
5.4.7	The glioma model with DTI data from a human brain	137
6	Conclusions	145
A	Calculation details	151
A.1	Notation for vector and matrix calculus	151
A.2	Monomial integrals	152
A.3	The tumor diffusion tensor for a peanut ansatz	153
A.4	Real valued spherical harmonics	155
A.5	The eigenstructure of the Kershaw moment system	156
A.6	A second-order time stepping	159
B	Software and data	161
B.1	Used software	161
B.2	Computational experiments	161
B.2.1	The ARCHIVIST	163
	Bibliography	167
	List of figures	178
	List of tables	179
	Image Credits	181
	Glossary	183
	Academic curriculum vitae	185
	Akademischer Lebenslauf	187

1

Introduction

It might take you an hour to get over that tree. A lot of people never got past it. You prod and poke at it, exploring the limits of your reach and strength, trying to find a way up. And there's a sense of truth in that lack of compromise.

Bennet Foddy — Getting over it

Gliomas are brain tumors originating from various types of glia in the central nervous system. Grade IV¹ astrocytoma, also termed **glioblastoma multiforme (GBM)** are the most prevalent and deadly type. The severity of this diagnosis is best described with some quotations:

Because they generally grow and invade extensively before the patient notes any symptoms, gliomas are almost impossible to cure. ([69])

Partly because of their growth pattern, curative treatment for diffuse gliomas is generally impossible. ([29])

Malignant gliomas, the most common sub-type of primary brain tumors, are aggressive, highly invasive, and neurologically destructive tumors considered to be among the deadliest of human cancers. In its most aggressive manifestation, glioblastoma (GBM), median survival ranges from 9 to 12 months, despite maximum treatment efforts—a statistical fact that has changed little over several decades of technological advances in neurosurgery, radiation therapy, and clinical trials of conventional and novel therapeutics. ([103])

Especially the invasive nature of glioma cells, which leads to a diffuse growth pattern, poses a challenge for treatment, let alone cure. Through several pathways and mechanisms, individual glioma cells are able to migrate far away from the bulk tumor mass [124]. Those “guerilla warriors” [29] are impossible to detect with current imaging technology and also difficult to target without excessive damage to the healthy tissue. A standard practice in radiotherapy is to define the target volume as the visible tumor plus a constant safety margin of 2 cm [91]. In the end, only a few tumor cells need to survive to start a renewed growth after therapy. Thus, even combined radiotherapy and gross tumor resection prolong the median survival by maximum 16 weeks [85].

A predictive model of tumor growth and infiltration could make the invisible parts of the tumor accessible, and therefore lead to improved target volumes in resection and radiotherapy. This

¹The WHO classifies brain tumors into the grades I to IV of increasing malignancy. [57]

could prolong the time until tumor recurrence and reduce the side effects of treatment. Growth patterns of GBM vary significantly from patient to patient. Tumor shapes can be nearly spherical or finger-like. In some cases, the invasion margins are sharp and in other cases diffuse. These facts indicate that tumor growth depends strongly on the individual. Any feasible description must therefore incorporate patient specific measurements and possibly contains many parameters. The possibility of model assisted therapy depends on advances in imaging technology, oncology, and theoretical as well as applied mathematics. This thesis is a result of the project “Gliomen, Mathematische Modelle und Therapieansätze (GlioMaTh)”²³ in which knowledge from these fields is combined to develop predictive models for improved tumor therapies. The GlioMaTh project was funded by the German Federal Ministry of Education and Research (BMBF)⁴. We summarize the challenges of this ambitious enterprise most relevant to this thesis.

Firstly, the fundamental molecular mechanisms of tumor growth and infiltration are an active research area [29, 103, 117, 120]. These are very complex and not nearly understood yet. In this thesis we focus on one selected aspect: the migration of glioma guided by white matter tracts [55]. Fortunately, the highly anisotropic structure of fibers in white matter can be estimated noninvasively with *diffusion tensor imaging (DTI)*. Diffusion tensor images are obtained by a sequence of *magnetic resonance imaging (MRI)* scans and provide measurements of the mean diffusivity of water on a per-voxel basis with a resolution of 1 mm to 2 mm. Under the assumption that water diffuses faster along the fibers than across them, a coarse estimate of the fiber structure can be inferred. The main advantage of this method is that for diagnosis of GBM DTI is performed routinely and thus the data is readily available. Technologically, measurements with a higher angular and spatial resolution are possible, for instance by means of Q-Ball imaging [131]. However, this data would come at a significant additional cost because this is not standard medical practice.

Secondly, the aforementioned molecular processes have to be cast into a mathematical model for tumor growth. On the one hand, an individual tumor cell is about 30 μm long [12]. Its interactions with other cells or the environment—for example, in white matter this is constituted largely by *extracellular matrix (ECM)*—are determined by molecular processes that are observable only at the scale of nanometers. On the other hand, there are between one million and one hundred million cells in a tumor [23]. It is infeasible to compute a model in so much detail. However, in therapy the only quantity of interest is a contour of the invisible invasion front. The resolution is typically in the range of a few millimeters and is determined by measurement and treatment equipment. To incorporate the microscopic cellular processes in a macro-scale tumor description, a hierarchy of models on different length and time scales is needed, each carrying averaged information from the previous. In the context of statistical mechanics, the methods to derive a macroscopic description from a particle system have been studied since the late nineteenth century [19, 66] (see also [62, Introduction]). Opposed to mechanics, where particles are passive rigid bodies only subject to external forces, in biology particles describe living cells with complicated internals. Nevertheless, the basic procedure remains similar. As a first level of abstraction, models on the meso-scale consider PDEs—so-called kinetic equations—for the expected distribution of cells/particles in time, physical space and state space. Kinetic equations

²³Glioma, mathematical models and approaches to therapy

³<https://www.uni-muenster.de/GlioMaTh/>

⁴<https://www.bmbf.de/>

are characterized by a free-streaming transport term resulting from particle movement and a collision operator modeling particle interactions as instantaneous state changes. The connection between particle systems and kinetic equations has been established formally for example for neutron transport [62] and the movement of bacteria [127]. In the [kinetic theory of active particles \(KTAP\)](#) [14], models are formulated directly on this level of abstraction. The state of a particle is described by its velocity and its activity, which is a scalar variable that models a biological function. At larger scales only the resulting macroscopic population behavior can be observed, that is, the total number density of particles regardless of their internal microscopic state. To pass from the mesoscopic description to a population law, one considers the limit of the kinetic equation when the mean free path of particles tends to zero. Analytically, passage to the limiting macroscopic equation has been extensively studied for neutron transport [6, 94] and more recently also in the context of biological cell migration [24, 111]. When only interactions between particles and the environment are considered and interactions between particles are neglected, the collision operator is linear. In this case the resulting macroscopic equations are of diffusion-advection-reaction type [24].

Thirdly, in a clinical context a model is only useful, if it can be computed on standard hardware. On the meso-scale, the PDE for the distribution of particles in time, space, velocity, and activity is high-dimensional and thus costly to solve. In a moment model, the dependence on velocity is approximated by a finite number of moments. Closer to the diffusion limit, usually fewer moments are needed to obtain a good approximation. However, the classical low-order moment methods fail to capture the diffusion limit of the considered kinetic glioma model. It is thus necessary to modify these methods to incorporate the anisotropic equilibrium state of the collision operator. When the scales are clearly separated, it may be enough to solve the macroscopic model directly. This has been done for example in [44, 46, 76]. The separation of scales depends on the assumed model parameters, such as cell migration speed and turning rate, whose estimation is unreliable. However, when the mean free path is small but not negligible, the collision term is stiff and a straightforward discretization of the kinetic equation would need an infeasible spatial and temporal resolution to resolve the small scales accurately [93]. Therefore, a variety of so-called [asymptotic preserving \(AP\)](#) schemes has been developed [22, 63, 79, 81, 87, 96]. These methods are constructed in such a way that—for a fixed resolution—they converge to a discretization of the limit equation.

Last but not least, for parameter fitting and validation, the model needs to be compared against measurement data. However, it is notoriously difficult to obtain in-vivo tumor data due to a combination of factors. Hospitals run on tight budgets, measurements are an additional burden for the patients, and tumor growth is massively influenced by therapy. Furthermore, large portions of the active tumor are invisible to noninvasive measurements. Therefore, rudimentary model validation is often done with small data sets from one to at most a dozen patients [108, 129]. Another team in the GliomaTh project is developing a stationalization approach that makes better use of the already available data and mitigates some of these problems [48].

Any individual work can contribute only an $O(\varepsilon)$ part to the ambitious task of developing a patient-specific predictive cancer model based on fundamental biological observations which really improves therapy outcomes. This thesis is dedicated to the study of moment methods for the meso-scale kinetic equations in the model hierarchy, but the larger context is not ignored.

The glioma invasion model from [44, 46] serves as a prototype for hierarchic models. A detailed discussion of the model's assumptions is the foundation for more realistic models.

Structure

In the rest of this chapter we establish basic notation and concepts. In Section 1.1 we introduce some well-known but essential concepts for multi-scale models originating from particle systems, such as entropy dissipation, scaling, and the diffusion limit of the kinetic meso-scale equation. A simple run-and-tumble particle model for bacterial movement serves as an illustrative example. Section 1.2 then summarizes the method of moments for the classical kinetic equation. In Chapter 2 we give an overview of the biological aspects of tumor growth, with emphasis on cell migration. Then we review some existing mathematical models for glioma invasion on the macro and micro-scale. We also touch upon data acquisition with MRI. Chapter 3 details the transition from the subcellular modeling level to the macroscopic models. The focus lies on modeling, not so much on rigorous limit procedures. We identify a class of kinetic equations as a generalization of the meso-scale glioma model. In Chapter 4, we discuss moment methods for this so-called haptotaxis equation. From a relative entropy dissipation law, we derive modified moment methods that converge to the correct diffusion limit. In Chapter 5 we develop, analyze and numerically validate an AP method to handle the transition from the kinetic equation to the diffusion limit numerically. Finally, we summarize the results and discuss potential for further work in Chapter 6.

1.1 A toy example for multi-scale models

By means of a simple run-and-tumble model for the motion of bacteria, we introduce the main concepts and notation relevant for the multi-scale model in Chapter 3.

1.1.1 The micro-scale: A model for individual particles

We adopt Stroock's [127] model which is based on experimental observations on the *E. coli*⁵ bacterium [17]. The bacterium alternates between two phases of movement: the run phase and the tumble phase. During a run, the bacterium moves with constant speed c in a straight line. In the tumble phase, it stays in its place and turns its main axis to determine the direction of the next run phase. The tumble duration is short compared to the run duration.

On the micro-scale, the model describes the motion of a single bacterium. The bacterium is considered in abstract form as a particle of which we know only the position of its center $x = (\xi, \eta, \zeta)^T \in \mathbb{R}^3$ and its current movement direction $v = (v_\xi, v_\eta, v_\zeta)^T \in \mathbb{S}^2 := \{v \in \mathbb{R}^3 \mid |v| = 1\}$. Without any information on the biochemical processes inside the bacterium we rely on a stochastic description of tumbling that fits the observations. Furthermore, we assume that the tumble duration is negligible and describe the tumbling phase with a random and instantaneous change in direction, which we call turning event.

The evolution of the bacteria's state $\psi = (x, v)$ is governed by the following piece-wise deterministic Markov jump process [133]:

⁵*Escherichia coli*. A small bacterium that can be found in the human digestive tract.

1. In a run phase, the state evolves according to the ODE

$$\begin{aligned}\partial_t x &= cv, \\ \partial_t v &= 0.\end{aligned}$$

2. Turning events occur at the times t_i , which are Poisson distributed with constant rate parameter λ : The probability that no turning event happens in the time span $[s, t]$ is

$$\mathbb{P}(t_i \notin [s, t] | \forall i) = \exp(-\lambda(t - s)).$$

The turning rate is the inverse of the mean free flight duration $\frac{1}{\lambda}$: the expected time between turning events. The direction $v_i^+ := \lim_{t \downarrow t_i} (v(t))$ right after a turning event depends on the direction $v_i^- := \lim_{t \uparrow t_i} (v(t))$ immediately before the event. Let $K(v, v')$ be a probability density function in its first argument v , for each v' . The probability that the post-turning direction v_i^+ is in the set Ω_v , given that the pre-turning direction is v_i^- , is

$$\mathbb{P}(v_i^+ \in \Omega_v | v_i^-) = \int_{\Omega_v} K(v, v_i^-) dv.$$

Under the assumption that bacteria do not interact with each other, a collection of N bacteria is described by N instances of this stochastic process.

Remark 1.1 A similar model applies for neutrons moving through a medium and colliding with the nuclei therein [5, 62]. The collision times and post-collision velocities are determined by the obstacle configuration. Randomness enters the model through the uncertain configuration of obstacles, even if we assume hard-sphere collisions between neutrons and nuclei. Instead of the turning rate, the collisions are usually parameterized by the so-called scattering cross-section σ , which is the inverse of the mean free path. Let A be the interaction cross-section between a nucleus and a neutron, and n the number density of obstacles. For hard-sphere collisions of negligibly small neutrons with obstacles of radius R we have $A = \pi(2R)^2$. The scattering cross-section $\sigma = An$ can be interpreted as the interaction cross-section per volume. If the nuclei are independently Poisson distributed, the cross-section σ ($[\sigma] = \text{m}^{-1}$) is related to the collision rate λ ($[\lambda] = \text{s}^{-1}$), via

$$\lambda = c\sigma.$$

1.1.2 The meso-scale: A kinetic equation for the collective behavior

With a larger number of particles N , the individual realizations of the stochastic process contribute less and less to the collective behavior. An equation for the expectation is better suited to describe the collective. Let

$$\mu(\Omega_x \times \Omega_v) = \int_{\Omega_x} \int_{\Omega_v} f(t, x', v')' dv' dx'$$

be the expected number of particles in the phase space $\Omega_x \times \Omega_v$, that is, μ is the measure of the particle distribution function

$$f(t, x, v).$$

The expectation of the stochastic process is governed by the integro-differential equation

$$\partial_t f + c \nabla_x \cdot (vf) = \lambda \int_{\mathbb{S}^2} K(v, v') f(v') - K(v', v) f(v) dv' \quad (1.1)$$

for $f(t, x, v)$. Its derivation is outside the scope of this thesis. For details, we refer to [5, 62, 127].

We omit some or all arguments to f whenever this is unambiguous.

On the left-hand side of (1.1), the advection of $f(v)$ in direction v is due to linear movement of particles. The right-hand side is a balance of gains and losses for $f(v)$ due to turning events. We pose additional restrictions on the turning kernel K :

Definition 1.2 — Turning kernel. A turning kernel is a positive function $K(v, v') : \mathbb{S}^2 \times \mathbb{S}^2 \mapsto \mathbb{R}^+$ that is

- normalized with respect to its first argument, i.e,

$$\int_{\mathbb{S}^2} K(v, v') dv = 1, \quad (1.2)$$

- bounded by positive constants from below and above,

$$0 < K_{\min} \leq K(v, v') \leq K_{\max} < \infty, \quad (1.3)$$

- and symmetric in its arguments

$$K(v, v') = K(v', v). \quad (1.4)$$

The first assumption (1.2) ensures that the kernel K is a probability density such that the stochastic process associated with (1.1) is physically meaningful. Assumptions (1.3) and (1.4) are essential for the existence of a diffusion limit to the kinetic equation (see Section 1.1.3). In Section 3.5, we will generalize this definition by weakening assumption (1.4).

The right-hand side of (1.1) is completely parameterized by the turning rate λ and the turning kernel K . Therefore, the definition of a turning operator is natural:

Definition 1.3 — Turning operator. The turning operator $\mathcal{L} : L^2(\mathbb{S}^2) \mapsto L^2(\mathbb{S}^2)$ associated with a turning kernel K according to Definition 1.2, is given by

$$\mathcal{L}f = \int_{\mathbb{S}^2} K(v, v') f(v') - K(v', v) f(v) dv'. \quad (1.5)$$

The first summand in (1.5) counts the particles that turn from any direction v' into v , i.e., the gain for direction v . We give it a special name:

Definition 1.4 — Gain operator. A turning kernel K fulfilling Definition 1.2 defines a gain operator $\mathcal{K} : L^2(\mathbb{S}^2) \mapsto L^2(\mathbb{S}^2)$ via the kernel integral

$$\mathcal{K}f = \int_{\mathbb{S}^2} K(v, v') f(v') dv'.$$

Turning does not change the total number of particles, hence every gain for v comes from a loss for v' , and all losses for v' are given by

$$\int_{\mathbb{S}^2} K(v, v') f(v') dv = \int_{\mathbb{S}^2} K(v, v') dv f(v') = f(v').$$

Herein, we used the normalization of the $K(v, v')$. With Definition 1.4, we write $\mathcal{L}f = \mathcal{K}f - f = (\mathcal{K} - I)f$. By construction, the turning operator fulfills

$$\int_{\mathbb{S}^2} \mathcal{L}f(v)dv = 0,$$

and thus conserves the local particle mass $\rho = \int_{\mathbb{S}^2} f(v)dv$.

The particle distribution $f(v)$ is in local equilibrium if the gains and losses for each direction v cancel each other. For the equilibrium $E(v)$, the detailed balance condition

$$K(v, v')E(v) = K(v', v)E(v')$$

must hold for all v, v' such that the integrand in (1.5) is identically zero. Then, assuming spatial homogeneity, E is a steady state of (1.1):

$$\partial_t E = \lambda \mathcal{L}(E) = 0.$$

Due to symmetry (1.4) and strict positivity (1.3) of the turning kernel, the equilibria are exactly the constant functions. In the following, we denote with $E(v) = \frac{1}{|\mathbb{S}^2|}$ the constant function with unit mass.

Reduced space dimension

The kinetic model is valid for particles moving in a three-dimensional domain $\Omega_x \subseteq \mathbb{R}^3$. To simplify computations it is often useful to consider the model on a one or two-dimensional domain. In the following, the parametrization of the unit sphere

$$(v_\xi, v_\eta, v_\zeta)^\top = \left(\sqrt{1 - \mu^2} \cos(\phi), \sqrt{1 - \mu^2} \sin(\phi), \mu \right)^\top, \mu \in [-1, 1], \phi \in [0, 2\pi]$$

is useful.

In the slab geometry model, only one space dimension remains. Assume that the domain $\Omega_x = \mathbb{R}^2 \times \Omega_\zeta$ extends infinitely along the ξ and η axes. Further, assume that the initial conditions and coefficients are constant on each infinite slab $\{x \in \Omega_x \mid \zeta = \text{const}\}$. We can describe this setting with the kinetic equation for $f(t, \zeta, \mu)$:

$$\partial_t f + c\mu \partial_\zeta f = \lambda \int_{-1}^1 K_{\text{slab}}(\mu, \mu') f(\mu') - K_{\text{slab}}(\mu', \mu) f(\mu) d\mu'$$

wherein the direction v is projected onto the ζ -component. The turning kernel has to be integrated over ϕ :

$$K_{\text{slab}}(\mu, \mu') = \int_0^{2\pi} \int_0^{2\pi} K(v, v') d\phi d\phi'.$$

Considering a domain $\Omega_x = \Omega_{\xi, \eta} \times \mathbb{R}$ that is infinite in the ζ -direction and assuming that initial conditions and coefficients are constant for each line $\{x \in \Omega_x \mid \xi = \text{const}, \eta = \text{const}\}$, we obtain a two-dimensional model for $f(t, \xi, \eta, v)$:

$$\partial_t f + cv_\xi \partial_\xi f + cv_\eta \partial_\eta f = \lambda \int_{\mathbb{S}^2} K(v, v') f(v') - K(v', v) f(v) dv.$$

Here, the direction v remains on the unit sphere, but for the transport only the projection onto the ξ, η -plane is relevant.

This is different from the intrinsically two-dimensional model with $\tilde{x} \in \mathbb{R}^2$ and $\tilde{v} \in \mathbb{S}^1$:

$$\partial_t f + c\nabla_{\tilde{x}} \cdot (\tilde{v}f) = \lambda \int_{\mathbb{S}^1} K(\tilde{v}, \tilde{v}') f(\tilde{v}') - K(\tilde{v}', \tilde{v}) f(\tilde{v}) d\tilde{v}'.$$

Entropy dissipation

Equation (1.1) with the structure provided by Definition 1.2 and Definition 1.3 is endowed with an entropy dissipation law. Dissipation of entropy essentially drives f towards the equilibrium state E and is therefore a key ingredient for the diffusion limit [37] (see Section 1.1.3) as well as for the hyperbolic limit [27] (see Section 3.5.3).

Definition 1.5 — Entropy density / Entropy. We call a convex, twice continuously differentiable function $\eta : \mathbb{R} \mapsto \mathbb{R}$ an entropy density. This defines an entropy functional

$$h(f) = \int_{\mathbb{S}^2} \eta(f(v)) dv.$$

Multiplication of (1.1) by η' and integration over \mathbb{S}^2 gives the local entropy dissipation law

$$\partial_t h + c \nabla_x \cdot j = \lambda \int_{\mathbb{S}^2} \eta'(f) \mathcal{L}(f) dv \leq 0 \quad (1.6)$$

with entropy flux $j = \int_{\mathbb{S}^2} \eta(f) v dv$. The linear analog of the famous H-theorem [5, 19, 136] guarantees that the collision operator dissipates entropy:

Lemma 1.6 — Entropy dissipation of the turning operator. For an entropy according to Definition 1.5, the collision operator from Definition 1.3 fulfills

$$\int_{\mathbb{S}^2} \eta'(f) \mathcal{L}(f) dv \leq 0.$$

Equality holds, if and only if $f = E \in \mathcal{N}(\mathcal{L})$.

Proof. The proof relies on the symmetry of the kernel, $K(v, v') = K(v', v)$, and the convexity of the entropy η . See Lemma 2 in [37]. The proof of Lemma 4.2 is conceptually similar. ■

This lemma holds for any entropy η . Of all functions with mass ρ , the equilibrium function $\rho E(v) \equiv \frac{\rho}{|\mathbb{S}^2|}$ minimizes the entropy functional $h(f)$. We show this with Jensen's inequality:

$$\begin{aligned} \frac{1}{|\mathbb{S}^2|} h(f) &= \frac{1}{|\mathbb{S}^2|} \int_{\mathbb{S}^2} \eta(f) dv \geq \eta \left(\frac{1}{|\mathbb{S}^2|} \int_{\mathbb{S}^2} f dv(v) \right) \\ &= \eta \left(\frac{\rho}{|\mathbb{S}^2|} \right) \\ &= \frac{1}{|\mathbb{S}^2|} \int_{\mathbb{S}^2} \eta \left(\frac{\rho}{|\mathbb{S}^2|} \right) dv \\ &= \frac{1}{|\mathbb{S}^2|} h \left(\frac{\rho}{|\mathbb{S}^2|} \right). \end{aligned}$$

Because \mathcal{L} locally diminishes the entropy, which is minimal in equilibrium, it drives f locally towards E . In this sense, the entropy measures the distance of f to the equilibrium. Locally, the entropy h can increase due to the transport term. Consider the total entropy $H = \int_{\Omega_x} h(f) dx$ in the domain Ω_x . Integration of the local entropy dissipation law gives

$$\frac{dH}{dt} + c \int_{\partial\Omega_x} j \cdot n dx \leq 0.$$

Unsurprisingly, the advection term does not change the total entropy in the domain interior. But through fluxes over the boundary, entropy can either enter or leave the system.

1.1.3 The macro-scale: Scaling and diffusion limit

Scaling

Equation (1.1) is defined in terms of the physical variables $(t, x, v) \in \Omega_{txv}$ on the physical domain $\Omega_{txv} = \Omega_t \times \Omega_x \times \mathbb{S}^2$. With the coordinate transformations $t = T\hat{t}$, and $x = X\hat{x}$ we rewrite it in terms of non-dimensional variables $(\hat{t}, \hat{x}, v) \in \hat{\Omega}_{txv} = \hat{\Omega}_t \times \hat{\Omega}_x \times \mathbb{S}^2$. The direction v is already non-dimensional and therefore does not need to be transformed. With the total duration as the time scale T and the largest side-length of the bounding box of Ω_x as the length scale X , the reference domain is normalized: The temporal domain becomes $\hat{\Omega}_t = [0, 1]$ and the spatial domain $\hat{\Omega}_x$ fits into the unit square. Depending on the situation, another choice may be more appropriate. For example, if the domain has features of a certain characteristic size L , we can define $X = L$.

The non-dimensional particle distribution \hat{f} is defined via $f(t, x, v) = f_0 \hat{f}(\hat{t}, \hat{x}, v)$, with an arbitrary reference quantity f_0 for particles. Using the chain rule, we express for instance the time derivative in non-dimensional quantities as:

$$\partial_t f = f_0 \frac{\partial \hat{f}}{\partial \hat{t}} \frac{\partial \hat{t}}{\partial t} = \frac{f_0}{T} \partial_{\hat{t}} \hat{f}.$$

After multiplication with $\frac{T}{f_0}$, the non-dimensional equation reads:

$$\partial_{\hat{t}} \hat{f} + \frac{Tc}{X} \nabla_{\hat{x}} \cdot (v \hat{f}) = T\lambda \mathcal{L} \hat{f}.$$

The characteristic numbers of this equation are the Strouhal number

$$\text{St} = \frac{X}{Tc},$$

which is the ratio of the time $\frac{X}{c}$ a particle needs to travel the reference distance to the reference time T , and the Knudsen number

$$\text{Kn} = \frac{1}{T\lambda},$$

the ratio of mean free time $\frac{1}{\lambda}$ to the reference time scale T . In terms of these characteristic numbers, the equation reads

$$\partial_{\hat{t}} \hat{f} + \frac{1}{\text{St}} \nabla_{\hat{x}} \cdot (v \hat{f}) = \frac{1}{\text{Kn}} \mathcal{L} \hat{f}. \quad (1.7)$$

We may combine the characteristic numbers in any non-degenerate way to produce a different set of two characteristic numbers and reformulate equation (1.7) accordingly. There are then two perspectives we can take. From an analytical point of view, we may assume full control over the physical parameters and set the characteristic numbers arbitrarily. Because there are four physical parameters T, X, c, λ and two equations relating those parameters to the characteristic numbers, we can choose two physical parameters freely. This determines the remaining two physical parameters corresponding to the chosen characteristic numbers. From an applied perspective, all physical parameters are already determined. Thus, we have no choice left. The two characteristic numbers are completely determined by their definitions. We may use them to classify a given physical situation.

■ **Example 1.7** Given a set of parameters T, X, c, λ , we want to write the equation equivalently with new parameters $\tilde{T}, \tilde{X}, \tilde{c}, \tilde{\lambda}$ with unit speed $\tilde{c} = 1$. To keep the characteristic numbers $\text{St} = \tilde{\text{St}}$ and $\text{Kn} = \tilde{\text{Kn}}$ constant over this transformation, we keep $\tilde{X} = X$ unchanged and set

$$\tilde{T} = cT, \quad \tilde{\lambda} = \frac{1}{c}\lambda.$$

Parabolic scaling and diffusion limit

We write equation (1.7) in the form

$$\partial_{\hat{t}} \hat{f} + \frac{\delta}{\varepsilon} \nabla_{\hat{x}} \cdot (v \hat{f}) = \frac{\delta}{\varepsilon^2} \mathcal{L} \hat{f}. \quad (1.8)$$

A comparison of coefficients yields the characteristic numbers

$$\varepsilon = \frac{\text{Kn}}{\text{St}} = \frac{c}{X\lambda},$$

$$\delta = \frac{\text{Kn}}{\text{St}^2} = \frac{c^2 T}{\lambda X^2}.$$

This so-called parabolic scaling is motivated by the limit of (1.8) as ε tends to zero. As we have seen in Section 1.1.2, the turning operator locally relaxes f towards its equilibrium state due to entropy dissipation. When ε tends to zero, turning dominates advection, and we can expect that the distribution converges to the local equilibrium $\hat{f}_0 = \hat{\rho}_0(\hat{t}, \hat{x})E(v)$. Indeed, when ε tends to zero while δ is constant, equation (1.8) converges to the diffusion equation

$$\partial_{\hat{t}} \hat{\rho}_0 - \delta \nabla_{\hat{x}} \cdot (\hat{D} \nabla_{\hat{x}} \hat{\rho}_0) = 0, \quad (1.9)$$

for the particle density

$$\hat{\rho}_0 = \int_{\mathbb{S}^2} \hat{f}_0(v) dv.$$

The diffusion tensor $\hat{D} \in \mathbb{R}^{3 \times 3}$ is given by

$$\hat{D} = -\frac{1}{4\pi} \int_{\mathbb{S}^2} v \mathcal{L}^{-1}(v^\top) dv. \quad (1.10)$$

Herein, the term $\mathcal{L}^{-1}(v^\top)$ is the inverse of \mathcal{L} applied component-wise to v^\top . The inverse is well-defined thanks to the following lemma:

Lemma 1.8 — Properties of turning operators. With respect to the scalar product on $L^2(\mathbb{S}^2)$, the turning operator \mathcal{L} has these properties:

1. \mathcal{L} is self-adjoint.
2. The one-dimensional nullspace of \mathcal{L} is spanned by the constant functions: $\mathcal{N}(\mathcal{L}) = \text{span}\{1\}$. The range of \mathcal{L} is the orthogonal complement of its nullspace $\mathcal{R}(\mathcal{L}) = \mathcal{N}^\perp(\mathcal{L}) = \left\{ g \mid (g, 1) = \int_{\mathbb{S}^2} g dv = 0 \right\}$.
3. $\mathcal{L} : \mathcal{R} \mapsto \mathcal{R}$ restricted to $\mathcal{R}(\mathcal{L})$ is bijective: There exists a unique solution $f \in \mathcal{R}(\mathcal{L})$ to $\mathcal{L}f = g$, if and only if $g \in \mathcal{R}(\mathcal{L})$.

Proof. See [38, Chapter XXI, Section 5.2, Lemma 1]. Assumptions (1.3), (1.4) are necessary ingredients for the proof. The proof of Lemma 3.11 in Section 3.5 implies the proof of this lemma. ■

Because of $\int_{\mathbb{S}^2} v dv = 0$, v is in the range of \mathcal{L} and the inverse $\mathcal{L}^{-1}(v^\top)$ exists and is unique. A derivation of the diffusion limit via a Hilbert expansion follows for the more general case in Section 3.5.2. For a rigorous proof, see [38, Chapter XXI., Section 5.2, Theorem I].

The reverse transformation of 1.9 into physical coordinates yields

$$\partial_t \rho_0 - \nabla_x \cdot \left(\frac{X^2 \delta}{TD_0} D \nabla_x \rho_0 \right) = 0,$$

with a reference diffusion parameter D_0 and $D = D_0 \hat{D}$. The coefficient in front of the diffusion term should be equal to one. This defines a relation between the characteristic number δ on the meso-scale and the macroscopic reference diffusion speed D_0 :

$$\delta = \frac{TD_0}{X^2}.$$

We interpret δ as the ratio of the total time T to a characteristic diffusion time $\frac{X^2}{D_0}$.

■ **Example 1.9 — Isotropic scattering.** When the velocities after collisions are distributed uniformly, i.e.,

$$K(v, v') = \frac{1}{|\mathbb{S}^2|} = \frac{1}{4\pi},$$

equation (1.1) becomes

$$\partial_t f + c \nabla_x \cdot (vf) = \lambda \left(\frac{1}{4\pi} \langle f \rangle - f \right).$$

For any g in the range of \mathcal{L} , i.e., $\int_{\mathbb{S}^2} g dv = 0$, we have $\mathcal{L}(-g) = g$, thus the inverse operator is

$$\mathcal{L}^{-1}(g) = -g.$$

There is an explicit formula for the diffusion tensor:

$$\hat{D} = - \int_{\mathbb{S}^2} v(-v)^\top dv = \frac{1}{3}I.$$

1.2 A summary of moment models

The diffusion limit is an example of a situation where the full distribution $f(v)$ can be reconstructed approximately from a few degrees of freedom. Close to the diffusion limit, we can infer $f(v) \approx \rho E(v)$ from the single moment ρ . A moment model is an approximation of the six-dimensional PDE (1.1) by a system of equations for the moments of f with respect to v . From a numerical perspective, it is a discretization of the velocity space by a Galerkin method.

Let

$$\mathbf{a}^\infty = (a_0, a_1, \dots)^\top$$

be a basis of the normalized velocity space $L^2(\mathbb{S}^2)$ with components $a_k(v)$. When the basis consists of polynomials on the full sphere, we write

$$\mathbf{a}^\infty = \begin{pmatrix} \mathbf{a}^{(0)} \\ \mathbf{a}^{(1)} \\ \vdots \end{pmatrix}$$

and collect all basis functions of polynomial degree l in the vector $\mathbf{a}^{(l)}$. We consider only such spectral polynomial methods in this work. For completeness, note that in principle any other basis is possible. In particular, basis functions with partial support on the sphere lead to so-called partial moment methods. Full and partial moment methods are discussed in detail by Schneider [121] in his PhD thesis.

The shorthand notation

$$\langle \cdot \rangle = \int_{\mathbb{S}^2} \cdot dv$$

for integrals over the angular domain \mathbb{S}^2 will be handy in the following. Integrals over vectors or matrices are always meant component-wise as in $\langle v \rangle = (\langle v_\xi \rangle, \langle v_\eta \rangle, \langle v_\zeta \rangle)^\top$.

The moments of $f(v)$ are defined as

$$\begin{aligned} \mathbf{u}^\infty &= \langle \mathbf{a}^\infty(v) f(v) \rangle, \\ u_k &= \langle a_k(v) f(v) \rangle. \end{aligned}$$

In principle, we can expand f in terms of the basis

$$f = \sum_{k=0}^{\infty} \alpha_k a_k(v)$$

and test (1.1) with the basis components to get an infinite system for the moments:

$$\partial_t u_k + c \nabla_x \cdot \langle a_k v f \rangle = \lambda \langle a_k \mathcal{L} f \rangle, \quad k = 0, 1, \dots$$

We obtain a finite-dimensional approximation to (1.1) if we test with the truncated basis

$$\mathbf{a}^N = \begin{pmatrix} \mathbf{a}^{(0)} \\ \vdots \\ \mathbf{a}^{(N)} \end{pmatrix} = \begin{pmatrix} a_0 \\ \vdots \\ a_{n-1} \end{pmatrix}$$

which spans an n -dimensional subspace $V = \text{span} \{a_0, \dots, a_{n-1}\} \subset L^2(\mathbb{S}^2)$, containing exactly the polynomials of order less than or equal to N . We call N the moment order of the system. The moments with respect to the finite basis are $\mathbf{u}^N = \langle \mathbf{a}^N f \rangle$. We omit the superscript N when the moment order is unambiguous. The truncated system is equivalent to the condition that the projection of (1.1) onto the finite-dimensional subspace V is fulfilled:

$$\partial_t \mathbf{u} + c \nabla_x \cdot \langle v \mathbf{a}^\top f \rangle = \lambda \langle \mathbf{a} \mathcal{L} f \rangle. \quad (1.11)$$

The so-called flux moments $\langle v a^\top f \rangle$ are a $3 \times n$ matrix with entries $\langle v_i a_k f \rangle, i = 1, 2, 3, k = 0, \dots, n-1$. The spatial divergence contracts components of the gradient with the columns of the flux matrix.

Remark 1.10 All moment systems with arbitrary polynomial basis \mathbf{a} of moment order N are equivalent, because one can always find a coordinate transformation that maps one basis to another. Therefore, the choice of basis has no influence on the approximation quality. However, from a practical/programming perspective, some terms may be easier to interpret/evaluate in one basis than in another.

Unfortunately, the functions $v a^{(l)\top}$ have polynomial degree $l+1$ and the moments $\langle v a^{(l)\top} f \rangle$ are some linear combination of moments in $\mathbf{a}^{(l+1)}$. When the basis is truncated at polynomial order N , then for $l = N$ the corresponding flux moments cannot be expressed exactly in terms of the known moments. We need a moment closure: A method to approximate the higher-order moments from the known moments.

One method is to first reconstruct an approximate distribution $\tilde{f}[\mathbf{u}]$ from the moments \mathbf{u} . This reconstruction should fulfill the moment constraints

$$\langle \mathbf{a} \tilde{f} \rangle = \langle \mathbf{a} f \rangle = \mathbf{u}, \quad (1.12)$$

but of course it will differ from the true distribution in its higher moments. When we insert this ansatz into the moment system (1.11), we obtain a closed approximation

$$\partial_t \mathbf{u} + c \nabla_x \cdot \langle v \mathbf{a}^\top \tilde{f} \rangle = \lambda \langle \mathbf{a} \mathcal{L} \tilde{f} \rangle.$$

The linear closure P_N and the entropy closure M_N fit into this construction method (see Section 1.2.3). Alternatively, one can approximate the higher-order moments directly from the known moments, which is done for example in the Kershaw closure.

The end result is always a system of conservation laws with source term

$$\partial_t \mathbf{u} + c \nabla_x \cdot \mathcal{F}(\mathbf{u}) = \mathcal{R}(\mathbf{u}).$$

The system is strictly hyperbolic, if for every normal $\mathbf{n} \in \mathbb{R}^3$ the flux Jacobian

$$J_{\mathcal{F}_n} = \frac{\partial(\mathcal{F}(\mathbf{u}) \cdot \mathbf{n})}{\partial \mathbf{u}} = \left\langle v \cdot \mathbf{n} \mathbf{a} \frac{\partial \tilde{f}}{\partial \mathbf{u}} \right\rangle$$

is diagonalizable with real eigenvalues.

It will often be helpful to write the equations in terms of the normalized moments

$$\hat{\mathbf{u}} = \frac{1}{\langle f \rangle} \langle \hat{\mathbf{a}} f \rangle := \frac{1}{\langle f \rangle} \langle (a_1, a_2, \dots, a_{n-1})^\top f \rangle.$$

Two extreme situations deserve special names: When the particle distribution is in equilibrium, that is, $f = \rho E = \frac{\rho}{\langle 1 \rangle}$, the moments are given by

$$\mathbf{u}_E = \frac{\rho}{\langle 1 \rangle} \langle \mathbf{a} \rangle.$$

These are the isotropic moments. When all particles move in the same direction, the distribution is a Dirac-delta $f = \delta_{v^*}(v)$ and the moments are

$$\mathbf{u}_\delta = \mathbf{a}(v^*).$$

These are called the free-streaming moments, because this situation arises if no collisions occur.

1.2.1 Monomial bases

A basis of monomials of $L^2(\mathbb{S}^2)$ is

$$\mathbf{a}^\infty = \left(v_\xi^i v_\eta^j v_\zeta^k; i, j, k \geq 0, k \in \{0, 1\} \right)^\top.$$

On the sphere, the functions $v_\xi^2, v_\eta^2, v_\zeta^2$ are linearly dependent due to the identity $v_\zeta^2 = v_\xi^2 + v_\eta^2$. The basis cannot contain the monomials $v_\xi^i v_\eta^j v_\zeta^k$ for all combinations of indices. In the definition above, we arbitrarily chose to exclude monomials with $k > 1$. The second-order monomial basis $\mathbf{a}^2(v) : \mathbb{S}^2 \mapsto \mathbb{R}^9$ is for example

$$\mathbf{a}^2 = \left(1, v_\xi, v_\eta, v_\zeta, v_\xi^2, v_\eta^2, v_\xi v_\eta, v_\xi v_\zeta, v_\eta v_\zeta \right)^\top.$$

The low-order moments of f in this basis have physical interpretations and deserve special names [114]. Let

$$\begin{aligned} \rho &= \langle f \rangle \in \mathbb{R}, \\ q &= \langle v f \rangle \in \mathbb{R}^3, \\ P &= \langle v v^\top f \rangle \in \mathbb{R}^{3 \times 3}, \end{aligned}$$

denote the zeroth-order moment, the vector of first-order moments, and a tensor of second-order moments, respectively. With these definitions, the first-order moment model of the transport equation reads

$$\begin{aligned} \partial_t \rho + c \nabla_x \cdot q &= 0 \\ \partial_t q + c \nabla_x \cdot P &= \lambda C = \lambda(C^+ - q). \end{aligned} \tag{1.13}$$

In analogy with the Euler equations, we call ρ the mass (density), q the momentum (density) and P the pressure tensor. Concerning the units, this nomenclature is misleading: The distribution is the number of particles per volume and surface angle which is measured in units $[f] = \text{mol m}^{-3} \text{sr}^{-1}$. Consequently, ρ is really a number density with units $[\rho] = \text{mol m}^{-3}$. To compute the physical mass density $M\rho$ we need to multiply by the molar mass of particles M . Similarly, the physical momentum density is given by Mcq .

The normalized first-order moments

$$\hat{q} = \frac{q}{\rho},$$

indicate how aligned the particles are. In equilibrium there is no net momentum: $\hat{q} = 0$. But in the free-streaming situation with $f = \delta_{v^*}(v)$, the momentum is $q = \rho v^*$. The normalized momentum $\hat{q} = v^*$ has magnitude one: $|\hat{q}| = 1$.

The closure problem consists of finding an approximation to the pressure tensor and collision moments

$$\begin{aligned} P^A[\rho, q] &\approx P = \langle v v^\top f \rangle, \\ C^A[\rho, q] &\approx C = \langle v \mathcal{L} f \rangle, \end{aligned}$$

in terms of the known moments ρ, q . When a reconstruction $\mathfrak{f}[\rho, q]$ is defined, these moments are naturally obtained by $P^A = \langle v v^\top \mathfrak{f} \rangle, C^A = \langle v \mathcal{L} \mathfrak{f} \rangle = \langle v \mathcal{K} \mathfrak{f} \rangle - q$.

The flux function \mathcal{F} for this system is

$$\mathcal{F}(\rho, q) = \begin{pmatrix} q^\top \\ P^A \end{pmatrix} = \rho \begin{pmatrix} \hat{q}^\top \\ \hat{P}^A \end{pmatrix},$$

with Jacobian

$$J\mathcal{F}_n = \begin{pmatrix} 0 & n^\top \\ \frac{\partial P^A_n}{\partial \rho} & \frac{\partial P^A_n}{\partial q} \end{pmatrix} = \begin{pmatrix} 0 & n^\top \\ \hat{P}^A_n - \frac{\partial \hat{P}}{\partial \hat{q}} \hat{q} & \frac{\partial \hat{P}^A_n}{\partial \hat{q}} \end{pmatrix}. \quad (1.14)$$

Herein we assumed that the pressure tensor can always be written in terms of normalized moments as $P^A[\rho, q] = \rho \hat{P}^A[\hat{q}]$.

1.2.2 Realizability

We have seen that there are certain bounds on the moments when they arise from a physically meaningful particle distribution $f(v) \geq 0$. For example, the magnitude of the normalized momentum $|\hat{q}|$ is between zero in the equilibrium and one in the free-streaming regime. Thus, not all vectors $\mathbf{u} \in \mathbb{R}^n$ are the moments of a positive distribution. The physically meaningful moment vectors are characterized by the following definition:

Definition 1.11 — Realizable moments. A moment vector \mathbf{u} is called realizable, if there exists a non-negative function $f(v) \geq 0$ that reproduces these moments: $\langle \mathbf{a} f \rangle = \mathbf{u}$. Any such function, of which there might be more than one, is called a representing distribution. The set of realizable moments is

$$\mathfrak{R}(\mathbf{a}) = \{ \mathbf{u} \mid \exists f(v) \geq 0 : \langle \mathbf{a} f \rangle = \mathbf{u} \}.$$

Finding an explicit characterization of the realizable set \mathfrak{R} , that is, determining if a vector is realizable, becomes increasingly difficult with higher order and space dimension [121]. Here, we give formulas for the first-order and second-order monomial basis. A moment vector (ρ, q) is realizable with respect to the monomial basis $(1, v)$, if and only if $\rho \geq 0$ and the normalized momentum is less than one, i.e., $|\hat{q}| = \frac{|q|}{\rho} \leq 1$. For the second-order basis we get the additional conditions that $\text{tr}(\hat{P}) = 1$ and the matrix $\hat{P} - \hat{q}\hat{q}^\top$ is positive semi-definite. Because the mass can be factored out of the moments, the set \mathfrak{R} can always be described by conditions on the normalized moments $\hat{\mathbf{u}}$ and the condition $\rho \geq 0$.

A given ansatz \mathfrak{f} might not be defined for all moment vectors \mathbf{u} .

Definition 1.12 — Ansatz space. The ansatz space

$$\mathfrak{A}(\mathbf{a}, \mathfrak{f}) = \{ \mathbf{u} \mid \exists \mathfrak{f}[\mathbf{u}] \}$$

includes all moments for which the ansatz $\mathfrak{f}[\mathbf{u}]$ is well-defined.

Ideally, we would like to have an ansatz with $\mathfrak{R}(\mathbf{a}) = \mathfrak{A}(\mathbf{a}, \mathfrak{f})$. Then the ansatz can produce all physically relevant moments, but nothing more.

1.2.3 Minimum entropy closures

Minimum entropy closures are proposed by Levermore [100, 102] in the context of gas kinetics. We point to [71] for a short summary of the method for linear kinetic equations. To respect the

entropy dissipation law (1.6) we want to take the ansatz \mathfrak{f} with minimal entropy. For a given entropy η , finding the ansatz that minimizes this entropy is an infinite-dimensional, constrained minimization problem:

$$\mathfrak{f} = \operatorname{argmin}_{g, \langle a g \rangle = u} \{ \langle \eta(g) \rangle \}.$$

With the help of the Legendre transform, this can be cast as a finite-dimensional, unconstrained minimization problem for the Lagrange multipliers instead.

Definition 1.13 — Legendre transform. The Legendre transform ϕ_* of a convex function $\phi : \mathbb{R}^n \mapsto \mathbb{R}$ is defined by

$$\phi_*(y) = \sup_{z \in \mathbb{R}^n} \{ y \cdot z - \phi(z) \}.$$

It has two important properties:

$$\begin{aligned} (\phi_*)_* &= \phi, \\ (\phi_*)' \circ \phi' &= I. \end{aligned}$$

The dual optimization problem is given by

$$\hat{\alpha}(u) = \operatorname{argmin}_{\alpha} \{ \langle \eta_*(\alpha \cdot a) \rangle - \alpha \cdot u \} =: \operatorname{argmin}_{\alpha} \{ F_u(\alpha) \}, \quad (1.15)$$

wherein α are the Lagrange multipliers for the moment constraints $\langle a \mathfrak{f} \rangle = u$ in the original optimization problem. Once the multipliers have been determined by the moments, the ansatz is given by

$$\mathfrak{f}[u] = \eta'_*(\hat{\alpha} \cdot a). \quad (1.16)$$

It can be shown that moment systems defined in this way are symmetric hyperbolic [101, 121]. Furthermore, the moment system is endowed with the entropy dissipation law

$$\partial_t h^{\mathfrak{f}} + c \nabla_x \cdot \eta^{\mathfrak{f}} \leq 0$$

with entropy $h^{\mathfrak{f}} = \langle \eta(\mathfrak{f}) \rangle$ and entropy flux $j^{\mathfrak{f}} = \langle v \eta(\mathfrak{f}) \rangle$. The ansatz that reconstructs the equilibrium moments u_E with minimal entropy is of course the equilibrium E itself. Because \mathfrak{f} minimizes the entropy, it is automatically equal to the equilibrium if the equilibrium moments are given: $\mathfrak{f}[u_E] = E$.

From the gradient $G_u := \frac{\partial F_u}{\partial \alpha} = \langle a \mathfrak{f}[u] \rangle - u$ of the objective function F_u we recover the moment constraints. Numerically, the optimization problem (1.15) is typically solved [59] with a stabilized Newton method for the equation $G_u(\hat{\alpha}) = 0$. The Newton method needs the symmetric positive definite Hessian

$$H_u(\alpha) = \left\langle \eta''_*(\alpha \cdot a) a a^T \right\rangle = \left\langle a \frac{\partial \mathfrak{f}}{\partial \alpha} \right\rangle$$

to calculate the descent direction. The integrals in the objective function, the gradient and the Hessian may have to be evaluated by a potentially costly high-order quadrature rule. Additionally, the Hessian can be poorly conditioned if the moments are close to the border of the realizable set [1].

The M_N method

The minimum entropy method with the Maxwell-Boltzmann entropy

$$\eta(f) = f \log(f) - f,$$

is the well-known M_N method [42]. The Legendre dual is in this case simply $\eta_*(f) = \exp(f)$ and the ansatz according to (1.16) is of exponential form

$$\hat{f}[\mathbf{u}] = \exp(\boldsymbol{\alpha} \cdot \mathbf{a}).$$

This ansatz is always positive and all moments reconstructed from it are automatically realizable. Furthermore, Junk showed in [83] that the ansatz space is equal to the set of realizable moments: $\mathfrak{R}(\mathbf{a}, \hat{f}) = \mathfrak{R}(\mathbf{a})$. For each realizable moment vector $\mathbf{u} \in \mathfrak{R}(\mathbf{a})$ there exists a unique vector of multipliers $\hat{\boldsymbol{\alpha}}(\mathbf{u})$ such that the ansatz reproduces the moments. The objective function, gradient, and Hessian in the optimization problem (1.15) are

$$\begin{aligned} F_{\mathbf{u}} &= \langle \exp(\boldsymbol{\alpha} \cdot \mathbf{a}) \rangle - \boldsymbol{\alpha} \cdot \mathbf{u}, \\ G_{\mathbf{u}} &= \langle \exp(\boldsymbol{\alpha} \cdot \mathbf{a}) \mathbf{a} \rangle - \mathbf{u}, \\ H_{\mathbf{u}} &= \langle \exp(\boldsymbol{\alpha} \cdot \mathbf{a}) \mathbf{a} \mathbf{a}^T \rangle. \end{aligned}$$

For a first-order monomial basis, the exponential ansatz becomes

$$\hat{f} = \exp(a + b \cdot v),$$

with multipliers $a \in \mathbb{R}, b \in \mathbb{R}^3$. These follow from the solution of the nonlinear moment constraints (1.12):

$$\begin{aligned} \langle \exp(a + b \cdot v) \rangle &= \rho, \\ \langle v \exp(a + b \cdot v) \rangle &= q. \end{aligned}$$

We can compute the multipliers b independently of a via

$$\frac{\langle v \exp(b \cdot v) \rangle}{\langle \exp(b \cdot v) \rangle} = \frac{q}{\rho} = \hat{q}.$$

The resulting pressure tensor has the form $P^A[\rho, q] = \rho \hat{P}^A[\hat{q}]$. When the equilibrium moments $\mathbf{u}_E = (\rho, 0)$ are given, the M_1 -pressure tensor

$$P^A = \frac{\rho}{3} I_3$$

equals the exact pressure tensor $P = \langle v v^T E \rangle$.

The P_N method

The quadratic entropy

$$\eta(f) = \frac{1}{2} f^2$$

leads to a linear ansatz

$$\hat{f}[\mathbf{u}] = \hat{\boldsymbol{\alpha}} \cdot \mathbf{a},$$

which minimizes the L^2 -norm:

$$\hat{f} = \operatorname{argmin}_{g, \langle ga \rangle = u} \left\{ \frac{1}{2} \langle g^2 \rangle \right\}.$$

This is the classical P_N method [21] [114, Chapter III, Section 5].

Finding multipliers $\hat{\alpha}$ such that (1.12) is fulfilled is the linear problem

$$\langle \hat{\alpha} \cdot \mathbf{a} \mathbf{a}^\top \rangle = \langle \mathbf{a} \mathbf{a}^\top \rangle \hat{\alpha} = \mathbf{u}.$$

With an orthonormal basis, such as the spherical harmonics (see Section A.4), the matrix $\langle \mathbf{a} \mathbf{a}^\top \rangle = I$ becomes the identity, and the optimization problem reduces to

$$\alpha = \mathbf{u}.$$

This also shows that all moment vectors $\mathbf{u} \in \mathbb{R}^n$ can be reproduced by the linear ansatz. It is well-known that solutions to the P_N equations can develop negative density [106], which fits with the observation $\mathfrak{A}(\mathbf{a}, \hat{f}) = \mathbb{R}^n \supset \mathfrak{R}(\mathbf{a})$.

The flux moments for the P_N method are

$$\begin{aligned} \langle v \mathbf{a}^\top \hat{f} \rangle &= \langle v \mathbf{a}^\top \alpha \cdot \mathbf{a} \rangle \\ &= \langle v \otimes \mathbf{a} \otimes \mathbf{a} \rangle \langle \mathbf{a} \mathbf{a}^\top \rangle^{-1} \mathbf{u}. \end{aligned}$$

The flux Jacobian is the tensor $\langle v \otimes \mathbf{a} \otimes \mathbf{a} \rangle \langle \mathbf{a} \mathbf{a}^\top \rangle \in \mathbb{R}^{3 \times n \times n}$ in which the last component of $\langle v \otimes \mathbf{a} \otimes \mathbf{a} \rangle$ is contracted with the first component of $\langle \mathbf{a} \mathbf{a}^\top \rangle^{-1}$.

Using a first-order monomial basis, the ansatz becomes

$$\hat{f} = a + b \cdot v.$$

The multipliers a, b are the solution of the linear moment constraints

$$\begin{pmatrix} \langle 1 \rangle & \langle v^\top \rangle \\ \langle v \rangle & \langle v v^\top \rangle \end{pmatrix} \begin{pmatrix} a \\ b \end{pmatrix} = \begin{pmatrix} \rho \\ q \end{pmatrix}.$$

The formulas in Section A.2 yield

$$4\pi \begin{pmatrix} 1 & 0 \\ 0 & \frac{1}{3} I_3 \end{pmatrix} \begin{pmatrix} a \\ b \end{pmatrix} = \begin{pmatrix} \rho \\ q \end{pmatrix},$$

with the solution $a = \frac{1}{4\pi} \rho$, $b = \frac{3}{4\pi} q$. Therefore, we obtain the explicit formula

$$\hat{f}[\rho, q] = \frac{1}{4\pi} (\rho + 3q \cdot v),$$

for the ansatz. The pressure tensor in the P_1 equations is

$$P^A[\rho, q] = \frac{1}{4\pi} \langle v v^\top (\rho + 3q \cdot v) \rangle = \frac{\rho}{3} I_3.$$

It does not depend on the momentum q . When $|\hat{q}| > \frac{1}{\sqrt{3}}$, the moments (ρ, q, P) are not realizable, because the matrix $\hat{P} - \hat{q} \hat{q}^\top$ is not positive definite. This can lead to unphysical zeroth and first moments, for example, a negative density [72].

Using formula (1.14) for the flux Jacobian, we have

$$J\mathcal{F}_n = \begin{pmatrix} 0 & n^\top \\ \frac{1}{3}n & 0 \end{pmatrix}.$$

An eigendecomposition of $J\mathcal{F}_n$ shows that there are two longitudinal waves with speed $\pm \frac{1}{\sqrt{3}}$ and two transversal waves with speed 0. In the free-streaming limit, the kinetic equation just transports the initial mass with unit speed along the direction q^* . Clearly, in this case the P_1 model underestimates the forward propagation speed.

1.2.4 Kershaw closures

The Kershaw closure [86] for the first-order moment system (1.13) constructs the pressure tensor P^A directly from the known moments ρ, q such that the second-order moments (ρ, q, P^A) are realizable. Kershaw shows that the moments in the resulting system stay realizable. A convex combination of isotropic and free-streaming pressure tensors is one possible construction of a Kershaw closure. The normalized isotropic pressure tensor is $\hat{P}_E = \frac{1}{3}I$. Let $q^* = \frac{\hat{q}}{|\hat{q}|}$ be the mean direction of particles. If all particles moved in that direction, the distribution would be $f(v) = \delta_{q^*}(v)$ and the corresponding normalized free streaming moments are $\hat{P}_{\delta(q^*)} = q^* q^{*\top}$. A pressure tensor that respects the realizability constraints is given by the convex combination

$$\hat{P}^A = \alpha \hat{P}_E + (1 - \alpha) \hat{P}_{\delta(q^*)},$$

with $\alpha = 1 - |\hat{q}|^2$, which reads

$$\hat{P}^A = (1 - |\hat{q}|^2) \frac{1}{3}I + \hat{q} \hat{q}^\top.$$

The moments \hat{P}^A are realizable because $\text{tr} \hat{P}^A = 1$ and

$$\hat{P}^A - \hat{q} \hat{q}^\top = (1 - |\hat{q}|^2) \frac{1}{3}I$$

is positive definite when the first-order moments are realizable, i.e., when $|\hat{q}| \leq 1$ holds. Not only does this procedure construct the correct pressure tensor for isotropic moments, but also when the moments correspond to the free-streaming situation. Furthermore, the resulting system is strictly hyperbolic for all \hat{q} in the interior of the realizable set. Kershaw computes the eigenvalues of $J\mathcal{F}_n$ and shows that they take all values between -1 and 1 , which is exactly the range of characteristic velocities of the transport equation. When $\hat{q} = 0$, the characteristic field is identical to that of the P_1 system: longitudinal waves move at speed $\pm \frac{1}{\sqrt{3}}$, independently of the direction n . But in the free-streaming limit with $\hat{q} = q^*$, looking parallel to the movement direction $n = q^*$, the longitudinal waves move at speeds 1 and $\frac{1}{3}$.

1.2.5 The diffusion limit of the first-order moment system

The first-order moment system (1.13) in parabolic scaling reads

$$\begin{aligned} \partial_t \rho + \frac{1}{\varepsilon} \nabla_x \cdot q &= 0, \\ \partial_t q + \frac{1}{\varepsilon} \nabla_x \cdot P &= \frac{1}{\varepsilon^2} C. \end{aligned}$$

When ε is small, the kinetic distribution f is close to the equilibrium, and we write $f = \frac{1}{\langle 1 \rangle} \rho + \varepsilon g$. At least in this situation the moment system should adequately approximate the kinetic equation. Of course, in the limit $\varepsilon \rightarrow 0$ the moment system should converge to the same diffusion equation as the kinetic equation. In the following, we derive necessary conditions that the kinetic equation and the ansatz must fulfill to achieve the correct diffusion limit. A rigorous proof of the diffusion limit of the M_1 system can be found in [37].

The natural condition for the ansatz \tilde{f} is that it should reproduce the equilibrium distribution, i.e., $\tilde{f}[\rho, 0] = \frac{\rho}{\langle 1 \rangle}$. As discussed in Section 1.2.3, all ansätze of minimum-entropy form have this property by construction. This automatically implies that the moments

$$\begin{aligned} P^A[\rho, 0] &= P\left(\frac{\rho}{\langle 1 \rangle}\right) = \rho \frac{\langle v v^\top \rangle}{\langle 1 \rangle} = \frac{\langle v_\xi^2 \rangle}{\langle 1 \rangle} \rho I, \\ C^A[\rho, 0] &= C\left(\frac{\rho}{\langle 1 \rangle}\right) = \rho \left\langle v \mathcal{L}\left(\frac{1}{\langle 1 \rangle}\right) \right\rangle = 0 \end{aligned}$$

are reproduced exactly in this situation. When no ansatz is made, we just pose these conditions on the moments directly.

We can say more about the ansatz function close to the isotropic point. From the decomposition $f = \frac{\rho}{\langle 1 \rangle} + \varepsilon g$, we see that $q = \varepsilon \langle v g \rangle =: \varepsilon q^1$ is of the order ε . The Taylor expansion in q around the isotropic point $q = 0$ is

$$\tilde{f}[\rho, q] = \frac{\rho}{\langle 1 \rangle} + \varepsilon \left. \frac{\partial \tilde{f}}{\partial q} \right|_{q=0} q^1 + \dots$$

But \tilde{f} must fulfill the moment constraints. This means that

$$q = \langle v \tilde{f} \rangle = \varepsilon \left\langle v \left. \frac{\partial \tilde{f}}{\partial q} \right|_{q=0} \right\rangle q^1$$

must hold which in turn is fulfilled when $\left\langle v \left. \frac{\partial \tilde{f}}{\partial q} \right|_{q=0} \right\rangle = I$. We see that

$$\left. \frac{\partial \tilde{f}}{\partial q} \right|_{q=0} = \frac{v^\top}{\langle v_\xi^2 \rangle}.$$

Now we derive the diffusion limit of the closed moment system. To even have a limit, the moment system must have an entropy dissipation (recall Section 1.1.2), which is the case for the P_1 and M_1 method. Matching terms in the momentum equation order by order, we have for ε^{-2} simply $C^A[\rho, 0] = 0$. This is the discrete version of the condition that the kinetic distribution is in the nullspace of the collision operator, $f \in \mathcal{N}(\mathcal{L})$. As we have seen above, the condition is always fulfilled when C^A is computed with an ansatz that reproduces the equilibrium. The order ε^{-1} terms provide us with

$$\nabla_x \cdot P^A[\rho, 0] = \left. \frac{\partial C^A}{\partial q} \right|_{q=0} q^1$$

equivalent to

$$q^1 = \frac{\langle v_\xi^2 \rangle}{\langle 1 \rangle} \left(\left. \frac{\partial C^A}{\partial q} \right|_{q=0} \right)^{-1} \nabla_x \rho.$$

We obtain the derivative of C in the isotropic point via

$$\left. \frac{\partial C^A}{\partial q} \right|_{q=0} = \left\langle v \mathcal{L} \left(\left. \frac{\partial \tilde{f}}{\partial q} \right|_{q=0} \right) \right\rangle = \frac{1}{\langle v_\xi^2 \rangle} \langle v \mathcal{L}(v^\top) \rangle.$$

Finally, the order ε^0 terms in the mass equation are

$$\partial_t \rho + \nabla_x \cdot q^1 = \partial_t \rho - \nabla_x \cdot (\hat{D}^A \nabla_x \rho) = 0$$

with the diffusion tensor

$$\hat{D}^A = -\frac{\langle v_\xi^2 \rangle^2}{\langle 1 \rangle} \langle v \mathcal{L}(v^\top) \rangle^{-1}.$$

Compare this to the diffusion tensor $\hat{D} = -\frac{1}{\langle 1 \rangle} \langle v \mathcal{L}^{-1}(v) \rangle$ of the kinetic equation (see (1.10)). If v is an eigenfunction of the collision operator to the negative eigenvalue $-\gamma$, that is $\mathcal{L}(v) = -\gamma v$, then we have also $\mathcal{L}^{-1}(v) = -\frac{1}{\gamma} v$. In this case, the diffusion tensors are equal: $\hat{D}^A = \hat{D} = \frac{\langle v_\xi^2 \rangle}{\gamma \langle 1 \rangle} I$. Therefore, we make the additional assumption for the collision operator:

Assumption 1.14 The turning operator \mathcal{L} from Definition 1.3 has v as an eigenfunction, i.e., there is a $\gamma > 0$ such that

$$\mathcal{L}(v) = -\gamma v.$$

The same assumption is also made in [37]. It is fulfilled if the turning kernel only depends on the angle $\cos(\theta) = v \cdot v'$ between directions, and not on the absolute direction v' before turning:

Lemma 1.15 All turning operators \mathcal{L} with a kernel of the form $K(v, v') = K(v \cdot v') = K(\mu)$ fulfill the eigenvalue equation

$$\mathcal{L}(v) = -\gamma v,$$

with eigenvalue $-\gamma = g - 1$. Herein

$$g = 2\pi \int_{-1}^1 K(\mu) \mu d\mu$$

is the mean cosine of the turning angle.

Proof. First, we show

$$\mathcal{K}(v) = gv.$$

The claim then follows from $\mathcal{L} = \mathcal{K} - I$.

Let R_v be a rotation matrix that rotates the unit vector $e_3 = (0, 0, 1)^\top$ onto v : $R_v e_3 = v$. Expressing $v' = R_v \tilde{v}'$ in this basis, we have

$$\begin{aligned} \mathcal{K}(v) &= \int_{\mathbb{S}^2} K(v \cdot v') v' dv \\ &= R_v \int_{\mathbb{S}^2} K(e_3 \cdot \tilde{v}') \tilde{v}' d\tilde{v}'. \end{aligned}$$

With the parametrization $\tilde{v}' = (\sqrt{1 - \tilde{\mu}'^2} \cos(\tilde{\phi}'), \sqrt{1 - \tilde{\mu}'^2} \sin(\tilde{\phi}'), \tilde{\mu}')^\top$, this becomes

$$R_v \int_{-1}^1 \int_0^{2\pi} K(\tilde{\mu}') \begin{pmatrix} \sqrt{1 - \tilde{\mu}'^2} \cos(\tilde{\phi}') \\ \sqrt{1 - \tilde{\mu}'^2} \sin(\tilde{\phi}') \\ \tilde{\mu}' \end{pmatrix} d\tilde{\phi}' d\tilde{\mu}' = R_v \begin{pmatrix} 0 \\ 0 \\ 2\pi \int_{-1}^1 K(\tilde{\mu}') \tilde{\mu}' d\tilde{\mu}' \end{pmatrix} = g R_v e_3 = g v.$$

■

To demonstrate that the diffusion tensor of the moment system can differ from the diffusion tensor of the kinetic equation when Assumption 1.14 is not fulfilled, we show the following example.

■ **Example 1.16 — Bad diffusion approximation.** The kernel

$$K_w = \frac{1}{2\pi} \left[\frac{45}{4096} (\mu + 1)^4 (\mu' + 1)^4 - \frac{9}{256} (\mu + 1)^4 - \frac{9}{256} (\mu' + 1)^4 + \frac{49}{80} \right]$$

fulfills all properties of Definition 1.2, but we have

$$\mathcal{L}(v) = \begin{pmatrix} -v_\xi \\ -v_\eta \\ \frac{1}{320} [-33 - 260\mu + 90\mu^2 + 60\mu^3 + 15\mu^4] \end{pmatrix},$$

thus v is not an eigenvector of the collision operator. Symbolic computations yield the diffusion tensor of the moment system

$$\hat{D}^A = -\frac{4\pi}{9} \langle v \mathcal{L}(v^\top) \rangle^{-1} = \begin{pmatrix} \frac{1}{3} & 0 & 0 \\ 0 & \frac{1}{3} & 0 \\ 0 & 0 & \frac{10}{21} \end{pmatrix}.$$

By symbolic calculations it can be verified that the solution to $\mathcal{L}(w) = v$ is

$$w(v) = \begin{pmatrix} -v_\xi \\ -v_\eta \\ \frac{1}{64} [11 - 84\mu - 30\mu^2 - 20\mu^3 - 5\mu^4] \end{pmatrix}$$

which gives the diffusion tensor for the kinetic equation:

$$\hat{D} = -\frac{1}{4\pi} \langle v w^\top \rangle = \begin{pmatrix} \frac{1}{3} & 0 & 0 \\ 0 & \frac{1}{3} & 0 \\ 0 & 0 & \frac{1}{2} \end{pmatrix}.$$

These tensors differ indeed in their last component by $\frac{1}{42}$.

The diffusion tensor of the kinetic equation contains moments of the inverse \mathcal{L}^{-1} . In the moment system, this is approximated by the inverse of the moments of \mathcal{L} . When Assumption 1.14 is not fulfilled, a higher-order moment system may provide a better approximation.

Similar computations as before yield the diffusion tensor of the P_N system:

$$\hat{D}^A = -\frac{1}{\langle 1 \rangle} \mathcal{P} \langle p p^\top \rangle \langle p \mathcal{L}(p^\top) \rangle^{-1} \langle p v^\top \rangle,$$

wherein \mathbf{p} is the basis \mathbf{a} excluding the constant function $\mathbf{a}^{(0)} = 1$ and $\mathcal{P}\mathbf{m} = \mathbf{q}$ projects the moment vector $\mathbf{m} = \langle \mathbf{p} \mathbf{f} \rangle$ onto the momentum $\mathbf{q} = \langle \mathbf{v} \mathbf{f} \rangle$. We return to the previous Example 1.16:

■ **Example 1.17 — Bad diffusion approximation.** With the kernel from Example 1.16, the diffusion tensors for the P_2 and P_3 moment systems are

$$\hat{D}^{P_2} = \begin{pmatrix} \frac{1}{3} & 0 & 0 \\ 0 & \frac{1}{3} & 0 \\ 0 & 0 & \frac{445}{894} \end{pmatrix},$$

$$\hat{D}^{P_3} = \begin{pmatrix} \frac{1}{3} & 0 & 0 \\ 0 & \frac{1}{3} & 0 \\ 0 & 0 & \frac{1}{2} \end{pmatrix}.$$

The P_2 -diffusion tensor is closer to the correct tensor than the P_1 -tensor. For this particular kernel, the P_3 -system already produces the correct diffusion tensor, which is not too surprising, considering that the kernel has a polynomial form.

2

Biological and medical aspects of glioma

I itch all the time. Deep beneath my skin, where the bone sits enshrined in flesh I feel it. Something, not moving, but that wants to move, wants to be free. It itches; and I don't think I want it. [...] I need it to be seen, to be seen in the cold light of knowledge, which is anathema to the things that crawl and slither and swarm in the corners and cracks [...]

Jonathan Simms — The Magnus Archives (Ep. 32)

To put the model in Chapter 3 in context, to see where it makes assumptions, how it could be improved and to appreciate its simplicity, we review some aspects of glioma growth and the associated mathematical models. There are two levels of description to consider. On the one hand, noninvasive medical imaging tools (see Section 2.3) provide information on the macroscopic structure of the tumor. On the other hand, this structure is the result of microscopic interactions between individual tumor cells and their environment, which are in turn mediated by complicated molecular processes inside the cell. Information about tumor composition can only be gained by invasive procedures, i.e., by a biopsy and histological examination of tissue samples.

2.1 Aspects of glioma growth

2.1.1 Macroscopic characteristics

As their name suggests, *GBM* come in a variety of shapes and growth patterns. Figure 2.1 displays some examples. Tumors can grow into round (Figure 2.1a) or irregular shapes (Figure 2.1b). The butterfly pattern (Figure 2.1c) typically occurs when the tumor grows on both hemispheres. It is possible that small groups of glioma infiltrate distant regions of the brain and start another growth site (Figure 2.1d). Cystic tumors (Figure 2.1e) grow compact, whereas a diffuse infiltration leads to the gliomatosis cerebri growth pattern (Figure 2.1f).

Tumor growth has several stages. At first, the tumor forms a small compact nucleus [51]. When it reaches a critical size, the tumor center becomes necrotic due to lack of oxygen and nutrients. It is hypothesized [23, 130] that this also marks the onset of diffuse infiltration. At later stages, glioblastoma are characterized by a central necrotic region, a ring of so-called enhancing tumor, which gives bright signal on contrast enhanced T1-MRI (see Section 2.3), and possibly an edema [51]. To secure its oxygen supply the tumor forms new blood vessels, a process which is termed angiogenesis. These permit the contrast agent to enter the brain due to an initially

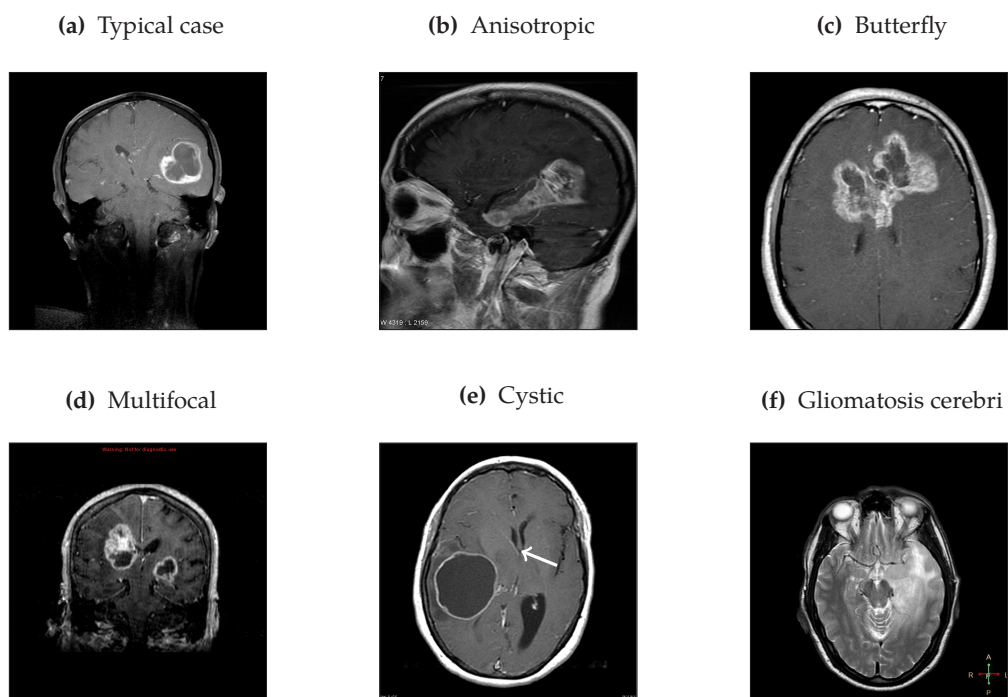


Figure 2.1: Growth patterns of GBM as seen on MRI. Figures 2.1a to 2.1d are contrast enhanced T1 images, Figure 2.1f is a T2 image. The white arrow (not in the original image) in Figure 2.1e points to visible mass effect. Images are taken from [Radiopaedia.org](https://radiopaedia.org). For full credits, see the Image Credits at the end of the document.

underdeveloped blood-brain barrier, hence the bright signal [56]. Larger tumors displace the surrounding healthy tissue. The resulting deformation of the brain, which is for example visible in Figure 2.1e, is called mass effect.

2.1.2 Microscopic processes

An exhaustive review of the microscopic processes involved in tumor formation would be outside the scope and purpose of this thesis. We sketch a few selected aspects in broad strokes to put the model in Chapter 3 in context. Most important is the fact that glioma cells migrate along a number of invasion routes, for instance along blood vessels and white matter tracts [55]. The reason why tumor cells are able to migrate may lie in their origin from mutated glial progenitor cells [120]. Glial progenitors differentiate into astrocytes, oligodendrocytes and ependymal cells. Each type fulfills a supporting function for neurons, for instance, astrocytes provide nutrition and constitute the blood-brain barrier. Gliomas are classified accordingly as astrocytoma, oligodendroglioma or ependymoma [117]. To complicate matters, multiple cell types can be present in one glioma.

The p53 gene prevents mutations from DNA damage to spread [90]. If a cell's DNA is damaged, p53 protein is produced which will cause the cell to either repair the damage or initiate apoptosis. If the p53 gene itself is damaged, this protection mechanism does not work and the mutant cell can proliferate. This may be one factor in cancer development and it also implies that cancer cells with a defect p53 gene are subject to further mutations. As a result, tumors are generally heterogeneous and consist of cells with numerous phenotypes [125].

The ECM provides structural support to glia and neurons. It consists largely of fibrous proteins such as collagen [117]. Cells can bind receptors on their surface—so-called integrins¹—to the fibronectin in ECM. Glioma cells migrate along the fibers by repeatedly attaching to ECM at the front, detaching integrins at the back and shifting their body forward [53].

According to [54], cell motion can be roughly classified into several modes. Which mode is preferred depends on the cell's environment and neighboring cells, and the modes themselves are not sharply separated. Amoeboid migration is an individual migration characterized by a low adhesion to ECM and other cells that predominantly occurs in a loose and randomly oriented environment. Mesenchymal motion is preferred in dense and oriented ECM [12]. If the fibers are too dense or do not provide suitable attachment points, some cells may chemically 'cut' the fibers, thus remodeling the environment more in their favor [53]. This process is called proteolysis. The mesenchymal mode is important for glioma migration inside white matter because there is evidence [12] that the white matter is indeed packed tightly with pore diameters even smaller than cell diameters. Collective migration of glioma cells along blood vessels [55] can be identified with the collective strand migration mode [54]. Finally, epithelial migration is a collective motion in form of sheets or clusters, when stable cell-cell adhesions are in place. Epithelial-mesenchymal transition as well as mesenchymal-amoeboid transition have been observed in glioma cells [113]. Numerous chemical compounds produced and absorbed by the tumor also influence its development. As all cells, glioma cells need oxygen and nutrients to survive and proliferate. If these factors are absent, the cells die, which eventually leads to the development of a necrotic core. To keep up their supply, glioma cells secrete growth factors that stimulate the growth of blood vessels. As a byproduct of their changed metabolism, which favors faster proliferation over

¹We do not differentiate further between the various types of integrins.

energy efficiency, tumor cells produce acid [89]. The acid itself inhibits proliferation and acts as a chemorepellant, i.e., the tumor cells preferentially move away from acidic environments. Last but not least, tumors compete with the immune system [15].

2.2 Mathematical models for tumor growth

2.2.1 The cell's perspective

We focus on models for cell-ECM interactions and the resulting cellular movement. But for the sake of completeness, we point to Metzcar et al. [107] who review cell-based models for cancer growth that feature many of the previously discussed effects, including angiogenesis, differentiation from stem cells and epithelial-mesenchymal transition. Anderson [3] proposes a hybrid model—cells are modeled as individuals, whereas chemicals are modeled as a continuum—for heterogeneous tumor populations, taking proteolysis and oxygen concentrations into account.

One of the earliest to describe haptotaxis, movement stimulated by a fixed chemical signal, was Carter [26] in 1967. He observed the movement of cells on coated glass and modeled haptotaxis as a result of surface tensions between the cell, the surface and the surrounding medium. This simple mechanical model corresponds to the amoeboid migration mode. Another mechanical model for haptotaxis is proposed by Dickinson and Tranquilo [41]. In their model, cellular movement is the result from forces generated by cell-surface attachments. They consider a fixed cell geometry and divided it into a few regions. In each region, binding and unbinding of receptors is subject to a stochastic process, with the transition probabilities determined by the concentration of adhesion sites. In a gradient, different regions of the cell sense different concentrations of adhesion sites, thus a net force is produced. The result is a Brownian motion with preference to migrate along the gradient. Recently, Uatay [133] developed a model along the same lines that is specific to interactions between glioma cells and ECM. The model considers also the internal structure of cells, specifically individual stress fibers forming between adhesion sites which are responsible for movement of the cell body after detachment of the rear. Stochasticity enters the model in the binding and unbinding of cell-ECM connections; the motion between those events is a deterministic result of the internal and external forces. This leads to a run-and-tumble motion, a model that is compatible with the multi-scale description in the [next chapter](#). Indeed, Uatay also derives intermediate and macroscopic descriptions from the particle model. Two important features of glioma migration are reproduced by this model, namely movement along gradients of fiber concentration and contact guidance. Contact guidance is the preference of cells to move parallel to directed fibers.

2.2.2 The doctor's perspective

Harpold et al. [69] review the development of macroscopic tumor models. A simple model [23] features a homogeneous reaction-diffusion equation for the cell density $\rho_0(t, x)$ with an exponential growth term

$$\partial_t \rho_0 + \nabla_x \cdot (D \nabla_x \rho_0) = \mu \rho_0,$$

in which D is a scalar and constant diffusion coefficient. Assuming a point initial condition, there is an analytic solution to this model. Although this model cannot predict the anisotropic

growth patterns of glioblastoma, it is still useful to assess the influence of diffusion and growth on survival time and the visible fraction of tumor cells. Essentially, the fraction $\frac{D}{\mu}$ determines the detectable fraction of tumor, whereas the product $D\mu$ determines the speed of the invasion front [69]. High-grade tumors grow fast and diffuse, hence they are characterized by large $\frac{D}{\mu}$ and $D\mu$. A first step towards the prediction of anisotropic growth patterns is the model by Swanson [130]. This model assigns different values to $D(x)$ inside gray and white matter. The assumed five-fold diffusion speed in white matter as opposed to gray matter is purely phenomenological.

The next logical step is to simulate migration along white matter tracts with an anisotropic diffusion tensor $D(x) : \mathbb{R}^3 \mapsto \mathbb{R}^{3 \times 3}$. Jbabdi [78] estimates tumor diffusion tensors from DTI measurements of water diffusion (see Section 2.3). The construction of tumor diffusion tensors uses the shape indices (2.3) to increase anisotropy in fiber directions. This procedure does not take any microscopic phenomena into account.

For therapy, it is more important to resolve the invasion front than the complete tumor volume. Therefore, the model by Mosayebi et al. [108] tracks only this front, using the Fisher approximation for reaction-diffusion systems. Hoge et al. present an approach to include the mass effect in the model [75]. They consider a reaction-diffusion model for the tumor growth coupled with the description of brain matter as a linear elastic material.

A review of comparative studies between patient data and mathematical models can be found in [108, 129]. Swan et al. [129] additionally provide comparisons between Swanson's model [130] and the anisotropic infiltration model by Painter et al. [112]. They compare model simulations to clinical tumor segmentations of ten patients.

2.2.3 Multi-scale descriptions

The microscopic cell-based models are useful to observe the fundamental mechanisms of cell migration in detail. But it is not feasible to model entire tumor populations that consists of 10^8 cells in this detail. The macroscopic models we reviewed are better suited for this task, however, they are mostly based on observations on the gross tumor behavior. Multi-scale descriptions consist of a hierarchy of models. Thus, the population dynamics follow from a microscopic description of cell migration via a scaling limit.

A description based on kinetic PDEs is a helpful intermediate step to derive macroscopic models. The quantities of interest are particle distribution functions $p(t, x, v, y)$ that describe the expected number of particles in a potentially high-dimensional state space. The KTAP [13, 14] is a general framework to model systems of living entities directly on this meso-scale. In this framework, functional subsystems serve as the basic building blocks. The following definition is taken directly from [14]:

Definition 2.1 — Functional subsystem. A functional subsystem is a collection of active particles, which have the ability to express the same activity, which is regarded as a scalar variable. The whole system is constituted by several interacting functional subsystems.

In classical kinetic theory, particles are passive, that is, they only obey the laws of mechanics and are fully described by the mechanical variables x and v . The active particles in KTAP express an additional function. This is modeled by the scalar activity variable y . Bellomo et al. model for example the competition between tumor cells and the immune system [13, 15] using four functional subsystems, one for immune cells, one for endothelial cells and two for different

species of tumor cells.

In the [next chapter](#), we discuss the multi-scale model by Engwer et al. [44, 46] in detail. The model only considers interactions between tumor cells and the [ECM](#). We justify some assumptions therein by observations from Uatay's haptotaxis model [133]. The haptotaxis model also fits into the [KTAP](#) framework. There is only one functional subsystem, namely the population of tumor cells. The activity variable models the fraction of integrins that are bound to [ECM](#). The [ECM](#) takes the place of an outer system in the framework: its distribution is known and does not evolve in time. In [Section 4.3.5](#) we promote the fiber distribution to a functional subsystem and include proteolysis in the model. In a recent work [35], the effects of necrosis, acid production and proteolysis are also included into the model.

2.3 Diffusion tensor imaging

[MRI](#) is a standard tool for diagnosis of brain tumors and the subsequent planning of therapy. It is a rich source of three-dimensional data that is readily available input for mathematical models. In contrast to [computed tomography \(CT\)](#), [MRI](#) is especially useful to differentiate soft tissues as found in the brain. The tissue to be probed is placed in a strong magnetic field, which aligns the atomic nuclei therein. After excitation with a radiofrequency pulse, the nuclei are turned out of the direction of the magnetic field but realign to the base state at a tissue dependent rate. Measurements of the alignment shortly after the excitation produces a grayscale image with voxels of 1 mm to 2 mm side length. Measurement procedures can be varied a lot to produce images with different weighting, encoding different tissue properties². Radiopaedia [56] is an excellent online source of information on [MRI](#) for radiologists. With a combination of such images at hand, the radiologist can assign a tissue type to each voxel, for example gray matter, white matter, living tumor, or necrotic tumor.

[DTI](#) is an [MRI](#) sequence that measures the anisotropic diffusion of water in the tissue in form of a symmetric positive-definite diffusion tensor $D_W \in \mathbb{R}^{3 \times 3}$. In a magnetic field modulated with a gradient, the signal that water molecules generate on [MRI](#) depends on their movement speed in gradient direction. Hence, to measure the diffusion tensor of water one needs at least six such images [95]. Because tissue restricts the diffusion of water, the water diffusion tensor indirectly provides directional information on the tissue.

The glioma model [44] that we discuss in [Chapter 3](#) models the interaction of cells with the [ECM](#) in white matter. The myelinated axon bundles in white matter let water molecules diffuse relatively freely in fiber direction but restrict diffusion perpendicular to the fiber. Therefore, [DTI](#) data can be used to estimate directional information on the fibers.

On the microscopic scale, tissue is not homogeneous. Water diffusion is different in the intracellular compartment, i.e., inside the cells, and the extracellular compartment, i.e., the space between the cells, which is occupied by [ECM](#). [DTI](#) provides only one diffusion tensor per voxel, which has to be interpreted as a weighted average over the compartments and tissue types. Furthermore, a diffusion tensor cannot resolve two fibers that intersect in a voxel.

²Two relaxation times are involved. The time to realign the net magnetization, and the time the precession of magnetization vectors loses phase coherence after excitation. Sequences attuned to these times produce the T1 and T2 weighted images, respectively.

2.3.1 Scalar diffusion quantities

From the full tensor information, several scalar quantities can be derived. These are useful to visualize the tensor data and can also help with tumor diagnosis and assessment of its malignancy grade [88, 128]. Let $\lambda_1 \geq \lambda_2 \geq \lambda_3 \geq 0$ denote the eigenvalues of the diffusion tensor D_W . The **apparent diffusion coefficient (ADC)**

$$\text{ADC} = \text{tr}(D_W) = \sum_{i=1,2,3} \lambda_i$$

measures the total diffusion independent of the direction. The anisotropy of a diffusion tensor can be measured in several ways. A popular measure is the **fractional anisotropy (FA)**

$$\text{FA} = \left(\frac{3 \sum_{i=1}^3 (\lambda_i - \bar{\lambda})^2}{2 \sum_{i=1}^3 \lambda_i^2} \right)^{\frac{1}{2}}, \quad (2.1)$$

wherein $\bar{\lambda} = \frac{1}{3} \text{tr}(D_W)$ is the average eigenvalue. **FA** is zero for isotropic diffusion $\lambda_1 = \lambda_2 = \lambda_3$, one for completely degenerate diffusion $\lambda_2 = \lambda_3 = 0$, and takes intermediate values in all other situations. Under the assumption that diffusion in **ECM** fibers is degenerate and diffusion outside of fibers is isotropic, the **FA** serves as a rough estimate of the volume fraction that is occupied by fibers. In [45], a different estimate for the volume fraction is proposed. This is based on the estimation of a characteristic diffusion length scale and is defined as

$$\text{CL} = 1 - \left(\frac{\text{tr}(D_W)}{4\lambda_1} \right)^{\frac{3}{2}}. \quad (2.2)$$

The **characteristic length estimate (CL)** ranges from $1 - \left(\frac{3}{4}\right)^{\frac{3}{2}} \approx 0.35$ for isotropic diffusion to $1 - \left(\frac{1}{4}\right)^{\frac{3}{2}} = \frac{7}{8} = 0.875$ for degenerate diffusion. The **FA** and **CL** estimates are shown for the Camino [30] DTI data set in Figure 2.3.

To visualize a diffusion tensor, the associated ellipsoid, i.e., the isosurface of $v^T D_W^{-1} v = 1$, is helpful. If there is one dominating eigenvalue, the ellipsoid has an elongated form with the axis in direction of the eigenvector corresponding to λ_1 . If two eigenvalues are of the same order of magnitude, and one eigenvalue is much smaller, the ellipsoid has a flat shape. When all eigenvalues are the same, the ellipsoid is a sphere. These situations are encoded in the linear, planar, and spherical shape indices [78]

$$\text{LSI} = \frac{\lambda_1 - \lambda_2}{\text{tr}(D_W)}, \quad \text{PSI} = \frac{2(\lambda_2 - \lambda_3)}{\text{tr}(D_W)}, \quad \text{SSI} = \frac{3\lambda_3}{\text{tr}(D_W)}. \quad (2.3)$$

These indices are in the interval zero to one and sum to one. Examples of ellipsoids and corresponding shape indices are shown in Figure 2.2.

2.3.2 Estimates for the fiber distribution

A model for the interactions of glioma cells with the **ECM** fibers requires directional information about the fibers. In diffusion-MRI at least six gradient images are needed to estimate a diffusion tensor, but typical data sets are sampled with 15 to 32 directions [68]. This is mainly done to increase the signal-to-noise ratio for the diffusion tensors [95], not to increase the angular resolution. However, the Q-Ball imaging method uses as much as 252 gradient directions to

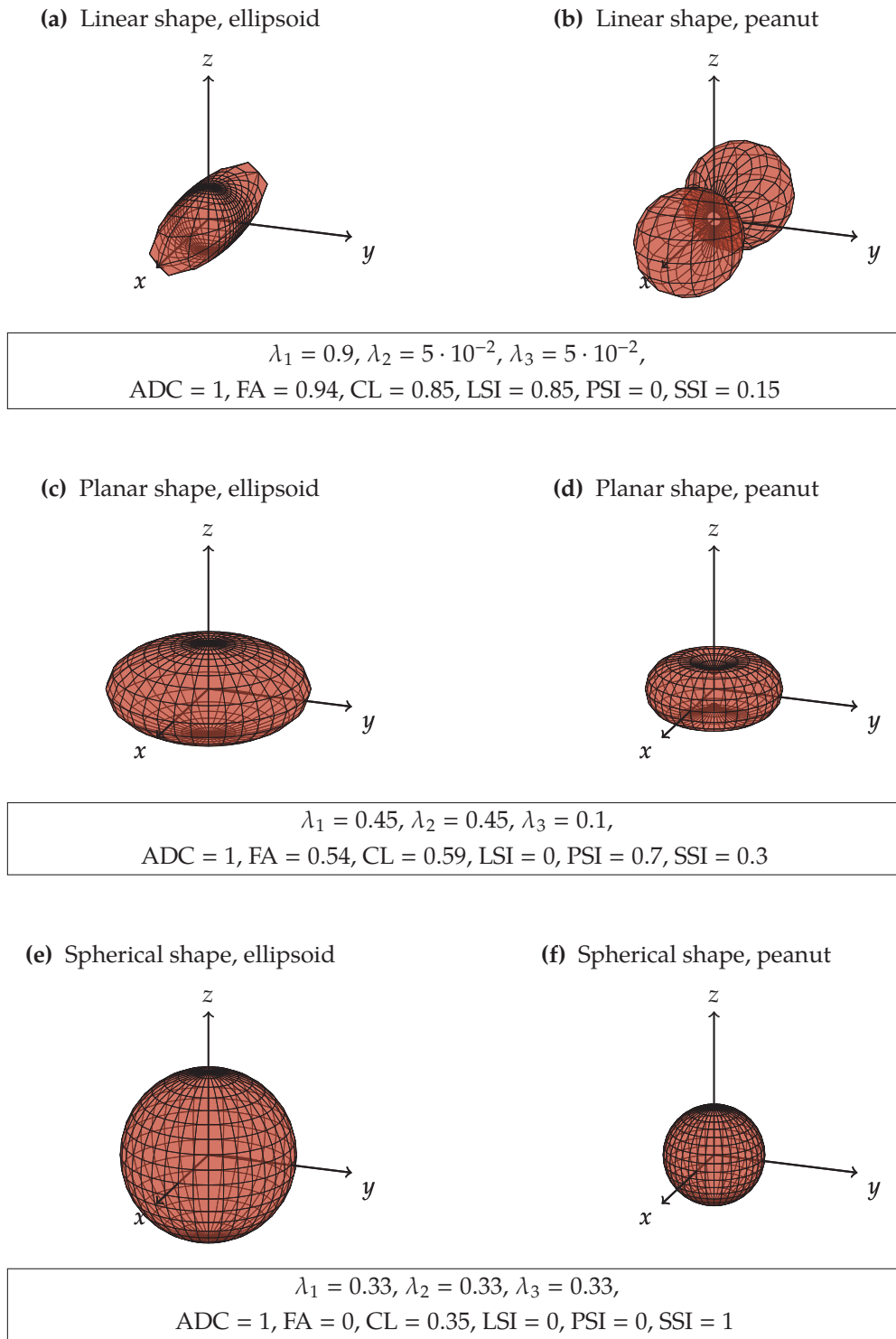


Figure 2.2: Ellipsoids and peanuts for various combinations of eigenvalues of D_W . Eigenvectors are aligned with the coordinate axes. Top row: One dominating eigenvalue; middle row: Two dominating eigenvalues; Bottom row: Isotropic diffusion tensor.

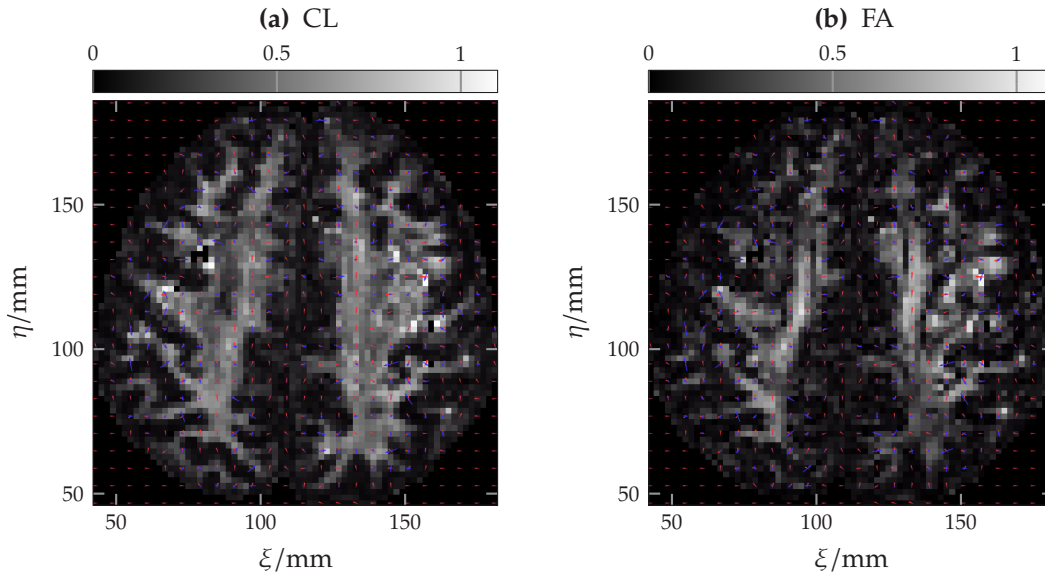


Figure 2.3: The indices [CL](#) (2.2) and [FA](#) (2.1) for a two-dimensional slice of the Camino [30] DTI data set. The red arrows point along the main direction of D_W .

reconstruct directional diffusion information with a higher angular resolution and is able to resolve also fiber crossings inside a voxel [131]. But the values [ADC](#) and [FA](#) are used for tumor diagnosis and segmentation [88, 128] such that diffusion tensor data is available for the model without additional effort. This may not be the case with high resolution data. Hence, we consider the water diffusion tensors as given and ignore additional information in the raw data sets. This is in accordance with the models in [44, 46, 76, 112]. Any estimate of the fiber distribution based on diffusion tensors alone is unable to represent two crossing fibers.

Nevertheless, the general model in Section 3.2 is ignorant of the original data. It needs only a fiber distribution $E(v)$ that fulfills some general assumptions, namely that it is strictly positive, normalized and symmetric with respect to its first moment (cf. Definition 3.3). Thus, when high resolution data becomes available, it could be used without too many changes in the model.

The simplest ansatz for the fiber distribution is the so-called peanut distribution

$$E_{\text{peanut}}(v) = \frac{3}{4\pi \text{tr}(D_W)} v^\top D_W v. \quad (2.4)$$

To see where the name comes from, look at Figure 2.2b. The peanut distribution is computationally inexpensive to evaluate and there are analytic formulas for its moments. Its main drawback is that the resulting tumor diffusion (see Section 3.5.2) always has an isotropic component (see Appendix A.3), even if D_W is completely degenerate.

An arbitrary amount of anisotropy in the macroscopic model can be obtained with the bimodal von Mises-Fisher distribution [46, 112]

$$E_{\text{vMF}}(v) = \frac{k}{8\pi \sinh(k)} (\exp(kv_1 \cdot v) + \exp(-kv_1 \cdot v)),$$

with v_1 the eigenvector corresponding to the largest eigenvalue λ_1 of D_W and some function $k(\text{FA})$ that determines the concentration of the two peaks. This ansatz introduces an additional

model parameter and is more costly to evaluate, although there are analytical formulas for up to second-order moments [74]. Another problem is the representation of a fiber crossing. When there are two dominating eigenvalues of similar magnitude, the direction v_1 of the peaks in the von Mises-Fisher ansatz is rather arbitrary and subject to data noise. The peanut ansatz shown in Figure 2.2d is not correct either but it is more robust with respect to noise.

Many other choices for E are possible. For instance, Hunt [76] uses the orientation distribution function (ODF). Due to its simplicity we use the peanut ansatz for all computations in this thesis.

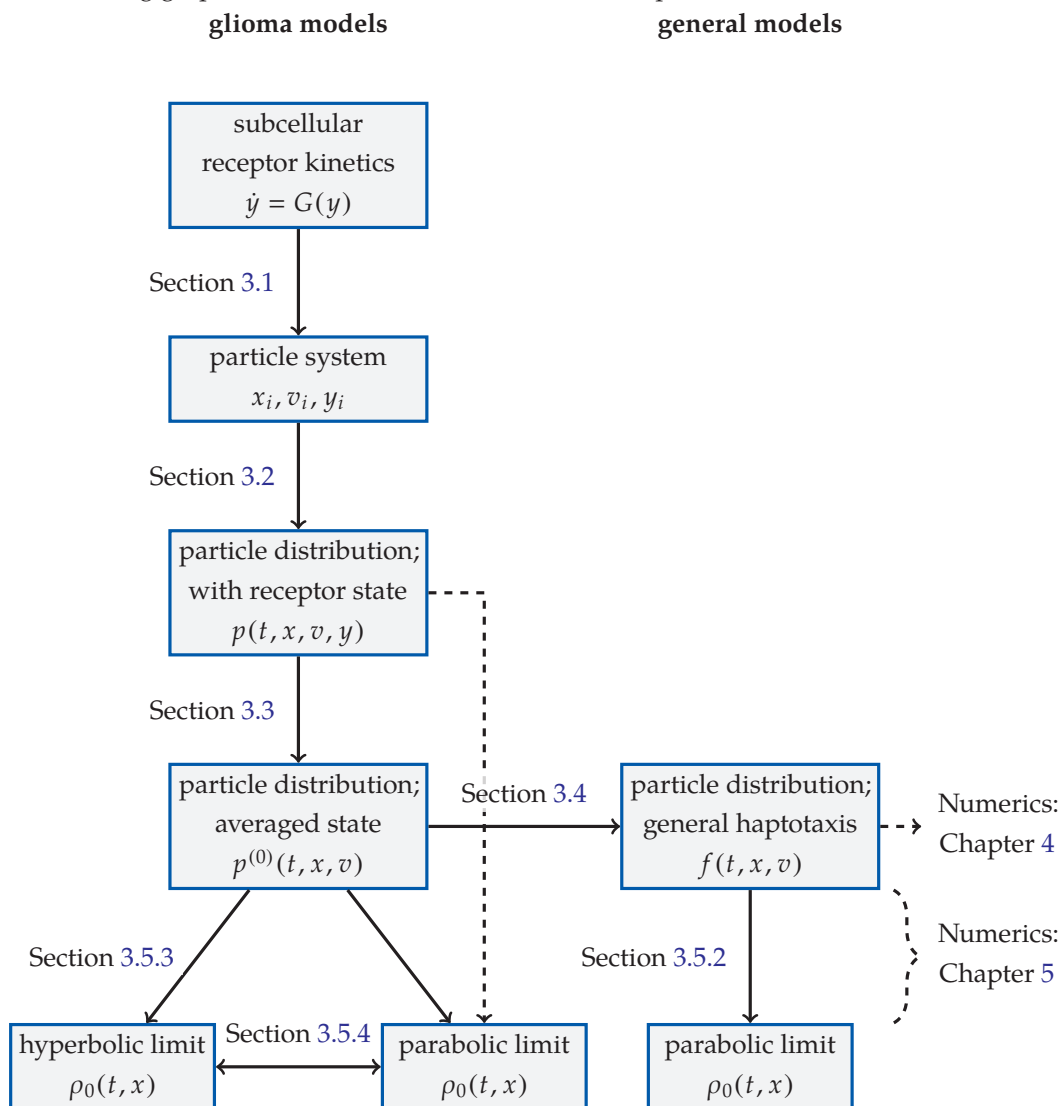
3

A multi-scale haptotaxis model

Ich sah hinaus zum Horizont. Und das was ich da sah,
das gab mir doch zu denken: Man kann fahr'n so weit man kann,
wo blau und blau sich treffen kommt man trotzdem niemals an.

Joint Venture — Blau und blau

The following graphic illustrates the structure of this chapter:



In this chapter, we discuss the transition from a subcellular model of haptotaxis to a macroscopic description of the tumor growth. There are four layers of description to consider. Firstly, we need to model the molecular processes inside a single cell that determine its interaction with the ECM. Because we are ultimately interested in the higher-level descriptions, the model on this scale only mimics observed cell behavior qualitatively. Thus, the second level models cells as particles with position x , velocity cv and activity y . Most interactions are randomly occurring events that change a cell's state (x, v, y) . Thirdly, instead of tracking the random path of each individual cell, we consider the expected behavior of particles. This so-called meso-scale description is a PDE for the particle distribution function $p(t, x, v, y)$: the expected number of particles with a given state. Before we pass to a truly macroscopic equation, there is an intermediate step. Under suitable assumptions, an equation for $p^{(0)}(t, x, v)$, the marginal distribution w.r.t. activity y , is accurate enough. At this point, we take a step back and consider a general class of kinetic equations, of which the glioma model is a special case. Finally, we derive a macroscopic advection-diffusion-reaction model for the local particle density $\rho_0(t, x)$ from the general kinetic equation.

The Engwer-Hillen-Knappitsch-Surulescu model (EHKS model) [44] serves as a foundation for the following discussion. Some parts of this chapter have been presented in [36], although in less detail.

3.1 A particle model with subcellular receptor dynamics

In this section we define a particle model for glioma cells that features proliferation, death and movement due to haptic interactions with the ECM. Because the haptotactic movement is facilitated through binding of integrins to ECM, the particle model includes a minimal description of the cell's receptor dynamics. Throughout the section we compare our modeling choices with Uatay's [133], who considers a much more detailed description of a cell's internal mechanisms.

3.1.1 Subcellular receptor dynamics

Let us start with the binding dynamics. We assume that all integrins are indistinguishable and attach to the same point in space, i.e., a cell can only probe a single point. The reaction scheme between integrins and attachment sites is



A free integrin and a free ECM attachment site form cell-ECM bonds with rate k^+ . The bonds dissociate with rate k^- . In Uatay's model the rates k^+, k^- are functions of the force at the attachment point. Because we do not model the internal cell structure or individual integrin, we have no information about the forces and therefore assume constant rates. We assume that attachment sites are abundant, i.e., their number will not change in a reaction. The number of attachment sites that is accessible to the cell is proportional to the volume fraction of ECM Q . Let n_f, n_b be the number of free and bound receptors, respectively. The total number of receptors $N_I = n_f + n_b$ is conserved. Therefore, we only need one equation

$$\begin{aligned} \dot{n}_b &= k^+ Q n_f - k^- n_b \\ &= k^+ Q (N_I - n_b) - k^- n_b, \end{aligned}$$

for the bound receptors to describe the mass action kinetics. Therein the attachment rate k^+ is not a classical rate constant, because Q is not a number, but a fraction. Rather, k^+ has to be interpreted as the reaction constant multiplied with the maximum number of available attachment sites. The mass action kinetics are only valid if N_I is large enough. Estimates for the number of integrins range from ten [133] to 10^5 [41, 44]. We refer to [41] for a model that respects the fact that N_I is finite. To make the model independent of the total number of receptors, we define the activity $y = \frac{n_b}{N_I}$ as the bound fraction of a cell's receptors. The reaction kinetics in terms of activity are

$$\begin{aligned} G(y) &:= \dot{y} = k^+Q(1-y) - k^-y \\ &= -(k^+Q + k^-)y + k^+Q \end{aligned} \quad (3.1)$$

Under the ODE (3.1), the activity y stays in the interval $[0, 1]$, because $G(0) = k^+Q > 0$ and $G(1) = -k^- < 0$.

The value

$$y^* = \frac{k^+Q}{k^+Q + k^-} \quad (3.2)$$

is a steady state of the ODE. It is a stable equilibrium, because the second derivative $\dot{y}|_{y^*} = -(k^+Q + k^-) < 0$ is strictly negative.

3.1.2 Model assumptions

In our model, each cell is described only by its position x , velocity cv , and activity y . Without detailed information about a cell's internal life we have to rely on stochastic processes to describe the relevant phenomena. The particle model is primarily designed with the population-level descriptions in mind. The major assumptions are:

Assumption 3.1

1. A cell moves in a straight line, until it changes its velocity instantly in a turning event.
2. Turning events happen randomly and are uncorrelated in time. Their frequency depends on the internal state of a cell. The direction after reorientation is also random but depends on the direction before the event.
3. The cell speed $c = \|cv\|$ is constant and equal for all cells.
4. Cells die randomly. Dead cells are removed from the population.
5. A cell proliferates at random and uncorrelated times. The original cell is removed from the population and two new cells with uncorrelated velocity and activity appear at the same position.

The first two assumptions reflect our lack of knowledge about internal cell structure and forces. The resulting model resembles bacterial run-and-tumble motion, which has been modeled for example by Stroock [127] or Erban and Othmer [49, 50] for E.coli. In contrast, Uatay models the forces and moments a cell generates through adhesion to ECM. The cell's path is a direct consequence of these forces, which result from different receptors probing different locations. Thus, his model is able to reproduce two experimentally observed phenomena for glioma cell

migration in white matter: gradient detection [84] and contact guidance [105, 116]. Nevertheless, we justify our assumptions. Firstly, the particle model is very simple, but we can include gradient detection and contact guidance through a suitable choice of the turning process. Secondly, to derive a macroscopic model, Uatay assumes that binding/unbinding happen on a much faster time scale than cell movement. Therefore, our assumption of instant turning is asymptotically valid. Thirdly, the resulting macroscopic models are structurally similar.

The third assumption is a simplification that reduces the dimension of the velocity space: Instead of $cv \in \mathbb{R}^3$, we only have to consider $v \in \mathbb{S}^2$. Uatay observes approximately gamma-distributed cell speeds. We could incorporate this observation into the turning kernel without introducing many structural differences later on.

Cell death is a consequence of environmental conditions, such as lack of oxygen or acid concentration. We model this with a death rate that depends on the cell density ρ_N in a neighborhood. In reality, dead cells do not simply vanish but take up space and therefore inhibit proliferation and also movement. To predict the necrotic tumor regions, we would have to model dead cells as a second species. But we expect that this complication would not improve the model's prediction for the diffuse invasion margin, in which we are primarily interested. To include the effect of crowding, we simply choose a proliferation rate that depends on ρ_N .

The fifth assumption is mainly justified by its simplicity. In reality, proliferation times are highly correlated because cells follow a cycle and divide in regular intervals. Cell division is a slow process and our assumption that it happens instantly is clearly wrong on the particle level. The debated go-or-grow hypothesis states that glioma cells either proliferate or migrate. At the cost of introducing more unknown parameters, we could model this hypothesis with two species, one for the migrating cells and one for the dividing cells.

3.1.3 The particle model

Let the triplet $\psi(t) = (x(t), v(t), y(t))$ encode the state of a cell at time t : the position $x \in \mathbb{R}^3$, direction $v \in \mathbb{S}^2$ and activity $y \in \mathbb{R}$. At time t , the cell is in the state ψ_0 . Its evolution is then governed by the following stochastic process:

1. Between reorientation times the cell moves in a straight line and its activity evolves according to (3.1):

$$\begin{aligned}\partial_t x &= cv, \\ \partial_t v &= 0, \\ \partial_t y &= G(y; Q(x)).\end{aligned}$$

2. At certain times t_i , the cell instantly changes its direction. These reorientation times t_i are Poisson distributed with rate $\lambda(\psi)$, which possibly depends on the state $\psi(t)$. Given the state $\psi(s)$ at some time s , the probability that no turning event happens in the time interval $[s, t]$ is

$$\mathbb{P}(t_i \notin [s, t] \forall i) = \exp\left(-\int_s^t \lambda(\psi(s')) ds'\right).$$

The state $\psi_i^+ = \lim_{t \downarrow t_i} (\psi(t))$ after a turning event is determined by the state before $\psi_i^- =$

$\lim_{t \uparrow t_i}(\psi(t))$. Position and internal state remain unchanged:

$$\begin{aligned}x_i^+ &= x_i^-, \\y_i^+ &= y_i^-.\end{aligned}$$

The direction v_i^+ after reorientation is chosen randomly according to the probability density function $K(v_i^+; v_i^-, x_i^-)$. Hence, the probability that the new direction v_i^+ is in the set Ω_v , given that it was v_i^- before, is

$$\mathbb{P}(v_i^+ \in \Omega_v | v_i^-, x_i^-) = \int_{\Omega_v} K(v'; v_i^-, x_i^-) dv'.$$

We often omit the last argument from the turning kernel and write $K(v', v)$ to simplify the notation.

3. The cell dies at a random time t_{death} , which is drawn from a Poisson distribution. The death rate $\mu^-(\rho_N)$ depends on the density of cells in a neighborhood of the cell. With probability

$$\mathbb{P}(t_{\text{death}} \notin [s, t]) = \exp\left(\int_s^t -\mu^-(\rho_N(s', x(s')))\text{d}s'\right),$$

the cell does not die in the interval $[s, t)$. When the cell dies, it is removed from the population.

4. Similarly, proliferation events are Poisson distributed with the rate μ^+ :

$$\mathbb{P}(t_{\text{prol}} \notin [s, t]) = \exp\left(\int_s^t -\mu^+(\rho_N(s', x(s')))\text{d}s'\right).$$

In a proliferation event, the original cell is removed and replaced with two new cells at the same position. The velocity and activity of both new cells follow the probability laws

$$\begin{aligned}\mathbb{P}(v^+ \in \Omega_v | v^-) &= \int_{\Omega_v} \chi^v(v'; v^-) dv', \\ \mathbb{P}(y^+ \in \Omega_y | y^-) &= \int_{\Omega_y} \chi^y(y'; y^-) dy'.\end{aligned}$$

Contact guidance enters our model via the turning kernel. We assume that a fiber orientation distribution $E(v; x)$ is given, for example by the estimates from Section 2.3. In its original interpretation [44] E encodes the fiber orientation statistically. To model contact guidance, the cell's preference to change its direction to v should correlate with the fiber orientation. The simplest way to achieve this is to set

$$K(v; v', x) = E(v; x). \quad (3.3)$$

The distribution function E provides coarse information for the fibers that fits well with the stochastic nature of our microscopic model and also with the available DTI data. But we are careful with its interpretation on the micro-scale. In light of (3.3), we should interpret E as the cell's preference to turn towards some direction, given an unknown fiber geometry. Nevertheless, we refer to E as the fiber distribution, to be consistent with the literature.

Dickinson and Tranquilo [41] describe several mechanisms that let a cell move up a stimulus gradient. When the cell's turning rate depends on the stimulus magnitude, they speak of klinokinesis. In our model, gradient detection is the result of indirect klinokinesis: The turning rate $\lambda(y)$ depends on the receptor activity, which depends on the volume fraction of fibers $Q(x)$ in turn. We choose the same turning rate

$$\lambda(y) = \lambda_0 - \lambda_1 y^* + \lambda_1 y, \quad (3.4)$$

as in a model for E. Coli bacteria by Erban and Othmer [49, 50]. The mechanism to detect a gradient works as follows: When a cell's receptor state is in equilibrium y^* , it turns with a base turning rate λ_0 . Suppose a cell moved downwards a fiber concentration gradient. Coming from a denser region, where y^* is greater (see (3.2)), the cell has more bound receptors than needed for the local equilibrium. According to equation (3.4), its turning rate is increased compared to the base rate. Similarly, cells moving upwards a gradient will change direction less frequently. Note that the turning rate correlates with the frequency of unbinding events due to equation (3.1). This fits with Uatay's model, wherein the cell moves and rotates only after unbinding events. We do not model the proliferation in detail but rather consider a few simple options for the proliferation kernels. Cells could have no preferred direction after proliferation, they could be preferentially oriented in fiber direction or not change their current direction at all:

$$\begin{aligned} \chi_{\text{iso}}^v(v, v') &= \frac{1}{|\mathbb{S}^2|}, \\ \chi_{\text{eq}}^v(v, v') &= E(v), \\ \chi_{\text{id}}^v(v, v') &= \delta_{v'}(v). \end{aligned}$$

For the change of receptor activity we consider the kernels

$$\begin{aligned} \chi_{\text{zero}}^y(y, y') &= \delta_0(y), \\ \chi_{\text{eq}}^y(y, y') &= \delta_{y^*}(y), \\ \chi_{\text{id}}^y(y, y') &= \delta_{y'}(y). \end{aligned}$$

The first means that cells unbind all their receptors during growth, the second corresponds to the case that activity is in local equilibrium and the third option means that there is no change in receptor activity.

3.2 A meso-scale kinetic description

From the description of an individual cell in the [last section](#) follows a mesoscopic model for the entire population. The quantity of interest is the so-called particle distribution $p(t, x, v, y)$. It is the density of the measure

$$\mu(\Omega_\psi) = \int_{\Omega_\psi} p(t, \psi') d\psi' = \int_{\Omega_x} \int_{\Omega_v} \int_{\Omega_y} p(t, x', v', y') dy' dv' dx'$$

for the expected number of particles in the volume $\Omega_x \times \Omega_v \times \Omega_y$ at time t . The derivation of the kinetic equation is outside the scope of this work. We refer to [127] in the context of a bacterial run-and-tumble model, and to [62] in the context of neutron transport. Note that in the

KTAP framework [13, 14], the models are formulated directly on the meso-scale. The governing equation for p is given by

$$\partial_t p + c \nabla_x \cdot (vp) + \partial_y (Gp) = \lambda(y) \mathcal{L}p + \mu(\rho) \mathcal{S}p. \quad (3.5)$$

Its left-hand side describes the cell movement through physical and activity space. The cell-tissue interactions are encoded in the turning operator

$$\mathcal{L}p = \int_{\mathbb{S}^2} K(v, v'; x) p(v') - K(v', v; x) p(v) dv'. \quad (3.6)$$

Assumption 3.2 To factor the turning rate λ out of the collision operator in (3.5), it is crucial that λ does not depend on v .

Proliferation and death are modeled by the source term

$$\begin{aligned} \mu(\rho) \mathcal{S}p &= -\mu^-(\rho) p(v) + \mu^+(\rho) \left(-p(v, y) + 2 \int_{\mathbb{S}^2} \int_{\Omega_y} \chi^y(y, y') \chi^v(v, v') p(v', y') dy' dv' \right) \\ &= -(\mu^-(\rho) + \mu^+(\rho)) p(v, y) + 2\mu^+(\rho) \int_{\mathbb{S}^2} \int_{\Omega_y} \chi^y(y, y') \chi^v(v, v') p(v', y') dy' dv' \end{aligned}$$

wherein the net growth rate is

$$\mu := \mu^+ - \mu^-$$

and $\rho = \int_{\mathbb{S}^2} p dv'$ is the local particle density. If we assume that no changes in direction and state occur during growth this simplifies to

$$\mu(\rho) p(v, y),$$

i.e, $\mathcal{S} = I$.

The following definition provides essential structure to the equation. The derivation of the diffusion limit in Section 3.5.2 and the numerical methods in Chapter 4 and Chapter 5 heavily depend on it.

Definition 3.3 — Turning kernel. A positive function $K(v, v') : \mathbb{S}^2 \times \mathbb{S}^2 \mapsto \mathbb{R}^+$ is a turning kernel, if it is

- normalized, i.e.,

$$\int_{\mathbb{S}^2} K(v, v') dv = 1, \quad (3.7)$$

- bounded by positive constants from below and above

$$0 < K_{\min} < K(v, v') < K_{\max}, \quad (3.8)$$

- and L^2 -integrable

$$\int_{\mathbb{S}^2} \int_{\mathbb{S}^2} K^2(v, v') dv' dv < \infty. \quad (3.9)$$

Further, there is a strictly positive function $E : \mathbb{S}^2 \mapsto \mathbb{R}^+$ that fulfills the detailed balance

condition

$$K(v, v')E(v') = K(v', v)E(v). \quad (3.10)$$

This equilibrium function is normalized, i.e.,

$$\int_{\mathbb{S}^2} E(v)dv = 1 \quad (3.11)$$

and first-order symmetric, i.e.,

$$\int_{\mathbb{S}^2} vE(v)dv = 0. \quad (3.12)$$

Assumptions (3.7) – (3.9) are the same as in classical kinetic theory and identical to (1.2) – (1.4) in Definition 1.2. Because the turning kernel is a probability distribution in its first argument, its positivity and normalization (3.7) follow immediately. We need the bounds in (3.8) for the diffusion limit in Section 3.5.2. They pose only minor restrictions on the model. If the velocity space is compact, for example the unit sphere \mathbb{S}^2 , integrability (3.9) follows from the bounds. Assumption (3.10) is a generalization from classical kinetic theory. In the glioma model, the equilibrium is the fiber distribution. The normalization (3.11) of the equilibrium is mostly for convenience but it fits the interpretation of the fiber distribution. First-order symmetry (3.12) is crucial for the existence of a diffusion limit. Considering that the fiber distribution comes from DTI measurements, which are inherently symmetric, this assumption is not a real restriction.

The turning operator \mathcal{L} in equation (3.6) is a balance of gains and losses in $p(v)$. Its first summand counts the gains from particles changing their velocity from v' to v during reorientation. This leads us to the following definition:

Definition 3.4 — Gain operator. A turning kernel K fulfilling Definition 3.3, defines a gain operator $\mathcal{K} : L_E^2(\mathbb{S}^2) \mapsto L_E^2(\mathbb{S}^2)$ via the integral

$$\mathcal{K}p = \int_{\mathbb{S}^2} K(v, v')p(v')dv'.$$

Due to normalization (3.7), the turning operator can be written as

$$\mathcal{L}p = (\mathcal{K} - I)p.$$

In the following sections 3.3 and 3.5 we need the properties of the spectrum of \mathcal{K} collected in the lemma:

Lemma 3.5 — Spectrum of gain operators. Let \mathcal{K} be a gain operator with equilibrium E . Then

1. The equilibrium E is an eigenfunction of \mathcal{K} to the simple eigenvalue $\nu = 1$.
2. The eigenvalue $\nu = 1$ is the largest eigenvalue in absolute value.
3. E is the only positive eigenfunction and all other eigenfunctions F fulfill $\int_{\mathbb{S}^2} F(v)dv = 0$.

Proof. By the definition of the equilibrium (3.10) and normalization of the turning kernel (3.7)

we have

$$\mathcal{K}E = \int_{\mathbb{S}^2} K(v, v')E(v')dv' = \int_{\mathbb{S}^2} K(v', v)E(v)dv = E(v),$$

thus E is an eigenfunction of \mathcal{K} to eigenvalue $\nu = 1$. Under assumption (3.8), the Krein-Rutmann theorem [70, Chapter III, Theorem 10.1] states that there is a unique positive eigenfunction. This eigenfunction belongs to a positive eigenvalue that is larger in absolute value than any other eigenvalue. E is a positive eigenfunction, therefore its corresponding eigenvalue $\nu = 1$ must be the eigenvalue of the largest absolute value.

Integrating the characteristic equation $\mathcal{K}F = \nu F$ gives

$$\begin{aligned} \int_{\mathbb{S}^2} \int_{\mathbb{S}^2} K(v, v')F(v')dv'dv &= \nu \int_{\mathbb{S}^2} F(v)dv, \\ \int_{\mathbb{S}^2} \int_{\mathbb{S}^2} K(v, v')dvF(v')dv' &= \nu \int_{\mathbb{S}^2} F(v)dv, \\ 1 \int_{\mathbb{S}^2} F(v)dv &= \nu \int_{\mathbb{S}^2} F(v)dv, \end{aligned}$$

which is equivalent to

$$\nu = 1 \vee \int_{\mathbb{S}^2} F(v)dv = 0.$$

Thus, any eigenfunction other than E must integrate to zero. ■

Remark 3.6 — More properties of the gain operator.

- Because of (3.9), \mathcal{K} is a Hilbert-Schmidt operator and as such bounded and compact [2, Theorem 3.12].
- In [111] it has been shown that \mathcal{K} has a pure point spectrum, i.e., all values in the spectrum are eigenvalues.

3.3 An activity-averaged kinetic model

The mass-action kinetics (3.1) drive the activity y towards its local equilibrium value y^* . But two effects disturb this equilibrium. A cell moving in a gradient $\nabla_x Q$ experiences a change in y^* and therefore its activity deviates from the local steady state. Also, the proliferation kernel χ^y may disturb the steady state. When the receptor dynamics dominate, the deviation from equilibrium is small and a reduced model for $p^{(0)}(t, x, v)$, the zeroth moment of $p(t, x, v, y)$, is accurate enough. We investigate under which conditions this is applicable for glioma migration. We rewrite equation (3.5) in terms of the deviation from steady state

$$z := y^* - y.$$

The temporal evolution of z is governed by the ODE

$$\begin{aligned} \dot{z} &= \dot{y}^* - \dot{y}(z) \\ &= \dot{y}^* - G(y^* - z). \end{aligned}$$

The steady state $y^*(Q(x))$ is a function of the volume fraction of fibers $Q(x)$ and therefore a function of x . Assuming that Q is constant in time, the temporal change in y^* , as observed by a particle moving in a straight line $x = x_0 + cvt$, is

$$\dot{y}^* = \frac{\partial y^*}{\partial x} \frac{\partial x}{\partial t} = \frac{\partial y^*}{\partial Q} c \nabla_x Q \cdot v.$$

In total, the particle's activity evolves according to

$$\begin{aligned} \dot{z} &= \frac{\partial y^*}{\partial Q} c \nabla_x Q \cdot v - (k^+ Q + k^-) z \\ &=: \beta \cdot v - \alpha z, \end{aligned}$$

with the definitions $\beta = \frac{\partial y^*}{\partial Q} c \nabla_x Q$ and $\alpha = (k^+ Q + k^-)$.

The kinetic equation in terms of $p(t, x, v, z)$ is then given by:

$$\partial_t p + c \nabla_x \cdot (vp) + \partial_z ((\beta \cdot v - \alpha z)p) = \lambda(z) \mathcal{L}p + \mu(\rho) \mathcal{S}p. \quad (3.13)$$

Applying the change of variables to the turning rate (3.4) leads to

$$\lambda(z) = \lambda_0 - \lambda_1 z.$$

Let

$$p^{(k)}(t, x, v) = \int_{\Omega_z} z^k p(t, x, v, z) dz$$

denote the k -th moment of p with respect to activity. The boundaries $z = y^* - 1$ and $z = y^*$ correspond to the situation that all or no receptors are bound, respectively. Under zero Dirichlet boundary conditions $p(y^* - 1) = p(y^*) = 0$, the moments of equation (3.13) are

$$\partial_t p^{(k)} + c \nabla_x \cdot (vp^{(k)}) - k (\beta \cdot v p^{(k-1)} - \alpha p^{(k)}) = \lambda_0 \mathcal{L}p^{(k)} - \lambda_1 \mathcal{L}p^{(k+1)} + \mu(\rho) \int_{\Omega_z} \mathcal{S}(p) z^k dz. \quad (3.14)$$

3.3.1 The decay of moments

It is sensible to truncate the infinite moment system (3.14) after a finite k if the moments $p^{(k)}$ decay fast enough. To obtain an estimate of the moment decay, we consider a simplified situation. We assume zero net growth, i.e., $\mu^+ = \mu^-$ and ignore velocity changes due to turning and proliferation. The stationary, spatially homogeneous version of equation (3.14) is

$$-k (\beta \cdot v p^{(k-1)} - \alpha p^{(k)}) = -2\mu^+ p^{(k)} + 2\mu^+ \int_{\Omega_z} \int_{\Omega_z} \chi^z(z, z') p(z') z^k dz' dz$$

When there is no change in receptor state during proliferation, we have $\chi_{\text{id}}^z(z, z') = \delta_{z'}(z)$ and the moment system is simply

$$-k (\beta \cdot v p^{(k-1)} - \alpha p^{(k)}) = 0.$$

The k -th moment is therefore recursively determined by the $k - 1$ -th moment

$$\begin{aligned} p^{(k)} &= \frac{\beta \cdot v}{\alpha} p^{(k-1)} \\ &= \left(\frac{\beta \cdot v}{\alpha} \right)^k p^{(0)}. \end{aligned}$$

The rate

$$\frac{\beta \cdot v}{\alpha} \leq \frac{k^+ k^-}{(k^+ Q + k^-)^3} c \|\nabla_x Q\|$$

of this exponential decay depends on the specific parameters. Rough estimates for the parameters in the situation of glioma migration are summarized in Table 5.4. The binding and unbinding rates are of the order 0.1 s^{-1} . Cell migration speed is approximately $10^{-4} \text{ mm s}^{-1}$ and the gradient magnitude as estimated from DTI data is of order 0.1 mm^{-1} . As a result, the decay rate is of order 10^{-4} and the moments decay rapidly.

Under the assumption that cell activity is in local equilibrium after proliferation, which corresponds to the growth kernel $\chi_{\text{eq}}^z = \delta_0(z)^1$, the moments

$$p^{(k)} = \frac{\beta \cdot v}{\alpha + 2\frac{\mu^+}{k}} p^{(k-1)}$$

decay even faster.

When the cells unbind all their receptors during proliferation, the growth kernel is $\chi_{\text{zero}}^z(z, z') = \delta_{y^*}(z)^2$. Even if we ignore the perturbation due to the fiber gradient, the decay

$$\begin{aligned} \alpha k p^{(k)} &= -2\mu^+ p^{(k)} + 2\mu^+ p^{(0)} y^{*k}, \\ p^{(k)} &= p^{(0)} \frac{2\mu^+}{\alpha k + 2\mu^+} y^{*k} \end{aligned}$$

is not fast enough to justify cutting off the expansion after the first moment. We still have an exponential decay of moments, but y^* is not much less than one.

3.3.2 A zeroth-order approximation

With the right choice of parameters and growth kernel, the moments decay fast enough to justify a zeroth-order approximation of the system (3.14). Because of the estimates from the previous section, we discard the kernel χ_{zero}^z . With the growth kernel $\chi_{\text{id}}^z = \delta_{z'}(z)$, and

$$\mathcal{P}p = \int_{\mathbb{S}^2} \chi^v(v, v') p(v') dv',$$

the equation for the zeroth moment is

$$\partial_t p^{(0)} + c \nabla_x \cdot (v p^{(0)}) = \lambda_0 \mathcal{L}p^{(0)} - \lambda_1 \mathcal{L}p^{(1)} - (\mu^+ + \mu^-) p^{(0)} + 2\mu^+ \mathcal{P}p^{(0)}. \quad (3.15)$$

To close this equation, we need to approximate the first moment $p^{(1)}$ from the zeroth moment. Letting $p^{(1)} = 0$ is not an option, because then no information on the activity dynamics would remain in the model. Instead, we assume that the first moment equilibrates so rapidly that we can neglect the time derivative and the transport term in the first-order equation. Of course, this equation in turn depends on the second moment $p^{(2)}$. Due to the fast decay of moments, we assume that second-order or higher moments are zero. These considerations lead to a stationary and local approximation of $p^{(1)}$

$$-\beta \cdot v p^{(0)} + \alpha p^{(1)} = \lambda_0 \mathcal{L}p^{(1)} - (\mu^+ + \mu^-) p^{(1)} + 2\mu^+ \mathcal{P}p^{(1)}$$

¹Because of $z = y^* - y$, the value $z = 0$ marks the local equilibrium of receptor dynamics.

²The value $z = y^*$ corresponds to $y = 0$.

in terms of $p^{(0)}$. After reordering the terms, we have

$$[(\alpha + \lambda_0 + (\mu^+ + \mu^-))I - (\lambda_0\mathcal{K} + 2\mu^+\mathcal{P})]p^{(1)} = \beta \cdot vp^{(0)}. \quad (3.16)$$

If the operator on the left-hand side is invertible, we can solve this relation for $p^{(1)}$ and close equation (3.15). The next lemma guarantees invertibility for two special choices of \mathcal{P} .

Lemma 3.7 — Invertibility of the left-hand side. Given positive constants $\alpha, \lambda_0, \mu^+, \mu^-$, fulfilling

$$\alpha > (\mu^+ - \mu^-),$$

and a gain operator \mathcal{K} according to Definition 3.4, the operator

$$[(\alpha + \lambda_0 + (\mu^+ + \mu^-))I - (\lambda_0\mathcal{K} + 2\mu^+\mathcal{P})]$$

is invertible in either one of these special situations:

1. \mathcal{P} is a gain operator.
2. $\chi^v = \chi_{id}^v = \delta_{v'}(v)$, thus $\mathcal{P} = I$.

Proof.

1. \mathcal{P} is a gain operator. Define the operator $\mathcal{T} = \lambda_0\mathcal{K} + 2\mu^+\mathcal{P}$. As in the proof of Lemma 3.5, the integral of the characteristic equation for \mathcal{T} yields

$$v_{\mathcal{T}} = \lambda_0 + 2\mu^+ \vee \int_{\mathbb{S}^2} F(v)dv = 0$$

as a necessary condition for eigenvalues/eigenfunctions. As a consequence of the Krein-Rutmann theorem [70, Chapter III, Theorem 10.1], there is a positive eigenfunction $E_{\mathcal{T}}$ that belongs to the largest absolute eigenvalue. Because $E_{\mathcal{T}}$ is positive it cannot fulfill $\int_{\mathbb{S}^2} E_{\mathcal{T}}(v)dv = 0$ and therefore must belong to the eigenvalue $v_{\mathcal{T},1} = \lambda_0 + 2\mu^+$. Thus, $v_{\mathcal{T},1}$ is the largest eigenvalue.

Both \mathcal{K} and \mathcal{P} are gain operators, therefore \mathcal{T} is a Hilbert-Schmidt operator and in particular a compact operator. Then the Fredholm theorem [2, Theorem 9.11] applies. Let $\eta > 0$ and consider the homogeneous equation

$$[(v_{\mathcal{T},1} + \eta)I - \mathcal{T}]p = 0.$$

This eigenvalue equation cannot have a non-zero solution, because the spectral radius of \mathcal{T} is $v_{\mathcal{T},1}$. Therefore,

$$[(v_{\mathcal{T},1} + \eta)I - \mathcal{T}]p = f$$

has a unique solution for all right-hand sides $f \neq 0$. A comparison of coefficients yields $\eta = \alpha - (\mu^+ - \mu^-)$; thus the condition $\alpha > (\mu^+ - \mu^-)$.

2. \mathcal{P} is the identity. The left-hand side is simplified to $[(\alpha + \lambda_0 - (\mu^+ - \mu^-))I - \lambda_0\mathcal{K}]$. A similar argument can be made with the spectral radius of $\lambda_0\mathcal{K}$.

■

In the following we consider a special choice of \mathcal{K} for which we can solve (3.16) explicitly. With (3.16) in mind, we solve

$$(I - a\mathcal{K})h(v) = r(v)$$

for h . Let $\mathcal{K}(v, v') = E(v)$ be a simple relaxation kernel. The gain operator is in this case $\mathcal{K}p = E(v) \langle p \rangle$ and the previous equation becomes

$$h(v) - a \langle h(v) \rangle E(v) = r(v). \quad (3.17)$$

Integration over the velocity space yields

$$\langle h \rangle = \frac{1}{1-a} \langle r \rangle.$$

We substitute this into (3.17) to solve for h :

$$h = r + \frac{a}{1-a} E \langle r \rangle.$$

Moreover, the turning operator $\mathcal{L}h$ applied to the solution of (3.17) is

$$\mathcal{L}h = \mathcal{L}r.$$

If either $\mathcal{P} = I$ or $\mathcal{P} = \mathcal{K}$, we can apply this solution formula to the first-order equation (3.16). In the case $\mathcal{P} = I$, (3.16) reduces to³

$$(\alpha + \lambda_0 - \mu) p^{(1)}(v) - \lambda_0 E(v) \langle p^{(1)} \rangle = \beta \cdot vp^{(0)}.$$

A comparison with (3.17) yields

$$a = \frac{\lambda_0}{\alpha + \lambda_0 - \mu},$$

$$r(v) = \frac{1}{\alpha + \lambda_0 - \mu} \beta \cdot vp^{(0)},$$

thus

$$\mathcal{L}p^{(1)} = \frac{1}{\alpha + \lambda_0 - \mu} \beta \cdot (E \langle vp^{(0)} \rangle - vp^{(0)}).$$

Remembering the definition $\beta = \frac{\partial y^*}{\partial Q} c \nabla_x Q$, the zeroth-order equation (3.15) becomes

$$\begin{aligned} \partial_t p^{(0)} + c \nabla_x \cdot (vp^{(0)}) &= \lambda_0 (E \langle p^{(0)} \rangle - p^{(0)}) - \lambda_H c \nabla_x Q \cdot (E \langle vp^{(0)} \rangle - vp^{(0)}) + \mu p^{(0)}, \\ \partial_t p^{(0)} + c \nabla_x \cdot (vp^{(0)}) &= \lambda_0 \mathcal{L}p^{(0)} - \lambda_H c \nabla_x Q \cdot \mathcal{L} [vp^{(0)}] + \mu p^{(0)}, \end{aligned} \quad (3.18)$$

wherein

$$\lambda_H = \frac{\lambda_1}{\alpha + \lambda_0 - \mu} \frac{\partial y^*}{\partial Q}. \quad (3.19)$$

Note that $\mathcal{L}(vp^{(0)})$ is applied to each component of the vector $vp^{(0)}$.

³Remember $\mu = \mu^+ - \mu^-$.

In the case $\mathcal{P} = \mathcal{K}$, (3.16) becomes

$$(\alpha + \lambda_0 + (\mu^+ + \mu^-)) p^{(1)} - (\lambda_0 + 2\mu^+) E \langle p^{(1)} \rangle = \beta \cdot v p^{(0)},$$

and as a consequence we have

$$r = \frac{1}{\alpha + \lambda_0 + (\mu^+ + \mu^-)} \beta \cdot v p^{(0)}.$$

The resulting zeroth-order equation reads

$$\partial_t p^{(0)} + c \nabla_x \cdot (v p^{(0)}) = \lambda_0 \mathcal{L} p^{(0)} - \tilde{\lambda}_H c \nabla_x Q \cdot \mathcal{L} [v p^{(0)}] - (\mu^+ + \mu^-) p^{(0)} + 2\mu^+ E \langle p^{(0)} \rangle, \quad (3.20)$$

with

$$\tilde{\lambda}_H = \frac{\lambda_1}{\alpha + \lambda_0 + (\mu^+ + \mu^-)} \frac{\partial y^*}{\partial Q}.$$

3.4 The generalized haptotaxis equation

We take a step back and define a class of equations that generalizes the models from the previous section. The general haptotaxis equation for the particle distribution $f(t, x, v)$ has the form

$$\partial_t f + c \nabla_x \cdot (v f) = \lambda_D \mathcal{L}_D f + \lambda_a \mathcal{L}_a f + \mu \mathcal{S} f. \quad (3.21)$$

The strictly positive turning rate $\lambda_D(x) \geq \lambda_{\min} > 0$, the perturbation rate $\lambda_a(x)$ and the net growth rate $\mu(x, \rho)$ are functions of space. In the following, we define the interaction terms on the right-hand side of (3.21).

With equation (3.6) and Definition 3.3 in mind, we give the definition:

Definition 3.8 — Turning operator. The turning operator $\mathcal{L} : L_E^2(\mathbb{S}^2) \rightarrow L_E^2(\mathbb{S}^2)$ associated with a turning kernel K according to Definition 3.3 is given by

$$\begin{aligned} \mathcal{L} f &= \int_{\mathbb{S}^2} K(v, v') f(v') - K(v', v) f(v) dv', \\ &= (\mathcal{K} - I) f. \end{aligned}$$

The operator \mathcal{L}_D is such a turning operator with associated turning kernel $K_D(v, v'; x)$. We allow the kernel to depend on position x , thus also the equilibrium $E(x, v)$ may be a function of position.

The other linear operator \mathcal{L}_a should be interpreted as a perturbation to \mathcal{L}_D . It is defined via the kernel integral

$$\mathcal{L}_a f = \int_{\mathbb{S}^2} k_a(v, v') f(v') - k_a(v', v) f(v) dv',$$

but it is not a turning operator, because k_a is not a turning kernel. In particular, k_a can be negative and does not have an equilibrium.

To normalize the kernel, we demand

$$\max_{v' \in \mathbb{S}^2} \left\{ \left| \int_{\mathbb{S}^2} k_a(v, v') dv \right| \right\} = 1.$$

This is necessary, because in contrast to a turning kernel, $\int_{\mathbb{S}^2} k_a(v, v') dv$ can depend on v' . To interpret the perturbed operator $\lambda_D \mathcal{L}_D + \lambda_a \mathcal{L}_a$ as a generator of a microscopic jump process it is necessary that the perturbed kernel

$$0 < k_{min} \leq \lambda_D K_D(v, v') + \lambda_a k_a(v, v') \leq k_{max} < \infty \quad (3.22)$$

is strictly positive and bounded from above.

The growth operator is normalized via

$$\int_{\mathbb{S}^2} \mathcal{S}f dv = \int_{\mathbb{S}^2} f dv = \rho.$$

3.4.1 Properties of turning operators

The following properties are essential for the derivation of the macroscopic limit in Section 3.5. Per construction, an operator defined via the kernel integral $\mathcal{L} = \int_{\mathbb{S}^2} k(v, v') f(v') - k(v', v) f(v) dv'$ conserves mass:

$$\int_{\mathbb{S}^2} \mathcal{L}f dv = 0.$$

This holds for \mathcal{L}_D and \mathcal{L}_a .

Turning operators defined as in Definition 3.8, have many more properties:

Lemma 3.9 — Spectrum of turning operators. Let \mathcal{L} be a turning operator according to Definition 3.8, with associated turning kernel K and equilibrium E . Then

1. The equilibrium is an eigenfunction of \mathcal{L} to the eigenvalue $\nu_{\mathcal{L}} = 0$.
2. The one-dimensional nullspace of \mathcal{L} is spanned by the equilibrium: $\mathcal{N}(\mathcal{L}) = \text{span}\{E\}$.
3. All other eigenvalues fulfill $|\nu_{\mathcal{L}} + 1| \leq 1$, and in particular $\text{Re}(\nu_{\mathcal{L}}) \leq 0$.

Proof.

1. Due to

$$\mathcal{L}f = (\mathcal{K} - I)f = (\nu_{\mathcal{K}} - 1)f = \nu_{\mathcal{L}}f \quad (3.23)$$

the spectrum of \mathcal{L} is just the spectrum of the associated gain operator shifted by minus one. Lemma 3.5 states that E is an eigenfunction of \mathcal{K} to eigenvalue $\nu_{\mathcal{K}} = 1$, thus it is an eigenfunction of \mathcal{L} to eigenvalue $\nu_{\mathcal{L}} = 0$.

2. The equilibrium is in the nullspace $\mathcal{N}(\mathcal{L})$ because of the equilibrium property (3.10): $K(v, v')E(v') = K(v', v)E(v)$. The first claim also follows directly from this. From Lemma 3.5 we know that $\nu_{\mathcal{L}}$ is a simple eigenvalue. It follows that E is the only function in the nullspace.
3. This follows from application of (3.23) to $|\nu_{\mathcal{K}}| \leq 1$.

■

Definition 3.10 — Weighted scalar product / weighted L^2 -space. The weighted scalar product

$$(f(v), g(v))_E := \int_{\mathbb{S}^2} f(v)g(v) \frac{1}{E(v)} dv$$

for $f, g : \mathbb{S}^2 \mapsto \mathbb{R}$ induces the weighted L^2 -space $L_E^2(\mathbb{S}^2)$.

Lemma 3.11 — Properties of turning operators. With respect to the weighted scalar product and corresponding space $L_E^2(\mathbb{S}^2)$ from Definition 3.10, the turning operator \mathcal{L} has these properties:

1. \mathcal{L} is self-adjoint.
2. The range of \mathcal{L} is the orthogonal complement of its nullspace:
 $\mathcal{R}(\mathcal{L}) = \mathcal{N}^\perp(\mathcal{L}) = \left\{ g \mid (g, E)_E = \int_{\mathbb{S}^2} g(v)dv = 0 \right\}$.
3. $\mathcal{L} : \mathcal{R} \mapsto \mathcal{R}$ restricted to \mathcal{R} is bijective: There exists a unique solution $f \in \mathcal{R}$ to $\mathcal{L}f = g$, if and only if $g \in \mathcal{R}$.

Proof.

1. We show self-adjointness of the gain operator \mathcal{K} . Then $\mathcal{L} = \mathcal{K} - I$ is also self-adjoint. We have

$$\begin{aligned} (\mathcal{K}f, g)_E &= \int_{\mathbb{S}^2} \int_{\mathbb{S}^2} K(v, v') f(v') dv' \frac{g(v)}{E(v)} dv, \\ &= \int_{\mathbb{S}^2} \int_{\mathbb{S}^2} f(v') g(v) \frac{K(v, v')}{E(v)} dv' dv, \\ &= \int_{\mathbb{S}^2} \int_{\mathbb{S}^2} f(v') g(v) \frac{K(v', v)}{E(v')} dv' dv, \\ &= \int_{\mathbb{S}^2} \int_{\mathbb{S}^2} f(v) g(v') \frac{K(v, v')}{E(v)} dv dv', \\ &= \int_{\mathbb{S}^2} \int_{\mathbb{S}^2} K(v, v') g(v') dv' \frac{f(v)}{E(v)} dv, \\ &= (f, \mathcal{K}g)_E, \end{aligned}$$

wherein we expand Definition 3.4 and Definition 3.10, move all terms into the inner integral, apply the detailed balance property (3.10), swap the names of v and v' , and factor out the v -dependent terms.

2. The gain operator \mathcal{K} is compact (see Remark 3.6). Thus, the Riesz-Schauder theorem for compact operators [2, Theorem 9.9] applies, which gives us $\mathbb{S}^2 = \mathcal{N}(\mathcal{L}) \oplus \mathcal{R}(\mathcal{L})$. Therefore, $\mathcal{R}(\mathcal{L}) = \mathcal{N}^\perp(\mathcal{L}) = \left\{ g \mid (g, E)_E = 0 \right\}$.
3. The Fredholm theorem [2, Theorem 10.8] gives us necessary and sufficient conditions that a unique solution of $\mathcal{L}f = g$ exists. For any solution h to the adjoint homogeneous equation $(\tilde{\mathcal{K}} - I)h = 0$, the right-hand side g must fulfill $(g, \tilde{h})_E = 0$. \mathcal{K} is self-adjoint and therefore $h \in \mathcal{N}(\mathcal{L}) = \text{span}\{E\}$. Thus the condition on the right-hand side is $(g, E)_E = \int_{\mathbb{S}^2} g(v)dv = 0$, i.e., $g \in \mathcal{N}^\perp(\mathcal{L}) = \mathcal{R}(\mathcal{L})$.

■

3.4.2 The glioma model in this setting

We cast the models (3.18) and (3.20) into the general form (3.21). Recall the model (3.18):

$$\partial_t f + c \nabla_x \cdot (vf) = \lambda_0 (E \langle f \rangle - f) + \lambda_H c \|\nabla_x Q\| \widehat{\nabla_x Q} \cdot (vf - E \langle vf \rangle) + \mu f, \quad (3.24)$$

with the gradient direction $\widehat{\nabla_x Q} = \frac{\nabla_x Q}{\|\nabla_x Q\|}$. A comparison with (3.21) yields the coefficients

$$\begin{aligned} \lambda_D &= \lambda_0, \\ \lambda_a &= c \lambda_H \|\nabla_x Q\|, \end{aligned} \quad (3.25)$$

and the kernels

$$\begin{aligned} K_D(v, v') &= E(v), \\ k_a(v, v') &= -\widehat{\nabla_x Q} \cdot v' E(v). \end{aligned} \quad (3.26)$$

We compute the inverse of \mathcal{L}_D in Lemma 3.11 explicitly for the right-hand side g with $\langle g \rangle = 0$. Because of

$$\mathcal{L}_D(-g) = E \langle -g \rangle - (-g) = g,$$

the inverse operator is

$$\mathcal{L}_D^{-1}(g) = -g. \quad (3.27)$$

3.4.3 Stroock's E.Coli model

We revisit Stroock's model [127] for the movement of E. Coli bacteria from the introductory Section 1.1. In his article, he considered a turning rate $\lambda = \lambda(x, v)$ that depends on space and direction. This violates Assumption 3.2 for the kinetic equation (3.5). If the turning rate depends on the current orientation of the bacterium, we cannot factor it out of the balance between gains and losses. All bacteria that turn from v towards any other direction v' contribute to the loss $\int_{\mathbb{S}^2} \lambda(v) K(v', v) f(v) dv'$ for v . Similarly, the gain for v is caused by the bacteria turning from any direction v' towards v : $\int_{\mathbb{S}^2} \lambda(v') K(v, v') f(v') dv'$. A bacterium with orientation v' has the turning rate $\lambda(v')$. We write the balance as

$$\tilde{\mathcal{L}} f(v) = \int_{\mathbb{S}^2} \tilde{K}(v, v') f(v') - \tilde{K}(v', v) f(v) dv'$$

with the (not normalized) kernel $\tilde{K}(v, v') = \lambda(v') K(v, v')$.

Remark 3.12 — Correction. Stroock erroneously used the balance

$$\lambda(v) \int_{\mathbb{S}^2} K(v, v') f(v') - K(v', v) f(v) dv'$$

in the the governing PDE. In contradiction with the underlying particle model, this term does not preserve mass.

With some additional structure, Stroock's model is equivalent to the glioma model from the previous Section 3.4.2. Assume that some external stimulus $Q(x)$ is given. The bacterium can

detect the magnitude of that stimulus, and the rate of change $\frac{dQ}{dt} = c\nabla_x Q \cdot v$ as it moves. It adjusts its turning rate according to both pieces of information:

$$\lambda(x, v) = \lambda_0 \alpha_x(Q) - \beta_v c \nabla_x Q \cdot v.$$

The activation function α_x and parameter β_v encode the sensitivity of the turning rate to stimulus magnitude and rate of change, respectively.

This leads to the PDE

$$\partial_t f + c \nabla_x \cdot (vf) = \lambda_0 \alpha_x(Q) \mathcal{L}_D f - \beta_v c \|\nabla_x Q\| \mathcal{L}_a f,$$

with

$$\begin{aligned} \mathcal{L}_D f &= \int_{\mathbb{S}^2} K(v, v') f(v') - K(v', v) f(v) dv', \\ \mathcal{L}_a f &= \int_{\mathbb{S}^2} \widehat{\nabla_x Q} \cdot v' K(v, v') f(v') - \widehat{\nabla_x Q} \cdot v K(v', v) f(v) dv'. \end{aligned}$$

For the kernel $K(v, v') = E(v)$, this is identical to the glioma model.

3.5 Macroscopic population dynamics

In this section, we derive macroscopic models for the particle density $\rho_0(t, x)$ from the haptotaxis equation (3.21). A parabolic scaling of (3.21) leads to an advection-diffusion-reaction equation in the limit. Here we repeat the calculation of this diffusion limit, which has been done in [36]. The same limit is obtained directly from the model (3.5) for $p(t, x, v, y)$ in [44]. We refer also to [24, 50, 73, 111] for the diffusion limit in related models. Additionally, we introduce a hydrodynamic scaling (see also [24, 73]) and derive a hyperbolic limit equation for the P_1 approximation of the glioma model.

3.5.1 The non-dimensional equation and its characteristic numbers

To write equation (3.21) in non-dimensional form on the reference domain $\hat{\Omega}_{txv} = [0, 1] \times \hat{\Omega}_x \times \mathbb{S}^2$, we introduce non-dimensional variables $t = T\hat{t}$, $x = X\hat{x}$. The direction v is already a non-dimensional quantity. We also set $\lambda_D(x) = L_D \hat{\lambda}_D(\hat{x})$, $\lambda_a(x) = L_a \hat{\lambda}_a(\hat{x})$, and $\mu(x, \rho) = M \hat{\mu}(\hat{x}, \hat{\rho})$ with reference constants L_D, L_a, M chosen such that $\hat{\lambda}_D(\hat{x})$, $\hat{\lambda}_a(\hat{x})$, $\hat{\mu}(\hat{x}, \hat{\rho})$ are comparable to one. The non-dimensional form of (3.21) reads

$$\partial_{\hat{t}} \hat{f} + \frac{Tc}{X} \nabla_{\hat{x}} \cdot (v\hat{f}) = TL_D \hat{\lambda}_D \mathcal{L}_D \hat{f} + TL_a \hat{\lambda}_a \mathcal{L}_a \hat{f} + TM \hat{\mu} \mathcal{S} \hat{f}. \quad (3.28)$$

We recognize the Strouhal number $St = \frac{X}{Tc}$ and the Knudsen numbers $Kn_D = \frac{1}{TL_D}$, $Kn_a = \frac{1}{TL_a}$, $Kn_P = \frac{1}{TM}$ for turning, perturbation, and proliferation and write (3.28) as

$$\partial_{\hat{t}} \hat{f} + \frac{1}{St} \nabla_{\hat{x}} \cdot (v\hat{f}) = \frac{1}{Kn_D} \hat{\lambda}_D \mathcal{L}_D \hat{f} + \frac{1}{Kn_a} \hat{\lambda}_a \mathcal{L}_a \hat{f} + \frac{1}{Kn_P} \hat{\mu} \mathcal{S} \hat{f}. \quad (3.29)$$

The characteristic numbers in (3.29) relate certain characteristic times of the model to the global reference time T . The Strouhal number St is the ratio of the time that one particle needs to cross the domain to the reference time and the Knudsen number Kn_D compares the expected time between reorientations to the reference time.

When the parameter functions $\lambda_D(x), \lambda_a(x)$ assume a wide range of values throughout the domain, the global Knudsen numbers will fail to characterize the situation locally. Therefore, we also define local Knudsen numbers that include the space-dependent non-dimensional parameter functions $\hat{\lambda}_D(\hat{x}), \hat{\lambda}_a(\hat{x}), \hat{\mu}(\hat{x}, \hat{\rho})$. For example, the local Knudsen number for \mathcal{L}_D is

$$\overline{\text{Kn}}_D = \frac{1}{T\lambda_D(x)} = \frac{1}{TL_D\hat{\lambda}_D(\hat{x})}.$$

Equation (3.28) can be rewritten with different sets of characteristic numbers. In the following, we present two such choices: Parabolic and hyperbolic scaling.

3.5.2 A parabolic scaling and the diffusion limit

Parabolic scaling

The parabolic scaling number

$$\varepsilon = \frac{\text{Kn}_D}{\text{St}} = \frac{c}{XL_D},$$

is the ratio of the expected time between turning events and the time a particle needs to cross the domain. With the characteristic numbers

$$\delta = \frac{\text{Kn}_D}{\text{St}^2} = \frac{c^2T}{L_DX^2}, \quad \nu = \frac{\text{Kn}_D}{\text{Kn}_a \text{St}} = \frac{L_aTc}{L_DX}, \quad \theta = \frac{1}{\text{Kn}_p} = TM, \quad (3.30)$$

we rewrite (3.28) in the form

$$\partial_t \hat{f} + \frac{\delta}{\varepsilon} \nabla_{\hat{x}} \cdot (v \hat{f}) = \frac{\delta}{\varepsilon^2} \hat{\lambda}_D \mathcal{L}_D \hat{f} + \frac{\nu}{\varepsilon} \hat{\lambda}_a \mathcal{L}_a \hat{f} + \theta \hat{\mu} \mathcal{S} \hat{f}. \quad (3.31)$$

This so-called parabolic scaling is motivated by the limit of (3.31), when ε tends to zero and the other numbers δ, ν, θ are fixed. The limit is given by the diffusion-advection-reaction equation

$$\partial_t \hat{\rho}_0 - \nabla_{\hat{x}} \cdot \left(\delta \frac{1}{\hat{\lambda}_D} \left(\hat{D} \nabla_{\hat{x}} \hat{\rho}_0 + \hat{a}_D \hat{\rho}_0 \right) - \nu \frac{\hat{\lambda}_a}{\hat{\lambda}_D} \hat{a} \hat{\rho}_0 \right) = \theta \hat{\mu} \hat{\rho}_0, \quad (3.32)$$

wherein $\hat{D} \in \mathbb{R}^{3 \times 3}$ is the non-dimensional diffusion tensor and $\hat{a}, \hat{a}_D \in \mathbb{R}^3$ are non-dimensional drift vectors. In physical coordinates, with physical diffusion $D = D_0 \hat{D}$ and drift $a = a_0 \hat{a}$, the diffusion equation is

$$\partial_t \rho_0 - \nabla_x \cdot \left(\frac{X^2 \delta}{TD_0} \frac{1}{\hat{\lambda}_D} \left(D \nabla_x \rho_0 + a_D \rho_0 \right) - \frac{X \nu}{Ta_0} \frac{\hat{\lambda}_a}{\hat{\lambda}_D} a \rho_0 \right) = \frac{\theta}{MT} \mu \rho_0.$$

Thus,

$$\delta = \frac{TD_0}{X^2}$$

is the ratio of the global reference time T to a characteristic diffusion time $\frac{X^2}{D_0}$. Furthermore,

$$\nu = \frac{a_0 T}{X}$$

is the ratio of the global timescale T to the timescale $\frac{X}{a_0}$ for advection. Finally,

$$\theta = MT$$

relates the global timescale to the timescale of proliferation. There are other possible variants of characteristic numbers that could be used to define a parabolic scaling. However, with the current definition, we get the same interpretation of ε as in [79].

Diffusion Limit

We derive the diffusion limit (3.32) formally via the Hilbert expansion

$$\hat{f}^\varepsilon = \hat{f}^0 + \varepsilon \hat{f}^1 + \varepsilon^2 \hat{f}^2 + \dots$$

We insert \hat{f}^ε into (3.31), multiply the equation with ε^2 and sort by powers of ε . To zeroth order this yields

$$\mathcal{L}_D \hat{f}^0 = 0.$$

Remembering the nullspace $\mathcal{N}(\mathcal{L}_D) = \text{span}\{E\}$ from Lemma 3.9, we write

$$\hat{f}^0 = \hat{\rho}_0 E, \quad (3.33)$$

with $\hat{\rho}_0 = \langle \hat{f}^0 \rangle$. The terms of order ε^1 are

$$\delta \nabla_{\hat{x}} \cdot (v \hat{f}^0) = \delta \hat{\lambda}_D \mathcal{L}_D \hat{f}^1 + v \hat{\lambda}_a \mathcal{L}_a \hat{f}^0. \quad (3.34)$$

Due to first-order symmetry $\langle E v \rangle = 0$ of the equilibrium (see Definition 3.3), the term $v \hat{f}^0$ is in the range $\mathcal{R}(\mathcal{L}_D)$. Because the perturbation operator conserves mass, $\mathcal{L}_a \hat{f}^0$ is also in the range. Hence, Lemma 3.11 guarantees that (3.34) has a unique solution for \hat{f}^1 :

$$\hat{f}^1 = \frac{1}{\hat{\lambda}_D} \mathcal{L}_D^{-1} \left(\nabla_{\hat{x}} \cdot (v E \hat{\rho}_0) - \frac{v}{\delta} \hat{\lambda}_a \mathcal{L}_a (E \hat{\rho}_0) \right). \quad (3.35)$$

Finally, to the order of ε^2 we have

$$\partial_{\hat{t}} \hat{f}^0 + \delta \nabla_{\hat{x}} \cdot (v \hat{f}^1) = \delta \hat{\lambda}_D \mathcal{L}_D \hat{f}^2 + v \hat{\lambda}_a \mathcal{L}_a \hat{f}^1 + \theta \hat{\mu} \mathcal{S} \hat{f}^0.$$

Using Lemma 3.11 again, we see that the second-order term \hat{f}^2 is defined uniquely if and only if the projection of this equation onto the nullspace $\mathcal{N}(\mathcal{L}_D)$ vanishes. Applying the projection, which is just integration over \mathbb{S}^2 , and inserting (3.33), (3.35) gives

$$\begin{aligned} \partial_{\hat{t}} \hat{\rho}_0 + \delta \nabla_{\hat{x}} \cdot \left\langle v \frac{1}{\hat{\lambda}_D} \mathcal{L}_D^{-1} \left(\nabla_{\hat{x}} \cdot (v E \hat{\rho}_0) - \frac{v}{\delta} \hat{\lambda}_a \mathcal{L}_a (E \hat{\rho}_0) \right) \right\rangle &= \theta \hat{\mu} \hat{\rho}_0, \\ \partial_{\hat{t}} \hat{\rho}_0 + \nabla_{\hat{x}} \cdot \left(\frac{\delta}{\hat{\lambda}_D} \left(\langle v \mathcal{L}_D^{-1} (v^\top E) \rangle \cdot \nabla_{\hat{x}} \hat{\rho}_0 + \langle v \mathcal{L}_D^{-1} (v \cdot \nabla_{\hat{x}} E) \rangle \hat{\rho}_0 \right) - v \frac{\hat{\lambda}_a}{\hat{\lambda}_D} \langle v \mathcal{L}_D^{-1} \mathcal{L}_a (E) \rangle \hat{\rho}_0 \right) &= \theta \hat{\mu} \hat{\rho}_0. \end{aligned}$$

We write this as

$$\partial_{\hat{t}} \hat{\rho}_0 - \nabla_{\hat{x}} \cdot \left(\delta \frac{1}{\hat{\lambda}_D} \left(\hat{D} \nabla_{\hat{x}} \hat{\rho}_0 + \hat{a}_D \hat{\rho}_0 \right) - v \frac{\hat{\lambda}_a}{\hat{\lambda}_D} \hat{a} \hat{\rho}_0 \right) = \theta \hat{\mu} \hat{\rho}_0,$$

with the diffusion tensor

$$\hat{D} = - \langle v \mathcal{L}_D^{-1} (v^\top E) \rangle, \quad (3.36)$$

and drift vectors

$$\hat{a}_D = - \langle v \mathcal{L}_D^{-1} (v \cdot \nabla_{\hat{x}} E) \rangle \quad (3.37)$$

$$\hat{a} = - \langle v \mathcal{L}_D^{-1} \mathcal{L}_a E \rangle. \quad (3.38)$$

The term $\mathcal{L}_D^{-1}(v^\top E)$ is to be understood as component wise application of the inverse.

When the inverse \mathcal{L}_D^{-1} does not depend on space, we can swap it with the gradient in the expression (3.37) for \hat{a}_D and get

$$\hat{a}_D = \nabla_{\hat{x}} \cdot \langle v \mathcal{L}_D^{-1}(v^\top E) \rangle = \nabla_{\hat{x}} \cdot \hat{D},$$

which leads to the simplified form

$$\partial_t \hat{\rho}_0 - \nabla_{\hat{x}} \cdot \left(\delta \frac{1}{\hat{\lambda}_D} \nabla_{\hat{x}} \cdot (\hat{D} \hat{\rho}_0) - v \frac{\hat{\lambda}_a}{\hat{\lambda}_D} \hat{a} \hat{\rho}_0 \right) = \theta \hat{\mu} \hat{\rho}_0.$$

Remark 3.13 — Glioma model. For the glioma model in Section 3.4.2, the inverse of \mathcal{L}_D is given by (3.27). Hence, explicit formulas for the diffusion tensor and drift vector are

$$\begin{aligned} \hat{D} &= \langle v v^\top E(v) \rangle, \\ \hat{a}_D &= \nabla_{\hat{x}} \cdot \hat{D}. \end{aligned}$$

When E is the peanut distribution from (2.4), the diffusion tensor is

$$D_T = \frac{1}{5} \left(I_3 + \frac{D_W + D_W^\top}{\text{tr}(D_W)} \right). \quad (3.39)$$

For details of this computation, see equation (A.1) in Section A.3. Using first-order symmetry (3.12) of E , we also have

$$\begin{aligned} \mathcal{L}_a E &= \widehat{\nabla_x Q} \cdot (vE - E \langle vE \rangle) \\ &= \widehat{\nabla_x Q} \cdot vE, \end{aligned}$$

thus the drift vector \hat{a} is given by

$$\begin{aligned} \hat{a} &= \langle v \mathcal{L}_a E \rangle, \\ &= \widehat{\nabla_x Q} \cdot \langle v v^\top E \rangle, \\ &= \widehat{\nabla_x Q} \cdot \hat{D}. \end{aligned} \quad (3.40)$$

3.5.3 A hyperbolic scaling and the hyperbolic limit

We keep the definitions $\varepsilon = \frac{c}{X L_D}$, $\theta = TM$ and define two new characteristic numbers:

$$\mathcal{A} = \frac{1}{\text{St}} = \frac{Tc}{X}, \quad \mathcal{H} = \frac{\text{Kn}_D}{\text{Kn}_a \text{St}} = \frac{L_a Tc}{L_D X}.$$

In terms of $\varepsilon, \mathcal{A}, \mathcal{H}, \theta$, equation (3.29) reads

$$\partial_t \hat{f} + \mathcal{A} \nabla_{\hat{x}} \cdot (v \hat{f}) = \frac{\mathcal{A}}{\varepsilon} \hat{\lambda}_D \mathcal{L}_D \hat{f} + \frac{\mathcal{H}}{\varepsilon} \hat{\lambda}_a \mathcal{L}_a \hat{f} + \theta \hat{\mu} \mathcal{S} \hat{f}. \quad (3.41)$$

We derive the limit as ε tends to zero only for the P_1 -approximation to the glioma model from Section 3.4.2. This model is essentially the p -system treated by Jin and Levermore [79] and we follow their example closely.

To define the P_1 -approximation for equation (3.24) we preempt results from Chapter 4. In essence, we make the ansatz

$$f(t, x, v) = \rho(t, x)E(x, v) + g(t, x, v),$$

and assume that all second-order or higher moments of g are zero, i.e. $\langle vv^\top g \rangle = 0$. Taking zeroth and first moments of (3.24) yields the system

$$\begin{aligned} \partial_t \rho + c \nabla_x \cdot q &= \mu \rho, \\ \partial_t q + c \nabla_x \cdot (\hat{D} \rho) &= -\lambda_D q + \lambda_a \widehat{\nabla_x Q} \cdot (\hat{D} \rho) + \mu q \end{aligned}$$

for the density $\rho = \langle f \rangle$ and flux $q = \langle vf \rangle = \langle vg \rangle$. The pressure tensor is given by $\hat{D} = \langle vv^\top E \rangle$ and the fiber gradient direction is $\widehat{\nabla_x Q} = \frac{\nabla_x Q}{\|\nabla_x Q\|}$. We apply the hyperbolic scaling from (3.41) and get the non-dimensional system

$$\begin{aligned} \partial_t \hat{\rho} + \mathfrak{d} \nabla_{\hat{x}} \cdot \hat{q} &= \theta \hat{\mu} \hat{\rho}, \\ \partial_t \hat{q} + \mathfrak{d} \nabla_{\hat{x}} \cdot (\hat{D} \hat{\rho}) &= -\frac{\mathfrak{d}}{\varepsilon} \hat{\lambda}_D \hat{q} + \frac{\mathfrak{H}}{\varepsilon} \hat{\lambda}_a \widehat{\nabla_x Q} \cdot \hat{D} \hat{\rho} + \theta \hat{\mu} \hat{q}. \end{aligned} \quad (3.42)$$

We make a Hilbert expansion in ε for the flux \hat{q} :

$$\hat{q}^\varepsilon = \hat{q}^0 + \varepsilon \hat{q}^1 + \dots,$$

insert this into the system, multiply everything by ε and group by powers of ε . The terms of order ε^0 are

$$\hat{q}^0 = \frac{\mathfrak{H}}{\mathfrak{d}} \frac{\hat{\lambda}_a}{\hat{\lambda}_D} \widehat{\nabla_x Q} \cdot \hat{D} \hat{\rho} =: \frac{\mathfrak{H}}{\mathfrak{d}} \hat{a} \hat{\rho}.$$

To order ε^1 we have

$$\begin{aligned} \partial_t \hat{\rho}^0 + \mathfrak{d} \nabla_{\hat{x}} \cdot \hat{q}^0 &= \theta \hat{\mu} \hat{\rho}^0, \\ \partial_t \hat{q}^0 + \mathfrak{d} \nabla_{\hat{x}} \cdot (\hat{D} \hat{\rho}^0) &= -\mathfrak{d} \hat{\lambda}_D \hat{q}^1 + \theta \hat{\mu} \hat{q}^0. \end{aligned}$$

We insert the definition of \hat{q}^0 and use the first equation to eliminate $\partial_t \hat{\rho}^0$ in the second equation. Then, we solve the second equation for \hat{q}^1 :

$$\hat{q}^1 = \frac{\mathfrak{H}^2}{\mathfrak{d}^2 \hat{\lambda}_D} \hat{a} \nabla_{\hat{x}} \cdot (\hat{a} \hat{\rho}^0) - \frac{1}{\hat{\lambda}_D} \nabla_{\hat{x}} \cdot (\hat{D} \hat{\rho}^0).$$

Finally, the $\hat{\rho}^0$ -equation including order ε terms is

$$\begin{aligned} \partial_t \hat{\rho}^0 + \mathfrak{d} \nabla_{\hat{x}} \cdot \hat{q}^0 &= -\varepsilon \mathfrak{d} \nabla_{\hat{x}} \cdot \hat{q}^1 + \theta \hat{\mu} \hat{\rho}^0, \\ \partial_t \hat{\rho}^0 + \mathfrak{H} \nabla_{\hat{x}} \cdot (\hat{a} \hat{\rho}^0) &= -\varepsilon \nabla_{\hat{x}} \cdot \left[\frac{\mathfrak{H}^2}{\mathfrak{d} \hat{\lambda}_D} \hat{a} \nabla_{\hat{x}} \cdot (\hat{a} \hat{\rho}^0) - \frac{\mathfrak{H}}{\hat{\lambda}_D} \nabla_{\hat{x}} \cdot (\hat{D} \hat{\rho}^0) \right] + \theta \hat{\mu} \hat{\rho}^0. \end{aligned} \quad (3.43)$$

This is a drift-dominated equation. Consider the equation in physical variables:

$$\partial_t \rho + \nabla_x \cdot (a \rho) = -\varepsilon \nabla_x \cdot \left[\frac{b}{\hat{\lambda}_D} a \nabla_x \cdot (a \rho) - \frac{1}{\hat{\lambda}_D} \nabla_x \cdot (D \rho) \right] + \mu \rho.$$

The time b matches the units of the terms in brackets. We compare the non-dimensional equation

$$\partial_{\hat{t}} \hat{\rho}^0 + \frac{Ta_0}{X} \nabla_{\hat{x}} \cdot (\hat{a} \hat{\rho}^0) = -\varepsilon \nabla_{\hat{x}} \cdot \left[\frac{Ta_0^2 b}{X^2} \frac{1}{\hat{\lambda}_D} \hat{a} \nabla_{\hat{x}} \cdot (\hat{a} \hat{\rho}^0) - \frac{TD_0}{X^2} \frac{1}{\hat{\lambda}_D} \nabla_{\hat{x}} \cdot (\hat{D} \hat{\rho}^0) \right] + TM \hat{\mu} \hat{\rho}^0,$$

with (3.43), and obtain the relations

$$\mathfrak{H} = \frac{Ta_0}{X}, \quad \mathfrak{D} = \frac{TD_0}{X^2}, \quad \mathfrak{D} = \frac{T}{b}$$

between mesoscopic characteristic numbers $\mathfrak{D}, \mathfrak{H}$ and macroscopic characteristic numbers D_0, a_0 . The coefficient $b = \frac{X^2}{D_0}$ follows directly from the previous relations. The characteristic number \mathfrak{H} is the ratio of the global time scale to the advection time scale and \mathfrak{D} is the ratio of the diffusion time scale to the global time-scale.

Remark 3.14 We do not have enough structure for \mathcal{L}_a to derive a hyperbolic limit in the general case. We would need an equilibrium \tilde{E} to the perturbed turning operator that fulfills $\lambda_D \mathcal{L}_D \tilde{E} + \lambda_a \mathcal{L}_a \tilde{E} = 0$ and also an entropy dissipation law. Even for the glioma-model it is not clear if such an equilibrium exists. We could compute the limit in the special case of the P_1 -glioma model, because we could find an equilibrium distribution $(\rho^0, q^0) = (\rho_0, a\rho_0)$ for the reaction terms on the right-hand side of the equation.

3.5.4 The transition between parabolic and hyperbolic scalings

Let $\mathfrak{D} = \frac{1}{\varepsilon}$ in the hyperbolic scaling (3.41). This is identical to the parabolic scaling (3.31) with $\delta = 1$ and $\nu = \mathfrak{H}$. Vice versa, the parabolic scaling (3.31) with $\delta = \varepsilon$ yields the hyperbolic scaling with $\mathfrak{H} = \nu$. It is thus possible to blend between both regimes. Define the blending parameter $\Xi \in [0, 1]$ and let

$$\begin{aligned} \delta &= \varepsilon^\Xi, \\ \mathfrak{D} &= \varepsilon^{\Xi-1}. \end{aligned}$$

The value $\Xi = 0$ corresponds to parabolic scaling and $\Xi = 1$ to hyperbolic scaling. In terms of this blending parameter, the scaled equation reads

$$\partial_{\hat{t}} \hat{f} + \varepsilon^{(\Xi-1)} \nabla_{\hat{x}} \cdot (v \hat{f}) = \varepsilon^{(\Xi-2)} \hat{\lambda}_D \mathcal{L}_D \hat{f} + \nu \varepsilon^{(-1)} \hat{\lambda}_a \mathcal{L}_a \hat{f} + \theta \hat{\mu} \mathcal{S} \hat{f}.$$

We observe that for $\Xi = 1$, the hyperbolic limit equation (3.43) is equal to the parabolic limit equation (3.32).

The macroscopic limits are idealizations that become increasingly accurate for ε close to zero. In any given physical situation, we cannot choose the parameters and characteristic numbers. But the numbers ε and Ξ are useful for classification. The value of Ξ locates any given situation on a spectrum between the hyperbolic and parabolic limit situations. Of course, the value of ε measures the proximity to any of the two limits.

3.5.5 The sub-characteristic condition

The hyperbolic limit (3.43) only exists if the so-called sub-characteristic condition is satisfied. This condition states that the wave speeds in the limit system cannot be faster than the wave

speeds of the original system. It also ensures that the $O(\varepsilon)$ correction term in (3.43) is dissipative. For an arbitrary unit vector n , the characteristic speeds of the left-hand side of (3.42) are 0 and $\pm_{\mathcal{D}}\sqrt{n^\top \hat{D}n}$. Comparing equation (3.42) with the p -system in [27, 79], we see that the sub-characteristic condition translates to

$$\begin{aligned} \frac{\hat{\lambda}_a}{\hat{\lambda}_D} |\widehat{\nabla_x Q} \cdot \hat{D}n| &<_{\mathcal{D}} \sqrt{n^\top \hat{D}n}, \\ \frac{\lambda_a}{\lambda_D} |\widehat{\nabla_x Q} \cdot \hat{D}n| &< \sqrt{n^\top \hat{D}n}. \end{aligned}$$

In the parabolic limit the sub-characteristic condition is always fulfilled, because with $\mathcal{D} = \varepsilon^{-1}$ the right-hand side of the condition tends to infinity. In the hyperbolic limit however, the condition poses a restriction on the gradient field $\nabla_x Q$ in relation to the coefficients λ_0, λ_H .

It is not practical to check the condition for every normal n . Therefore, we give an estimate based on the eigenvalues of the diffusion tensor. Let $\Lambda_{\min}(\hat{D})$ and $\Lambda_{\max}(\hat{D})$ denote the smallest and largest eigenvalues of \hat{D} , respectively. Due to $n^\top \hat{D}n > \Lambda_{\min}(\hat{D})$ and $|\widehat{\nabla_x Q} \cdot \hat{D}n| < \Lambda_{\max}(\hat{D})$, the condition

$$\|\nabla_x Q\| < \frac{\lambda_0}{c\lambda_H} \frac{\sqrt{\Lambda_{\min}(\hat{D})}}{\Lambda_{\max}(\hat{D})}$$

implies the sub-characteristic condition.

To keep a physically meaningful connection between mesoscopic haptotaxis models of the form (3.21) and microscopic particle models, we have assumed that the perturbed kernel is positive. The following lemma extends this connection to the macro-scale in the sense that a physically meaningful particle model leads to a meaningful hyperbolic limit.

Lemma 3.15 When the perturbed kernel

$$\lambda_D K_D(v, v') + \lambda_a k_a(v, v') > 0, \quad \forall v, v' \in \mathbb{S}^2,$$

is strictly positive according to (3.22), the sub-characteristic condition for the P_1 -glioma model (3.42) is fulfilled.

Proof. With the definitions (3.25) and (3.26), the condition (3.22) translates to

$$\lambda_a \widehat{\nabla_x Q} \cdot v' E(v) < \lambda_D E(v), \quad \forall v, v' \in \mathbb{S}^2.$$

Because this holds true for all v' , we can choose

$$v' = \begin{cases} v, & \widehat{\nabla_x Q} \cdot v \geq 0, \\ -v, & \widehat{\nabla_x Q} \cdot v < 0, \end{cases}$$

such that $\widehat{\nabla_x Q} \cdot v' = |\widehat{\nabla_x Q} \cdot v|$. Then both sides of the inequality

$$\lambda_a |\widehat{\nabla_x Q} \cdot v| E(v) < \lambda_D E(v), \quad \forall v \in \mathbb{S}^2$$

are positive. We multiply with $-v^\top n$ and integrate over all v with $v^\top n < 0$. On the left-hand side this yields

$$\begin{aligned} \left\langle |\widehat{\nabla_x Q} \cdot v| E(v) (-v)^\top n \right\rangle_{v^\top n < 0} &= \left\langle \widehat{\nabla_x Q} v E(v) (-v)^\top n \right\rangle_{v^\top n < 0}, \\ &= \left\langle \widehat{\nabla_x Q} v E(v) v^\top n \right\rangle_{v^\top n < 0}, \end{aligned}$$

and we estimate the right-hand side from above with

$$\begin{aligned} \langle E(v)(-v)^\top n \rangle_{v^\top n < 0} &= \left| \langle E(v)(-v)^\top n \rangle_{v^\top n < 0} \right|, \\ &\leq \langle |E(v)(-v)^\top n| \rangle_{v^\top n < 0}, \\ &= \langle |E(v)v^\top n| \rangle_{v^\top n < 0}. \end{aligned}$$

Altogether, the inequality becomes

$$\lambda_a \langle |\widehat{\nabla_x Q} v E(v)v^\top n| \rangle_{v^\top n < 0} < \lambda_D \langle |E(v)v^\top n| \rangle_{v^\top n < 0}.$$

We now multiply with $v^\top n$ and integrate over all v with $v^\top n > 0$. The same steps as before lead to

$$\lambda_a \langle |\widehat{\nabla_x Q} v E(v)v^\top n| \rangle_{v^\top n > 0} < \lambda_D \langle |E(v)v^\top n| \rangle_{v^\top n > 0}.$$

We add both inequalities together, which, because all numbers involved are positive, yields

$$\lambda_a \langle |\widehat{\nabla_x Q} v E(v)(v)^\top n| \rangle < \lambda_D \langle |E(v)(v)^\top n| \rangle.$$

On the left-hand side of this, swapping the absolute value and the integral only weakens the inequality. On the right-hand side, we use the Cauchy-Schwarz inequality

$$\begin{aligned} \langle |E(v)v^\top n| \rangle^2 &\leq \langle (E^{\frac{1}{2}} |v^\top n|)^2 \rangle \langle (E^{\frac{1}{2}})^2 \rangle, \\ &= \langle E |v^\top n|^2 \rangle, \\ &= \langle E (v^\top n)^2 \rangle, \\ &= \langle E n^\top v v^\top n \rangle, \\ &= n^\top \langle E v v^\top \rangle n. \end{aligned}$$

Finally, we arrive at

$$\begin{aligned} \lambda_a |\widehat{\nabla_x Q} \langle E v v^\top \rangle n| &< \lambda_D \sqrt{n^\top \langle E v v^\top \rangle n}, \\ \lambda_a |\widehat{\nabla_x Q} \hat{D} n| &< \lambda_D \sqrt{n^\top \hat{D} n}. \end{aligned}$$

■

4

Moment methods for the haptotaxis equation

Same old song, just a drop of water in an endless sea.
All we do crumbles to the ground, though we refuse to see.
Dust in the wind, all we are is dust in the wind

Kansas — Dust in the wind

In this chapter we apply moment methods to the general haptotaxis equation (3.21)

$$\partial_t f + c \nabla_x \cdot (vf) = \lambda_D \mathcal{L}_D f + \lambda_a \mathcal{L}_a f + \mu \mathcal{S} f$$

from Section 3.5. The structure of the turning kernel K_D makes it necessary to modify the standard methods to represent the equilibrium E . Therefore, in Section 4.1 we introduce a different notion of entropy and derive the corresponding modified moment methods. In Section 4.2, we take a detailed look at first-order moment systems and their diffusion limits. Finally, we investigate the modified moment systems numerically in Section 4.3.

4.1 Modified entropy closures

4.1.1 Relative entropy

The classical entropy $h(f) = \langle \eta(f) \rangle$ measures the distance of f to the isotropic distribution $\frac{\rho}{\langle 1 \rangle}$ in the following sense: The isotropic distribution minimizes any entropy h . Because the turning operator in the classical radiative transport equation (1.1) dissipates any entropy, f approaches the isotropic distribution with respect to the entropy. We have seen in Section 1.2.5 that entropy closures extend this property to the moment system.

In the setting of the haptotaxis equation (3.21), we expect that the turning operator \mathcal{L}_D relaxes f towards its equilibrium E . But an anisotropic equilibrium does not minimize any classical entropy. Therefore, we need a different entropy, one that is minimized by E and dissipated by \mathcal{L}_D , to control the approach to the equilibrium.

Definition 4.1 — Relative entropy density / relative entropy. Let $\eta(f)$ be a classical entropy density (see Definition 1.5), that is, η is twice continuously differentiable and strictly convex. The entropy density of f relative to E is defined as

$$\eta_r(f|E) = \eta(f) - \eta(E) - \eta'(E)(f - E).$$

The relative entropy density induces the relative entropy functional:

$$h_r(f|E) = \int_{\mathbb{S}^2} \eta_r(f(v)|E(v)) dv.$$

A related, but conceptually different application of relative entropy is the study of the limit of hyperbolic relaxation systems [132]. The same concept is applied to prove convergence of the BGK model to the system of isentropic gas dynamics [18].

The equilibrium E has zero entropy relative to itself and it is the unique global minimizer of $\eta_r(f|E)$. To see this, we compute the first derivative $\partial_f \eta_r(f|E) = \eta'(f) - \eta'(E)$, which is zero for the equilibrium. Furthermore, the second derivative is given by $\partial_{ff} \eta_r(f|E) = \eta''(f)$, therefore the relative entropy is strictly convex with respect to its first argument.

We now show that the turning operator \mathcal{L}_D dissipates the Maxwell-Boltzmann entropy relative to E . The Maxwell-Boltzmann entropy is

$$\eta(f) = f \log(f) - f \quad (4.1)$$

with derivative $\eta'(f) = \log(f)$. Note the following relation between the absolute entropy and the relative entropy in this special case:

$$\eta_r(f|E) = E \eta\left(\frac{f}{E}\right) + E.$$

Hence,

$$\partial_f \eta_r(f|E) = \eta'(f) - \eta'(E) = \eta'\left(\frac{f}{E}\right) \quad (4.2)$$

holds for the first derivative.

The detailed balance $K_D(v, v')E(v') = K_D(v', v)E(v)$ in the turning kernel (see (3.10)) is crucial for entropy dissipation.

Lemma 4.2 — Entropy dissipation of the turning operator. The turning operator given by Definition 3.8 dissipates the Maxwell-Boltzmann entropy relative to its equilibrium E :

$$s_r = \int_{\mathbb{S}^2} \partial_f \eta_r(f|E) \mathcal{L}_D(f) dv \leq 0.$$

If $f = E$ a.e., the entropy dissipation is zero: $s_r = 0$. If $f \leq f_{\max} < \infty$, $s_r = 0$ implies $f = E$ a.e.

Proof. We insert the Definition 3.8 of the turning operator and use the detailed balance (3.10) to obtain

$$\begin{aligned} s_r &= \int_{\mathbb{S}^2} \partial_f \eta_r(f|E) \mathcal{L}_D(f) dv = \int_{\mathbb{S}^2} \int_{\mathbb{S}^2} \partial_f \eta_r(f(v)|E(v)) [K_D(v, v')f(v') - K_D(v', v)f(v)] dv' dv \\ &= \int_{\mathbb{S}^2} \int_{\mathbb{S}^2} \partial_f \eta_r(f(v)|E(v)) \left[K_D(v, v')f(v') - \frac{E(v')}{E(v)} K_D(v, v')f(v) \right] dv' dv \\ &= \int_{\mathbb{S}^2} \int_{\mathbb{S}^2} \partial_f \eta_r(f(v)|E(v)) \frac{K_D(v, v')}{E(v)} [E(v)f(v') - E(v')f(v)] dv' dv, \end{aligned}$$

relying on strict positivity (3.8) to factor out E . We swap the names of v and v' , and use the detailed balance again:

$$s_r = \int_{\mathbb{S}^2} \int_{\mathbb{S}^2} \partial_f \eta_r(f(v')|E(v')) \frac{K_D(v, v')}{E(v)} [E(v')f(v) - E(v)f(v')] \, dv dv'.$$

The sum of both equations multiplied by one half is

$$s_r = \frac{1}{2} \int_{\mathbb{S}^2} \int_{\mathbb{S}^2} [\partial_f \eta_r(f(v)|E(v)) - \partial_f \eta_r(f(v')|E(v'))] \frac{K_D(v, v')}{E(v)} [E(v)f(v') - E(v')f(v)] \, dv' dv.$$

We rewrite the first bracket

$$\begin{aligned} \partial_f \eta_r(f(v)|E(v)) - \partial_f \eta_r(f(v')|E(v')) &= \eta'(f(v)) - \eta'(E(v)) - \eta'(f(v')) + \eta'(E(v')) \\ &= \eta'(f(v)E(v')) - \eta'(f(v')E(v)), \end{aligned}$$

using relation (4.2). This is the only step in the proof in which we use that η is the Maxwell-Boltzmann entropy. The entropy dissipation then reads:

$$s_r = \frac{1}{2} \int_{\mathbb{S}^2} \int_{\mathbb{S}^2} [\eta'(f(v)E(v')) - \eta'(f(v')E(v))] \frac{K_D(v, v')}{E(v)} [E(v)f(v') - E(v')f(v)] \, dv' dv.$$

Because η is strictly convex, η' is strictly monotone increasing and for each v, v' the integrand is less than or equal to zero, thus $s_r \leq 0$ holds.

If $f = E$, the second bracket in the integrand is always zero and therefore $s_r = 0$. Application of the mean value theorem on the first bracket yields the estimate

$$s_r \leq -\frac{1}{2} C \int_{\mathbb{S}^2} \int_{\mathbb{S}^2} [E(v)f(v') - E(v')f(v)]^2 \, dv' dv,$$

with the constant $C = \min_{v, v' \in \mathbb{S}^2} \left\{ \frac{K_D(v, v')}{E(v)} \right\} \inf_{v, v' \in \mathbb{S}^2} \{ \eta''(f(v)E(v')) \} \geq 0$. If $f \leq f_{\max} < \infty$, the infimum equals the minimum, and we have $C < 0$. Using the orthogonal decomposition $\mathbb{S}^2 = \mathcal{R}(\mathcal{L}_D) \oplus \mathcal{N}(\mathcal{L}_D)$ from Lemma 3.11, we write $f = \rho E + g$ with $\langle g \rangle = 0$. Only the perturbation g contributes to the dissipation of entropy:

$$s_r \leq -\frac{1}{2} C \int_{\mathbb{S}^2} \int_{\mathbb{S}^2} [E(v)g(v') - E(v')g(v)]^2 \, dv' dv.$$

Assume $g \neq 0$ on a subset of \mathbb{S}^2 with positive measure. Due to $\langle g \rangle = 0$, the sets $V = \{v \mid g(v) < 0\}$, $V' = \{v' \mid g(v') > 0\}$ have positive measure. The Cartesian product $V \times V' \subset \mathbb{S}^2 \times \mathbb{S}^2$ has also positive measure and because E is strictly positive, the integral is strictly positive. Thus, from $f < \infty$ and $g \neq 0$ follows $s_r < 0$, therefore $f < \infty$ and $s_r = 0$ implies $f = E$ a.e. \blacksquare

Equipped with the entropy dissipation of the turning operator, we write an entropy dissipation law for the kinetic equation

$$\partial_t f + \nabla_x \cdot (vf) = \mathcal{L}_D(f)$$

without the perturbation operator \mathcal{L}_a and sources \mathcal{S} . Multiplication by $\partial_f \eta_r(f|E)$ and integration over the velocity space yields

$$\begin{aligned} \langle \partial_f \eta_r(f|E) \partial_t f \rangle + \langle \partial_f \eta_r(f|E) \nabla_x \cdot (vf) \rangle &= \langle \partial_f \eta_r(f|E) \mathcal{L}_D(f) \rangle, \\ \partial_t \langle \eta_r(f|E) \rangle + \nabla_x \cdot \langle v \eta_r(f|E) \rangle - \langle \partial_E \eta_r(f|E) \nabla_x \cdot (vE) \rangle &= \langle \partial_f \eta_r(f|E) \mathcal{L}_D(f) \rangle. \end{aligned}$$

When the equilibrium is constant in space, the entropy dissipation law

$$\partial_t h_r + \nabla_x \cdot j_r = \langle \partial_f \eta_r(f|E) \mathcal{L}_D(f) \rangle \leq 0,$$

with entropy $h_r = \langle \eta_r(f|E) \rangle$ and entropy flux $j_r = \langle v \eta_r(f|E) \rangle$ follows from Lemma 4.2. However, spatial gradients in the equilibrium lead to the additional term

$$-\langle \partial_E \eta_r(f|E) \nabla_x \cdot (vE) \rangle = \langle \eta''(E)(f - E) \nabla_x \cdot (vE) \rangle,$$

which can act both as entropy source and sink. Additionally, entropy can either enter or leave the system through source terms, the perturbation kernel \mathcal{L}_a and the boundary conditions.

4.1.2 The modified minimum-entropy method

Moment systems of the classical radiative transport equation closed with the minimum entropy ansatz inherit the entropy dissipation law. We modify the approach from Section 1.2.3 such that the reconstruction minimizes the relative entropy instead. Given the moments $\mathbf{u} = \langle f \mathbf{a} \rangle$, the reconstruction should satisfy

$$\hat{f} = \operatorname{argmin}_{g, \langle g \mathbf{a} \rangle = \mathbf{u}} \{ \langle \eta_r(g|E) \rangle \}.$$

With the Legendre transform (see Definition 1.13) we formulate this as an unconstrained finite-dimensional optimization problem for the Lagrange multipliers $\boldsymbol{\alpha}$:

$$\hat{\boldsymbol{\alpha}} = \operatorname{argmin}_{\boldsymbol{\alpha}} \{ \langle \eta_{r_*}(\boldsymbol{\alpha} \cdot \mathbf{a}|E) \rangle - \boldsymbol{\alpha} \cdot \mathbf{u} \}.$$

Herein $\eta_{r_*}(f|E)$ is the Legendre transform of η_r with respect to its first argument f . Analogously to (1.16), the reconstruction has the form

$$\hat{f}[\mathbf{u}] = \partial_f \eta_{r_*}(\boldsymbol{\alpha} \cdot \mathbf{a}|E).$$

A formula for the derivative

$$\partial_f \eta_{r_*}(f|E) = (\eta')^{-1}(f + \eta'(E)) \quad (4.3)$$

follows from the property $\phi' \circ \phi_*' = I$ of the Legendre transform and $\partial_f \eta_r(f|E) = \eta'(f) - \eta'(E)$. The inverse $(\eta')^{-1}$ always exists, because η' is strictly monotone increasing.

Modified exponential closure $\mathbf{M}_N^{(E)}$

We insert the Maxwell-Boltzmann entropy (4.1) into formula (4.3):

$$\partial_f \eta_{r_*}(f|E) = E \exp(f).$$

Thus the minimum entropy ansatz is given by

$$\hat{f}[\mathbf{u}] = E \exp(\boldsymbol{\alpha} \cdot \mathbf{a}).$$

This ansatz is always positive and all moments generated from it are automatically realizable, i.e., $\mathfrak{A}(\mathbf{a}, \hat{f}) \subset \mathfrak{R}(\mathbf{a})$. Junk [83] showed that $\mathfrak{A}(\mathbf{a}, \hat{f}) = \mathfrak{R}(\mathbf{a})$ holds for the standard \mathbf{M}_N -method, which is thus able to reproduce all realizable moments. To show the same for the modified $\mathbf{M}_N^{(E)}$ -method is an open problem. We propose to reexamine Junk's proof for the weighted space $L_E^1(\mathbb{S}^2) = \{ f \mid Ef \in L^1(\mathbb{S}^2) \}$.

Modified linear closure $P_N^{(E+)}$

Although we could only show relative entropy dissipation for the Maxwell-Boltzmann entropy, we can still use other entropies to derive moment closures. With the entropy $\eta(f) = \frac{1}{2}f^2$ and the corresponding relative entropy $\eta_r(f|\rho E)$ we define the modified $P_N^{(E+)}$ ansatz

$$\mathfrak{f}[u] = \alpha \cdot a + \rho E.$$

This ansatz is the basis of the AP method in Chapter 5 because it respects the orthogonal decomposition $\mathbb{S}^2 = \mathcal{R}(\mathcal{L}_D) \oplus \mathcal{N}(\mathcal{L}_D)$.

4.2 First-order monomial systems

In the following, we take a closer look at the modified moment systems induced by a first-order monomial basis

$$\mathbf{a} = \begin{pmatrix} \mathbf{a}^{(0)} \\ \mathbf{a}^{(1)} \end{pmatrix} = \begin{pmatrix} 1 \\ v \end{pmatrix}$$

with moments

$$\mathbf{u} = \langle \mathbf{a} f \rangle = (\langle f \rangle, \langle v f \rangle) =: (\rho, q),$$

defined in Section 1.2.1. The first-order moment system for the haptotaxis equation reads

$$\begin{aligned} \partial_t \rho + c \nabla_x \cdot q &= \mu \rho, \\ \partial_t q + c \nabla_x \cdot P &= \lambda_D C + \lambda_a R + \mu S. \end{aligned} \tag{4.4}$$

Therein $P = \langle v v^\top f \rangle$ is the pressure tensor, $C = \langle v \mathcal{L}_D(f) \rangle$ denotes the moments of the turning operator, $R = \langle v \mathcal{L}_a(f) \rangle$ are the moments of the perturbation, and $S = \langle v \mathcal{S}(f) \rangle$ are the moments of the source. In the continuity equation, we used that \mathcal{L}_D and \mathcal{L}_a conserve mass and that the source \mathcal{S} is normalized. To close the system we need to prescribe approximations $P^A[\rho, q]$, $C^A[\rho, q]$, $R^A[\rho, q]$ and $S^A[\rho, q]$ to the unknown moments.

For the glioma model from Section 3.4.2 we have $C = -q$, $R = \widehat{\nabla_x Q} \cdot P$ and $S = q$. The momentum equation is given by

$$\partial_t q + c \nabla_x \cdot P = -\lambda_D q + \lambda_a \widehat{\nabla_x Q} \cdot P + \mu q.$$

It remains to compute the pressure tensor to close this system.

An important quantity is the pressure tensor of the equilibrium

$$P_E := \langle v v^\top E \rangle.$$

Remark 4.3 The standard P_1 and M_1 closures fail to capture the behavior of the haptotaxis equation. For example, the P_1 closure for the glioma model from Section 3.4.2 prescribes the pressure tensor

$$P^A = \langle v v^\top \mathfrak{f} \rangle = \frac{1}{3} I \rho.$$

Hence, the momentum equation reduces to

$$\partial_t q + \frac{1}{3} c \nabla_x \rho = -\lambda_D q + \frac{1}{3} \lambda_a \widehat{\nabla_x Q} \rho + \mu q.$$

No information about the fiber distribution E remains in this approximation. In Section 1.2.5, we have seen that the ansatz \mathfrak{f} must reconstruct the nullspace $\mathcal{N}(\mathcal{L}_D)$ of the turning operator to recover the correct diffusion limit. This is clearly not the case for the standard first-order closures. The defect is visible in the results for Experiment 4.6 (see Figure 4.2) and Experiment 4.7 (see Figure 4.9).

4.2.1 The diffusion limit of the first-order moment system

In analogy to Section 1.2.5, we compute the diffusion limit for the first-order moment system. This limit is only equal to the diffusion limit (3.32) of the kinetic equation under additional conditions on the ansatz and the turning operator. For clarity, we ignore the source terms and assume constant coefficients λ_D, λ_a in the following. We also set the scaling parameters $\delta = \nu = 1$ and obtain the closed first-order moment system in scaled form

$$\begin{aligned} \partial_t \rho + \frac{1}{\varepsilon} \nabla_x \cdot q &= 0, \\ \partial_t q + \frac{1}{\varepsilon} \nabla_x \cdot P^A &= \frac{1}{\varepsilon^2} C^A + \frac{1}{\varepsilon} R^A. \end{aligned}$$

As before, the crucial property of the ansatz is that it reconstructs the equilibrium: $\mathfrak{f}[\rho, 0] = \rho E$. In this case, the unknown moments $P^A[\rho, 0] = P(E) = \rho \langle v v^\top E \rangle$, $C^A[\rho, 0] = \rho C(E) = 0$, $R^A[\rho, 0] = \rho R(E)$ are reproduced exactly in the equilibrium.

We write $q = \varepsilon q^1$ and make the Taylor expansion

$$\mathfrak{f}[\rho, q] = \rho E + \varepsilon \left. \frac{\partial \mathfrak{f}}{\partial q} \right|_{q=0} q^1$$

for the ansatz. The moment constraints $\langle \mathfrak{f} v \rangle = q$ from (1.12) are fulfilled if

$$\left. \frac{\partial \mathfrak{f}}{\partial q} \right|_{q=0} = v \cdot \langle v v^\top H(v) \rangle^{-1} H(v), \quad (4.5)$$

holds for some strictly positive function $H(v)$.

We expand the moments in the first-order system, for instance $C^A[\rho, q] = C^A[\rho, 0] + \varepsilon \left. \frac{\partial C^A}{\partial q} \right|_{q=0} q^1$, and separate powers of ε . To the order ε^{-2} we get the condition $C^A[\rho, 0] = 0$, which is naturally fulfilled if \mathfrak{f} reconstructs the equilibrium. Solving the order ε^{-1} momentum equation for q^1 yields

$$\begin{aligned} q^1 &= \left(\left. \frac{\partial C^A}{\partial q} \right|_{q=0} \right)^{-1} (\nabla_x \cdot P^A[\rho, 0] - R^A[\rho, 0]) \\ &= \left(\left\langle v \mathcal{L}_D \left(\left. \frac{\partial \mathfrak{f}}{\partial q} \right|_{q=0} \right) \right\rangle \right)^{-1} (\nabla_x \cdot (\rho \langle v v^\top E \rangle) - \rho \langle v \mathcal{L}_a(E) \rangle) \\ &= \left(\langle v \mathcal{L}_D(v^\top H) \rangle \langle v v^\top H \rangle^{-1} \right)^{-1} (\nabla_x \cdot (\rho \langle v v^\top E \rangle) - \rho \langle v \mathcal{L}_a(E) \rangle) \\ &= \langle v v^\top H \rangle \langle v \mathcal{L}_D(v^\top H) \rangle^{-1} (\nabla_x \rho \cdot \langle v v^\top E \rangle + \rho \nabla_x \cdot \langle v v^\top E \rangle - \rho \langle v \mathcal{L}_a(E) \rangle). \end{aligned}$$

We insert q^1 into the order $\varepsilon = 0$ continuity equation

$$\partial_t \rho + \nabla_x \cdot q^1 = 0,$$

and obtain

$$\partial_t \rho - \nabla_x \cdot (\hat{D}^A \nabla_x \rho + \hat{a}_D^A \rho - \hat{a}^A \rho) = 0,$$

with

$$\begin{aligned} \hat{D}^A &= -\langle v v^\top H \rangle \langle v \mathcal{L}_D(v^\top H) \rangle^{-1} \langle v v^\top E \rangle, \\ \hat{a}_D^A &= -\langle v v^\top H \rangle \langle v \mathcal{L}_D(v^\top H) \rangle^{-1} \nabla_x \cdot \langle v v^\top E \rangle, \\ \hat{a}^A &= -\langle v v^\top H \rangle \langle v \mathcal{L}_D(v^\top H) \rangle^{-1} \langle v \mathcal{L}_a(E) \rangle. \end{aligned}$$

Compare this with the diffusion tensor and drift vectors for the kinetic equation

$$\begin{aligned} \hat{D} &= -\langle v \mathcal{L}_D^{-1}(v^\top E) \rangle, \\ \hat{a}_D &= -\langle v \mathcal{L}_D^{-1}(v \cdot \nabla_x E) \rangle, \\ \hat{a} &= -\langle v \mathcal{L}_D^{-1} \mathcal{L}_a E \rangle. \end{aligned}$$

The diffusion tensors are equal $\hat{D}^A = \hat{D} = \frac{1}{\gamma} \langle v v^\top E \rangle$, if both vE and vH are eigenfunctions of \mathcal{L}_D to the same eigenvalue $-\gamma$. The former is an assumption on the turning operator similar to Assumption 1.14 and the latter is a condition for the ansatz \mathfrak{f} . To obtain the correct drift vectors, we need even more assumptions: $v \cdot \nabla_x E$ and $\mathcal{L}_a E$ must be eigenfunctions of \mathcal{L}_D to the same eigenvalue $-\gamma$. Especially the first assumption is either restrictive on the turning operator or the gradient field $\nabla_x E$. One turning operator that complies to these restrictions is the BGK-type operator $\mathcal{L}_D(f) = E(v) \langle f \rangle - f$ in the glioma model. Every function with zero mass is an eigenfunction of this operator to eigenvalue -1 . It is not clear if the restrictive assumptions above allow any other operator. Considering Example 1.17 in the introduction, a better diffusion approximation may be obtained in a higher-order moment system.

4.2.2 Some examples for closures

In this section we present examples for closures of the first-order moment system. The closures $P_1^{(E+)}$ and $M_1^{(E)}$ are specializations of the minimum entropy closures $P_N^{(E+)}$ and $M_N^{(E)}$ from Section 4.1. Examples for modified closures that do not belong to the class of minimum-entropy closures are $P_1^{(E)}$ and $K_1^{(E)}$. These ansätze are modified from their classical counterparts P_1 and K_1 to reconstruct the equilibrium. $P_1^{(E)}$, $M_1^{(E)}$ and $K_1^{(E)}$ have been introduced originally in [36].

Additive linear closure $P_1^{(E+)}$

This is the first-order specialization of the modified $P_N^{(E+)}$ closure with the ansatz

$$\rho E + b \cdot v.$$

From the moment constraints $\langle b \cdot v v \rangle = q$ follow the multipliers $b = \langle v v^\top \rangle^{-1} q$. The pressure tensor is given by

$$\begin{aligned} P^A &= \langle v v^\top \mathfrak{f} \rangle \\ &= \rho P_E + \langle v v^\top \rangle^{-1} \langle v v^\top v \cdot q \rangle \\ &= \rho P_E. \end{aligned}$$

As a representative of the minimum-entropy methods, the closure reconstructs P correctly for equilibrium moments $(\rho, 0)$. But P^A is constant with respect to q , hence it fails to approximate the pressure tensor in free-streaming situations.

For the derivative of the ansatz with respect to the momentum we obtain

$$\frac{\partial \mathfrak{f}}{\partial q} = v^\top \cdot v v^\top{}^{-1}.$$

A comparison to equation (4.5) yields $H(v) = 1$. Therefore, in addition to Assumption 1.14, the moment system produces the correct diffusion tensor in the limit, if v and vE are eigenfunctions of the turning operator \mathcal{L}_D to the same eigenvalue $-\gamma$.

Multiplicative linear closure $P_1^{(E)}$

Another way to adapt the P_1 -closure for an anisotropic equilibrium is proposed in [36]. The standard P_1 ansatz is simply multiplied by the equilibrium:

$$\mathfrak{f} = E(a + b \cdot v).$$

Because of $\langle vE \rangle = 0$, the moment constraints (1.12) yield $a = \rho$ and $P_E b = q$. We obtain the pressure tensor

$$P^A = \rho P_E + \langle v v^\top v E \rangle P_E^{-1} q.$$

If the equilibrium is an even function of v , i.e., $E(v) = E(-v)$ holds, then the third moments of E vanish and the pressure tensor is reduced to

$$P^A = \rho P_E.$$

The multiplicative ansatz leads to the same pressure tensor as the additive ansatz. However, the procedures differ in the diffusion limit. We have

$$\frac{\partial \mathfrak{f}}{\partial q} = v \cdot P_E^{-1} E,$$

which yields $H(v) = E(v)$ by comparison to (4.5). Therefore, the ansatz poses no restriction on \mathcal{L}_D to get the correct diffusion tensor, apart from the usual Assumption 1.14.

To derive the Godunov scheme for the $P_1^{(E)}$ system in Section 4.3.1, we compute the flux Jacobian $J\mathcal{F}_n$ and its eigenstructure. Equation (1.14) yields the flux Jacobian in n -direction:

$$J\mathcal{F}_n = \begin{pmatrix} 0 & n^\top \\ P_E n & 0 \end{pmatrix}.$$

With $n = e_\xi = (1, 0, 0)^\top$ for instance, the Jacobian reads:

$$J\mathcal{F}_\xi = \begin{pmatrix} 0 & 1 & 0 & 0 \\ \langle v_\xi v_\xi E \rangle & 0 & 0 & 0 \\ \langle v_\eta v_\xi E \rangle & 0 & 0 & 0 \\ \langle v_\zeta v_\xi E \rangle & 0 & 0 & 0 \end{pmatrix}.$$

There are two waves with zero speed. For any direction n^\perp normal to n , the vector

$$v = \begin{pmatrix} 0 \\ n^\perp \end{pmatrix}$$

is an eigenvector of $J\mathcal{F}_n$ to eigenvalue $\lambda = 0$. Furthermore, there are two waves with speed $\lambda_{\pm} = \pm\sqrt{n^{\top}P_E n}$ to the eigenvectors

$$v_{\pm} = \begin{pmatrix} \lambda_{\pm} \\ P_E n \end{pmatrix}.$$

Modified exponential closure $M_1^{(E)}$

The modified minimum-entropy ansatz with Maxwell-Boltzmann entropy and first-order monomial basis reads

$$\mathfrak{f} = E \exp(a + b \cdot v).$$

The multipliers a, b solve the nonlinear system

$$\begin{aligned} \rho &= \exp(a) \langle \exp(b \cdot v) E \rangle, \\ q &= \exp(a) \langle v \exp(b \cdot v) E \rangle, \end{aligned}$$

of moment constraints. Equivalently, the multipliers minimize the objective function

$$F_{\rho,q}(a, b) = \langle E \exp(a + b \cdot v) \rangle - a\rho - b \cdot q.$$

In normalized moments the second equation

$$\hat{q} = \frac{q}{\rho} = \frac{\langle v \exp(b \cdot v) E \rangle}{\langle \exp(b \cdot v) E \rangle}$$

is independent of a . The multipliers that correspond to equilibrium moments $(\rho, \hat{q}) = (\rho, 0)$ are $(a, b) = (\log(\rho), 0)$. In this case, the pressure tensor reduces to $P^A = \rho P_E$. As for the $P_1^{(E)}$ ansatz, we have

$$\left. \frac{\partial \mathfrak{f}}{\partial q} \right|_{q=0} = v \cdot P_E^{-1} E.$$

Modified Kershaw closure $K_1^{(E)}$

We adapt the Kershaw [86] closure from Section 1.2.4 for anisotropic equilibrium E and construct the pressure tensor as a convex combination between equilibrium and free-streaming moments. In equilibrium $f = E$, the pressure tensor is $P_E = \langle v v^{\top} E \rangle$. In the free-streaming limit all particles move in the same direction $q^* = \frac{\hat{q}}{|\hat{q}|}$, hence the distribution is the Dirac delta $f = \delta_{q^*}(v)$. The free-streaming pressure tensor $\hat{P}_{\delta} = q^* q^{*\top}$ is not affected by the choice of the equilibrium. Analogously to Section 1.2.4, the pressure tensor is the convex combination $\hat{P}^A = \alpha P_E + (1 - \alpha) \hat{P}_{\delta}$ with $\alpha = 1 - |\hat{q}|^2$:

$$\begin{aligned} \hat{P}^A &= (1 - |\hat{q}|^2) P_E + |\hat{q}|^2 q^* q^{*\top} \\ &= (1 - |\hat{q}|^2) P_E + \hat{q} \hat{q}^{\top}. \end{aligned} \tag{4.6}$$

The only difference between the modified and standard Kershaw closures is the equilibrium pressure tensor. For the isotropic equilibrium $E = \frac{1}{\langle 1 \rangle}$ we obtain the standard Kershaw closure K_1 . Due to $\text{tr} \hat{P}^A = 1$ and $\hat{P}^A - \hat{q} \hat{q}^{\top} > 0$ for $|\hat{q}| < 1$ the second moments are realizable.

A detailed computation of the eigenstructure of the resulting moment system is done in Appendix A.5. From the results therein, we conclude the following lemma.

Lemma 4.4 — Hyperbolicity of the generalized Kershaw moment system. The first-order moment system (4.4) with the Kershaw closure (4.6) is strictly hyperbolic for moment vectors (ρ, q) in the interior of the realizable set $|q| < \rho$. On the surface of the realizable set $|q| = \rho$, the Jacobian has real eigenvalues but cannot be diagonalized.

Proof. See the computations in Appendix A.5. ■

Remark 4.5 — Correction. The original version of this lemma published in [36] states that the Jacobian is not diagonalizable only if $|q| = \rho$ and q is parallel to an eigenvector of P_E . That the system loses strict hyperbolicity for all ρ on the boundary of the realizable set has been overlooked.

Kershaw [86] gives the atomic representing density

$$\hat{f}(v) = \rho \sum_{i=1,2,3} \sum_{\pm} \omega^{i\pm} \delta_{v^{i\pm}}(v)$$

for realizable the moments ρ, \hat{q}, \hat{P} . The weights $\omega^{i\pm}$ and positions $v^{i\pm}$ are constructed in a rotated frame of reference $\phi = R^\top v$ in which the pressure tensor $\Lambda = R^\top P_E R$ is diagonal. We start from the vector of normalized first moments in the rotated frame $\hat{r} = R^\top \hat{q}$, which lies in the interior of \mathbb{S}^2 . Then we move parallel to the coordinate axis i in positive or negative direction, until we intersect the sphere \mathbb{S}^2 . This construction, which is sketched in Figure 4.1, yields the positions

$$\phi^{1\pm} = \left(\pm \sqrt{\alpha + \hat{r}_1^2}, \hat{r}_2, \hat{r}_3 \right)^\top, \quad \phi^{2\pm} = \left(\hat{r}_1, \pm \sqrt{\alpha + \hat{r}_2^2}, \hat{r}_3 \right)^\top, \quad \phi^{3\pm} = \left(\hat{r}_1, \hat{r}_2, \pm \sqrt{\alpha + \hat{r}_3^2} \right)^\top.$$

The corresponding weights are

$$\omega^{i\pm} = \frac{\lambda_i}{2} \left(1 \pm \frac{\hat{r}_i}{\sqrt{\alpha + \hat{r}_i^2}} \right).$$

With elementary but lengthy calculations it can be checked that

$$\begin{aligned} \sum_{i\pm} \omega^{i\pm} &= 1, \\ \sum_{i\pm} \omega^{i\pm} \phi^{i\pm} &= \hat{r}, \\ \sum_{i\pm} \omega^{i\pm} \phi^{i\pm} (\phi^{i\pm})^\top &= \alpha \Lambda + \hat{r} \hat{r}^\top \end{aligned}$$

hold, thus the atomic representing density reproduces the moments. In Section 4.3.1 we use the atomic distribution to write a kinetic scheme for the Kershaw system.

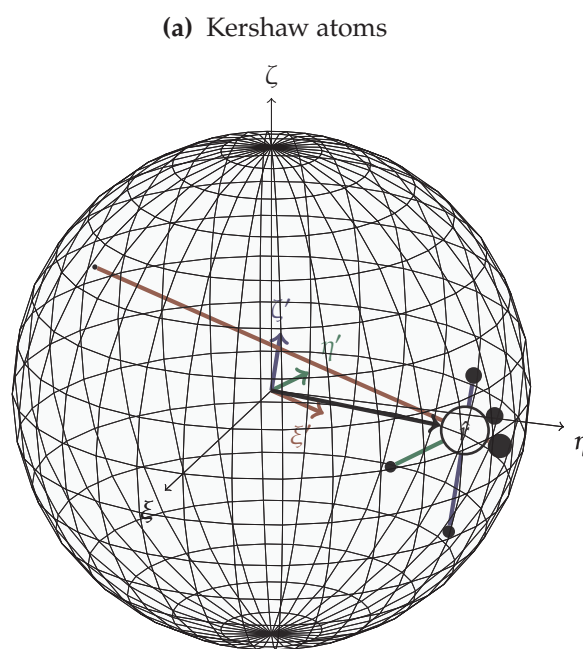


Figure 4.1: The construction of the atomic representing density. In the rotated coordinate system ξ', η', ζ' (red, green and blue arrows) in which the pressure tensor is diagonal, the atom positions (black spheres) are the intersections of the unit sphere with lines parallel to the axes.

4.3 Numerical experiments

To investigate the structure of the modified moment methods, and to compare them to their classical counterparts, we perform a range of numerical experiments. We consider the methods $P_N^{(E)}$, $M_N^{(E)}$ and $K_1^{(E)}$. The $P_N^{(E+)}$ models are treated separately in Chapter 5. The following Section 4.3.1 contains details on the numerical scheme. All experiments are variants of the line source benchmark [58], although sometimes with many modifications. In Section 4.3.2, we describe the default setup for the experiments. To reveal the general structure of the moment models, we first consider a homogeneous setting in Section 4.3.3. The properties of two specialized numerical flux functions are shown in an experiment with heterogeneous equilibrium in Section 4.3.4. We describe how to treat an instationary equilibrium with the modified moment methods in Section 4.3.5. Finally, in Section 4.3.6 we discuss the failure of the numerical scheme in the diffusive regime.

4.3.1 The space and time discretization

For the numerical experiments we use the scheme from [36]. All considered moment systems can be cast in the form

$$\partial_t \mathbf{u} + \nabla_x \cdot \mathcal{F}(\mathbf{u}, x) = \mathcal{R}(\mathbf{u}, x)$$

of a hyperbolic system with sources. When the equilibrium E varies in space also the flux function \mathcal{F} and reaction terms \mathcal{R} depend on space. In the glioma models, the fiber distribution E is estimated from the piece-wise constant measurements of the water diffusion tensor D_W . Therefore, we only treat piece-wise constant flux functions here. We derive a second-order realizability preserving scheme for this system. First, we employ the operator splitting approach and consider the two equations:

$$\partial_t \mathbf{u} + \nabla_x \cdot \mathcal{F}(\mathbf{u}, x) = 0, \quad (4.7)$$

$$\partial_t \mathbf{u} = \mathcal{R}(\mathbf{u}, x). \quad (4.8)$$

When each of the steps is solved with a second-order accurate realizability preserving scheme, the resulting scheme is also second order and realizable, as long as the second-order Strang splitting is used to combine the steps. We use a finite-volume method and write an approximation for the cell averages

$$\mathbf{u}_j \approx \{\mathbf{u}\}_{\Omega_j} := \frac{1}{|\Omega_j|} \int_{\Omega_j} \mathbf{u} dx.$$

The flux system

For the fluxes (4.7), this yields the semi-discrete system

$$\partial_t \mathbf{u}_j + \frac{1}{|\Omega_j|} \sum_{\mathfrak{R}_j} |\partial\Omega_{j,k}| \{\hat{\mathcal{F}}\}_{\partial\Omega_{j,k}}^Q \cdot \mathbf{n}_{j,k} = 0. \quad (4.9)$$

Herein $\hat{\mathcal{F}}(\mathbf{u}_L, \mathbf{u}_R)$ is a numerical flux function, which depends on the left and right states at the interface. $\{\hat{\mathcal{F}}\}_{\partial\Omega_{j,k}}^Q$ is the average of this numerical flux over the interface $\partial\Omega_{j,k}$, approximated by a quadrature rule Q . The interface values are obtained from a cell-wise continuous reconstruction

$\hat{\mathbf{u}}_j(x)$, evaluated at the quadrature nodes. In the first-order scheme a piece-wise constant reconstruction $\hat{\mathbf{u}}_j(x) = \mathbf{u}_j$ is of course sufficient. The second-order scheme needs a piece-wise linear reconstruction

$$\hat{\mathbf{u}}_j(x) = \mathbf{u}_j + S_j \cdot (x - x_j).$$

The slope matrix $S_j \in \mathbb{R}^{n \times d}$ is reconstructed from the cell means of the neighbors. On a tensor-product grid this can be done for each direction independently, for example the slope in ξ -direction depends only on the cell mean at the cell itself and its left and right neighbors. We use the minmod reconstruction, which is

$$S_j = \frac{1}{\Delta x} V_j \text{minmod}(\tilde{\mathbf{u}}_{j+1} - \tilde{\mathbf{u}}_j, \frac{1}{2}(\tilde{\mathbf{u}}_{j+1} - \tilde{\mathbf{u}}_{j-1}), \tilde{\mathbf{u}}_j - \tilde{\mathbf{u}}_{j-1}),$$

$$\text{minmod}(a_1, a_2, a_3) = \begin{cases} \text{sign}(a_1) \min(|a_1|, |a_2|, |a_3|), & \text{sign } a_1 = \text{sign } a_2 = \text{sign } a_3, \\ 0, & \text{else,} \end{cases}$$

in one space dimension on a cell with length Δx . To avoid spurious oscillations, this is done in characteristic variables

$$\tilde{\mathbf{u}}_j = V_j^{-1} \mathbf{u}_j,$$

where V_j contains the eigenvectors of the flux Jacobian $J\mathcal{F}_\xi(\mathbf{u}_j)$.

Additionally, we need to ensure that the reconstruction $\hat{\mathbf{u}}_j(x)$ is a realizable moment vector on the entire cell Ω_j . Therefore, we employ the realizability limiter from [28, 110, 121]. Essentially, this means finding the largest τ , such that $\hat{\mathbf{u}}_j(x) = \mathbf{u}_j + \tau S_j \cdot (x - x_j)$ is realizable on the cell. Because the domains of realizable moments are complicated for higher moment orders, this is only implemented for the first-order moment systems. In that case, the problem boils down to solving a quadratic equation for τ .

To discretize the time derivative in (4.9), we employ an SSP¹ scheme of adequate order [64, 65]. For a first-order scheme, this is simply the explicit Euler method. A second-order SSP scheme is Heun's method. In [121, Chapter 3, Theorem 3.19], it is shown for similar schemes that the cell means remain realizable after one forward Euler step under an appropriate CFL condition. Because explicit SSP schemes are just convex combinations of explicit Euler steps, this guarantees the realizability of the cell means in the second-order scheme, if the realizability limiter is applied in each stage of the method.

We consider two choices for the numerical flux function that work with any moment method. The simplest choice is of course the Lax-Friedrichs flux

$$\hat{\mathcal{F}}^{LF}(\mathbf{u}_L, \mathbf{u}_R) = \frac{1}{2} (\mathcal{F}(\mathbf{u}_L) + \mathcal{F}(\mathbf{u}_R) - c(\mathbf{u}_R - \mathbf{u}_L)).$$

The largest eigenvalue of the flux Jacobian $J\mathcal{F}_n$ is bounded by the particle speed c . Thus, we simply take c as the viscosity constant. The Lax-Friedrichs flux is easy to implement for arbitrary flux functions, cheap to evaluate and adequate for smooth solutions. When the solution has discontinuities or the flux function itself is discontinuous in space, then it may produce too much numerical diffusion.

¹Strong stability preserving

In the underlying kinetic equation, the distribution $f(t, x, v)$ is transported in direction v . Therefore, an upwind scheme per direction is natural. In the moment system, we use the reconstruction $\mathfrak{f}(\mathbf{u})$ from moments to define the kinetic flux

$$\hat{\mathcal{F}}^K(\mathbf{u}_L, \mathbf{u}_R) = \langle v \mathbf{a} \mathfrak{f}(\mathbf{u}_L) \rangle_{v \cdot \mathbf{n} > 0} + \langle v \mathbf{a} \mathfrak{f}(\mathbf{u}_R) \rangle_{v \cdot \mathbf{n} < 0}.$$

The integral $\langle \cdot \rangle_{v \cdot \mathbf{n} > 0}$ is only taken over those directions v with positive component $v \cdot \mathbf{n}$ normal to the interface. The kinetic flux automatically handles jumps in the flux function correctly. However, it is more costly, especially for higher moment orders, because we need to compute the reconstructions and the integrals have to be approximated by a quadrature. If the Kershaw ansatz from Section 4.2.2 is used, the kinetic flux can be written with the atomic representing density. In that case the integrals reduce to

$$\langle v \mathbf{a}(v) \mathfrak{f}(\mathbf{u}_L) \rangle_{v \cdot \mathbf{n} > 0} = \rho \sum_{v^{i\pm} \cdot \mathbf{n}_{j,k} > 0} \omega^{i\pm} v^{i\pm} \mathbf{a}(v^{i\pm}).$$

In the special case of the $P_1^{(E)}$ -model (with monomial basis), we have the linear system

$$\partial_t \mathbf{u} + \partial_\xi (J\mathcal{F}_\xi \mathbf{u}) + \partial_\eta (J\mathcal{F}_\eta \mathbf{u}) + \partial_\zeta (J\mathcal{F}_\zeta \mathbf{u}) = 0,$$

with moments $\mathbf{u} = (\rho, q)^\top$. The flux Jacobian $J\mathcal{F}_n$ and its characteristic field are detailed in Section 4.2.2. Due to its simple eigenstructure, we can write the Godunov scheme for the heterogeneous conservation law according to [97, 98]. The Riemann problem at a cell interface is determined by the initial data $\mathbf{u}_L, \mathbf{u}_R$ and the equilibria E_L, E_R on the left and right cells. Its solution consists of a left-going shock satisfying the Rankine-Hugoniot conditions $J\mathcal{F}_{n,L}(\mathbf{u}_{L^*} - \mathbf{u}_L) = \lambda_L(\mathbf{u}_{L^*} - \mathbf{u}_L)$ in the left cell, a right-going shock satisfying a similar RH-condition in the right cell, and two stationary shocks at the interface that connect \mathbf{u}_{L^*} and \mathbf{u}_{R^*} and ensure the continuity of fluxes $J\mathcal{F}_{n,L}\mathbf{u}_{L^*} = J\mathcal{F}_{n,R}\mathbf{u}_{R^*}$. Instead of the left and right states, which are discontinuous at the interface, we connect the left and right flux via

$$J\mathcal{F}_{n,R}\mathbf{u}_R - J\mathcal{F}_{n,L}\mathbf{u}_L = v_L \beta_L + v_R \beta_R,$$

where v_L is the eigenvector to the negative eigenvalue λ_L in the left cell. This is a linear system with four equations for the two unknowns β_L, β_R , which we can solve nevertheless because the flux Jacobians $J\mathcal{F}_{n,L}, J\mathcal{F}_{n,R}$ have the same nullspace. Then the Godunov flux at the interface is

$$\hat{\mathcal{F}}^G(\mathbf{u}_L, \mathbf{u}_R) = \mathcal{F}(\mathbf{u}_L) + \beta_L v_L = \mathcal{F}(\mathbf{u}_R) - \beta_R v_R.$$

The reactions

The finite-volume projection for the reactions (4.8) leads to the semi-discrete system

$$\partial_t \mathbf{u}_j = \{\mathcal{R}(\mathbf{u})\}_{\Omega_j} = \mathcal{R}(\mathbf{u}_j) + \mathcal{O}(\Delta x^2). \quad (4.10)$$

This is an ODE for \mathbf{u}_j in each cell Ω_j . For simplicity, we therefore neglect the spatial index j and just write $\partial_t \mathbf{u} = \mathcal{R}(\mathbf{u})$. The discontinuous-Galerkin scheme [11, 61] is unconditionally A-stable and with even polynomial order also realizability-preserving without time step restriction.

The weak form of (4.10), using test functions $\phi(t)$ with support on the temporal cell $[t_n, t_{n+1})$, is

$$\int_{t_n}^{t_{n+1}} \partial_t \mathbf{u} \phi(t) dt - \int_{t_n}^{t_{n+1}} \mathcal{R}(\mathbf{u}) \phi(t) dt + \phi(t_n^+) \mathbf{u}(t_n^+) = \phi(t_n^-) \mathbf{u}(t_n^-),$$

wherein for example $\mathbf{u}(t_n^-) = \lim_{t \uparrow t_n} \mathbf{u}(t)$. This means that the solution $\mathbf{u}(t)$ can be discontinuous at the temporal cell interfaces: $\mathbf{u}(t_n^-) \neq \mathbf{u}(t_n^+)$ is possible. After transformation $\tau = -1 + 2\frac{t-t_n}{t_{n+1}-t_n}$ to the reference interval $[-1, 1]$, this is

$$\int_{-1}^1 \partial_t \mathbf{u} \phi(\tau) d\tau - \frac{\Delta t}{2} \int_{-1}^1 \mathcal{R}(\mathbf{u}) \phi(\tau) d\tau + \phi(-1) \mathbf{u}(t_n^+) = \phi(-1) \mathbf{u}(t_n^-),$$

with $\Delta t = t_{n+1} - t_n$. We discretize this equation with a Lagrange basis of degree two for test and ansatz functions, with nodes $\tau_0 = -1, \tau_1 = 0, \tau_2 = 1$. The Lagrange functions are

$$\phi_0(\tau) = \frac{1}{2}(\tau^2 - \tau), \quad \phi_1(\tau) = 1 - \tau^2, \quad \phi_2(\tau) = \frac{1}{2}(\tau^2 + \tau),$$

and $\mathbf{u}_h(\tau)$ represented in this basis is

$$\mathbf{u}_h(\tau) = \sum_{i=1,2,3} \mathbf{u}_{n,i} \phi_i(\tau),$$

with coefficients

$$\mathbf{u}_{n,0} = \mathbf{u}(t_n^+), \quad \mathbf{u}_{n,1} = \mathbf{u}(t(\tau_1)) = \mathbf{u}\left(\frac{1}{2}(t_{n+1} + t_n)\right), \quad \mathbf{u}_{n,2} = \mathbf{u}(t_{n+1}^-).$$

We obtain the possibly nonlinear system

$$\int_{-1}^1 \partial_t \mathbf{u}_h \phi_i d\tau - \frac{\Delta t}{2} \int_{-1}^1 \mathcal{R}(\mathbf{u}_h) \phi_i d\tau + \delta_{i0} \mathbf{u}_{n,0} = \delta_{i0} \mathbf{u}_{n-1,2}, \quad i = 0, 1, 2$$

for the coefficients $\mathbf{u}_{n,i}$. The last value from the previous time step $\mathbf{u}_{n-1,2}$ enters this system as a right-hand side. The first integral term leads to a mass matrix M with $M_{ij} = \int_{-1}^1 \phi'_j(\tau) \phi_i(\tau) d\tau$, which can be computed analytically. We approximate the reaction integral by a Gauss quadrature. Finally, we solve this system with a Newton method. To evaluate the gradient, we need to calculate derivatives of the reaction term $\frac{\partial \mathcal{R}(\mathbf{u})}{\partial \mathbf{u}}$. The initial guess for the Newton iteration is a constant extrapolation of the last time step.

4.3.2 The basic setup

The definitions in this section serve as default values for the following experiments. All experiments are derived, sometimes with strong modifications, from the classical line source benchmark [58]. The line source problem is a well-known benchmark [59, 123] used to assess properties of angular discretization methods. In an infinite homogeneous medium with isotropic scattering, the particles are initially concentrated at the ζ -axis: $f(0, x, v) = \frac{1}{(4\pi)} \delta_0(\zeta)$. This situation admits the reduced two-dimensional description from Section 1.1.2. There is an analytic solution to the classical line source problem, which features a sharp circular wavefront moving at unit speed and a smooth trailing distribution consisting of the scattered particles. Here we want to adapt the problem formulation to investigate the structure of the modified moment methods when E is not isotropic. We do not have an analytic solution for this problem.

Recall the glioma equation from Section 3.4.2

$$\partial_t f + c \nabla_x \cdot (v f) = \lambda_0 (E \langle f \rangle - f) + \lambda_H c \nabla_x Q \cdot (v f - E \langle v f \rangle),$$

without growth and with constant rate parameters λ_0, λ_H . In all following experiments, we compute solutions to this equation. The equilibrium $E(v)$ is always a peanut distribution (2.4). We prescribe artificial water diffusion tensors

$$D_W(x) = \frac{1}{(A(x) + 2)} R(x) \begin{pmatrix} A(x) & 0 & 0 \\ 0 & 1 & 0 \\ 0 & 0 & 1 \end{pmatrix} R(x)^\top$$

in terms of the anisotropy factor $A(x)$ and the main diffusion direction v_1 . $R(x)$ is a rotation matrix that rotates the vector $(1, 0, 0)^\top$ onto v_1 . Because the peanut estimate is independent of $\text{tr } D_W$, we define D_W such that $\text{tr } D_W = 1$.

We have to be careful to respect the positivity condition (3.22). For the glioma model, this translates to

$$\lambda_H < \frac{\lambda_0}{c \|\nabla_x Q\|}.$$

The default initial condition is a narrow Gaussian with standard deviation $\sigma = 0.03$ mm:

$$f(0, x, v) = \frac{1}{\langle 1 \rangle} \max \left(10^{-4}, \exp \left(-\frac{\|x\|^2}{2\sigma^2} \right) \right). \quad (4.11)$$

Because only a finite number of cells can occupy a given volume, we choose an initial condition that is normalized with respect to the density ρ at its peak. Thus, ρ can be interpreted as the fraction of cells with respect to this maximum cell density. Of course the problem is linear, and the normalization does not influence the structure of the solution. The floor of 10^{-4} ensures positivity of the distribution for the $M_N^{(E)}$ and $K_N^{(E)}$ models.

Simulations cover a time span of $T = 1$ s and the spatial domain is $\Omega_x = [-1.5 \text{ mm}, 1.5 \text{ mm}]^2$ such that no interaction with the boundary happens. Nevertheless, at the boundary we prescribe a thermal reflection condition. If nothing else is defined, computations are performed on an equidistant grid with 200×200 grid cells with the second-order scheme and kinetic fluxes.

4.3.3 A homogeneous setting

To expose the structure of the modified moment methods, we prescribe a homogeneous fiber distribution. Hence, we choose the constant water diffusion tensor D_W with anisotropy factor $A = 6$ and main direction $v_1 = \frac{1}{\sqrt{3}}(2, -1, 0)^\top$. According to Section A.3, the resulting equilibrium pressure tensor P_E is given by

$$P_E = R \begin{pmatrix} \frac{1}{2} & 0 & 0 \\ 0 & \frac{1}{4} & 0 \\ 0 & 0 & \frac{1}{4} \end{pmatrix} R^\top.$$

Additionally, we prescribe a field Q with constant and normalized gradient $\nabla_x Q = \frac{1}{\sqrt{7}}(3, 1, 0)^\top$. The parameters in Table 4.1 describe a setting in the kinetic regime with some drift. The positivity condition (3.22) $0.5 = \lambda_H < 2$ is easily satisfied.

λ_0	2 s^{-1}	turning rate
λ_H	0.5	ratio of turning rate coefficients $\frac{\lambda_1}{\lambda_0}$
c	1 mm s^{-1}	cell speed
St	3	Strouhal number
Kn_D	0.5	Knudsen number for turning
Kn_a	6	Knudsen number for drift
ε	0.17	parabolic scaling number

Table 4.1: Base parameters for the line source benchmark.

No drift

To observe the effects of the anisotropic equilibrium in isolation, we switch off the drift term. In this setting, we compare the methods $P_N^{(E)}$, $M_N^{(E)}$ and $K_1^{(E)}$ to their classical counterparts, first in the kinetic regime and then in an intermediate regime.

■ **Experiment 4.6 — Kinetic regime.** We take the parameters from Table 4.1 but set $\lambda_H = 0$, thus $\text{Kn}_a = \infty$. We compute the modified linear moment models $P_N^{(E)}$ for $N = 1, 3, 5, 7, 9$ and the modified exponential models $M_N^{(E)}$ for $N = 1, 2$ as well as their classical counterparts P_N, M_N . Additionally, we compute the modified Kershaw model $K_1^{(E)}$. All computations except for the $M_2^{(E)}$ and M_2 models are done on a uniform grid with 200×200 cells and the second-order scheme. We did not implement a realizability limiter for $N > 1$ and therefore have to use a first-order scheme for the M_2 and $M_2^{(E)}$ models. To compensate, we increase the resolution to 400×400 grid cells.

Figures 4.2 - 4.7 display the results of Experiment 4.6. In Figure 4.2 and Figure 4.3 the density ρ in the solutions to the linear moment models $P_N^{(E)}$ and P_N , as well as their point-wise difference are plotted. For $N = 1, 3, 5, 7$, Figure 4.4 contains plots of the density along two lines. Starting from the origin, one line is parallel to the main axis v_1 and the other line is orthogonal to v_1 . In the classical P_N methods the fluxes do not depend on the equilibrium and wave propagation is independent of the direction. Therefore, the waves in the P_N solutions are always circular. In the P_1 solution, we observe the expected speed $\frac{1}{\sqrt{3}}$ in any direction. As discussed in Remark 4.3, the classical first-order moment models do not retain any information about the equilibrium. Consequently, the P_1 solution is rotationally symmetric. In the higher-order classical models, the equilibrium distribution is represented in the moments of the turning operator $\langle a \mathcal{L}_D f \rangle$. The amplitudes of their circular waves vary with direction. The modified moment methods incorporate the anisotropic equilibrium also in the fluxes. For the $P_1^{(E)}$ method we saw in Section 4.2.2 that there are two waves with speed $\pm \sqrt{n^\top P_E n}$. The observed propagation speed $\frac{1}{\sqrt{2}}$ in the main direction and $\frac{1}{2}$ in the orthogonal direction match that prediction. In the higher-order modified methods, the speed difference between main and orthogonal direction is greater for the slower waves. In the $P_7^{(E)}$ and $P_9^{(E)}$ solutions, the outer rings are almost circular, whereas in the inner ring the ellipsoid form is still visible, though less pronounced than in the lower-order

models.

Figure 4.5 and Figure 4.6 present the $M_N^{(E)}$ and M_N solutions for $N = 1, 2$. Like the linear first-order model, the M_N ansatz does not include any information about the equilibrium and is therefore rotationally symmetric. In the $M_1^{(E)}$ solution, there is a difference in wave speed between main and orthogonal directions, though less pronounced than in the $P_1^{(E)}$ solution. We expect that this difference vanishes in the free-streaming limit $\lambda_0 \rightarrow 0$, which we cannot compute, because the optimization problem to compute multipliers from moments becomes arbitrarily ill-conditioned. Because the floor of the initial condition interacts with the thermal boundary condition, the $M_N^{(E)}$ and M_N solutions differ also outside the central ring. Including the equilibrium into the ansatz seems to make the multiplier optimization problem easier to solve numerically. The $M_N^{(E)}$ solutions were computed with the kinetic flux, but for this setting, the optimizer in the M_N methods fails. We have to help the optimizer with a little bit of numerical diffusion and use the Lax-Friedrichs flux instead. A detailed numerical study of the optimization problem for the modified $M_N^{(E)}$ closure in analogy to [1] is an interesting line of future research. In the $M_2^{(E)}$ solution, the modified flux leads to a more concentrated central zero-speed wave². Finally, Figure 4.7 shows a comparison between the $K_1^{(E)}$, $M_1^{(E)}$, and $P_1^{(E)}$ solutions. Although the maximal wave speed of the $K_1^{(E)}$ model is one in all directions (see Section A.5), we observe an elliptical shape of the solution, because the maximum speed is only obtained at the realizability boundary.

■ **Experiment 4.7 — Intermediate regime.** We take the parameters from Table 4.1 and switch off the drift term, i.e., $\lambda_H = 0$ and $\text{Kn}_a = \infty$. Furthermore, we choose a turning rate $\lambda_0 = 10 \text{ s}^{-1}$, in the intermediate regime with $\text{Kn}_D = 0.1$ and $\varepsilon = 0.03$. We compute the linear moment models $P_N^{(E)}$, P_N for $N = 1, 3, 5$ and the $M_1^{(E)}$ and $K_1^{(E)}$ models.

Figure 4.9 shows the $P_N^{(E)}$ and P_N solutions in the intermediate regime. As before, the first-order classical ansatz fails to approximate the equilibrium and produces a circular solution. In the diffusion limit, the analytic solution to the anisotropic line source problem is a Gaussian with covariance matrix P_E^{-1} . The numerical scheme is not designed to work close to the diffusion limit (see Section 4.3.6), hence we do not discuss convergence to this solution here. However, visually, the third and fifth-order solutions are already close to an anisotropic Gaussian. In both first-order solutions, the reduced wave speed is still visible in the sharper transition at the edge of the cell cluster. The difference between $P_3^{(E)}$ and $P_1^{(E)}$ is about 10%. In this regime, a low moment order suffices to represent the solution adequately. The relative difference between the $P_5^{(E)}$ and $P_3^{(E)}$ solutions is below 1%.

The differences between modified and classical schemes vanish fast with increasing moment order. Already at $N = 5$, the relative difference is below 0.1% everywhere. The third and fifth-order ansätze are able to approximate the equilibrium, a second-order polynomial, exactly. In the diffusion limit we expect the difference between modified and classical models to vanish

²The flux matrices of the even-order P_N models have always one zero eigenvalue. For example, in one space dimension, the eigenvalues are the roots of the Legendre polynomial of order $N + 1$ [72, Sec. 3.2]. The M_N model has the same flux matrix as the P_N for equilibrium moments u_E . An in-depth discussion of the eigenstructure of moment models can be found in [121, Sec. I.2.5].

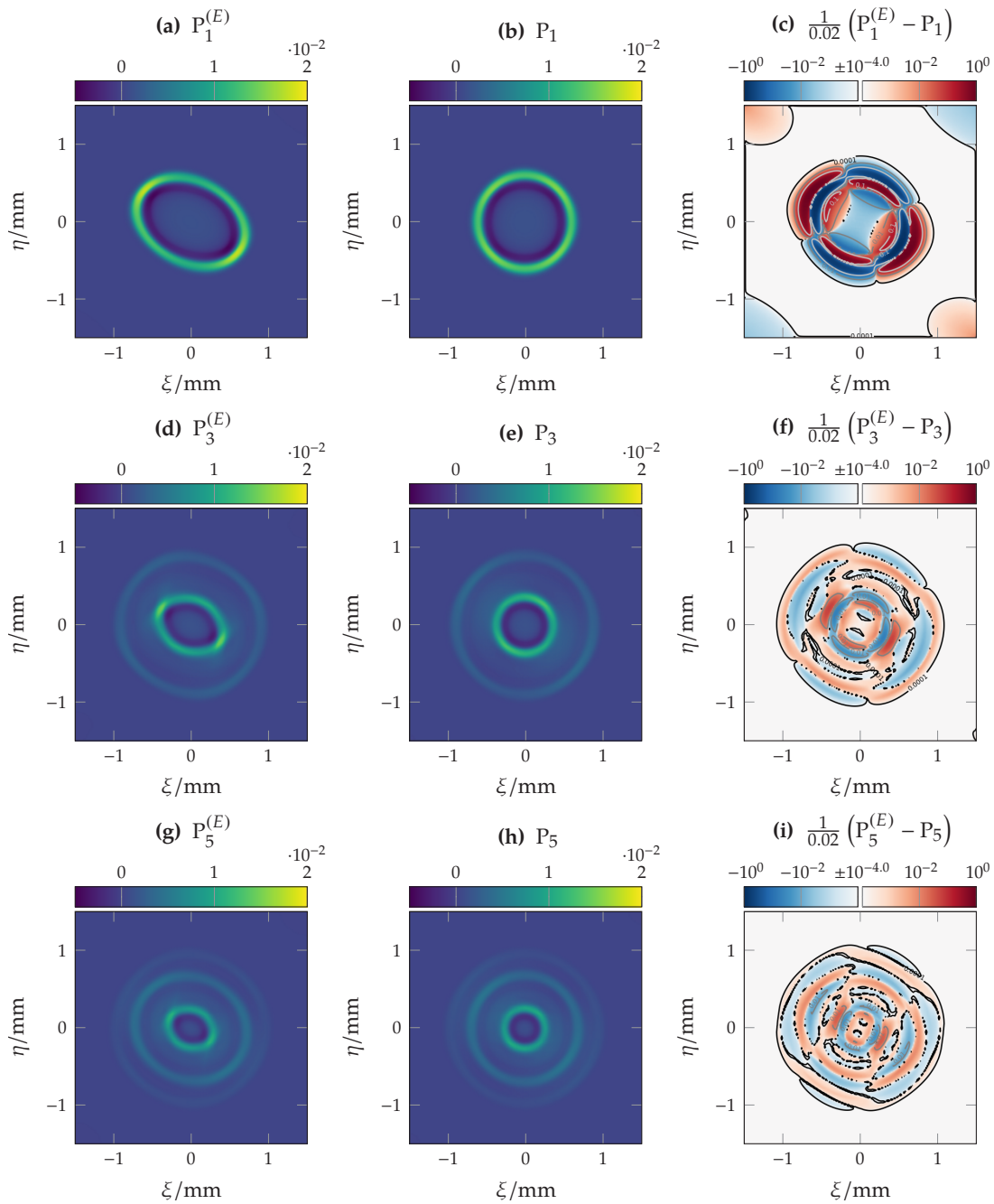


Figure 4.2: Results of Experiment 4.6—kinetic regime. First two columns: Density ρ of the $P_N^{(E)}$ and P_N solutions, respectively. Third column: Their point-wise relative difference on a signed logarithmic scale. The contours in the third column are drawn at 10%, 1% and 0.01% magnitude of the relative difference. Rows: $N = 1, 3, 5$.

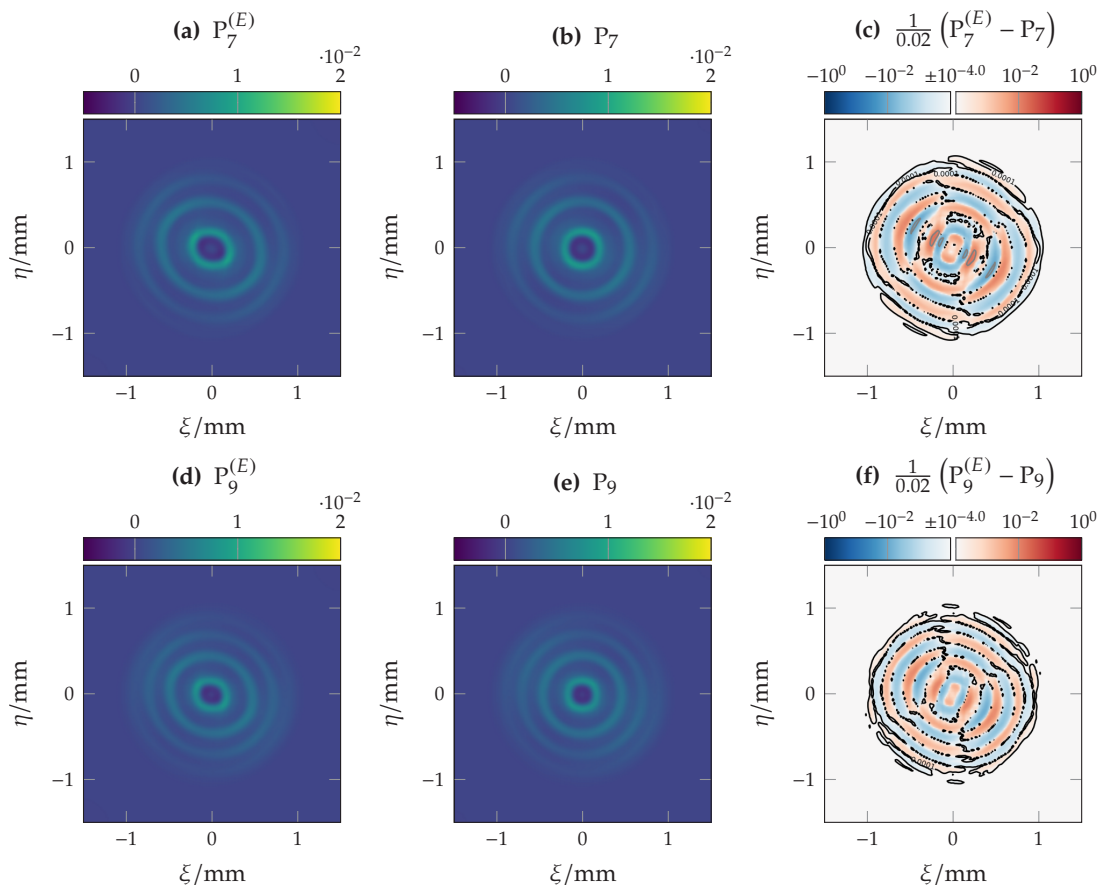


Figure 4.3: Results of Experiment 4.6—kinetic regime. The figure layout is the same as in Figure 4.2 but rows correspond to moment orders $N = 7, 9$

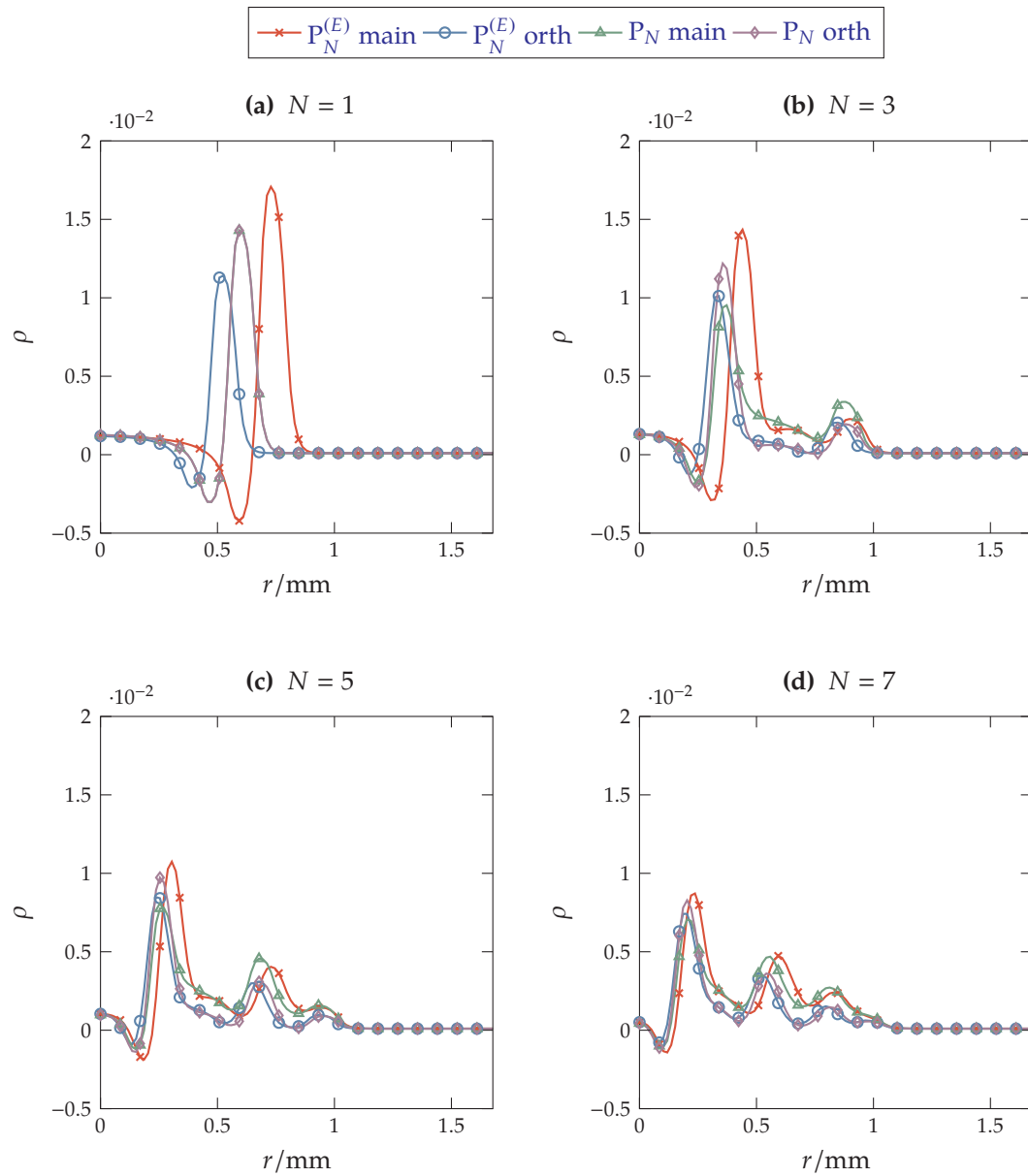


Figure 4.4: Results of Experiment 4.6—kinetic regime. In each subfigure, the density ρ of the $P_N^{(E)}$ and P_N solutions is plotted over two lines: One parallel to and one orthogonal to the main axis of D_W .

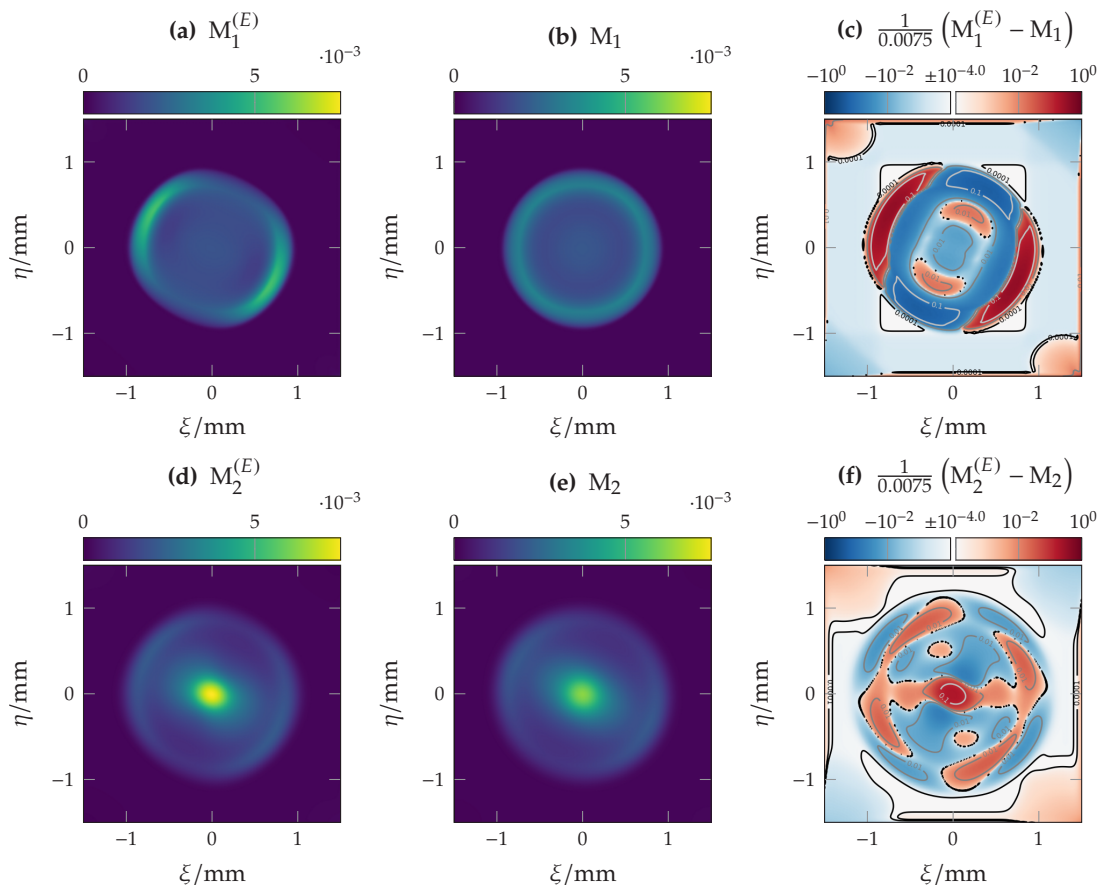


Figure 4.5: Results of the modified $M_N^{(E)}$ and classical M_N models, $N = 1, 2$ in Experiment 4.6—kinetic regime. Otherwise, the figure layout is the same as in Figure 4.2.

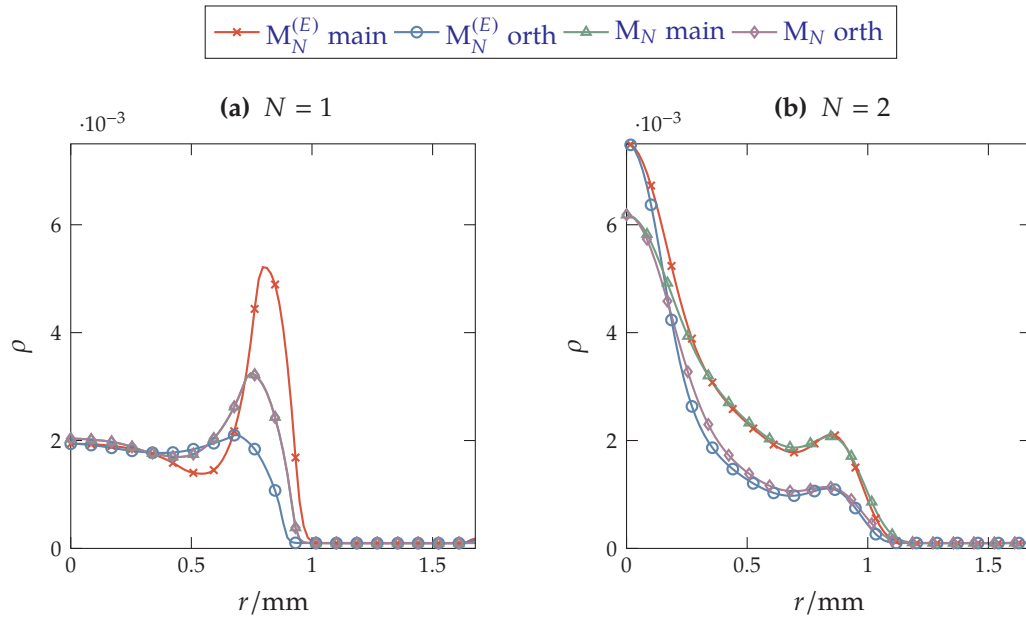


Figure 4.6: Results of the modified $M_N^{(E)}$ and classical M_N models, $N = 1, 2$ in Experiment 4.6—kinetic regime. Line plots of ρ over the main and orthogonal directions of D_W , as in Figure 4.4.

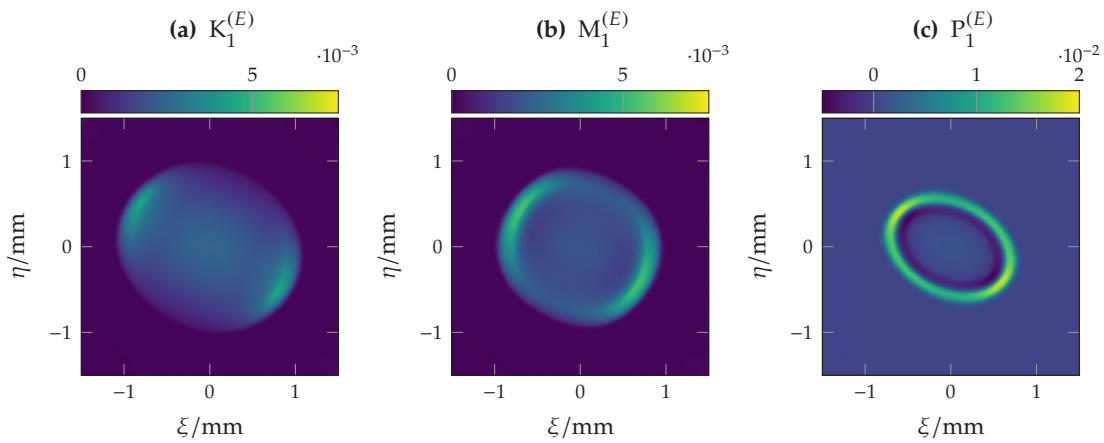


Figure 4.7: Results of Experiment 4.6—kinetic regime. Density ρ of the $K_1^{(E)}$, $M_1^{(E)}$, and $P_1^{(E)}$ solutions.

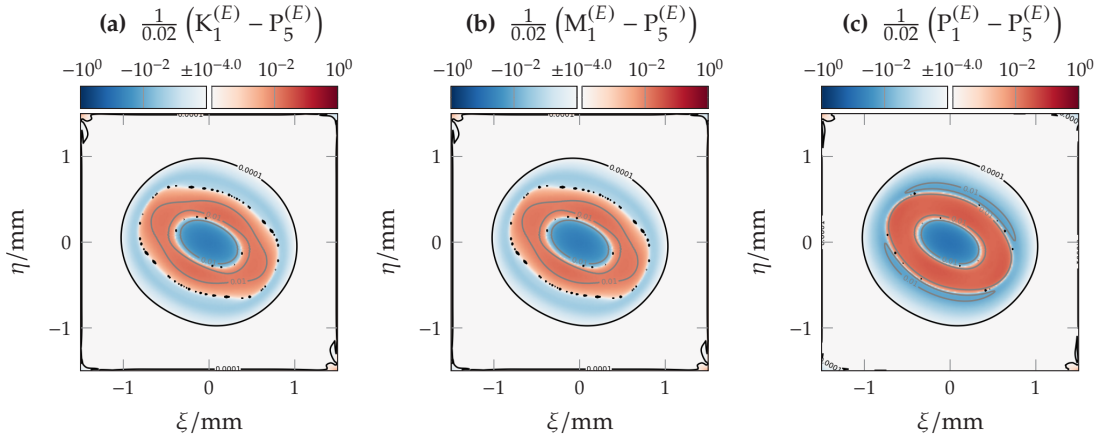


Figure 4.8: Results of Experiment 4.7—intermediate regime. Density ρ of the $K_1^{(E)}$, $M_1^{(E)}$, and $P_1^{(E)}$ solutions.

completely for $N \geq 3$. We hypothesize that differences between modified and classical schemes would be more pronounced if the equilibrium is not exactly represented by the ansatz. However, we did not test this numerically. In Figure 4.8 the relative differences of the first-order models to the $P_5^{(E)}$ solution are shown. All three models underestimate the reference at the outer edge, but the $P_1^{(E)}$ model makes the largest error. In this regime, $K_1^{(E)}$ and $M_1^{(E)}$ perform equally.

With drift term

The following experiment reveals the influence of the drift term on the structure of the solution.

■ Experiment 4.8 — Drift.

We take the parameters from Table 4.1 and compute solutions for the modified linear moment models $P_N^{(E)}$ for $N = 1, 3, 5$, the exponential models $M_N^{(E)}$ for $N = 1, 2$ and the Kershaw model $K_1^{(E)}$. All computations except for the $M_2^{(E)}$ model are done on a uniform grid with 200×200 cells and the second-order scheme. The $M_2^{(E)}$ solution is computed on a 400×400 grid using the first-order scheme.

The density ρ for all models in Experiment 4.8 is shown in Figure 4.10. Figure 4.11 displays two line plots per model, one in drift direction and one against it together with one line plot of the corresponding model without drift. In the presence of the drift term the particles preferentially move in drift direction. This effect is present in the solutions to all moment models. The amplitudes of the waves in drift direction are larger than against drift direction. But the drift term leaves the wave speeds and therefore the overall structure of the solutions unmodified.

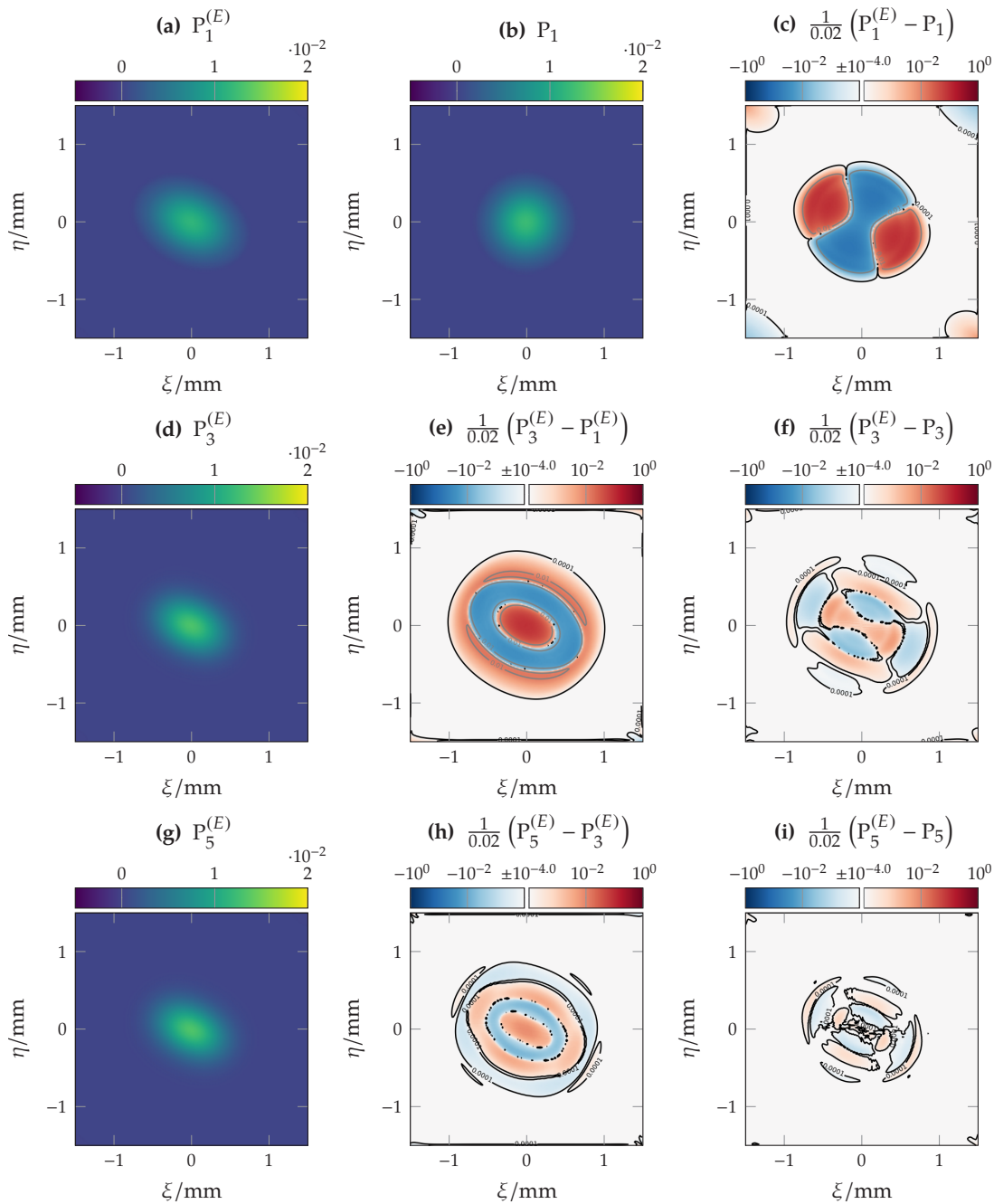


Figure 4.9: Results of Experiment 4.7—intermediate regime: Density ρ of the modified $P_N^{(E)}$ and classical P_N solutions with $N = 1, 3, 5$. First row: The $P_1^{(E)}$ and P_1 solutions and their point-wise difference. Second row: The $P_3^{(E)}$ solution, the difference to the $P_1^{(E)}$ solution and the difference to the P_3 solution. Third row: The $P_5^{(E)}$ solution, the difference to the $P_3^{(E)}$ solution and the difference to the P_5 solution.

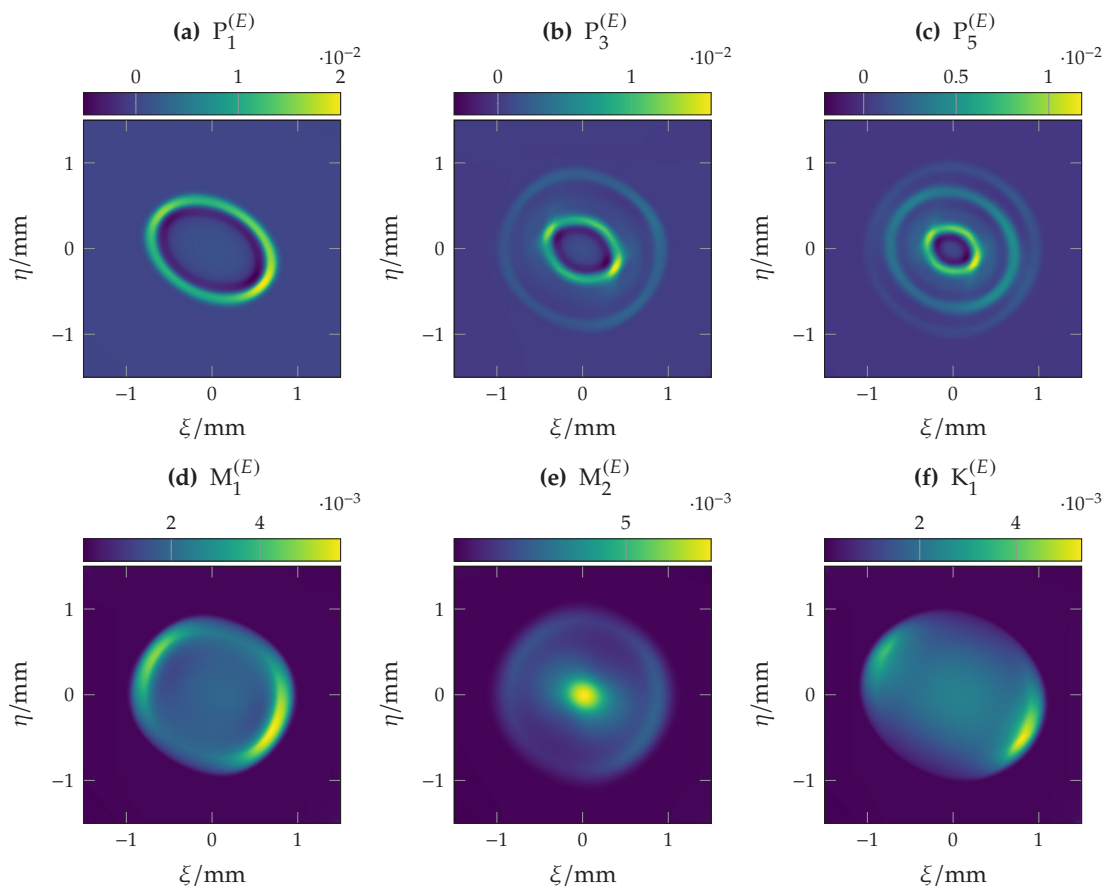


Figure 4.10: Density ρ of the $P_1^{(E)}$, $P_3^{(E)}$, $P_5^{(E)}$, $M_1^{(E)}$, $M_2^{(E)}$, and $K_1^{(E)}$ solutions to Experiment 4.8—drift.

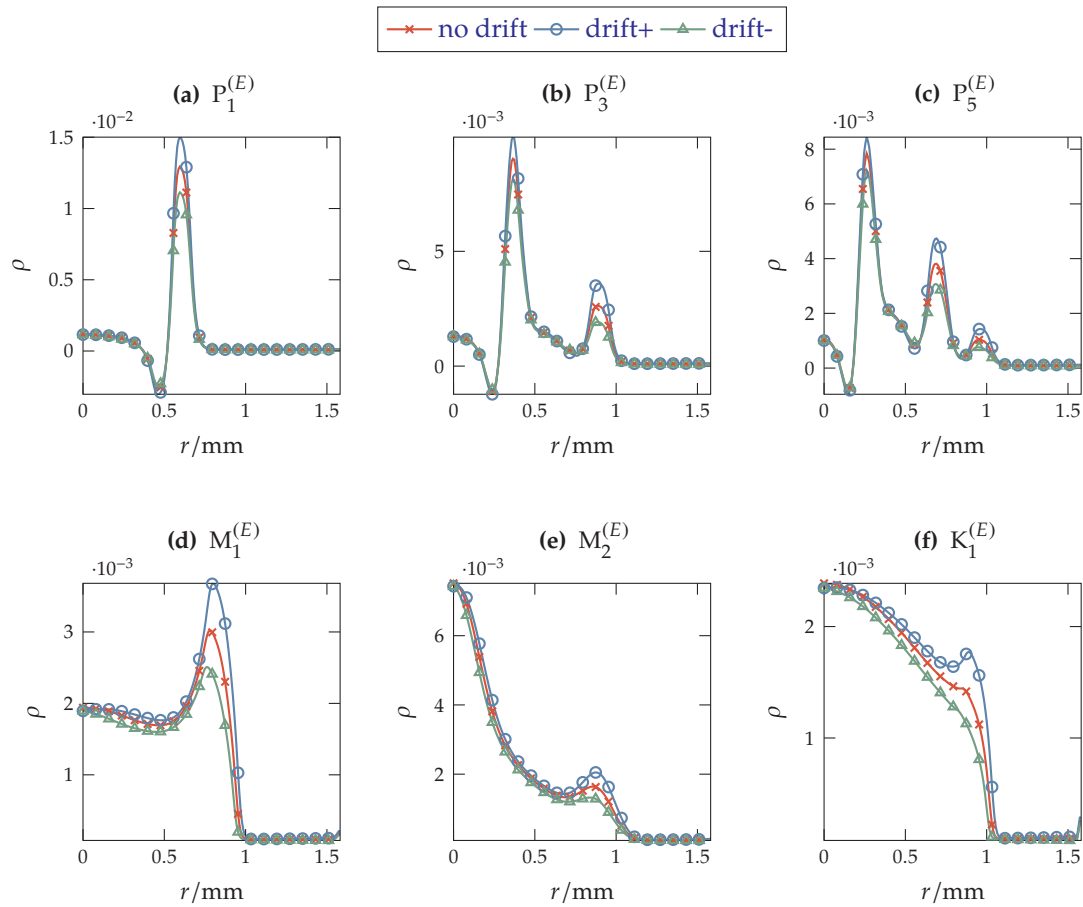


Figure 4.11: Results of Experiment 4.6—drift. In each subfigure, the density ρ of one model ($P_1^{(E)}$, $P_3^{(E)}$, $P_5^{(E)}$, $M_1^{(E)}$, $M_2^{(E)}$ and $K_1^{(E)}$) is plotted over two lines: One with (drift+) and one against (drift-) the drift direction. Also, for comparison the corresponding solution from Experiment 4.6—kinetic regime—without drift is shown.

4.3.4 Flux functions and heterogeneous media

This test is designed to show the differences in approximation quality between numerical flux functions. In Section 4.3, two specialized flux functions were introduced: the Godunov flux for the $P_1^{(E)}$ model, and the kinetic flux for the $K_1^{(E)}$ model. We expect both numerical fluxes to perform significantly better than the all-purpose Lax-Friedrichs flux, especially at material interfaces. The setup is similar to the line source benchmark in Section 4.3.2 without drift, except that the water diffusion tensor and therefore the equilibrium is discontinuous. We divide the domain of width $X = 3$ mm into N_s vertical stripes, in each of which D_W is constant:

$$D_W(x) = \begin{cases} D_{W,E}, & \lfloor \frac{N_s}{X} \xi + 0.5 \rfloor \text{ even,} \\ D_{W,O}, & \lfloor \frac{N_s}{X} \xi + 0.5 \rfloor \text{ odd.} \end{cases}$$

The anisotropy factor $A = 6$ is the same for $D_{W,E}$ and $D_{W,O}$, but the main diffusion directions meet at right angles at the interfaces. For $D_{W,E}$, the main direction is $\frac{1}{\sqrt{2}}(1, 1)^T$ and for $D_{W,O}$ it is $\frac{1}{\sqrt{2}}(1, -1)$. The chosen parameters in Table 4.2 correspond to a kinetic regime.

■ **Experiment 4.9 — Lax-Friedrichs vs. Godunov.** We compute solutions to the $P_1^{(E)}$ model for

1. a coarse stripe layout with $N_s = 10$,
2. a fine stripe layout with $N_s = 100$,

each with the Lax-Friedrichs flux and the Godunov flux for the parameters from Table 4.2. The end time is $T = 2$ s.

Figure 4.12 displays the results of Experiment 4.9: The solutions computed with the Lax-Friedrichs flux and the Godunov flux and their relative differences. In all solutions the single wave of the $P_1^{(E)}$ model is visible. Each time it hits an interface, a fraction of the wave is reflected. In both solutions for the coarse layout these reflections are clearly visible. Almost vertically travelling particles have a tendency to get trapped at the interfaces due to refraction. The Godunov flux has less numerical diffusion and produces a much sharper solution: The main wave is less smeared and the reflection patterns are clearer. For the fine layout, a homogenization technique [97] is applicable such that we can consider a single homogeneous medium with averaged properties as an approximation. The homogenization leads to an isotropic equilibrium with averaged wave speed $\lambda = \frac{1}{2}(\frac{1}{\sqrt{2}} + \frac{1}{2}) \approx 0.60$. In the horizontal direction, we observe exactly this behavior. Close to the vertical direction, the homogenization breaks down, because to an almost vertically travelling particle, the effective stripe width is comparable to the domain size. Hence, we observe remnants of the refraction and concentration at interfaces, at least in the Godunov solution. The

λ_0	2 s^{-1}	turning rate
λ_H	0	ratio of turning rate coefficients $\frac{\lambda_1}{\lambda_0}$
c	1 mm s^{-1}	cell speed

Table 4.2: Base parameters for the stripes benchmark.

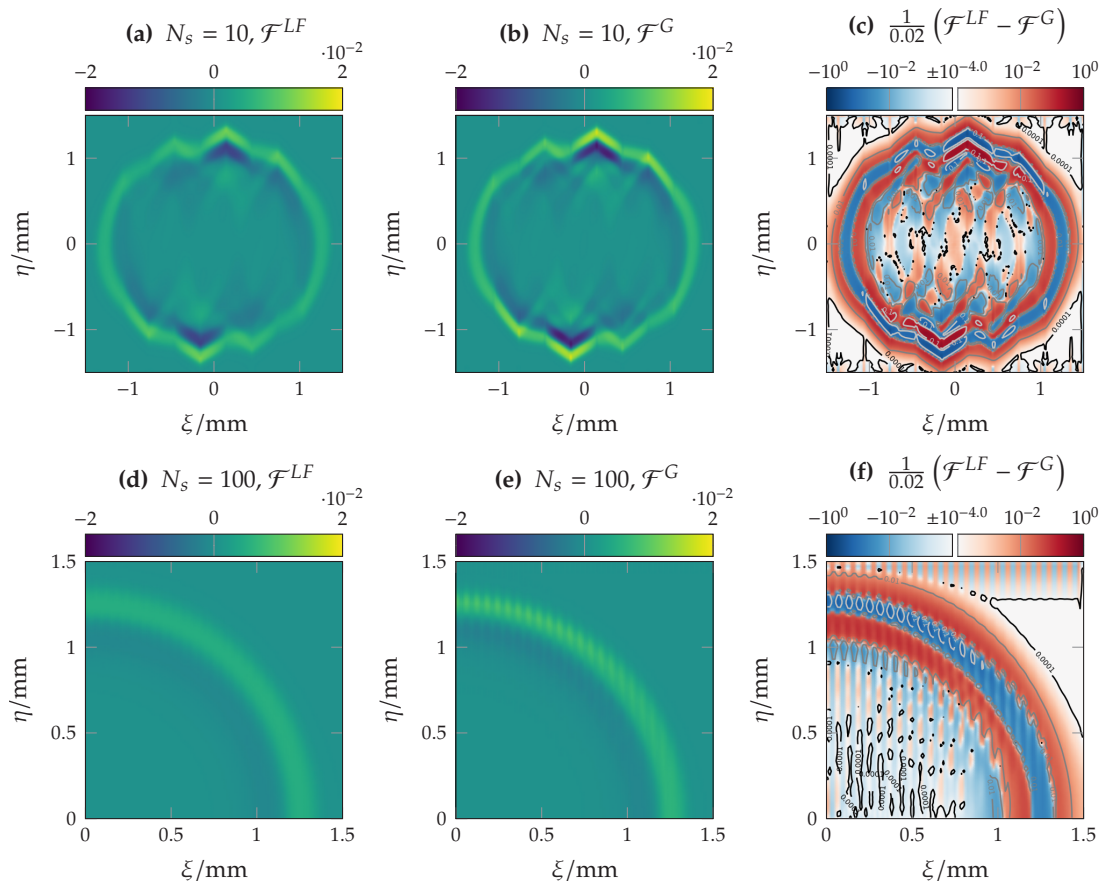


Figure 4.12: Results of Experiment 4.9—Lax-Friedrichs vs. Godunov. Top row: The coarse layout with $N_s = 10$. Bottom row: The fine layout with $N_s = 100$. Columns from left to right: Lax-Friedrichs flux, Godunov flux and their relative point-wise difference.

Lax-Friedrichs solution is too diffusive to show these fine-scale effects.

■ **Experiment 4.10 — Lax-Friedrichs vs. Kershaw-kinetic.** We compute solutions to the $K_1^{(E)}$ model for

1. a coarse stripe layout with $N_s = 10$,
2. a fine stripe layout with $N_s = 100$,

each with the Lax-Friedrichs flux and the Kershaw-kinetic flux, using the parameters from Table 4.2. The end time is $T = 1$ s.

Figure 4.13 shows the $K_1^{(E)}$ solutions to the stripes benchmark and their relative differences. The solutions produced with the kinetic scheme have much sharper features than the Lax-Friedrichs solutions. The results for the coarse layout show again the concentration of vertically moving particles at the interfaces. In the kinetic solution for the fine layout, this effect is captured well,

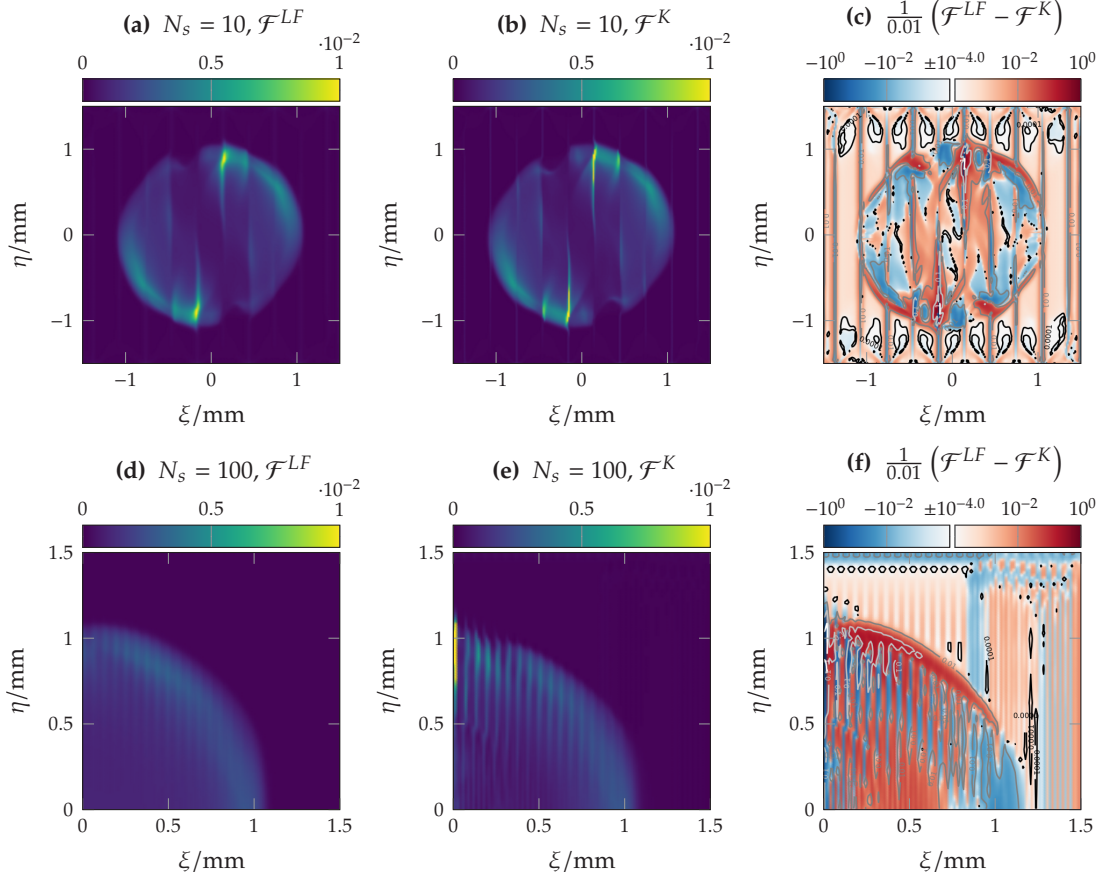


Figure 4.13: Results of Experiment 4.10—Lax-Friedrichs vs. Kershaw-kinetic. Top row: The coarse layout with $N_s = 10$. Bottom row: The fine layout with $N_s = 100$. Columns from left to right: Lax-Friedrichs flux, Kershaw-kinetic flux and their relative point-wise difference.

whereas it is almost completely smeared out in the Lax-Friedrichs solution.

4.3.5 A proteolysis model

Cancer cells actively remodel their environment by chemically cutting fibers [53], a process called proteolysis. Remodeling may either happen locally upon direct contact of the cells with ECM or through secretion and diffusion of matrix degrading enzymes. We incorporate a simple model of contact-dependent proteolysis [73] into the glioma model from Section 3.4.2:

$$\partial_t(QE(v)) = -\gamma QE(v) \int_{\mathbb{S}^2} (1 - |v \cdot v'|) f(v') dv'.$$

Herein, γ is a rate constant and QE is the total fiber distribution without normalization. The fiber distribution E is now a function of time, whose change depends only on the local cell distribution. The model assumes that cells preferentially cut fibers that are in their way, i.e., orthogonal to their current movement direction.

We discretize the velocity variables in this equation with a moment model. In [35], we use a similar approach in the context of a macroscopic glioma model with proteolysis. Although E

depends on space, the proteolysis equation acts locally. Thus, the resulting moment model is an ODE system for each point in space.

With the basis $\mathbf{b}(v)$, the corresponding moments $\mathbf{w} = \langle \mathbf{b}QE \rangle$, and an ansatz $Q\mathfrak{E}[\mathbf{w}]$ with multipliers β , we write the moment system:

$$\begin{aligned} \partial_t \mathbf{w} &= -\gamma \int_{\mathbb{S}^2} \mathbf{b}(v) Q\mathfrak{E}(v) \int_{\mathbb{S}^2} (1 - |v \cdot v'|) \mathfrak{f}(v') dv' dv \\ &= -\gamma \left(\mathbf{w}\rho - \int_{\mathbb{S}^2} \int_{\mathbb{S}^2} \mathbf{b}(v) |v \cdot v'| Q\mathfrak{E}(v) \mathfrak{f}(v') dv' dv \right). \end{aligned} \quad (4.12)$$

The peanut ansatz $Q\mathfrak{E} = v^\top D_W v$ can be interpreted as a monomial P_2 ansatz $Q\mathfrak{E}(v) = \beta \cdot \mathbf{b}(v)$. Normalization of \mathfrak{E} implies $Q = \langle v^\top D_W v \rangle = \frac{4\pi}{3} \text{tr} D_W$. We identify the entries of the water diffusion tensor D_W with components of the multipliers β and the entries of the tumor diffusion tensor $QP_E = \langle v^\top v \mathfrak{E} \rangle$ with the moments \mathbf{w} :

$$\mathbf{b} = \begin{pmatrix} 1 \\ v_\xi \\ v_\eta \\ v_\zeta \\ v_\xi^2 \\ v_\eta^2 \\ v_\xi v_\eta \\ v_\xi v_\zeta \\ v_\eta v_\zeta \end{pmatrix}, \quad \beta = \begin{pmatrix} D_{W,\zeta\zeta} \\ 0 \\ 0 \\ 0 \\ D_{W,\xi\xi} - D_{W,\zeta\zeta} \\ D_{W,\eta\eta} - D_{W,\zeta\zeta} \\ 2D_{W,\xi\eta} \\ 2D_{W,\xi\zeta} \\ 2D_{W,\eta\zeta} \end{pmatrix}, \quad \mathbf{w} = \langle \mathbf{b}QE \rangle = Q \begin{pmatrix} 1 \\ 0 \\ 0 \\ 0 \\ D_{T,\xi\xi} \\ D_{T,\eta\eta} \\ D_{T,\xi\eta} \\ D_{T,\xi\zeta} \\ D_{T,\eta\zeta} \end{pmatrix}.$$

Now the modified ansatz for particles \mathfrak{f} depends on the changing ansatz \mathfrak{E} in turn. The coupled moment system has the form

$$\partial_t \begin{pmatrix} \mathbf{u} \\ \mathbf{w} \end{pmatrix} + \nabla_x \cdot \begin{pmatrix} \mathcal{F}(\mathbf{u}, \mathbf{w}) \\ 0 \end{pmatrix} = \begin{pmatrix} \mathcal{R}_f(\mathbf{u}, \mathbf{w}) \\ \mathcal{R}_E(\mathbf{u}, \mathbf{w}) \end{pmatrix},$$

with $\mathcal{F}, \mathcal{R}_f$ from equations (4.7), (4.8) and \mathcal{R}_E given by the right-hand side of (4.12).

With a modified moment model for glioma, the \mathbf{u} equations depend on the tissue moments \mathbf{w} in two ways. Firstly, the fiber distribution \mathfrak{E} is part of the ansatz \mathfrak{f} and it also plays the role of an equilibrium in the turning operator \mathcal{L}_D . For example, the $P_N^{(E)}$ ansatz is $\mathfrak{E}\mathbf{a} \cdot \mathbf{a}$. The effects of an anisotropic equilibrium were discussed in Section 4.3.3. Secondly, fiber degradation produces gradients in Q , and hence leads to a drift in the particle equation. Therefore, to separate these effects, in each of the following experiments we perform three computations:

1. Both proteolysis and drift are switched off by setting $\lambda_H = 0$ and $\gamma = 0 \text{ s}^{-1}$.
2. Drift is disabled ($\lambda_H = 0$) but proteolysis is active.
3. Both proteolysis and drift are active.

A set of default parameters for the third option is given in Table 4.3. This choice corresponds to a kinetic regime with strong drift.

In the first experiment, we model a cluster of cells that starts at the origin with no preferred orientation and migrates through a homogeneous and aligned tissue.

λ_0	1 s^{-1}	turning rate
λ_H	0.5	ratio of turning rate coefficients $\frac{\lambda_1}{\lambda_0}$
c	1 mm s^{-1}	cell speed
γ	12 s^{-1}	rate of proteolytic degradation

Table 4.3: Base parameters for the proteolysis computations.

■ **Experiment 4.11 — Proteolysis, kinetic regime.** We prescribe a homogeneous initial condition $Q\mathfrak{C}(0, x, v) = Q_0\mathfrak{C}_0$ for fibers. The initial condition for the volume fraction is $Q_0 = 1$ and \mathfrak{C}_0 is a peanut distribution, with anisotropy factor $A = 10$ and main direction parallel to the ξ -axis. The cell cluster is initially described by a Gaussian as in (4.11) with standard deviation $\sigma = 0.2 \text{ mm}$. We compute solutions to the $P_1^{(E)}$ model, with a P_2 ansatz for the fiber distribution \mathfrak{C} .

Figure 4.14 displays the cell density ρ and the direction and anisotropy of D_W for the results of Experiment 4.11. Without drift and proteolysis the usual ellipsoidal wave of the $P_1^{(E)}$ model can be observed. When proteolysis is enabled, the cells degrade the tissue while spreading outwards and leave a hole that is visible on a plot of the volume fraction Q . We observe no change in the fiber orientation. The linear shape index LSI of D_W (see (2.3)) and thus the tissue anisotropy is increased throughout the domain. In horizontal direction, this is clear: Most cells move horizontally along the fiber direction and cut predominantly vertical fibers. But vertically moving cells predominantly cut horizontal cells, thus one could expect a decrease in LSI in vertical direction. Remember that a strong preference to move in fiber direction is built into the $P_1^{(E)}$ ansatz, even if f is not in equilibrium. Therefore, a large fraction of cells always moves in horizontal direction. The $P_1^{(E)}$ ansatz, which is constructed with the diffusion limit in mind, is not suited for the kinetic regime. In contrast, the $P_5^{(E)}$ solution for the same setting, which is not shown, features an increase in LSI in the vertical direction. Compared to the setting without proteolysis, the increased anisotropy in \mathfrak{C} means that the cells' preference for the horizontal direction is stronger. Hence, we observe higher peaks in ρ along the horizontal.

In the third setting with enabled drift, the cells detect gradients in Q and move out of the hole that they create by proteolysis. Hence, the horizontal peaks become even more pronounced. Also, an increased vertical migration can be observed. The fiber orientation remains unchanged also in this setting.

We repeat the previous experiment in an intermediate transport regime.

■ **Experiment 4.12 — Proteolysis, intermediate regime.** This experiment is identical to Experiment 4.11, except that we use a higher turning rate $\lambda_0 = 10 \text{ s}^{-1}$.

In Figure 4.15 we display results of Experiment 4.12 for the intermediate regime. The observations are similar to the observations in the kinetic regime. Enabling only proteolysis leads to increased anisotropy in D_W and therefore increased anisotropy in ρ in turn. With additional drift, the outward bound cell migration is faster in all directions. In contrast to the previous experiment,

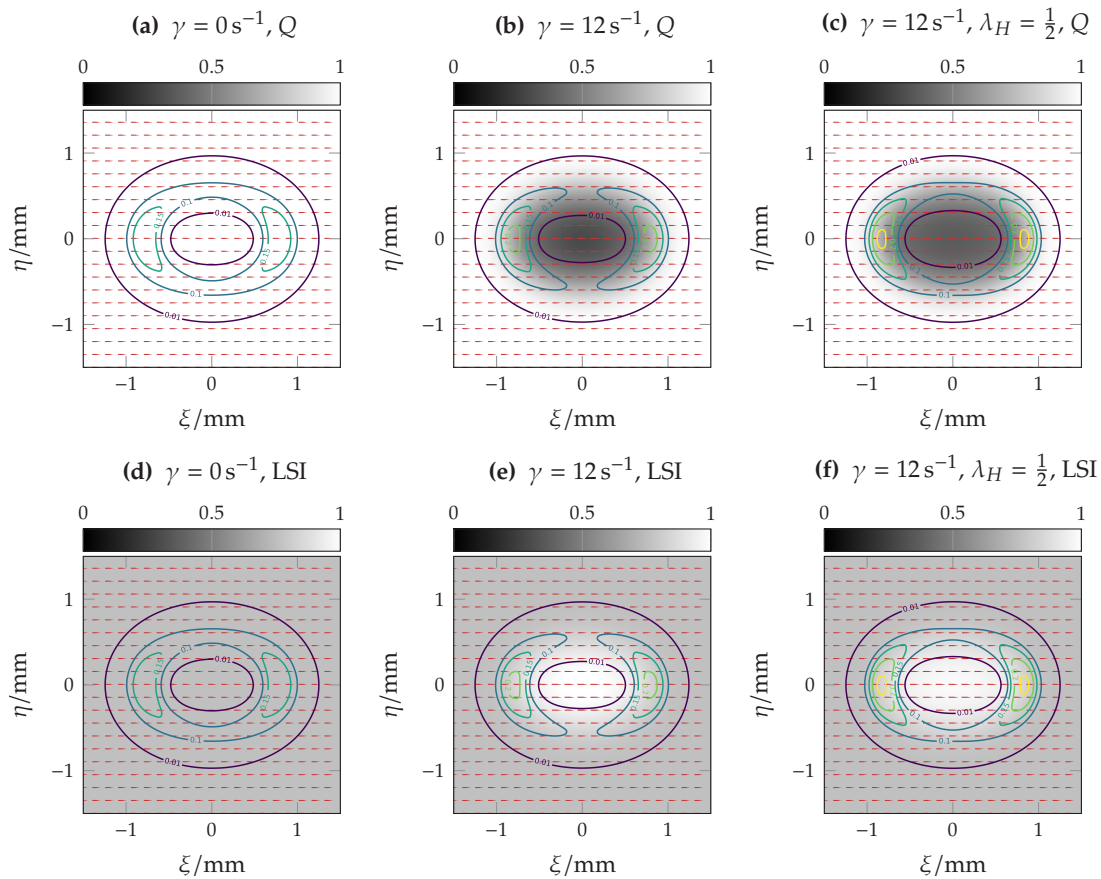


Figure 4.14: Results of Experiment 4.11—proteolysis, kinetic regime. The columns correspond to the three scenarios: Both effects off, only proteolysis and both effects on. The two rows show gray scale images of the volume fraction Q (top) and the linear shape index LSI (bottom) for the same computation. The red lines point in the main direction of D_W and scale with the anisotropy factor. The colored contours show the cell density ρ .

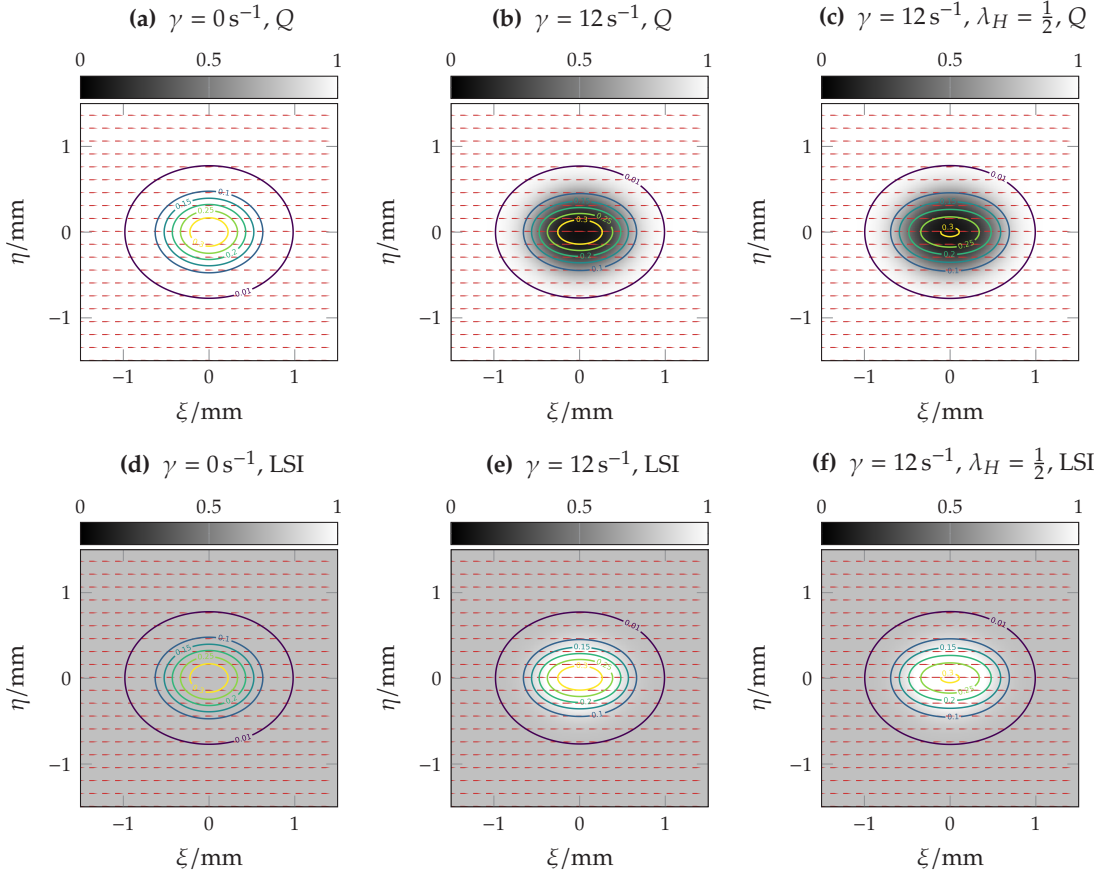


Figure 4.15: Results of Experiment 4.12—proteolysis, intermediate regime. The Figure layout is identical to Figure 4.14.

the shape of the ρ contours is the same as in the second scenario. The drift does not increase the anisotropy of the population. As we saw in the previous line source experiments (Experiment 4.7), the $P_1^{(E)}$ model is adequate for this intermediate regime. Here, the fact that LSI is decreased throughout the domain is expected, since \mathfrak{f} is closer to \mathfrak{C} .

The final experiment models the extreme situation that cells cut their way across aligned fibers. In this artificial setting, the cells start with a strong preference to move to the right, whereas the fibers are oriented vertically.

■ **Experiment 4.13 — Extreme remodeling.** The initial condition for fibers is homogeneous with volume fraction $Q_0 = 1$ and a peanut ansatz for \mathfrak{C}_0 with anisotropy $A = 10$ and main direction parallel to the η -axis. The cells are initially distributed as a Gaussian with $\sigma = 0.2$ mm at the origin and start with an orientation inside a fuzzy cone of angle $\frac{\pi}{12}$ around the ξ -axis:

$$f(0, x, v) = \exp\left(-\frac{\|x\|^2}{2\sigma^2}\right) \frac{12}{4\pi} \left(\frac{1}{\pi} \operatorname{atan}\left(5\left(\frac{\pi}{12} - \operatorname{acos}(v_\xi)\right)\right) + \frac{1}{2}\right).$$

We compute solutions to the $P_5^{(E)}$ model with a P_2 ansatz for the fiber distribution.

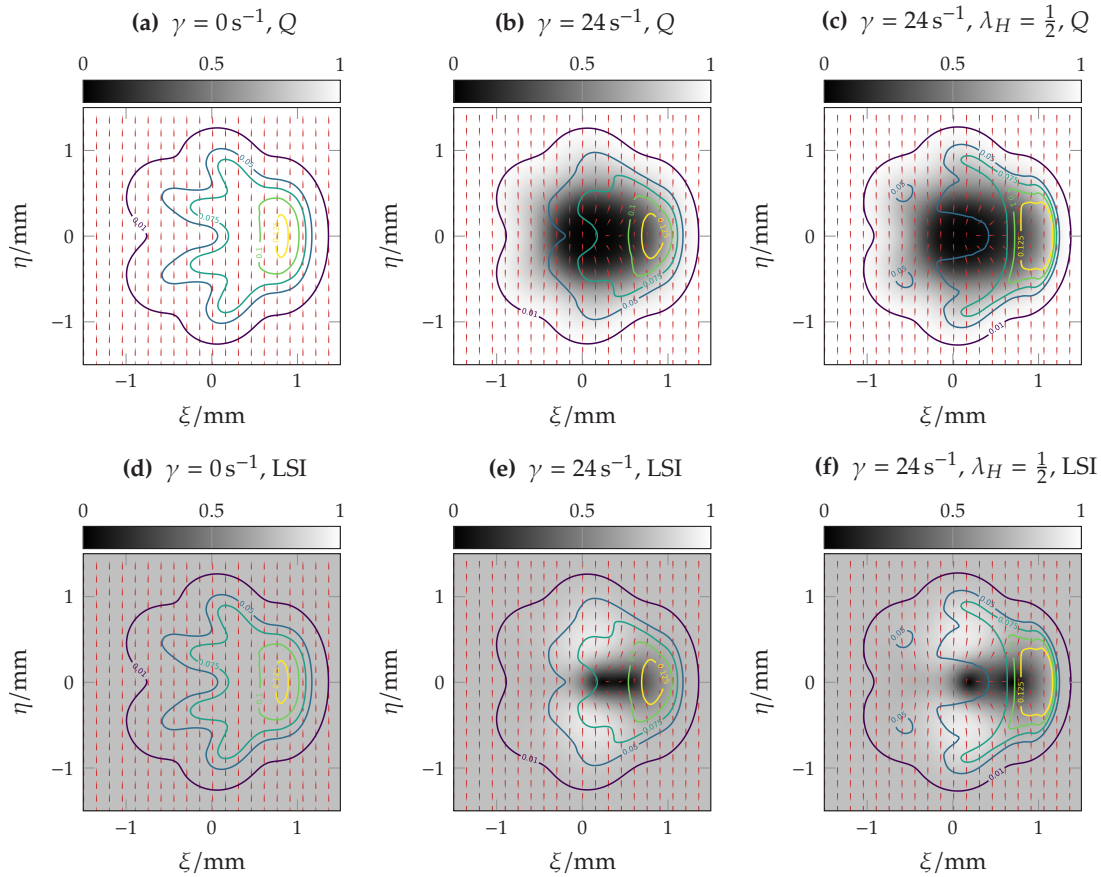


Figure 4.16: Results of Experiment 4.13—extreme remodeling. The Figure layout is identical to Figure 4.14.

Results of this experiment are shown in Figure 4.16. In the first scenario without proteolysis and drift, the cell cluster moves to the right, relatively unaffected by the fibers. At the tail, the usual P_N artifacts are visible. When proteolysis is enabled, the cells degrade the vertical fibers along their path which results in a decrease in LSI at the horizontal axis. Due to the changed equilibrium, fewer cells turn towards the vertical, and the cluster is more compact than without proteolysis. In agreement with Experiment 4.11, the cells that do move vertically increase LSI . We observe that in the path of the cells the main axis of D_W is turned out of the vertical. As before, the drift term lets cells detect the gradient of Q , which is caused by proteolysis. As a result, even more mass remains in the cell cluster and the effect of proteolysis is stronger along the horizontal axis. In one place, which appears on the LSI image as a lighter spot on the horizontal axis, so many vertical fibers have been cut that the fibers are now aligned horizontally.

4.3.6 Direct methods in the diffusion limit

Although the modified moment methods are designed with the diffusion limit in mind, the numerical scheme defined in Section 4.3.1 is not well suited for the diffusive regime. The scheme encounters two problems, when ε becomes small. Firstly, in the scaled kinetic equation (3.31) there is an ε^{-1} factor in front of the advection term. Because the scheme needs to respect the CFL condition, this enforces a prohibitively small time step

$$\Delta t \leq \frac{\varepsilon}{\delta} \Delta x$$

that tends to zero in the diffusion limit. Secondly, due to the stiffness ε^{-2} in the relaxation term, the scheme is dominated by numerical diffusion when the discretization is optically thick [93]. Optically thick grid cells are much larger than the mean free path. For the standard upwind finite-difference scheme, the ratio of numerical diffusion to physical diffusion is proportional to the Péclet number [79]:

$$\text{Pe} := \frac{\Delta x}{X} \frac{1}{\varepsilon} = \frac{\Delta x \lambda}{c}.$$

A $\text{Pe} \gg 1$ corresponds to the optically thick regime. Hence, the spatial resolution Δx must be chosen proportional to ε to ensure that the numerical diffusion does not dominate the solution when ε tends to zero. Considering the time step restriction, this means that $\Delta t \propto \varepsilon^2$. The run time of a computation is roughly proportional to $\left(\frac{X}{\Delta x}\right)^d \frac{1}{\Delta t}$, and therefore proportional to $\varepsilon^{-(2+d)}$. Even in one space dimension, computing situations close to the diffusion limit becomes prohibitively expensive. The following experiment demonstrates the failure of the scheme for an optically thick discretization.

■ **Experiment 4.14 — Numerical diffusion.** We compute the $P_1^{(E)}$ solution for the scaled equation (3.31) without drift ($v = 0$) and growth ($\theta = 0$) in one space dimension. For fixed parameter $\delta = 0.01$ we compute solutions for $\varepsilon = 0.1, 0.05, 0.01, 0.001$, and 0.0001 . At a constant grid resolution of $\Delta x = \frac{1}{200}$, the corresponding Péclet numbers are $\text{Pe} = 0.05, 0.1, 0.5, 5$, and 50 . The equilibrium is homogeneous, thus the diffusion constant is $\hat{D} = \frac{1}{3}$ and the diffusion limit is simply

$$\partial_t \rho_0 - \delta \hat{D} \partial_{\xi\xi} \rho_0 = 0.$$

The fundamental solution for the initial condition $f(0, \xi, v) = M \delta_{\xi}(0)$ is

$$\rho_0(t, \xi) = \frac{M}{\sqrt{4\pi\delta\hat{D}}} \frac{1}{\sqrt{t}} \exp\left(-\frac{1}{4t} \frac{\xi^2}{\delta\hat{D}}\right).$$

We start the simulation at time t_0 and use $f(0, \xi, v) = \frac{1}{\sqrt{4\pi\delta\hat{D}}} \rho_0(t_0, \xi)$ as initial condition. The final time is $t_0 + 1 = 1.135$. We choose $\sigma = 0.03$, $t_0 = \frac{\sigma^2}{2\delta\hat{D}} = 0.135$ and $M = \sqrt{t_0}$, such that the initial condition is a Gaussian with standard deviation σ and density $\rho = 1$ at the peak.

Results of Experiment 4.14 are shown in Figure 4.17. At $\varepsilon = 0.1$ and $\varepsilon = 0.05$ the solution is not yet accurately described by the diffusion limit. For the value $\varepsilon = 0.01$, the solution is already in the diffusive regime. At the corresponding Péclet number $\text{Pe} = 0.5$, the numerical diffusion is still relatively small. But on this grid, moving further to the diffusion limit results in dominating

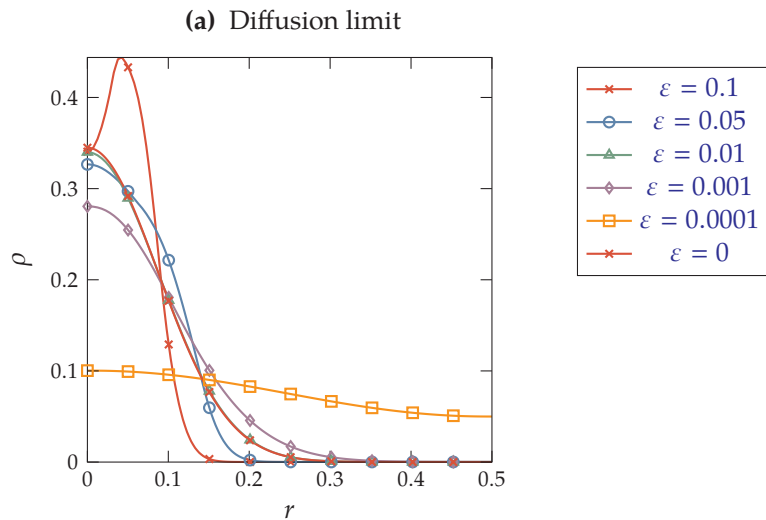


Figure 4.17: Results of Experiment 4.14—numerical diffusion. Due to symmetry, only the right half of the domain is shown. The $\varepsilon = 0$ line is the fundamental solution in the diffusion limit.

numerical diffusion, as seen in the solutions for $\varepsilon = 0.001$ and $\varepsilon = 0.0001$. To keep the Péclet numbers constant while approaching the diffusion limit, we could increase the spatial resolution. At $\varepsilon = 0.0001$, we would need a grid with 20 000 cells to keep $Pe = 0.5$ reasonably small. Note that the $\varepsilon = 0.0001$ solution needed already about 4.4×10^3 time steps (at $CFL = 0.9$) on the coarse grid with 200 cells. On the fine grid, we would therefore need 4.4×10^5 time steps. Compared to the $\varepsilon = 0.01$ solution on the coarse grid, this simulation would run one million times longer.

Two set of parameters for the model of glioma invasion in the human brain are listed in Table 5.4 in the next chapter. The resulting scaling numbers ε range from 6.2×10^{-7} to 1.2×10^{-6} . With the previous considerations in mind, it is clear that the direct numerical scheme from Section 4.3.1 is the wrong choice in this situation.

5

An asymptotic preserving method for the haptotaxis equation

The hardest thing to imagine, to really get your head around, is the scale at which the universe operates. You can drill down so small, that you reach particles and building blocks that your brain simply can't connect to the physical reality that you inhabit. [...] And at the other end, the sheer size at which the universe operates literally cannot be fully conceptualized by the human mind. We have to reduce it to factors, or long strings of comparative zeros.

Jonathan Simms — The Magnus Archives (Ep. 106)

Analytically we pass seamlessly from the kinetic equation (3.31) to the diffusion limit (3.32) when ε tends to zero. But the direct discretization in Section 4.3 is only valid for ε not too close to zero. As seen in Section 4.3.6, this method is dominated by numerical diffusion when the discretization is optically thick [93], i.e., when the mean free path is much smaller than the grid size. To pass to the diffusion limit with such a scheme would require infinite spatial and temporal resolution. On the other hand, there are numerous schemes for the diffusion equation, for example the [multi-point flux approximation \(MPFA\)](#) method [43]. In this chapter we fill this gap: We design a numerical scheme for the kinetic equation that is valid for all values of $\varepsilon > 0$ and that converges to a valid numerical scheme for the diffusion approximation as ε tends to zero. In the limit, the spatial and temporal resolution are bounded by a stability criterion for the limit equation. This class of scheme is called [AP](#)¹. There are many such schemes and in Section 5.1 we review a few of them. In Section 5.2 we apply the micro-macro decomposition of Lemou and Mieussens [96] to the haptotaxis equation. Based on their discretization on staggered grids, we derive a numerical scheme for the haptotaxis equation in three space dimensions, which we describe exhaustively in Section 5.3. Finally, we investigate the scheme numerically in Section 5.4, wherein we also present simulations of glioma invasion in white matter.

Most of the contents of this chapter have been published originally in [32]. The final three numerical experiments in Section 5.4.5, Section 5.4.6, and Section 5.4.7 are new.

¹In older literature, the term 'uniformly accurate' is used [81]

5.1 A review of asymptotic preserving schemes

For simplicity of exposition, we consider the one-dimensional slab-geometry transport equation with isotropic scattering. In the diffusive scaling, this equation reads:

$$\begin{aligned}\partial_t f + \frac{1}{\varepsilon} v \partial_x f &= \frac{1}{\varepsilon^2} \left(\frac{1}{2} \int_{-1}^1 f(v') dv' - f \right) \\ &= \frac{1}{\varepsilon^2} (\rho - f).\end{aligned}\tag{5.1}$$

Jin, Pareschi, and Toscani (JPT) [81] split the distribution f into an even and an odd part:

$$\begin{aligned}r(t, x, v) &= \frac{1}{2} [f(t, x, v) + f(t, x, -v)], \\ j(t, x, v) &= \frac{1}{2\varepsilon} [f(t, x, v) - f(t, x, -v)],\end{aligned}$$

and reformulate the transport equation (5.1) into the equivalent system

$$\begin{aligned}\partial_t r + v \partial_x j &= \frac{1}{\varepsilon^2} (\rho - r), \\ \partial_t j + \frac{1}{\varepsilon^2} v \partial_x r &= -\frac{1}{\varepsilon^2} j.\end{aligned}$$

Introducing the blending function $\phi(\varepsilon)$, $0 \leq \phi \leq \frac{1}{\varepsilon^2}$, the authors further rewrite this as a relaxation system

$$\begin{aligned}\partial_t r + v \partial_x j &= -\frac{1}{\varepsilon^2} (r - \rho), \\ \partial_t j + \phi v \partial_x r &= -\frac{1}{\varepsilon^2} (j + (1 - \varepsilon^2 \phi) v \partial_x r),\end{aligned}$$

in which the stiffness is isolated on the right-hand side. Due to symmetry of r and j , only the positive half of the velocity space, i.e., $v \geq 0$ has to be resolved. As ε tends to zero, the even and odd functions asymptotically approach $r = \rho$, $j = -v \partial_x r$, thus the r -equation integrated in v over $[-1, 1]$ becomes the diffusion equation

$$\partial_t \rho_0 - \frac{1}{3} \partial_{xx} \rho_0 = 0.$$

An operator splitting between fluxes and reactions—with an explicit-in-time discretization of the fluxes and an implicit discretization of the reactions—leads to an asymptotic preserving scheme. The reaction update can be computed explicitly when an implicit Euler scheme is used. In two space dimensions, the velocity space is divided into quadrants and f is split into four functions, two even and two odd ones. Applications of the JPT scheme include electron transport in semiconductors [80] and chemotaxis models for bacteria [25]. The JPT scheme with $\phi = 0$ is equivalent to Klar's splitting [87].

Jin and Levermore (JL) [79] propose a scheme for nonlinear two-by-two relaxation systems of the form

$$\begin{aligned}\partial_t \rho + \partial_x q &= 0, \\ \partial_t q + \partial_x p(\rho) &= -\frac{1}{\varepsilon} (q - r(\rho)).\end{aligned}$$

This formulation corresponds to the hyperbolic scaling in Section 3.5.3 and includes all first-order moment systems for (5.1): For example, the P_1 approximation leads to $p(\rho) = \frac{1}{3}\rho$ and $r(\rho) = 0$. To first order, the momentum equation is

$$q_0 = r(\rho) - \varepsilon(p'(\rho) - r'(\rho)^2)\partial_x \rho \quad (5.2)$$

for $\varepsilon \ll 1$. The JL scheme is based on a finite-volume discretization with a convex combination of numerical fluxes depending on the scaling parameter. In the kinetic regime, the upwind flux based on the face values $q_{i+\frac{1}{2}}^{(Up)} = q_i$ is appropriate. But for small ε , the momentum q approaches its limit value q_0 from (5.2). Face values $q_{i+\frac{1}{2}}^{(0)}$ that fulfill a discrete version of (5.2) should be used in the limit regime. The authors propose a convex combination $q_{i+\frac{1}{2}} = \phi(\text{Pe})q_{i+\frac{1}{2}}^{(Up)} + (1 - \phi(\text{Pe}))q_{i+\frac{1}{2}}^{(0)}$ that depends on the Péclet number $\text{Pe} = \frac{\Delta x}{X\varepsilon}$.

Buet et al. [22] extend the Jin-Levermore scheme to the hyperbolic heat equation

$$\begin{aligned} \partial_t \rho + \frac{1}{\varepsilon} \nabla_x \cdot q &= 0 \\ \partial_t q + \frac{1}{\varepsilon} \nabla_x \rho &= -\frac{1}{\varepsilon^2} q \end{aligned}$$

in two dimensions. Their nodal scheme, in which fluxes q are reconstructed on control-volumes around the vertices of the mesh, is designed for arbitrary triangular and quadrilateral meshes. A combination of kinetic and diffusive fluxes in analogy to the JL scheme ensures the AP property. Last but not least, Boscarino, Pareschi and Russo [20] design an AP scheme for the transport equation in a mixed scaling (see Section 3.5.4). In the transition from hyperbolic to parabolic scaling, they blend between different implicit-explicit (IMEX) schemes.

5.2 The micro-macro decomposition and the diffusion limit

In the next section, we follow the work of Lemou and Mieussens [96] quite closely to perform a micro-macro decomposition of equation (3.31) in the parabolic dimensionless form. This serves as the starting point for the numerical discretization scheme. From Lemma 3.9 and Lemma 3.11 we recall the nullspace $\mathcal{N}(\mathcal{L}_D) = \text{span}\{E\}$ and range $\mathcal{R}(\mathcal{L}_D) = \mathcal{N}^\perp(\mathcal{L}_D)$ of the turning operator. Orthogonal projections onto those spaces are

$$\begin{aligned} \Pi(\phi) &= \langle \phi \rangle E, \\ (I - \Pi)(\phi) &= \phi - \langle \phi \rangle E, \end{aligned}$$

respectively. With these projections, we decompose the particle distribution into an equilibrium part and a small perturbation:

$$f = \Pi f + (I - \Pi)f = \rho E + \varepsilon g. \quad (5.3)$$

Now the kinetic equation is split into a system of two equations—one for the macroscopic density $\rho(t, x)$ and one for the microscopic perturbation $g(t, x, v)$. To obtain the ρ -equation

$$\partial_t \rho + \delta \nabla_x \cdot \langle v g \rangle = \theta \mu \rho, \quad (5.4)$$

we insert the perturbation formula (5.3) into (3.31) and apply the projection Π , using the positivity and symmetry of the equilibrium (see Definition 3.3) and the mass conservation $\langle \mathcal{L}_D \rangle = 0, \langle \mathcal{L}_a \rangle = 0$ of the turning operators. The equation for g follows from application of $(I - \Pi)$ to (3.31) and division by ε :

$$\partial_t g + \frac{\delta}{\varepsilon} (I - \Pi) \nabla_x \cdot (vg) = -\frac{\delta}{\varepsilon^2} \nabla_x \cdot (v\rho E) + \frac{\delta \lambda_D}{\varepsilon^2} \mathcal{L}_D g + \frac{v\lambda_a}{\varepsilon^2} \mathcal{L}_a f + \frac{\theta\mu}{\varepsilon} (I - \Pi) \mathcal{S}f. \quad (5.5)$$

Apart from the new perturbation term \mathcal{L}_a , this is identical to the decomposition of Lemou and Mieussens [96]. They show that—for compatible initial and boundary conditions—the micro-macro decomposition is equivalent to the original kinetic equation.

Informally, it is easy to see the diffusion limit from this decomposition. In the limit of $\varepsilon \rightarrow 0$, only the $\frac{1}{\varepsilon^2}$ terms remain in (5.5), therefore it is reduced to

$$g_0 = \frac{1}{\lambda_D} \mathcal{L}_D^{-1} \left(\nabla_x \cdot (v\rho_0 E) - \frac{v}{\delta} \lambda_a \rho_0 \mathcal{L}_a E \right).$$

Since $\langle vE \rangle = \langle \mathcal{L}_a f \rangle = 0$, Lemma 3.11 assures that the inverse of \mathcal{L}_D in this expression exists and is unique. Inserting this into the macro equation (5.4) immediately gives the diffusion limit (3.32). We construct the micro-macro AP scheme as the discrete analog of this procedure. To update the solution from time t_n to time t_{n+1} , we compute the perturbation g^{n+1} with a discrete version of the micro equation (5.5) first. Then we insert g^{n+1} into the discretized macro equation (5.4) and compute the density ρ^{n+1} .

5.3 The asymptotic preserving method

We start from the micro-macro decomposition from the previous Section 5.2 and write it as

$$\begin{aligned} \partial_t \rho &= \Phi^p(\rho, g) + \Gamma^p(\rho, g), \\ \partial_t g &= \left(\Phi_E^g(\rho) + \Phi^g(\rho, g) \right) + \Gamma^g(\rho, g). \end{aligned} \quad (5.6)$$

Here, the individual terms are grouped into those that we discretize explicitly in time

$$\begin{aligned} \Phi^p(\rho, g) &= -\delta \nabla_x \cdot \langle vg \rangle + \theta\mu\rho, \\ \Phi_E^g(\rho) &= -\frac{\delta}{\varepsilon^2} \nabla_x \cdot (v\rho E), \\ \Phi^g(\rho, g) &= -\frac{\delta}{\varepsilon} (I - \Pi) (\nabla_x \cdot (vg)) + \frac{v\lambda_a}{\varepsilon^2} \mathcal{L}_a f + \frac{\theta\mu}{\varepsilon} (I - \Pi) (\mathcal{S}f), \end{aligned} \quad (5.7)$$

and those that we discretize implicitly

$$\begin{aligned} \Gamma^p(\rho, g) &= 0, \\ \Gamma^g(\rho, g) &= \frac{\delta \lambda_D}{\varepsilon^2} \mathcal{L}_D g. \end{aligned} \quad (5.8)$$

In [96] the authors argued that it is enough to treat only the term \mathcal{L}_D implicitly to get an AP scheme. We call the first and second-order minimally implicit schemes derived from equations (5.6)-(5.8) MM_{1m} and MM_{2m} , respectively. Without introducing an implicit coupling between

grid cells, we can also treat the other volume terms implicitly. That is, we regroup the terms into

$$\begin{aligned}
\tilde{\Phi}^\rho(\rho, g) &= -\delta \nabla_x \cdot \langle v g \rangle, \\
\tilde{\Phi}_E^g(\rho) &= -\frac{\delta}{\varepsilon^2} \nabla_x \cdot (v \rho E), \\
\tilde{\Phi}^g(\rho, g) &= -\frac{\delta}{\varepsilon} (I - \Pi)(\nabla_x \cdot (v g)), \\
\tilde{\Gamma}^\rho(\rho, g) &= \theta \mu \rho, \\
\tilde{\Gamma}^g(\rho, g) &= \frac{\delta \lambda_D}{\varepsilon^2} \mathcal{L}_D g + \frac{v \lambda_a}{\varepsilon^2} \mathcal{L}_a f + \frac{\theta \mu}{\varepsilon} (I - \Pi)(S f)
\end{aligned} \tag{5.9}$$

and treat $\tilde{\Phi}^\rho$, $\tilde{\Phi}_E^g$, $\tilde{\Phi}^g$ explicitly and $\tilde{\Gamma}^\rho$, $\tilde{\Gamma}^g$ partially² implicit. We call the first and second-order variants of the scheme with implicit volume terms MM_{1i} and MM_{2i} , respectively.

5.3.1 Primal-dual mesh pairs

Lemou and Mieussens [96] discretize the micro-macro system with finite differences on a staggered grid in one space dimension. To generalize the method to arbitrary dimension d , we reformulate the method in the context of finite volumes on primal-dual mesh pairs.

Although the implementation supports only tensor-product grids at the moment, we write the scheme for conforming polyhedral meshes. This has several benefits. Most aspects of the scheme do not depend on the tensor-product structure, and also the implementation in DUNE [7] (see Section B.1) is mesh-agnostic in most parts. The general notation is close to the implementation, which helps to understand the code and also will make an implementation on unstructured conforming meshes easier. Our notation and construction deliberately mirrors that of Buet et al. [22]

Firstly, we consider only the topology of the dual mesh associated with a conforming primal mesh. Secondly, we define the dual geometry for polyhedral primal meshes in two dimensions. And finally, we generalize the construction to three space dimensions.

Topology of the dual mesh

The two-dimensional example mesh in Figure 5.1a is helpful to visualize the following definitions. Each primal cell is identified with a dual vertex, and each primal vertex with a dual cell. Wherever two primal cells intersect in a face, two dual vertices are connected with an edge and where two primal vertices are connected, there is a face between two dual cells. Note that in two space dimensions, edges, entities of dimension one, coincide with faces, entities of dimension $d - 1 = 1$. We reserve the indices $j, k \in \mathbb{N}$ to label cells Ω_j, Ω_k in the primal mesh and $r, s \in \mathbb{N}$ to identify primal vertices x_r, x_s . To label an entity on either mesh, we use the indices i, i' . Any primal cell index j also identifies a dual vertex x_j and a primal vertex index r corresponds to a dual cell Ω_r . In one mesh, two cells $\Omega_i, \Omega_{i'}$ are neighbors if they intersect in a face $\partial\Omega_{i,i'} = \Omega_i \cap \Omega_{i'}$. Then the two vertices $x_i, x_{i'}$ in the other mesh are also neighbors, i.e., they are connected with an edge $\overline{x_i x_{i'}}$. In this sense, the neighbors of an index i are those indices i' for which in one mesh the corresponding cells are neighbors and thus in the other mesh the corresponding vertices are neighbors. We write \mathfrak{N}_i for the set of all neighbors of i . A related concept is the adjacency between entities of different dimension. If the edge $\overline{x_r x_s}$ is part of the cell Ω_j we say that Ω_j is

²In the discretization of $\partial_t g = \tilde{\Gamma}^g(\rho, g)$, only g is a function of time and ρ is constant (see Section 5.3.4)

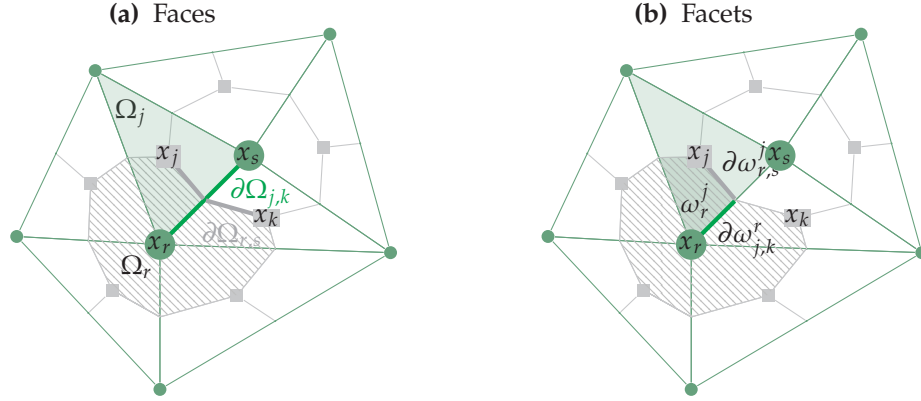


Figure 5.1: The primal-dual mesh pair in two dimensions. The primal cell Ω_j is marked green and the dual cell Ω_r is hatched in gray. Further, the primal vertices x_r, x_s and the dual vertices x_j, x_k are labelled. **5.1a:** Highlighted are the primal face $\partial\Omega_{j,k}$ and the dual face $\partial\Omega_{r,s}$. **5.1b:** The sub-cell $\omega_j^r = \Omega_j \cap \Omega_r$ is the intersection of the green and gray areas. Highlighted are the primal facet $\partial\omega_{j,k}^r = \partial\Omega_{j,k} \cap \Omega_r$ and the dual facet $\partial\omega_{r,s}^j = \partial\Omega_{r,s} \cap \Omega_j$.

adjacent to $\overline{x_r x_s}$, and denote this by $j \in \mathfrak{A}_{r,s}$. The index pair (r, s) also identifies a dual face $\partial\Omega_{r,s}$, thus $\mathfrak{A}_{r,s}$ equivalently is the set of all dual vertices x_j that are part of that face. Furthermore, we denote the set of a cell's vertices \mathfrak{V}_i .

Geometry of the dual mesh in two dimensions

We define the dual geometry associated with a conforming polyhedral primal mesh. The construction is identical to the definition of a control volume by Buet et al. in [22]. Figure 5.1b illustrates this construction. A dual face $\partial\Omega_{r,s}$, which is the intersection of two dual cells, does not need to be planar. In two space dimensions it can be constructed, however, from one planar facet $\partial\omega_{r,s}^j = \partial\Omega_{r,s} \cap \Omega_j$ for each intersection with an adjacent primal cell $\Omega_j : j \in \mathfrak{A}_{r,s}$. The facet $\partial\omega_{r,s}^j$ is the line $\overline{x_j x_{r,s}}$ between the primal cell's barycenter x_j and the barycenter $x_{r,s}$ of the edge $\overline{x_r x_s}$ (which coincides with a face $\partial\Omega_{j,k}$, for some k).

Geometry of the dual mesh in three dimensions

In three space dimensions the construction, sketched in Figure 5.2, is similar but more involved. Because the primal mesh is polyhedral and conforming, the facet $\partial\omega_{r,s}^j$ is bounded by line segments connecting the four points $x_j, x_{j,k}, x_{r,s}, x_{j,k'}$. The indices $k, k' \in \mathfrak{N}_j \cap \mathfrak{A}_{r,s}$ label those two neighbors of cell Ω_j that have $\overline{x_r x_s}$ as an edge. With $x_{j,k}, x_{j,k'}$ we denote the barycenters of the faces $\partial\Omega_{j,k}, \partial\Omega_{j,k'}$. As in the two-dimensional setting, $x_{r,s}$ is the barycenter of the edge $\overline{x_r x_s}$. In general, the four points do not have to lie in a plane. To obtain a polyhedral dual mesh, we must split the facet $\partial\omega_{r,s}^j$ into two triangles $\partial\omega_{r,s}^{j,1} \cup \partial\omega_{r,s}^{j,2} = \partial\omega_{r,s}^j$ defined by the triplets $x_j, x_{j,k}, x_{r,s}$, and $x_j, x_{r,s}, x_{j,k'}$. For tensor product grids and tetrahedral meshes (see [138]) the four points lie in a plane, which renders the split into triangles unnecessary.

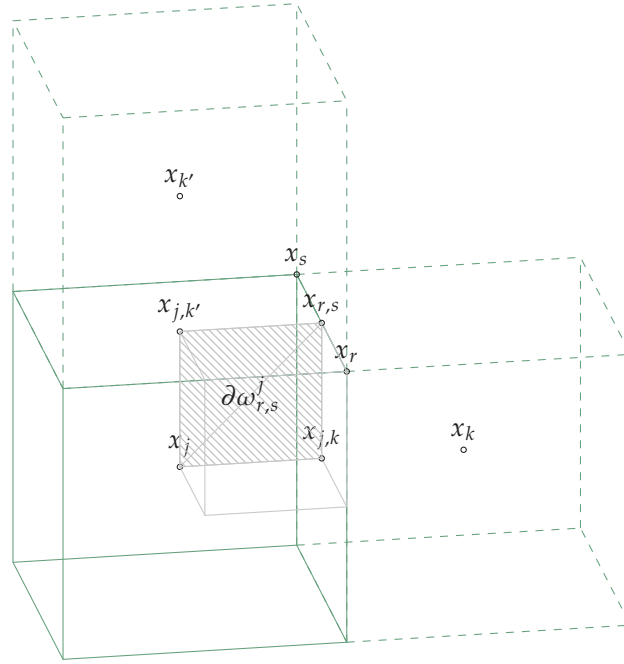


Figure 5.2: The primal-dual mesh pair in three dimensions. Shown are the primal cell Ω_j (green wire-frame), its two neighbors $\Omega_k, \Omega_{k'}$ that are also adjacent to the edge $\overline{x_r x_s}$, and the facet $\partial\omega_{r,s}^j = \partial\Omega_{r,s} \cap \Omega_j$ (gray hatched), i.e., the part of the dual face $\partial\Omega_{r,s}$ that lies in the primal cell Ω_j .

5.3.2 The space discretization

We use the symbol \mathcal{E}_i wherever any kind of entity on the mesh can be inserted (cell, face, edge, dual cell, ...) and denote the average over \mathcal{E}_i with

$$\{\cdot\}_{\mathcal{E}_i} := \frac{1}{|\mathcal{E}_i|} \int_{\mathcal{E}_i} \cdot dx,$$

in which $|\mathcal{E}_i| = \int_{\mathcal{E}_i} 1 dx$ is the volume of \mathcal{E}_i . In the following, we derive the minimally implicit variants MM_{1m}, MM_{2m} . All that is required to obtain the variants MM_{1i}, MM_{2i} with implicit volume terms is a reordering of terms as in (5.9). Let (ρ, g) be the solution of (5.6), with the average densities $\{\rho\}_{\Omega_r}$ on dual cells, and the average perturbations $\{g\}_{\Omega_j}$ on the primal cells. The projection of equation (5.6) onto the cell averages is a finite system of equations for the values $\rho_r \approx \{\rho\}_{\Omega_r}, g_j \approx \{g\}_{\Omega_j}$ which approximate the averages of the exact solution. We collect these values in the vectors $\bar{\rho} = (\dots, \rho_r, \rho_{r+1}, \dots)^\top$ and $\bar{g} = (\dots, g_j, g_{j+1}, \dots)^\top$ and write the resulting space-discrete system as

$$\begin{aligned} \partial_t \bar{\rho} &= \bar{\Phi}^\rho(\bar{\rho}, \bar{g}) & + \bar{\Gamma}^\rho(\bar{\rho}, \bar{g}) \\ \partial_t \bar{g} &= (\bar{\Phi}_E^g(\bar{\rho}) + \bar{\Phi}^g(\bar{\rho}, \bar{g})) + \bar{\Gamma}^g(\bar{\rho}, \bar{g}), \end{aligned} \quad (5.10)$$

using the same notation for the approximations of the projected operators. For instance, we have $\bar{\Phi}^\rho(\bar{\rho}, \bar{g}) = (\dots, \Phi_r^\rho(\bar{\rho}, \bar{g}), \Phi_{r+1}^\rho(\bar{\rho}, \bar{g}), \dots)^\top$, where Φ_r^ρ is an approximation to $\{\Phi^\rho\}_{\Omega_r}$. With second-order accuracy, the average $\{\cdot\}_{\mathcal{E}_i}$ can be swapped with a product or a chained function,

i.e., given functions $u(x), w(x) \in C^2(\mathcal{E}_i)$, and $z(u) \in C^2(u(\mathcal{E}_i))$ we have

$$\begin{aligned} \{u(x)w(x)\}_{\mathcal{E}_i} &= \{u(x)\}_{\mathcal{E}_i} \{w(x)\}_{\mathcal{E}_i} + \mathcal{O}(\Delta x^2) \\ \{z(u(x))\}_{\mathcal{E}_i} &= z(\{u(x)\}_{\mathcal{E}_i}) + \mathcal{O}(\Delta x^2). \end{aligned}$$

Up to second-order accurate approximations to the explicit operators on each cell are

$$\begin{aligned} \Phi_r^\rho &= -\delta \sum_{s \in \mathfrak{N}_r} F_{r,s}^{(\rho,g)} + \theta \mu(\rho_r) \rho_r, \\ \Phi_{E_j}^g &= -\frac{\delta}{\varepsilon^2} \sum_{k \in \mathfrak{N}_j} F_{j,k}^{(g,\rho)}, \\ \Phi_j^g &= -\frac{\delta}{\varepsilon} \sum_{k \in \mathfrak{N}_j} F_{j,k}^{(g,g)} + \frac{\nu \lambda_{a,j}}{\varepsilon^2} \mathcal{L}_a(\tilde{\rho}_j E_j + \varepsilon g_j) + \frac{\theta \mu(\tilde{\rho}_j)}{\varepsilon} (I - \Pi) \mathcal{S}(\tilde{\rho}_j E_j + \varepsilon g_j). \end{aligned}$$

The average density on a primal cell $\tilde{\rho}_j$ is not a degree of freedom of the scheme and needs to be computed from the averages on contributing dual cells:

$$\tilde{\rho}_j = \frac{1}{|\Omega_j|} \sum_{r \in \mathfrak{N}_j} |\omega_{r,j}^r| \rho_r. \quad (5.11)$$

The fluxes $F_{r,s}^{(\rho,g)}$ in density ρ , due to the perturbation g , follow from application of Gauss' theorem on the term $\{\Phi^\rho\}_{\Omega_r}$ from equation (5.7):

$$F_{r,s}^{(\rho,g)} = \frac{1}{|\Omega_r|} \sum_{j \in \mathfrak{N}_{r,s}} |\partial \omega_{r,s}^j| \{ \langle v g \rangle \}_{\partial \omega_{r,s}^j}^{\mathcal{Q}} \cdot n_{r,s}^j,$$

together with a quadrature rule \mathcal{Q} . The unit outer normal of a facet $\partial \omega_{r,s}^j$ is denoted $n_{r,s}^j$. The reconstruction $g(x)$ is a function that is piece-wise continuous on primal cells and interpolates the averages: $\{g\}_{\Omega_j} = g_j$. In the first-order scheme the reconstruction is piece-wise constant and equal to the cell average:

$$g(x)|_{\Omega_j} = g_j.$$

In the second-order scheme we prescribe a piece-wise linear reconstruction

$$g(x)|_{\Omega_j} = g_j + b \cdot (x - x_j),$$

wherein b is a limited estimate of the slope that can be obtained by a minmod³ or WENO⁴ ansatz. Because we compute the flux on dual faces, which are inside the primal cells where g is continuous, we do not need an approximate flux function and only have to approximate the integrals by a quadrature. For the piece-wise constant reconstruction, these simplify to a single evaluation of the cell mean.

Next we consider the fluxes $F_{j,k}^{(g,\rho)}$ resulting from $\{\Phi_E^g\}_{\Omega_j}$ in (5.7):

$$F_{j,k}^{(g,\rho)} = \frac{1}{|\Omega_j|} \left(\sum_{r \in \mathfrak{N}_{j,k}} |\partial \omega_{j,k}^r| \{ (v \rho E) \}_{\partial \omega_{j,k}^r}^{\mathcal{Q}} \right) \cdot n_{j,k}$$

³See Section 4.3.1.

⁴Weighted, essentially non-oscillatory: A high order reconstruction scheme for finite-volume methods.

This time, the facets $\partial\omega_{j,k}^r$ which are parts of the primal face $\partial\Omega_{j,k}$ all share the same constant normal $n_{j,k}$. $\rho(x)$ is a piece-wise continuous reconstruction of the density on dual cells.

Finally, application of the divergence theorem to $\{\Phi^g\}_{\Omega_j}$ in equation (5.7), together with the projection $(I - \Pi)(\nabla_x \cdot (vg)) = \nabla_x \cdot (vg) - (\nabla_x \cdot \langle vg \rangle)E$ gives:

$$F_{j,k}^{(g,g)} = \frac{|\partial\Omega_{j,k}|}{|\Omega_j|} \left(\{(\widehat{vg})\}_{\partial\Omega_{j,k}}^Q - \{\langle vg \rangle_{E_{\Omega_j}}\}_{\partial\Omega_{j,k}}^Q \right) \cdot n_{j,k}.$$

Here, \widehat{vg} is an approximate flux function, for example the upwind flux, that depends on the left and right state $g_{\Omega_j}, g_{\Omega_k}$ of the face $\partial\Omega_{j,k}$. The second term of the projection is not in conservation form. In the spirit of wave-propagation for heterogeneous media, as proposed by LeVeque [98], we simply evaluate the equilibrium E_{Ω_j} on the current cell Ω_j .

The approximate implicit operators are

$$\begin{aligned} \Gamma_r^p &= 0 \\ \Gamma_j^g &= \frac{\delta\lambda_{D,j}}{\varepsilon^2} \mathcal{L}_D g_j = \{\Gamma^g\}_{\Omega_j} + \mathcal{O}(\Delta x^2). \end{aligned}$$

If $\lambda_D(x)$ is a constant on each cell, this is even exact, because \mathcal{L}_D is linear. Note that the implicit operator on a cell only depends on the cell mean. Thus, the implicit part can be solved on each cell separately. This is still true for the MM_{1i} and MM_{2i} variants in which all volume terms are treated implicitly.

5.3.3 The resulting scheme on a square grid

In the following, we show the MM_{1m} scheme on a two-dimensional square-grid, i.e., a tensor-product grid where all primal vertices and cell centers are equally spaced:

$$x_{(l,m)} = (l, m)^\top \Delta x \qquad x_{(l+\frac{1}{2}, m+\frac{1}{2})} = (l + \frac{1}{2}, m + \frac{1}{2})^\top \Delta x.$$

The primal cells of this grid are the squares

$$\Omega_{(l+\frac{1}{2}, m+\frac{1}{2})} = \left\{ x \in \mathbb{R}^d \mid |x_{(l,m)}|_\infty \leq |x|_\infty \leq |x_{(l+1, m+1)}|_\infty \right\},$$

and the dual cells are

$$\Omega_{(l,m)} = \left\{ x \in \mathbb{R}^d \mid |x_{(l-\frac{1}{2}, m-\frac{1}{2})}|_\infty \leq |x|_\infty \leq |x_{(l+\frac{1}{2}, m+\frac{1}{2})}|_\infty \right\}.$$

In the first-order MM_{1m} scheme, the reconstructions ρ, g are piece-wise constant and equal to the cell means. All occurrences of a quadrature rule Q are replaced by the midpoint-rule. Then the right-hand side of the macro equation becomes

$$\begin{aligned} \Phi_{(l,m)}^\rho &= -\delta \frac{1}{2\Delta x} \left(-v_\xi (g_{(l-\frac{1}{2}, m-\frac{1}{2})} + g_{(l-\frac{1}{2}, m+\frac{1}{2})}) - v_\eta (g_{(l-\frac{1}{2}, m-\frac{1}{2})} + g_{(l+\frac{1}{2}, m+\frac{1}{2})}) \right. \\ &\quad \left. + v_\xi (g_{(l+\frac{1}{2}, m-\frac{1}{2})} + g_{(l+\frac{1}{2}, m+\frac{1}{2})}) + v_\eta (g_{(l+\frac{1}{2}, m+\frac{1}{2})} + g_{(l-\frac{1}{2}, m+\frac{1}{2})}) \right) \\ &\quad + \theta \mu (\rho_{(l,m)}) \rho_{(l,m)}, \end{aligned}$$

when we insert the fluxes on all four faces. The term Φ_E^g is

$$\begin{aligned} \Phi_{E(l+\frac{1}{2}, m+\frac{1}{2})}^g &= \\ &= -\frac{\delta}{\varepsilon^2} \frac{1}{2\Delta x} E_{(l+\frac{1}{2}, m+\frac{1}{2})} \left[-v_\xi (\rho_{(l,m)} + \rho_{(l, m+1)}) - v_\eta (\rho_{(l,m)} + \rho_{(l+1, m)}) \right. \\ &\quad \left. + v_\xi (\rho_{(l+1, m)} + \rho_{(l+1, m+1)}) + v_\eta (\rho_{(l+1, m+1)} + \rho_{(l, m+1)}) \right]. \end{aligned}$$

And finally we have:

$$\begin{aligned} \Phi_{(l+\frac{1}{2}, m+\frac{1}{2})}^g = & -\frac{\delta}{\varepsilon} \frac{1}{2\Delta x} \left[\overline{-v_\xi g}(g_{(l+\frac{1}{2}, m+\frac{1}{2})}, g_{(l-\frac{1}{2}, m+\frac{1}{2})}) \overline{-v_\eta g}(g_{(l+\frac{1}{2}, m+\frac{1}{2})}, g_{(l+\frac{1}{2}, m-\frac{1}{2})}) \right. \\ & \left. + \overline{v_\xi g}(g_{(l+\frac{1}{2}, m+\frac{1}{2})}, g_{(l+\frac{3}{2}, m+\frac{1}{2})}) + \overline{v_\eta g}(g_{(l+\frac{1}{2}, m+\frac{1}{2})}, g_{(l+\frac{1}{2}, m+\frac{3}{2})}) \right] \\ & + \frac{\nu \lambda_{a,j}}{\varepsilon^2} \left[\mathcal{L}_a \left(\tilde{\rho}_{(l+\frac{1}{2}, m+\frac{1}{2})} E_{(l+\frac{1}{2}, m+\frac{1}{2})} + \varepsilon g_{(l+\frac{1}{2}, m+\frac{1}{2})} \right) \right] \\ & + \frac{\theta \mu(\tilde{\rho}_{(l+\frac{1}{2}, m+\frac{1}{2})})}{\varepsilon} \left[\mathcal{S} \left(\tilde{\rho}_{(l+\frac{1}{2}, m+\frac{1}{2})} E_{(l+\frac{1}{2}, m+\frac{1}{2})} + \varepsilon g_{(l+\frac{1}{2}, m+\frac{1}{2})} \right) \right. \\ & \left. - \tilde{\rho}_{(l+\frac{1}{2}, m+\frac{1}{2})} E_{(l+\frac{1}{2}, m+\frac{1}{2})} \right] \end{aligned}$$

with the average density $\tilde{\rho}_{(l+\frac{1}{2}, m+\frac{1}{2})} = \frac{1}{4}(\rho_{(l,m)} + \rho_{(l+1,m)} + \rho_{(l+1,m+1)} + \rho_{(l,m+1)})$ over the primal cell $\Omega_{(l+\frac{1}{2}, m+\frac{1}{2})}$. The numerical flux function can be any of the usual methods, for example, the upwind flux

$$\overline{v_\xi g}(g_{(l+\frac{1}{2}, m+\frac{1}{2})}, g_{(l+\frac{3}{2}, m+\frac{1}{2})}) = \max(v_\xi, 0)g_{(l+\frac{1}{2}, m+\frac{1}{2})} + \min(v_\xi, 0)g_{(l+\frac{3}{2}, m+\frac{1}{2})}.$$

5.3.4 The time discretization

We use the stiffly accurate **IMEX** schemes from [4]. The time step size is denoted by Δt . In the first-order scheme, the forward-backward Euler scheme is used. For the particular system (5.10), this reads

$$\begin{aligned} \bar{\rho}^* &= \bar{\rho}^n + \Delta t \bar{\Phi}^\rho(\bar{\rho}^n, \bar{g}^n) \\ \bar{g}^* &= \bar{g}^n + \Delta t \left(\bar{\Phi}_E^g(\bar{\rho}^n, \bar{g}^n) + \bar{\Phi}^g(\bar{\rho}^n, \bar{g}^n) \right) \\ \bar{\rho}^{n+1} &= \bar{\rho}^* + \Delta t \bar{\Gamma}^\rho(\bar{\rho}^{n+1}, \bar{g}^*) \\ \bar{g}^{n+1} &= \bar{g}^* + \Delta t \bar{\Gamma}^g(\bar{\rho}^*, \bar{g}^{n+1}) \end{aligned} \quad \left. \begin{array}{l} \\ \\ \\ \end{array} \right\} \begin{array}{l} \text{explicit euler step} \\ \\ \text{implicit solve} \\ \text{without coupling.} \end{array}$$

In the minimally implicit variant MM_{1m} , we have $\bar{\Gamma}^\rho = 0$ and thus the implicit update for the density reduces to $\bar{\rho}^{n+1} = \bar{\rho}^*$. Lemou and Mieussens [96] proved that their scheme is stable under the time step restriction

$$\Delta t \leq \frac{1}{2} (\Delta t_{\text{micro}} + \Delta t_{\text{macro}}). \quad (5.12)$$

We do not try to prove a stability result, but all our computations indicate that this choice leads to a stable scheme. The microscopic time step restriction comes from the CFL condition in the discretization of the transport part and is given by $\Delta t_{\text{micro}} = \frac{1}{2} \frac{\Delta x}{c}$. On the macroscopic scale, the scheme must respect the stability condition of the diffusion approximation, as well as the CFL condition for advection. Hence, $\Delta t_{\text{macro}} = \max\left(\frac{\Delta x^2}{2\|D\|}, \frac{\Delta x}{2\|a\|}\right)$.

Remark 5.1 — Glioma equation. The implicit part in the MM_{1m} scheme can be solved analytically for the glioma model from Section 3.4.2. We have

$$\begin{aligned} g_j^{n+1} &= g_j^* + \Delta t \frac{\delta \lambda_{D,j}}{\varepsilon^2} \mathcal{L}_D g_j^{n+1} \\ &= g_j^* - \Delta t \frac{\delta \lambda_{D,j}}{\varepsilon^2} g_j^{n+1}, \end{aligned}$$

which is easily solved for the update:

$$g_j^{n+1} = \frac{1}{1 + \Delta t \frac{\delta \lambda_{D,j}}{\varepsilon^2}} g_j^*.$$

This is of course no longer possible for the schemes MM_{1i} and MM_{2i} with implicitly discretized volume terms.

The second-order scheme has to be chosen carefully to keep the asymptotic preserving property. We use the stiffly accurate IMEX scheme ARS(2,2,2) [4] in which the updated solution is identical to the last stage in a time step. The details of the application of that scheme to (5.10) can be found in Section A.6. Our numerical experiments indicate that the time step (5.12) needs to be restricted further by a factor of 0.2 to achieve stability with this scheme.

5.3.5 The asymptotic limit of the scheme

We consider the first-order minimally implicit variant MM_{1m} , which can—with some reordering of the steps—be written as

$$\begin{aligned} \bar{g}^* &= \bar{g}^n + \Delta t \left(\bar{\Phi}_E^g(\bar{\rho}^n, \bar{g}^n) + \bar{\Phi}^g(\bar{\rho}^n, \bar{g}^n) \right) \\ \bar{g}^{n+1} &= \bar{g}^* + \Delta t \bar{\Gamma}^g(\bar{g}^{n+1}) \\ \bar{\rho}^{n+1} &= \bar{\rho}^n + \Delta t \bar{\Phi}^\rho(\bar{\rho}^n, \bar{g}^{n+1}). \end{aligned}$$

This looks already like a discrete version of the considerations in Section 5.2 where we first computed the perturbation and then inserted this into the density equation. In the diffusion limit, only the $\frac{1}{\varepsilon^2}$ terms remain. Thus, the implicit perturbation update reduces to

$$g_j^{n+1} = -\frac{\varepsilon^2}{\Delta t \delta \lambda_{D,j}} \mathcal{L}_D^{-1} g_j^*$$

with

$$\begin{aligned} g_j^* &= \Delta t \left(\Phi_{E_j}^g(\bar{\rho}^n, \bar{g}^n) + \Phi_j^g(\bar{\rho}^n, \bar{g}^n) \right) \\ &= \Delta t \left(-\frac{\delta}{\varepsilon^2} \frac{1}{|\Omega_j|} \sum_{k \in \mathfrak{N}_j} \left(\sum_{r \in \mathfrak{N}_{j,k}} |\partial \omega_{j,k}^r| v \rho_r^n E_j \right) \cdot n_{j,k} + \frac{v \lambda_{a,j}}{\varepsilon^2} \mathcal{L}_a(E_j) \tilde{\rho}_j^n \right). \end{aligned}$$

Combining these two expressions yields

$$g_j^{n+1} = -\frac{1}{\lambda_{D,j}} \left(-\frac{1}{|\Omega_j|} \sum_{k \in \mathfrak{N}_j} \left(\sum_{r \in \mathfrak{N}_{j,k}} |\partial \omega_{j,k}^r| \mathcal{L}_D^{-1}(v E_j) \rho_r^n \right) \cdot n_{j,k} + \frac{v}{\delta} \lambda_{a,j} \mathcal{L}_D^{-1} \mathcal{L}_a(E_j) \tilde{\rho}_j^n \right).$$

Finally, we get the limit of the scheme as $\varepsilon \rightarrow 0$, when we insert this expression into the update for the density:

$$\rho_r^{n+1} = \rho_r^n + \Delta t \left(-\delta \frac{1}{|\Omega_r|} \sum_{s \in \mathfrak{N}_r} \sum_{j \in \mathfrak{N}_{r,s}} |\partial \omega_{r,s}^j| \langle v g_j^{n+1} \rangle \cdot n_{r,s}^j + \theta \mu(\rho_r^n) \rho_r^n \right).$$

This is an explicit scheme for the density ρ_r^{n+1} . The updated value ρ_r^{n+1} only depends on the previous values on the same dual cell Ω_r and those cells $\Omega_{s'}$ which are connected to it with at least a vertex, i.e., $\Omega_r \cap \Omega_{s'} \neq \emptyset$ or $\exists j : x_j \in \mathfrak{B}_r \wedge \mathfrak{B}_{s'}$.

On a square grid in two dimensions, this is equivalent to

$$\begin{aligned} g_{(l+\frac{1}{2},m+\frac{1}{2})}^{n+1} &= \frac{1}{\lambda_{D,j}} \frac{1}{2\Delta x} \mathcal{L}_D^{-1} \left(E_{(l+\frac{1}{2},m+\frac{1}{2})} \left[-v_\xi \left(\rho_{(l,m)}^n + \rho_{(l,m+1)}^n \right) - v_\eta \left(\rho_{(l,m)}^n + \rho_{(l+1,m)}^n \right) \right. \right. \\ &\quad \left. \left. + v_\xi \left(\rho_{(l+1,m)}^n + \rho_{(l+1,m+1)}^n \right) + v_\eta \left(\rho_{(l,m+1)}^n + \rho_{(l+1,m+1)}^n \right) \right] \right) \\ &\quad - \frac{\nu \lambda_{a,j}}{\delta} \frac{1}{\lambda_D} \mathcal{L}_D^{-1} \mathcal{L}_a \left(E_{(l+\frac{1}{2},m+\frac{1}{2})} \right) \frac{1}{4} \left(\rho_{(l,m)}^n + \rho_{(l+1,m)}^n + \rho_{(l+1,m+1)}^n + \rho_{(l,m+1)}^n \right), \\ \rho_{(l,m)}^{n+1} &= \rho_{(l,m)}^n - \frac{\Delta t \delta}{2\Delta x} \left\langle -v_\xi \left(g_{(l-\frac{1}{2},m-\frac{1}{2})}^{n+1} + g_{(l-\frac{1}{2},m+\frac{1}{2})}^{n+1} \right) - v_\eta \left(g_{(l-\frac{1}{2},m-\frac{1}{2})}^{n+1} + g_{(l+\frac{1}{2},m-\frac{1}{2})}^{n+1} \right) \right. \\ &\quad \left. + v_\xi \left(g_{(l+\frac{1}{2},m-\frac{1}{2})}^{n+1} + g_{(l+\frac{1}{2},m+\frac{1}{2})}^{n+1} \right) + v_\eta \left(g_{(l-\frac{1}{2},m+\frac{1}{2})}^{n+1} + g_{(l+\frac{1}{2},m+\frac{1}{2})}^{n+1} \right) \right\rangle \\ &\quad + \Delta t \theta \mu(\rho_{(l,m)}^n) \rho_{(l,m)}^n. \end{aligned}$$

For the special case that the equilibrium E and the factors λ_D , λ_a are constant in space, we write the limit scheme explicitly. We eliminate \bar{g}^{n+1} in the $\bar{\rho}$ equation⁵ and write the resulting scheme for $\bar{\rho}^{n+1}$

$$\bar{\rho}_{(l,m)}^{n+1} = \bar{\rho}_{(l,m)}^n + \Delta t \frac{\delta}{\lambda_D} \left(\overline{\nabla_x \cdot (D \nabla_x \rho)} \right) - \Delta t \frac{\nu \lambda_a}{\lambda_D} \left(\overline{\nabla_x \cdot (a \rho)} \right) + \Delta t \theta \mu(\bar{\rho}_{(l,m)}^n) \bar{\rho}_{(l,m)}^n,$$

with approximations to the diffusion

$$\begin{aligned} \overline{\nabla_x \cdot (D \nabla_x \rho)} &= \frac{1}{4\Delta x^2} \left(\rho_{(l,m)}^n (-4D_{\xi\xi} - 4D_{\eta\eta}) \right. \\ &\quad + \left(\rho_{(l-1,m)}^n + \rho_{(l+1,m)}^n \right) (2D_{\xi\xi} - 2D_{\eta\eta}) \\ &\quad + \left(\rho_{(l,m-1)}^n + \rho_{(l,m+1)}^n \right) (-2D_{\xi\xi} + 2D_{\eta\eta}) \\ &\quad + \left(\rho_{(l-1,m-1)}^n + \rho_{(l+1,m+1)}^n \right) (D_{\xi\xi} + 2D_{\xi\eta} + D_{\eta\eta}) \\ &\quad \left. + \left(\rho_{(l+1,m-1)}^n + \rho_{(l-1,m+1)}^n \right) (D_{\xi\xi} - 2D_{\xi\eta} + D_{\eta\eta}) \right) \end{aligned}$$

and drift

$$\begin{aligned} \overline{\nabla_x \cdot (a \rho)} &= -\frac{1}{8\Delta x} \left(\left(\rho_{(l-1,m)}^n - \rho_{(l+1,m)}^n \right) (2a_\xi) \right. \\ &\quad + \left(\rho_{(l,m-1)}^n - \rho_{(l,m+1)}^n \right) (2a_\eta) \\ &\quad + \left(\rho_{(l-1,m-1)}^n - \rho_{(l+1,m+1)}^n \right) (a_\xi + a_\eta) \\ &\quad \left. + \left(\rho_{(l+1,m-1)}^n - \rho_{(l-1,m+1)}^n \right) (-a_\xi + a_\eta) \right), \end{aligned}$$

wherein D is the diffusion tensor from (3.36) and a is the drift vector from (3.38). If the diffusion tensor is the identity $D = I$, which is the case for example in the glioma equation with isotropic equilibrium $E(v) = 1$, then the discrete diffusion reduces to a diagonal five-point stencil

$$\overline{\nabla_x \cdot (D \nabla_x \rho)} = \overline{\nabla_x \cdot (\nabla_x \rho)} = \frac{1}{2\Delta x^2} \left(-4\rho_{(l,m)}^n + \rho_{(l-1,m-1)}^n + \rho_{(l+1,m-1)}^n + \rho_{(l-1,m+1)}^n + \rho_{(l+1,m+1)}^n \right).$$

Figure 5.3 illustrates how the neighboring cells contribute to the limit stencil. In this special case, the presented AP-method is identical to the nodal scheme [22] proposed by Buet et al. As they already discussed, the scheme leads to a decoupling of meshes. If we start with a Dirac initial

⁵A symbolic toolbox is handy in these calculations.

condition on cell (l, m) , only every other cell $(l + l', m + m')$ with $l' + m' = 2q$ will ever receive some mass. The result is the checkerboard pattern observed in Experiment 5.10 (see Figure 5.12). The drift is approximated by a central scheme, which is also not ideal. For example, inserting the first unit vector $a = (1, 0)^\top$ for the drift, we get

$$\overline{\nabla_x \cdot (a\rho)} = \overline{\partial_\xi \rho} = \frac{1}{4\Delta x} \left(-2\rho_{(l-1,m)}^n + 2\rho_{(l+1,m)}^n - \rho_{(l-1,m-1)}^n + \rho_{(l+1,m-1)}^n - \rho_{(l-1,m+1)}^n + \rho_{(l+1,m+1)}^n \right).$$

In the next two subsections we show how to modify the AP-method in such a way that the diffusion and drift are better approximated in the limit. Particularly, on a tensor-product grid the diffusion will be approximated by a standard five-point stencil, and the drift by an upwind method.

5.3.6 An improved diffusion stencil in the limit

The numerical diffusion approximation results from a concatenation of the macroscopic flux $\Phi_r^\rho(\bar{\rho}^n, \bar{g}^{n+1})$ with $\mathcal{L}_D^{-1}\Phi_{E_j}^g(\bar{\rho}^n, \bar{g}^n)$ on overlapping primal cells $j \in \mathfrak{B}_r$. The goal of this section is to modify Φ_r^ρ and $\Phi_{E_j}^g$ such that—on a square grid in two dimensions—the resulting diffusion approximation becomes the standard five-point stencil. We distinguish the improved schemes by a superscript $+$, for example MM_{1m}^+ , from the naive schemes, denoted for example by MM_{1m}^\times . To simplify the following computations as much as possible, we set $\delta = 1$, $\lambda_D = 1$ and use a constant-in-space equilibrium $E(x, v) = E(v)$.

Recall the flux over primal faces in the most general form:

$$F_{j,k}^{(g,\rho)} = \frac{|\partial\Omega_{j,k}|}{|\Omega_j|} \left\{ (v\rho E) \cdot n_{j,k} \right\}_{\partial\Omega_{j,k}}^Q.$$

Together with a piece-wise constant reconstruction of the density $\rho|_{\Omega_r} = \rho_r$ this results in the formulation

$$F_{j,k}^{(g,\rho)} = \frac{1}{|\Omega_j|} \left(\sum_{r \in \mathfrak{B}_{j,k}} |\partial\omega_{j,k}^r| v \rho_r E_j \right) \cdot n_{j,k}.$$

This is a sum of constant fluxes over the facets $\partial\omega_{j,k}^r$, weighted by the facet volumes $|\partial\omega_{j,k}^r|$. In the derivation of the AP scheme on square grids in Section 5.3.3 we used this method. Considering the primal face $(l + \frac{1}{2}, m + \frac{1}{2})$, $(l + \frac{3}{2}, m + \frac{1}{2})$ in effect this method assigns equal weights $\frac{1}{2\Delta x}$ to both overlapping dual cells $(l + 1, m)$, $(l + 1, m + 1)$. We get the same weights if we reconstruct ρ as a globally continuous function from bilinear elements on each dual cell and use a midpoint quadrature rule on the faces. Starting from this interpretation, we define four variants of the microscopic flux

$$\Phi_{E,(l+\frac{1}{2},m+\frac{1}{2})}^{g,(\xi,+)} \quad \Phi_{E,(l+\frac{1}{2},m+\frac{1}{2})}^{g,(\xi,-)} \quad \Phi_{E,(l+\frac{1}{2},m+\frac{1}{2})}^{g,(\eta,+)} \quad \Phi_{E,(l+\frac{1}{2},m+\frac{1}{2})}^{g,(\eta,-)}$$

that use different weights on different faces. In the $(\xi, +)$ -variant, the flux on ξ -normal faces is evaluated with the topmost points, but for the η -normal faces equal weights are used:

$$\begin{aligned} \Phi_{E,(l+\frac{1}{2},m+\frac{1}{2})}^{g,(\xi,+)} = & -\frac{\delta}{\varepsilon^2} \frac{E}{\Delta x} \left[-v_\xi \rho_{(l,m+1)} - \frac{1}{2} v_\eta (\rho_{(l,m)} + \rho_{(l+1,m)}) \right. \\ & \left. + v_\xi \rho_{(l+1,m+1)} + \frac{1}{2} v_\eta (\rho_{(l,m+1)} + \rho_{(l+1,m+1)}) \right]. \end{aligned}$$

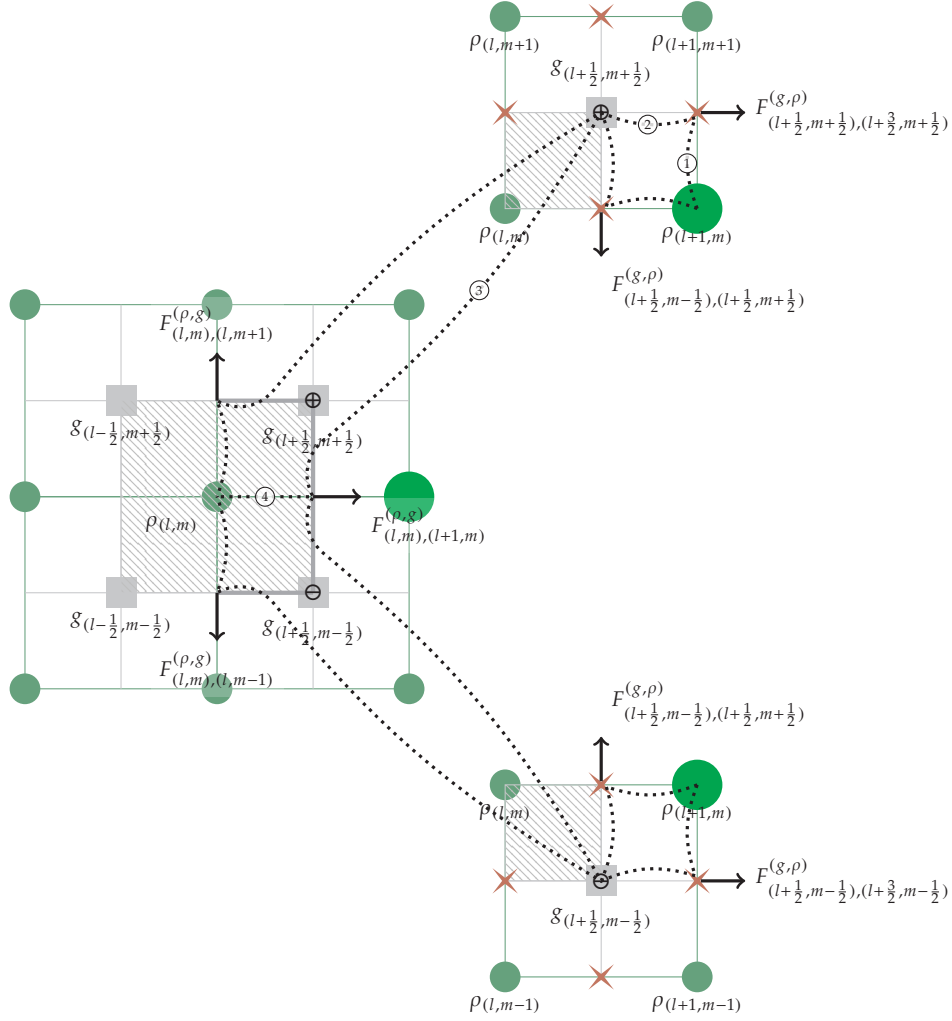


Figure 5.3: Contribution of the right neighbor $(l+1, m)$ (highlighted green) to the limit diffusion stencil around (l, m) . In the middle of the figure, the dual cell (l, m) (gray hatched) is shown together with the overlapping primal cells. At the top and bottom of the figure the primal cells $(l+\frac{1}{2}, m+\frac{1}{2})$ (marked \oplus) and $(l+\frac{1}{2}, m-\frac{1}{2})$ (marked \ominus) are shown again. Evaluation points for fluxes are shown as red stars. In the upper right primal cell, the right neighbor contributes the term $\frac{E}{2\Delta x} v_\xi \rho_{(l+1, m)}$ (⊙) to the flux $F_{(l+\frac{1}{2}, m+\frac{1}{2}), (l+\frac{3}{2}, m+\frac{1}{2})}^{(g, \rho)}$ over the primal face in positive ξ -direction. It also adds the term $-\frac{E}{2\Delta x} v_\eta \rho_{(l+1, m)}$ (not labelled) to the flux $F_{(l+\frac{1}{2}, m+\frac{1}{2}), (l+\frac{1}{2}, m-\frac{1}{2})}^{(g, \rho)}$ in negative η -direction. Both these fluxes contribute (e.g. ⊙ for the positive ξ -flux) to the update $g_{(l+\frac{1}{2}, m+\frac{1}{2})}^{(n+1)} = \mathcal{L}_D^{-1} g_{(l+\frac{1}{2}, m+\frac{1}{2})}^*$, which in turn is used for the fluxes over dual faces around (l, m) . For the positive ξ -flux $F_{(l, m), (l+1, m)}^{(\rho, g)}$, the value $g_{(l+\frac{1}{2}, m+\frac{1}{2})}^{(n+1)}$ contributes $\frac{1}{2\Delta x} \langle v_\xi g_{(l+\frac{1}{2}, m+\frac{1}{2})} \rangle$ (⊙) and similarly for the positive η -flux $F_{(l, m), (l, m+1)}^{(\rho, g)}$ it adds $\frac{1}{2\Delta x} \langle v_\eta g_{(l+\frac{1}{2}, m+\frac{1}{2})} \rangle$ (not labelled). Remembering that $D_{\xi\eta} = -\langle v_\xi \mathcal{L}_D^{-1}(v_\eta E) \rangle$, we get for the total contribution of $\rho_{(l+1, m)}$ via the upper right overlap $g_{(l+\frac{1}{2}, m+\frac{1}{2})}$ the term $\frac{1}{4\Delta x^2} (D_{\xi\xi} - D_{\eta\eta} - D_{\xi\eta} + D_{\eta\xi})$ (e.g. ⊙), which is zero for an isotropic tensor $D = I$. Analogously, the contributions via the lower right overlap cancel.

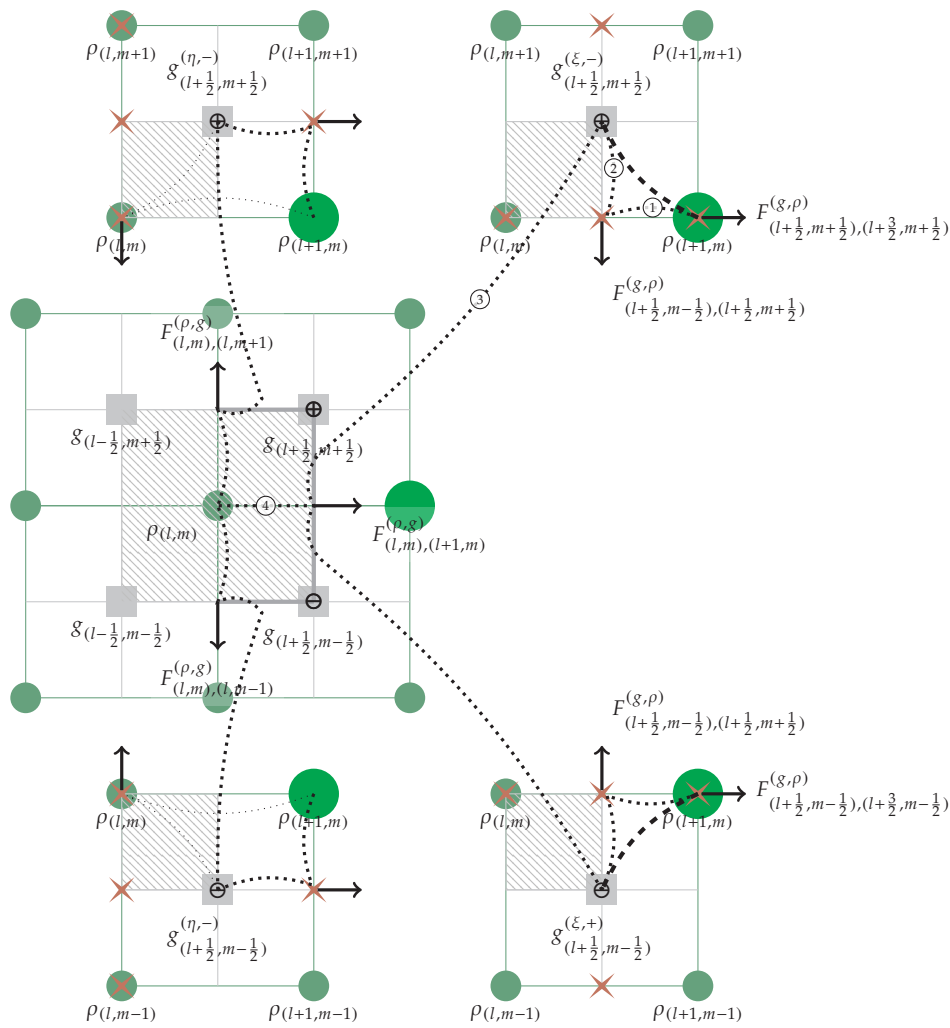


Figure 5.4: Improved diffusion stencil: Contribution of the right neighbor $(l + 1, m)$ (highlighted green) to the limit diffusion stencil around (l, m) . In the middle of the figure, the dual cell (l, m) (hatched gray) is shown together with the overlapping primal cells. At the top of the figure, the primal cell $(l + \frac{1}{2}, m + \frac{1}{2})$ is shown again twice (marked \oplus), on the top left to display the update variant $(\eta, -)$ and on the top right to display the variant $(\xi, +)$. Similarly, at the bottom the two update variants $(\eta, -)$ and $(\xi, +)$ are shown for the primal cell $(l + \frac{1}{2}, m - \frac{1}{2})$ (marked \ominus). Evaluation points for fluxes are shown as red stars. The lines show how different variants are used for fluxes over different dual facets, thin dots denoting zero weight, thick dots denoting weight $\frac{1}{2}$, and thick dashes denoting weight 1. With similar considerations as in Figure 5.3, we see that (follow e.g., ①–②–③–④) the right neighbor $\rho_{(l+1,m)}$ contributes with weights $\frac{1}{4\Delta x^2} (4D_{\xi\xi} + 0D_{\eta\eta} + 0D_{\eta\xi} + 0D_{\xi\eta})$.

Similarly, the $(\xi, -)$ -variant uses only the lowest points in ξ -normal faces:

$$\begin{aligned} \Phi_{E,(l+\frac{1}{2},m+\frac{1}{2})}^{g,(\xi,-)} &= -\frac{\delta}{\varepsilon^2} \frac{E}{\Delta x} \left[-v_\xi \rho_{(l,m)} - \frac{1}{2} v_\eta (\rho_{(l,m)} + \rho_{(l+1,m)}) \right. \\ &\quad \left. + v_\xi \rho_{(l+1,m)} + \frac{1}{2} v_\eta (\rho_{(l,m+1)} + \rho_{(l+1,m+1)}) \right]. \end{aligned}$$

The other variants are defined analogously for the η -normal faces. These weights can be interpreted as evaluations of a linear interpolation between cell means at the nodes of zeroth-order accurate Gauss-Radau quadrature rules. In the second-order scheme, we assign the weights according to first-order accurate Gauss-Radau rules instead. Figure 5.5 shows the evaluation points for the $(\xi, -)$ variant. We use each flux variant in the perturbation update $g_{(l+\frac{1}{2},m+\frac{1}{2})}^{n+1}$ in turn to compute the four modified perturbations

$$g_{(l+\frac{1}{2},m+\frac{1}{2})}^{n+1,(\xi,+)}, \quad g_{(l+\frac{1}{2},m+\frac{1}{2})}^{n+1,(\xi,-)}, \quad g_{(l+\frac{1}{2},m+\frac{1}{2})}^{n+1,(\eta,+)}, \quad g_{(l+\frac{1}{2},m+\frac{1}{2})}^{n+1,(\eta,-)}.$$

Now we modify the density flux $\Phi_{(l,m)}^\rho$. In each flux over a dual facet, one variant of the perturbation is used:

$$\begin{aligned} \rho_{(l,m)}^{n+1} &= \rho_{(l,m)}^n \\ &\quad - \frac{\Delta t \delta}{2\Delta x} \left\langle -v_\xi \left(g_{(l-\frac{1}{2},m-\frac{1}{2})}^{n+1,(\xi,+)} + g_{(l-\frac{1}{2},m+\frac{1}{2})}^{n+1,(\xi,-)} \right) - v_\eta \left(g_{(l-\frac{1}{2},m-\frac{1}{2})}^{n+1,(\eta,+)} + g_{(l+\frac{1}{2},m-\frac{1}{2})}^{n+1,(\eta,-)} \right) \right. \\ &\quad \left. + v_\xi \left(g_{(l+\frac{1}{2},m-\frac{1}{2})}^{n+1,(\xi,+)} + g_{(l+\frac{1}{2},m+\frac{1}{2})}^{n+1,(\xi,-)} \right) + v_\eta \left(g_{(l-\frac{1}{2},m+\frac{1}{2})}^{n+1,(\eta,+)} + g_{(l+\frac{1}{2},m+\frac{1}{2})}^{n+1,(\eta,-)} \right) \right\rangle \\ &\quad + \Delta t \theta \mu (\rho_{(l,m)}^n) \rho_{(l,m)}^n, \end{aligned}$$

By this procedure, which is depicted in Figure 5.4, weight is shifted from the diagonal neighbors to the direct neighbors.

In the limit, this gives the following diffusion approximation:

$$\begin{aligned} \overline{\nabla_x \cdot (D \nabla_x \rho)} &= \frac{1}{4\Delta x^2} \left(\rho_{(l,m)}^n (-8D_{\xi\xi} - 8D_{\eta\eta}) \right. \\ &\quad \left. + (\rho_{(l-1,m)}^n + \rho_{(l+1,m)}^n) (4D_{\xi\xi}) + (\rho_{(l,m-1)}^n + \rho_{(l,m+1)}^n) (4D_{\eta\eta}) \right. \\ &\quad \left. + (\rho_{(l-1,m-1)}^n - \rho_{(l+1,m-1)}^n - \rho_{(l-1,m+1)}^n + \rho_{(l+1,m+1)}^n) (2D_{\xi\eta}) \right), \end{aligned}$$

which is the classical five-point stencil

$$\overline{\nabla_x \cdot (D \nabla_x \rho)} = \overline{\nabla_x \cdot (\nabla_x \rho)} = \frac{1}{2\Delta x^2} \left(-4\rho_{(l,m)}^n + \rho_{(l-1,m)}^n + \rho_{(l+1,m)}^n + \rho_{(l,m-1)}^n + \rho_{(l,m+1)}^n \right)$$

if the diffusion tensor is isotropic.

Remark 5.2 — Extension to three dimensions. In three space dimensions the procedure is structurally similar but the notation becomes even more unwieldy. The computational cost also increases, because we need twelve variants, four for each normal direction. For example, in the variant $(\xi, ++)$, the fluxes over ξ -normal faces are evaluated at the top right node.

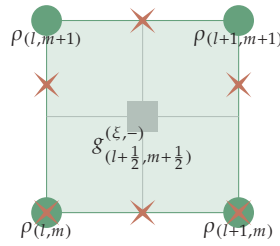


Figure 5.5: The second-order accurate shifted update variant $(\xi, -)$ around the primal cell $(l + \frac{1}{2}, m + \frac{1}{2})$. Evaluation points for fluxes are shown as red stars. A first-order accurate Gauss-Radau quadrature is used for the fluxes over ξ -normal faces. The fluxes over η -normal faces are approximated with the second-order accurate midpoint rule.

5.3.7 An upwind discretization of the drift in the limit

The limit drift approximation follows from a concatenation of the macroscopic flux Φ^p with $-\mathcal{L}_D^{-1} \mathcal{L}_a(E_j) \tilde{\rho}_j^n$. Using an average density $\tilde{\rho}_j$ weighted by the sub-cell volumes as in (5.11) leads to a central approximation of the drift as sketched in Figure 5.6a. But we know the local drift direction

$$a_j = \langle v \mathcal{L}_D^{-1} \mathcal{L}_a E_j \rangle$$

and want to assign more weight to those cells Ω_r that are upwind of the center x_j . We write x_j^* for the intersection of the ray

$$x_j - \tau a_j, \quad \tau \in \mathbb{R}^+$$

with the cell boundary $\partial\Omega_j$. Then we define

$$\tilde{\rho}_j = \rho(x_j^*)$$

with a continuous, piece-wise linear reconstruction ρ by hat-functions. In Figure 5.6b we show a sketch of this first-order accurate upwind discretization for the drift.

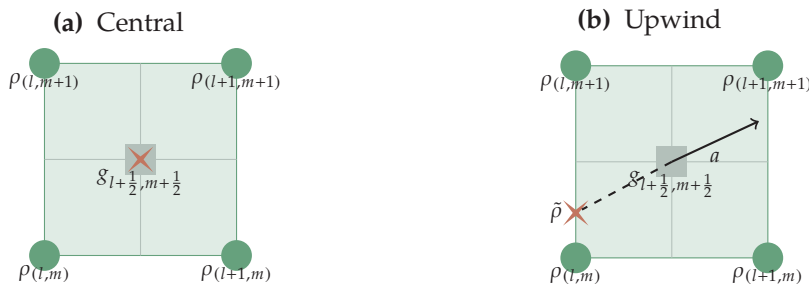


Figure 5.6: Drift discretizations on the primal cell $(l + \frac{1}{2}, m + \frac{1}{2})$: central and upwind scheme. Red stars are evaluation points for the density $\tilde{\rho}_{(l+\frac{1}{2}, m+\frac{1}{2})}$.

5.3.8 The treatment of boundary conditions

We consider only boundary conditions that preserve mass. On a macroscopic level this translates to a zero-flux Robin-type boundary condition for the density in (3.32):

$$-\delta D \cdot \nabla_x \rho_0 + \delta a_D \rho_0 - \nu \rho_0 a|_{\partial\Omega_x} = 0. \quad (5.13)$$

This does not determine the boundary conditions for the micro-equation uniquely. All reflective boundary conditions for the kinetic equation (3.31) for f preserve mass. At a reflective boundary, the values $f(v)$ are prescribed for incoming velocities $v \cdot n < 0$ and follow from the outgoing values via the reflection integral:

$$f(v) = \int_{v' \cdot n > 0} B(v, v') f(v') dv' \quad \forall v \cdot n < 0, \quad (5.14)$$

Of course, the reflection kernel B is defined such that the net mass flux across the boundary is zero, that is, it fulfills

$$\begin{aligned} 0 &= \int_{\mathbb{S}^2} (v \cdot n) f(v) dv = \int_{v \cdot n > 0} (v \cdot n) f(v) dv + \int_{v \cdot n < 0} (v \cdot n) f(v) dv \\ &= \int_{v \cdot n > 0} (v \cdot n) f(v) dv + \int_{v \cdot n < 0} (v \cdot n) \int_{v' \cdot n > 0} B(v, v') f(v') dv' dv. \end{aligned} \quad (5.15)$$

From the last line, we see that this is the case if

$$\int_{v \cdot n < 0} (v \cdot n) B(v, v') dv = -v' \cdot n$$

holds. To derive the boundary condition for g that is equivalent to (5.14), we insert the micro-macro decomposition (5.3) and obtain

$$g(v) = \frac{\rho}{\varepsilon} \left[\int_{v' \cdot n > 0} B(v, v') E(v') dv' - E(v) \right] + \int_{v' \cdot n > 0} B(v, v') g(v') dv'.$$

If the kernel is not compatible with the equilibrium state, then in the limit when ε tends to zero, g becomes unbounded at the boundary, and we need to solve a half-space problem to compute the boundary condition. Here we do not want to consider boundary layers and therefore demand that the equilibrium state E fulfills (5.14). Then the condition (5.14) also holds for g . The value for ρ is left unconstrained.

For the kernel, we consider two options. The 'u-turn' kernel models that cells turn around 180 degrees when encountering a wall, independent of the angle of collision. It is given by

$$B_{\text{uturn}}(v, v') = \delta_v(-v').$$

Because the equilibrium fulfills $E(v) = E(-v)$, the reflection equation (5.14) holds for the equilibrium. It is easy to check the zero-mass-flux condition (5.15) for this kernel.

Another option is that after a collision with the wall, the incoming particles are in equilibrium

$$f(v) = \alpha E(v) \quad \forall v \cdot n < 0.$$

This so-called thermal boundary condition can be achieved with the kernel

$$B_{\text{thermal}}(v, v') = \frac{\alpha E(v)}{\int_{v' \cdot n > 0} f(v') dv'}.$$

The parameter α is defined by

$$\alpha = -\frac{\int_{v \cdot n > 0} (v \cdot n) f(v) dv}{\int_{v \cdot n < 0} (v \cdot n) E(v) dv}$$

to fulfill the zero-mass-flux condition (5.15). For a symmetric equilibrium we have $\alpha = 1$, thus the boundary condition is compatible with the equilibrium. The resulting boundary condition for g is

$$g(v) = -\frac{\int_{v \cdot n > 0} (v \cdot n) g(v) dv}{\int_{v \cdot n < 0} (v \cdot n) E(v) dv} E(v) \quad \forall v \cdot n < 0. \quad (5.16)$$

Remark 5.3 — Specular reflection. The specular reflection kernel

$$B_{\text{spec}}(v, v') = \delta_v(v' - 2(v' \cdot n)n)$$

models hard-sphere collisions between particles and the wall. It conserves mass, but is not compatible with the equilibrium in general, only if the equilibrium is mirror symmetric around the outer boundary

$$E(v) = E(v - 2(v \cdot n)n).$$

Optionally, we can constrain the density $\rho_0|_{\partial\Omega_x} = \rho_{0b}$. Then, together with (5.13) this implies a condition for $\nabla_x \rho_0$, which can always be fulfilled because D is invertible. On the particle level, this yields the additional condition

$$\rho|_{\partial\Omega_x} = \int_{\mathbb{S}^2} f(v) dv \Big|_{\partial\Omega_x} = \rho_{0b}.$$

5.3.9 The discretization of the velocity space by a linear spectral method

The scheme that we derived in the previous sections is discrete in time and space. It remains to find a suitable discretization for the velocity space. We use a linear spectral Galerkin method based on real-valued spherical harmonics [21, 59, 123]. For a definition of the spherical harmonics, we refer to Appendix A.2. Remember the constrained space of perturbations g from Lemma 3.9

$$g \in \mathcal{N}^\perp(\mathcal{L}_D) = \{g \in L_E^2, (g, E)_E = \langle g \rangle = 0\}. \quad (5.17)$$

Let \mathbf{a}^∞ be a basis of spherical harmonics with the first basis function $a_0 = \frac{1}{\sqrt{4\pi}}$. Because of the orthogonality $\langle a_i a_j \rangle = \delta_{ij}$ of the spherical harmonics, all basis components except for a_0 fulfill the constraint $\langle g \rangle = 0$ in (5.17). Hence, we construct finite-dimensional basis vectors \mathbf{p}^N for the constrained space by leaving out the constant basis function a_0 :

$$\mathbf{p}^N = (\mathbf{p}^{(1)}, \dots, \mathbf{p}^{(N)}) = (\mathbf{a}^{(1)}, \dots, \mathbf{a}^{(N)}).$$

With the moments

$$\mathbf{m} = \langle \mathbf{p} g \rangle,$$

we write the discrete-in-velocity approximation of problem (5.6), which consists of finding moments (ρ, \mathbf{m}) that solve

$$\begin{aligned}\partial_t \rho &= \Phi^p(\rho, \mathfrak{g}) + \Gamma^p(\rho, \mathfrak{g}), \\ \partial_t \mathbf{m} &= \langle \mathbf{p} \Phi_E^g(\rho) \rangle + \langle \mathbf{p} \Phi^g(\rho, \mathfrak{g}) \rangle + \langle \mathbf{p} \Gamma^g(\rho, \mathfrak{g}) \rangle.\end{aligned}\tag{5.18}$$

To close the system, we make the linear ansatz $\mathfrak{g}(v) = \boldsymbol{\phi} \cdot \mathbf{p}(v) = \mathbf{m} \cdot \mathbf{p}$. This is the orthogonal projection of \mathfrak{g} onto the finite-dimensional subspace of $\mathcal{N}^\perp(\mathcal{L}_D)$ spanned by \mathbf{p} . The multipliers $\boldsymbol{\phi}$ are identical to the moments \mathbf{m} because the basis is orthonormal (see Section 1.2.3). Moments of the individual terms from (5.7), (5.8) are

$$\begin{aligned}\Phi^p(\rho, \mathfrak{g}) &= -\delta \nabla_x \cdot \langle v \mathfrak{g} \rangle + \theta \mu \rho, \\ \langle \mathbf{p} \Phi_E^g(\rho) \rangle &= -\frac{\delta}{\varepsilon^2} \nabla_x \cdot (\rho \langle v \mathbf{p}^\top E \rangle), \\ \langle \mathbf{p} \Phi^g(\rho, \mathfrak{g}) \rangle &= -\frac{\delta}{\varepsilon} [\nabla_x \cdot \langle v \mathbf{p}^\top \mathfrak{g} \rangle - \nabla_x \cdot \langle v \mathfrak{g} \rangle \langle \mathbf{p} E \rangle] + \frac{\nu \lambda_a}{\varepsilon^2} \langle \mathbf{p} \mathcal{L}_a(\rho E + \varepsilon \mathfrak{g}) \rangle + \frac{\theta \mu}{\varepsilon} \langle \mathbf{p} (I - \Pi) \mathcal{S}(\rho E + \varepsilon \mathfrak{g}) \rangle,\end{aligned}$$

and

$$\begin{aligned}\Gamma^p(\rho, \mathfrak{g}) &= 0, \\ \langle \mathbf{p} \Gamma^g(\rho, \mathfrak{g}) \rangle &= \frac{\delta \lambda_D}{\varepsilon^2} \langle \mathbf{p} \mathcal{L}_D(\mathfrak{g}) \rangle.\end{aligned}$$

The equations are coupled by the flux moments $\langle v \mathfrak{g} \rangle \in \mathbb{R}^d$, $\langle v \mathbf{p}^\top \mathfrak{g} \rangle \in \mathbb{R}^{n \times d}$ and moments of the collision term and source on the right-hand side. The macro equation is coupled with the micro equations by the moments

$$\langle v \mathfrak{g} \rangle = \frac{\sqrt{4\pi}}{\sqrt{3}} \langle \mathbf{p}^{(1)} \mathfrak{g} \rangle = \frac{\sqrt{4\pi}}{\sqrt{3}} \mathbf{m}^{(1)}.$$

In general, i -th order flux moments $\langle v \mathbf{p}^{(i)\top} \mathfrak{g} \rangle$ can be written as a combination of the moments $\langle \mathbf{p}^{(i+1)} \mathfrak{g} \rangle = \mathbf{m}^{(i+1)}$ of order $i+1$. Usually, this relation is written in matrix form. For instance, for the ξ -component of the velocity, we write

$$\langle v_\xi \mathfrak{p} \mathfrak{g} \rangle = M_\xi \mathbf{m} := \langle v_\xi \mathbf{p} \mathbf{p}^\top \rangle \mathbf{m}.$$

For details on how to compute these matrices for the full basis \mathbf{a} , see for example [123]. By orthogonality of the basis we can simply remove the first row and column of the matrix $\langle v_\xi \mathbf{a} \mathbf{a}^\top \rangle$ to get the matrix $M_\xi = \langle v_\xi \mathbf{p} \mathbf{p}^\top \rangle$ for the restricted basis \mathbf{p} . Because the turning operators are linear, we can also write their contribution to the moment system in matrix form:

$$\begin{aligned}\langle \mathbf{p} \mathcal{L}_D(\mathfrak{g}) \rangle &= C_D \mathbf{m}, \\ \langle \mathbf{p} \mathcal{L}_a(\mathfrak{g}) \rangle &= C_a \mathbf{m}.\end{aligned}$$

Remark 5.4 — Turning operators in the glioma equation. From equation (3.27) we have

$$\mathcal{L}_D(g) = -g,$$

thus

$$\langle \mathbf{p} \mathcal{L}_D(g) \rangle = -\langle \mathbf{p}g \rangle = -\mathbf{m},$$

and $C_D = -I$. The turning perturbation is given by

$$\mathcal{L}_a(g) = \widehat{\nabla_x Q} \cdot (E \langle v g \rangle - v g).$$

Its moments are

$$\langle \mathbf{p} \mathcal{L}_a(g) \rangle = \widehat{\nabla_x Q} \cdot (\langle v g \rangle \langle \mathbf{p}^\top E \rangle - \langle v \mathbf{p}^\top g \rangle)$$

The dot product is between components of the gradient $\widehat{\nabla_x Q}$ and components of the velocity v . The moments appearing in this expression have been calculated before. With some abuse of vector notation, we have

$$\langle \mathbf{p} \mathcal{L}_a(g) \rangle = \widehat{\nabla_x Q} \cdot \left(\frac{\sqrt{4\pi}}{\sqrt{3}} \mathbf{m}^{(1)} \langle \mathbf{p}^\top E \rangle - (M_\xi \mathbf{m}, M_\eta \mathbf{m}, M_\zeta \mathbf{m})^\top \right).$$

Because the source is $\mathcal{S}f = f$, its moments can be simplified to

$$\langle \mathbf{p} (I - \Pi) \mathcal{S}(\rho E + \varepsilon g) \rangle = \varepsilon \mathbf{m}.$$

Remark 5.5 Equation (5.18) is equivalent to the moment system

$$\partial_t \mathbf{u} = -\frac{\delta}{\varepsilon} \nabla_x \cdot \langle v \mathbf{a}^\top \mathfrak{f} \rangle + \frac{\delta}{\varepsilon^2} \lambda_D \langle \mathbf{a} \mathcal{L}_D \mathfrak{f} \rangle + \frac{\nu}{\varepsilon} \lambda_a \langle \mathbf{a} \mathcal{L}_a \mathfrak{f} \rangle + \theta \mu \langle \mathbf{a} \mathcal{S} \mathfrak{f} \rangle$$

for the original equation (3.31) with the approximation \mathfrak{f} and moments \mathbf{u} of the particle distribution f given by

$$\begin{aligned} \mathfrak{f} &= \mathbf{u} \cdot \mathbf{a} = \rho E + \varepsilon g, \\ u_i &= \langle a_i \mathfrak{f} \rangle = \begin{cases} \frac{1}{\sqrt{4\pi}} \rho & i = 0 \\ \rho \langle E p_i \rangle + \varepsilon m_i & i > 0 \end{cases} \end{aligned}$$

This corresponds to the modified $P_N^{(E+)}$ method introduced in Section 4.1.2.

The space and time discretization can be carried over to the moment system without change. It is of course possible to discretize the velocity space by any other method. Close enough to the diffusion limit, the choice of the discretization should become negligible. Due to its simplicity, one popular choice in the literature is the discrete-ordinates method [59, 92]. In three space dimensions this method needs at least eight degrees of freedom to preserve symmetry, twice as much as needed in the P_1 -method.

5.4 Numerical experiments

We investigate properties of the scheme numerically in a range of benchmarks. The fundamental solution to the drift-diffusion equation serves to verify the correct diffusion limit of the scheme and also its order of convergence with respect to grid refinement (see Section 5.4.1). Additionally, the order of convergence is verified in Section 5.4.2 with a manufactured solution for all transport regimes. In Section 5.4.3, we demonstrate the benefit of the stencil improvement from Section 5.3.6. Two benchmarks from the porous-media context are employed to investigate the behavior of the scheme in presence of discontinuities (see Section 5.4.4). The final benchmark in Section 5.4.5 shows properties of the temporal discretization using an approximate travelling wave solution to the Fisher-KPP equation.

Then, we consider two applications. In Section 5.4.6, we simulate Stroock's E.coli model in one space dimension to evaluate mechanisms of directed migration. And finally, we apply the scheme to the glioma model with realistic parameters and diffusion tensors from DTI.

All computations are performed on the glioma model from Section 3.4.2 with the peanut distribution (2.4). When not otherwise mentioned, we use the minimally implicit schemes MM_{1m}^+ and MM_{2m}^+ with the stencil improvements from Section 5.3.6 and Section 5.3.7. For the computations in Section 5.4.1 and Section 5.4.4 we need to prescribe the macroscopic diffusion tensor D_T . We achieve this by constructing artificial values for the water diffusion tensor

$$D_W = \frac{1}{2} (5D_T - I),$$

according to the inverse of (3.39). Whenever we prescribe the macroscopic drift a_T , we define the volume fraction Q according to the inverse of (3.40):

$$\nabla_x Q = \frac{1}{\lambda_H} a_T^\top D_T^{-1}.$$

5.4.1 The fundamental solution of the limit equation

When the diffusion tensor D and drift a are constant and the growth factor θ is zero, the limiting advection-diffusion equation (3.32) has the fundamental solution

$$\rho_{0,f} = \left((4\pi)^d \det D \right)^{-\frac{1}{2}} t^{-\frac{d}{2}} \exp \left(-\frac{1}{4t} (x - at)^\top D^{-1} (x - at) \right) \quad (5.19)$$

in physical coordinates. Our scheme should reproduce this solution when ε is small. For the test we choose

$$D_T = D_0 \frac{1}{4.5} R \begin{pmatrix} 2.5 & 0 & 0 \\ 0 & 1 & 0 \\ 0 & 0 & 1 \end{pmatrix} R^\top, \quad a_T = a_0 \frac{1}{\sqrt{10}} \begin{pmatrix} 3 \\ 1 \\ 0 \end{pmatrix}.$$

Herein, the matrix R rotates e_1 onto the main diffusion direction $(-1, 2, 0)^\top$. We choose the characteristic diffusion speed $D_0 = \frac{1}{100}$.

To smooth the initial Dirac-delta distribution, we choose the initial condition $\rho(0, x) = \rho_{0,f}(t_O, x)$ with the time offset $t_O = 0.2$. Then the solution at time t is given by $\rho_{0,f}(t + t_O, x)$.

First we test convergence with respect to grid refinement.

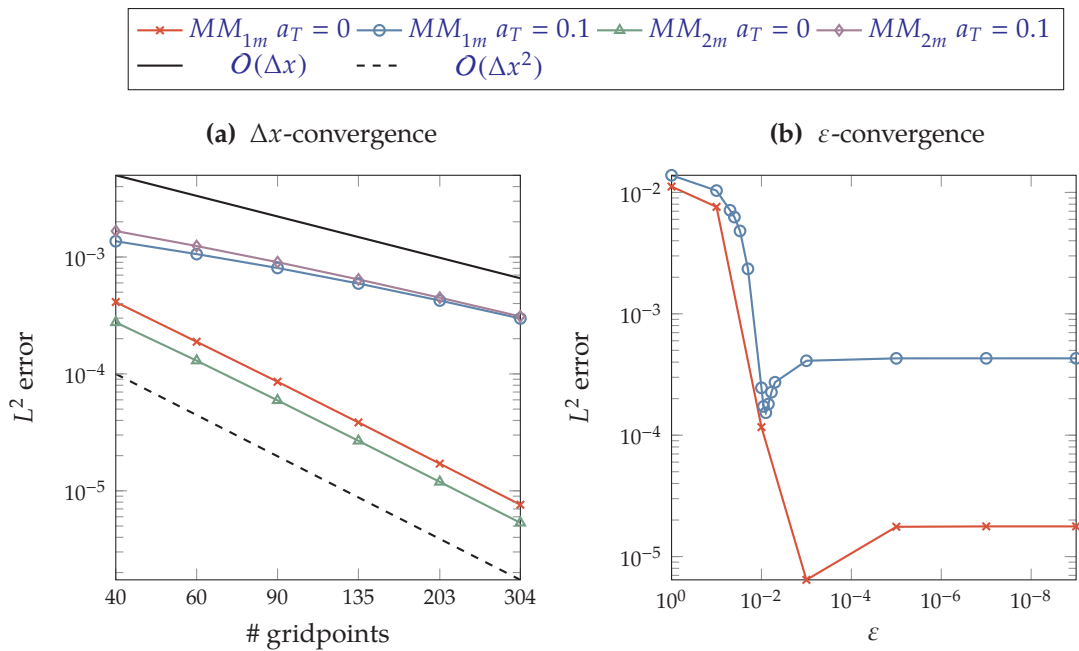


Figure 5.7: Results of Experiment 5.6—grid refinement—and Experiment 5.7—convergence to diffusion limit. 5.7a: L^2 errors over number of grid points on each axis. Shown are the errors for both MM_{1m}^+ and MM_{2m}^+ , each without drift $a_T = 0$ and with some drift $a_T = 0.1$. 5.7b: L^2 errors over parabolic scaling parameter ε , for a fixed grid with 200×200 cells. Errors for the MM_{1m}^+ are shown both without and with drift.

■ **Experiment 5.6 — Grid refinement.** We compute the MM_{1m}^+ and MM_{2m}^+ solutions of the $P_1^{(E)}$ model on five different grids each: starting at a 40×40 grid we refine five times by the factor 1.5. We perform two tests, one without drift, i.e., $a_0 = 0$, and one with drift speed $a_0 = 0.1$. The analytical solution is of course only valid in the diffusion limit, therefore, we choose $\varepsilon = 10^{-5}$.

The L^2 error over the number of grid points is plotted in Figure 5.7a. Without the drift term, both schemes converge with second order accuracy to the analytic solution, as is to be expected for a discretization of the pure diffusion equation. With the drift, the order of both schemes is reduced to about 0.9 and absolute errors are also much greater.

We are also interested in convergence as ε tends to zero.

■ **Experiment 5.7 — Convergence to diffusion limit.** We compute the MM_{1m}^+ solution of the $P_1^{(E)}$ model on a grid with 200×200 cells for some $\varepsilon \in [1 \times 10^{-9}, 1]$. We perform two tests, one without drift, i.e., $a_0 = 0$, and one with drift speed $a_0 = 0.1$.

From the grid refinement study, we see that at about 200×200 grid points, the error is roughly 2×10^{-5} without drift and 4×10^{-4} with the drift term. As ε approaches zero, we expect the total error to be dominated by this discretization error. In Figure 5.7b, the L^2 error of the first order

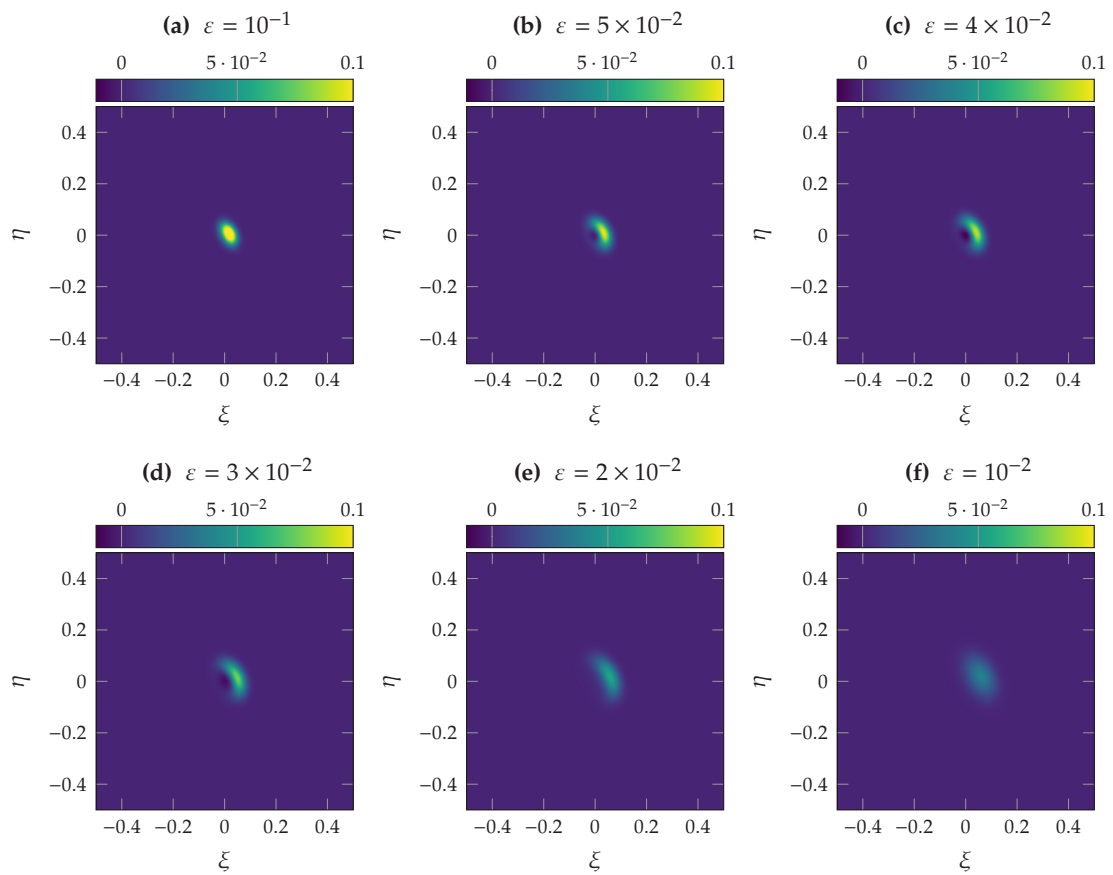


Figure 5.8: Results of Experiment 5.7—convergence to diffusion limit. Density ρ of the MM_{1m}^+ solution for various values of ε , ranging from the kinetic regime $\varepsilon = 0.1$ in 5.8a to the intermediate regime in 5.8f with $\varepsilon = 10^{-2}$.

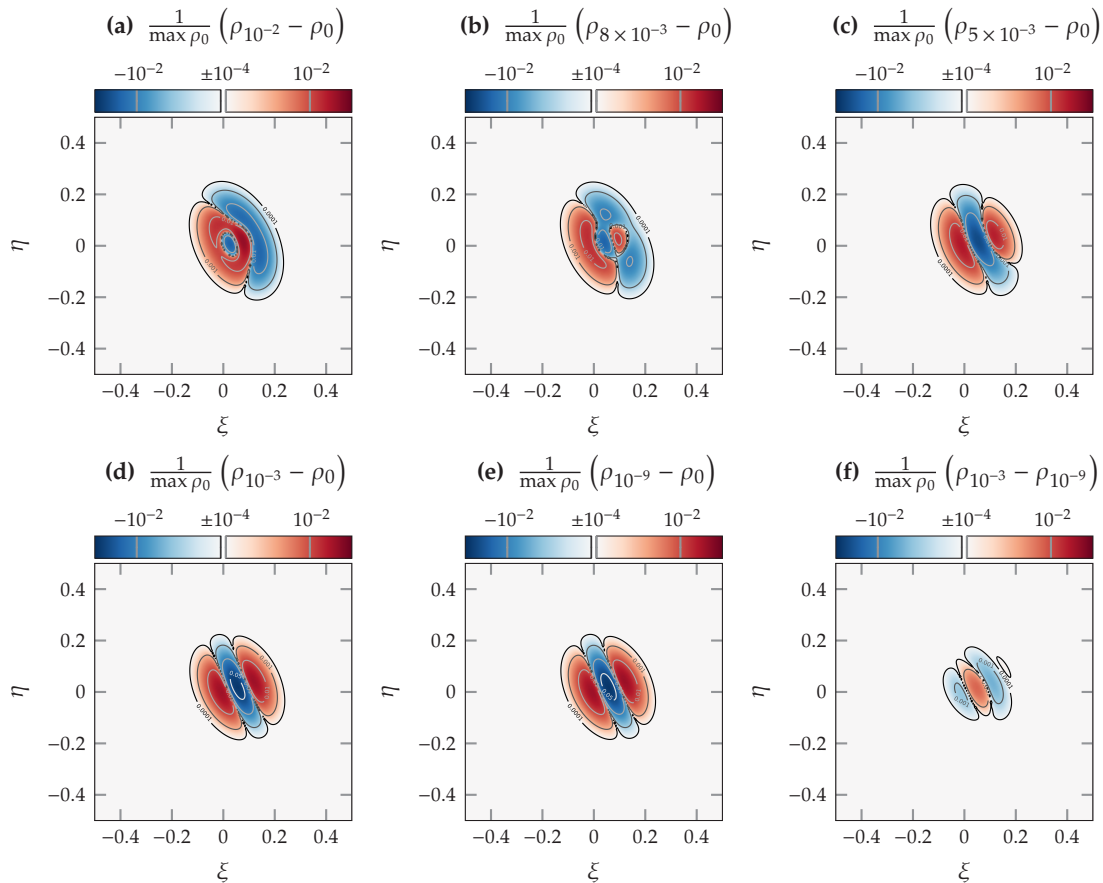


Figure 5.9: Results of Experiment 5.7—convergence to diffusion limit. Each plot shows the relative difference in density ρ between two solutions on a signed truncated logarithmic scale. Figure 5.9a - 5.9e show the relative difference between the numerical solution at various ε , and the exact solution (5.19). Figure 5.9f shows the difference between the numerical solutions at $\varepsilon = 10^{-3}$ and $\varepsilon = 10^{-9}$.

scheme at 200×200 grid points is plotted, over values of ε from one to 10^{-9} . We observe that the error levels out at the expected discretization error below a threshold value of ε , roughly 10^{-4} without drift and 10^{-3} with drift. Note that for certain intermediate values of ε , the error reaches a local minimum slightly below the limit discretization error because kinetic effects cancel out some numerical diffusion of the scheme. Numerical solutions in the kinetic to intermediate regime ($\varepsilon \in [0.1, 0.01]$) are shown in Figure 5.8. In the kinetic regime, the problem is similar to the line source problem [59]; only for anisotropic scattering. Indeed, the P_1 solutions feature a single ellipsoid wave, which travels at speed $\frac{1}{\sqrt{3}}c$ in the main diffusion direction and is biased towards the drift direction. With decreasing ε the diffusion dominates and the wave maximum is smeared out into a Gaussian. Below $\varepsilon \approx 10^{-2}$ the solutions are too similar for direct visual comparisons. Therefore, in Figure 5.9 we show relative differences on a signed logarithmic scale instead. Figure 5.9a to Figure 5.9f show relative differences between the numerical solution and the fundamental solution to the diffusion equation (5.19). The solution at $\varepsilon = 10^{-2}$ still has some small kinetic effects (see Figure 5.9a) of relative magnitude 10^{-2} . In Figure 5.9f the relative difference between the numerical solutions at $\varepsilon = 10^{-3}$ and $\varepsilon = 10^{-9}$ is plotted. We see that already at $\varepsilon = 10^{-3}$ the discretization error dominates the kinetic effects. From Figure 5.9b we see how the kinetic effects cancel some numerical diffusion. The numerical diffusion from the drift discretization becomes apparent from Figure 5.9e: looking in drift direction, the solution at $\varepsilon = 10^{-9}$ overestimates the fundamental solution before and after the peak and underestimates it at the peak.

With the fundamental solution we can also quantify the numerical diffusion of the scheme.

■ **Experiment 5.8 — Numerical diffusion.** We fit a multivariate Gaussian

$$\rho_{0,\text{fit}} = \left((4\pi)^d \det D_{\text{fit}} \right)^{-\frac{1}{2}} t^{-\frac{d}{2}} \exp \left(-\frac{1}{4t} (x - a_{\text{fit}}t)^\top D_{\text{fit}}^{-1} (x - a_{\text{fit}}t) \right)$$

to the results of Experiment 5.6 and estimate the numerical diffusion tensor via

$$D_{\text{num}} = D_{\text{fit}} - D.$$

In Figure 5.10, the two eigenvalues and the main direction of this estimated numerical diffusion D_{num} are plotted. We observe that numerical diffusion converges at the same rate as the L^2 error. When the drift term is active, it dominates the overall numerical diffusion by two orders of magnitude and the main axis of the numerical diffusion is parallel to the drift direction. Without the drift, we observe an interesting difference between the MM_{1m} scheme and the MM_{2m} scheme. For the MM_{2m} scheme, both eigenvalues are positive and their ratio is close to the anisotropy factor 2.5. Additionally, the main axes of physical and numerical diffusion are aligned. Thus, the numerical diffusion is proportional to the physical diffusion. In the MM_{1m} scheme the ratio of eigenvalues and main axis is the same. However, both eigenvalues are negative, which indicates that the leading numerical error is dispersive rather than diffusive.

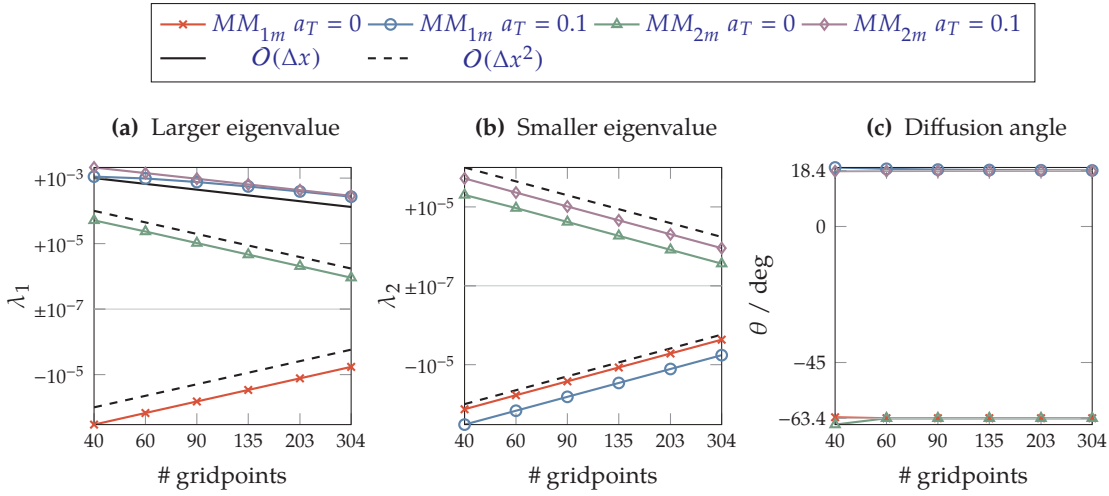


Figure 5.10: Results of Experiment 5.8—numerical diffusion. Figure 5.10a: The larger eigenvalue of the numerical diffusion tensor D_{num} in absolute value. Figure 5.10b: The smaller eigenvalue. Figure 5.10c: The direction of the main eigenvector.

5.4.2 Convergence analysis with manufactured solutions

We verify the expected order of convergence for MM_{1m}^+ and MM_{2m}^+ in all transport regimes. Apart from the theoretical concern to determine the convergence order for different transport regimes, convergence tests with manufactured solutions are useful to detect errors in the scheme and bugs in its implementation [119].

We consider only the two-dimensional setting. On the domain

$$\Omega_{txv} = [0, \frac{1}{4}] \times [0, 1]^2 \times \mathbb{S}^2$$

we prescribe the solution in terms of the density and perturbation

$$\begin{aligned} \rho_{ex}(t, x) &= \cos(2\pi t)(p_6(\xi)p_6(\eta)) + 2, \\ g_{ex}(t, x, v) &= \cos(2\pi t)(p_6(\xi)p_6(\eta)). \end{aligned} \quad (5.20)$$

The analytic solution at final time is simply $\rho_{ex}|_{t=\frac{1}{4}} \equiv 2$ and $g_{ex}|_{t=\frac{1}{4}} \equiv 0$. The sixth-order polynomial

$$p_6(\xi) = 32(-\xi^6 + 3\xi^5 - 3\xi^4 + \xi^3)$$

is carefully chosen such that its value, and its first and second derivative are zero at the boundary:

$$0 = p_6(0) = p_6(1) = p_6'(0) = p_6'(1) = p_6''(0) = p_6''(1).$$

We add artificial source terms \hat{S}_ρ, \hat{S}_g to the right-hand side of (5.4) and (5.5) such that ρ_{ex}, g_{ex} solve the equation. To observe the correct order of convergence, we need a smoothly varying fiber distribution. Here we use a distribution with increasing anisotropy along the ξ -axis:

$$D_W(x) = \begin{pmatrix} 1 + \xi & 0 & 0 \\ 0 & 1 & 0 \\ 0 & 0 & 1 \end{pmatrix}$$

We set $\delta = 0.1$ and ignore natural growth, i.e., set $\theta = 0$.

■ **Experiment 5.9 — Order of convergence.** We perform convergence tests for every combination of the following choices:

1. MM_{1m}^+ or MM_{2m}^+ ,
2. ith advection $\frac{v}{\delta} = 20$ or without advection $\frac{v}{\delta} = 0$,
3. $\varepsilon = 1, 10^{-1}, 10^{-2}, 10^{-3}, 10^{-5}$.

In each convergence test, we refine the grid five times, starting at 20 grid points and increasing by the factor 1.5 in each step. We compute the L^2 -differences between the numerical solutions and the analytic solution (5.20).

The results are plotted in Figure 5.11. Without the drift $\frac{v}{\delta} = 0$, the first-order code (see Figure 5.11a) shows the expected first-order convergence in the kinetic regime $\varepsilon = 1$ and second-order convergence in the diffusive regime $\varepsilon = 10^{-5}$. In the transition between the regimes, the convergence order increases from one to two. As expected, this increase in order is lost when the drift term is active (see Figure 5.11c) and the convergence order is one for all considered values of ε . We observe second-order convergence for the second-order code without drift, independently of the transport regime (see Figure 5.11b). However, presence of the drift, which is discretized by a first-order method, reduces the order to one (see Figure 5.11d). The second-order code still produces smaller absolute errors than the first-order code. Interestingly, absolute errors for the second-order code are much smaller with $\varepsilon = 1$ compared to all other values of ε .

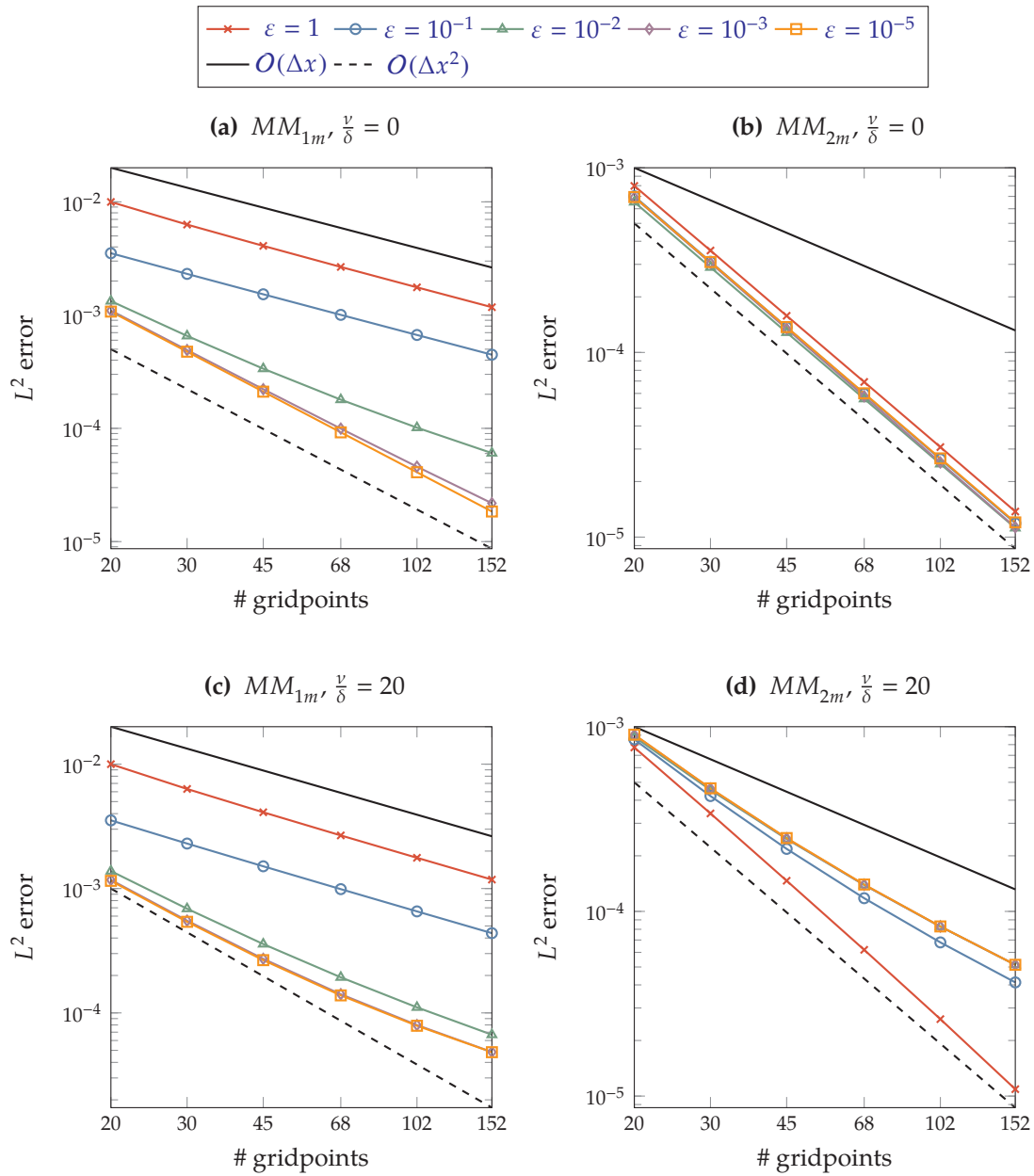


Figure 5.11: Results of Experiment 5.9—order of convergence: L^2 errors at the final time for various values of ε . Left column: first-order scheme. Right column: second-order scheme. Top row: without drift. Bottom row: with drift.

5.4.3 Stencil improvements

Using the line-source benchmark (see Section 4.3.2) we demonstrate the shortcomings of the naive MM_{1m}^\times scheme, which results in a diagonal five-point stencil in the limit.

■ **Experiment 5.10 — Improved stencil.** We compute the $P_1^{(E+)}$ solution for the isotropic line source benchmark, once with the naive scheme MM_{1m}^\times and once with the improved scheme MM_{1m}^+ . The domain $\Omega_x = [-1.5 \text{ mm}, 1.5 \text{ mm}]^2$ is discretized with 100×100 cells. Let $E = \frac{1}{(1)}$, $T = 1 \text{ s}$, $c = 1 \text{ mm s}^{-1}$, and $\lambda_D = 1 \text{ s}^{-1}$. The initial condition is a Gaussian with $\sigma = 0.015 \text{ mm}$.

The initial condition in Experiment 5.10 is concentrated almost entirely on a single cell. In the naive scheme, directly neighboring cells are not coupled, hence the checkerboard pattern in Figure 5.12. The improved scheme does not exhibit this property.

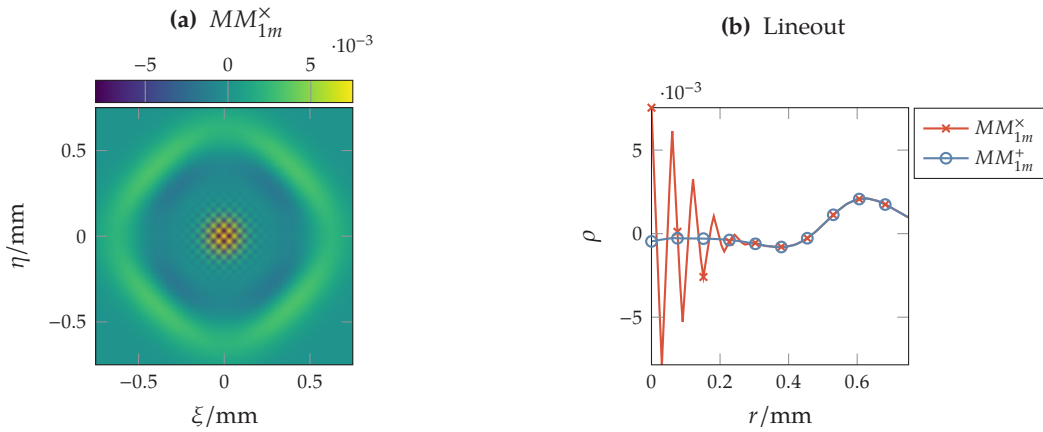


Figure 5.12: Results of Experiment 5.10—improved stencil. Axes are zoomed in. Figure 5.12a: Color plot of ρ for the naive scheme. Figure 5.12b: Line plot along the ξ -axis for both variants of the scheme.

5.4.4 Strong discontinuities in the diffusion coefficients

The coefficients in the glioma model from Section 3.4.2 are estimated from DTI measurements of the brain, which give a water diffusion tensor D_W per voxel. Voxels typically have a length of a few millimeters. On each voxel, the tensor is assumed constant and as such the resulting coefficients jump across the voxel boundaries. Apart from these artifacts, there are genuine jumps in the data when the underlying tissue orientation changes rapidly. Thus, we are interested in the behavior of our scheme in the presence of discontinuous coefficients, especially if ε is small. In the context of flow through porous media, a number of benchmarks with strong jumps in the diffusion coefficient have been developed [43, 118]. We adapt two benchmarks with an analytical solution for our scheme. The first is a special case of a benchmark with discontinuities in permeability at quadrant boundaries from Eigestad and Klausen [43] which we call isotropic quadrants test. The domain is divided into four quadrants of which each is assigned a constant and isotropic permeability. The other test is similar to the 'piece-wise uniform flow' in [43]. It features two domains of constant diffusion tensor with a single discontinuity. But here we align

the discontinuity with the x_2 -axis and choose constant anisotropic diffusion tensors whose main axes meet at an angle at the interface.

Note that the benchmarks are designed for the stationary porous media equation

$$\nabla_x \cdot (D \nabla_x \rho_0) = 0.$$

Our code is neither stationary nor does it solve the porous media equation. If growth and drift are neglected, the code should approximately solve

$$\partial_t \rho_0 - \delta \nabla_x \cdot (\nabla_x \cdot (D \rho_0)) = 0 \quad (5.21)$$

for small ε . However, we can run the simulations for a long enough time T^* , until a steady state is reached and choose ε small, i.e., 10^{-5} . This method is a very inefficient iterative solver for the stationary equation. In the steady state, the choice of δ does not play a role. As a convergence criterion we use the relative L^2 -difference between successive time steps, i.e., we abort the simulation if

$$\frac{\|\rho(t_{i-1}) - \rho(t_i)\|_2}{\|\rho(t_i)\|_2 \Delta t_i} < 10^{-6}.$$

In the benchmarks, we prescribe Dirichlet boundary conditions for ρ according to the exact solution and thermal boundary conditions (5.16) for the micro equation g .

Quadrants with jump in permeability

First, we switch to polar coordinates $(\xi, \eta)^\top = r(\cos(\theta), \sin(\theta))^\top$. The i -th quadrant is then $Q_i = (r, \theta) \in [0, \infty) \times [\frac{i\pi}{2}, \frac{(i+1)\pi}{2})$, for $i = 0, \dots, 3$. On each quadrant, we have a constant isotropic diffusion tensor $D_i = \kappa_i I$. The stationary solution to (5.21) has the form

$$\rho_{0,ex}(r, \theta) = r^\alpha (a_i \cos(\alpha\theta) + b_i \sin(\alpha\theta)) \quad (r, \theta) \in Q_i, \quad (5.22)$$

with coefficients α, a_i, b_i determined by the continuity of the density and the flux at the interfaces. Continuity of the density gives the four conditions

$$\rho_{0,ex}(r, \theta_i^-) = \rho_{0,ex}(r, \theta_i^+),$$

wherein θ_i^\pm mean that the interface at $\frac{i\pi}{2}$ is approached from the left or the right. Continuity of the fluxes translates into the conditions

$$\frac{\partial}{\partial n} D \rho_{0,ex}(r, \theta_i^-) = \frac{\partial}{\partial n} D \rho_{0,ex}(r, \theta_i^+),$$

with

$$\frac{\partial}{\partial n} D \rho_{0,ex}(r, \theta) = \kappa \frac{\partial}{\partial n} \rho_{0,ex} = \alpha r^{\alpha-1} (-a_i \sin(\alpha\theta) + b_i \cos(\alpha\theta)).$$

Here, we used that on each quadrant the coefficients are constant. Altogether we have eight conditions for nine coefficients. We arbitrarily set $a_0 = 1$ and solve for the remaining coefficients numerically.

Similar to [43], we take the permeability κ equal at diagonally opposite quadrants, and set

$$\kappa_0 = \kappa_2 = 100, \quad \kappa_1 = \kappa_3 = 1.$$

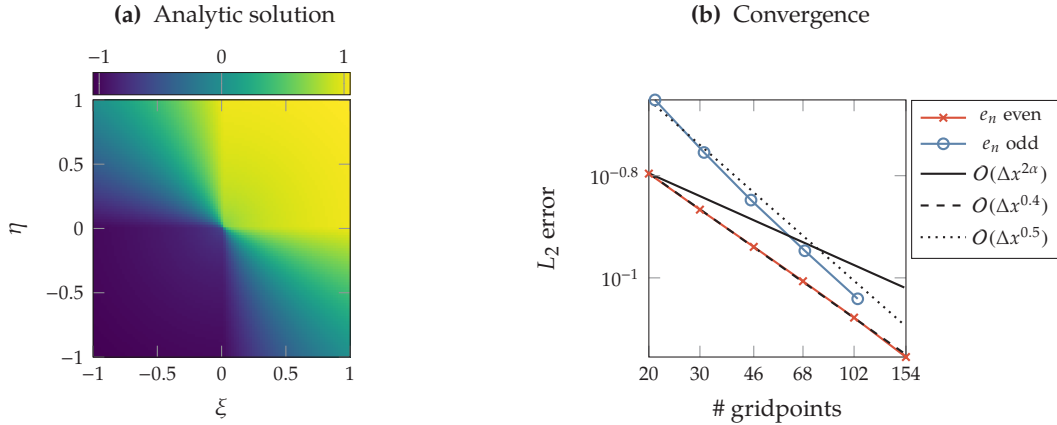


Figure 5.13: Figure 5.13a: Analytic solution for the quadrants benchmark. Figure 5.13b: Results of Experiment 5.11—quadrants benchmark: Convergence of L^2 -error with respect to grid refinement.

The coefficients that belong to this choice are listed in Table 5.1. They are identical to the values reported in [43]. A plot of the analytic solution (5.22) corresponding to these coefficients is shown in Figure 5.13a. Due to the discontinuous permeability, the solution to the diffusion equation only belongs to the fractional Sobolev space $H^{1+\alpha-\nu}$, $\forall \nu > 0$, i.e., it is at most $1 + \alpha$ times differentiable. Therefore, the maximum order of convergence we can expect with respect to grid refinement is 2α .

■ **Experiment 5.11 — Quadrants benchmark.** We perform two grid refinement studies for the quadrants benchmark. In each study, the grid is refined roughly by the factor 1.5, but in the first study, we enforce an even number of grid points per space direction and in the second study we enforce an odd number. The grid sizes are

1. 20, 30, 46, 68, 102 and 154 in the first study, and
2. 21, 31, 45, 69, 105 in the second study.

For each grid size, we compute the L^2 -difference between the MM_{1m}^+ solution of the $P_1^{(E+)}$ model and the analytic solution (5.22).

We plot the L^2 errors from Experiment 5.11 in Figure 5.13. For even grid sizes, we observe convergence with rate 0.4, and for odd grid sizes the order of convergence is even larger—about 0.5. These observed orders are significantly greater than the theoretical order $2\alpha \approx 0.25$. When the number of grid cells per direction is even, the primal edges are aligned with the quadrant boundaries, thus the absolute errors are smaller compared to the next odd-numbered discretization. Due to resource constraints, we consider only coarse grids. The absolute errors are quite large, and we suspect that the correct order of convergence could be observed on finer grids.

Interface with change in diffusion tensor axis

In this test, the diffusion tensor is constant but anisotropic on the left and right half-planes. At the interface—the η -axis—there is an abrupt change in the main direction of diffusion.

i	0	1	2	3
κ_i	100	1	100	1
a_i	1	2.960 396 04	-0.882 756 59	-6.456 461 75
b_i	0.1	-9.603 960 4	-0.480 354 87	7.701 564 88
α	0.126 902 069 721			

Table 5.1: Coefficients for the exact solution (5.22) of the quadrants test.

Let $R(\theta) \in SO(3)$ a rotation around the ζ -axis with angle θ . The diffusion tensor field is parameterized by left and right anisotropies a^L, a^R and left and right angles of main diffusion θ^L, θ^R . For $i \in \{L, R\}$ the diffusion tensor on each quadrant is

$$D^i = \frac{1}{a^i + 2} R^\top(\theta^i) \text{diag}(a^i \quad 1 \quad 1) R(\theta^i).$$

The piece-wise linear function

$$\rho_0(x) = \begin{cases} \rho_0^L = s^L \cdot x, & \xi < 0, \\ \rho_0^R = s^R \cdot x, & \xi > 0 \end{cases} \quad (5.23)$$

is a stationary solution to the diffusion equation (5.21) on each half-plane. For a given left slope s^L , we use the continuity of the solution and normal fluxes at the interface to compute the right slope s^R . Continuity of the solution and normal fluxes translate into equations for the slopes:

$$s_\eta^R = s_\eta^L, \quad s_\xi^R = \frac{1}{D_{\xi\xi}^R} \left(-D_{\eta\xi}^R s_\eta^R + D_{\xi\xi}^L s_\xi^L + D_{\eta\xi}^L s_\eta^L \right).$$

■ **Experiment 5.12** We set the anisotropy factor $a^L = a^R = 2.5$ and left and right angles $\theta^L = 80^\circ, \theta^R = 20^\circ$ and compare the MM_{1m}^+ solution on a 50×50 grid to the analytic solution (5.23).

The numerical solution is to machine precision identical to the analytic solution.

5.4.5 The Fisher-KPP equation

In absence of drift, with isotropic and homogeneous diffusion, and a logistic growth $\mu(\rho) = (1 - \rho)$, the diffusion limit (3.32) is equivalent to the Fisher-KPP equation

$$\partial_t \rho_0 - k \nabla_x \cdot \nabla_x \rho_0 = \theta \rho_0 (1 - \rho_0),$$

with $k = \frac{\theta}{3}$. This equation belongs to the class of diffusion-reaction systems, which are treated exhaustively in [137]. The Fisher equation admits so-called travelling wave solutions, which connect the two steady states of the reaction term: $\rho_0 = 0$ and $\rho_0 = 1$. In a reference frame that moves with the wave, its profile is constant. When the wave front is sharp, there is an approximation for the wave speed in terms of its radius of curvature. In two dimensions, a

ε	1×10^{-5}	parabolic scaling number
δ	0.0008	diffusion time ratio
ν	0	advection time ratio
θ	50	growth time ratio
R_0	0.1	initial front radius
$R(t = 1)$	0.330	final front radius

Table 5.2: Parameters for the Fisher-KPP benchmark.

circular wave front of radius R approximately moves with the speed

$$R' = w - \frac{k}{R},$$

$$w = 2\sqrt{k\theta}.$$

The solution to this ODE with initial condition $R(0) = R_0$ is implicitly given by

$$t = \frac{k}{w^2} \ln \left(\frac{wR - k}{wR_0 - k} \right) + \frac{1}{w} (R - R_0). \quad (5.24)$$

The parameters in Table 5.2 correspond to a situation close to the diffusion limit with a sharp front in the travelling wave. In this situation, the numerical scheme should reproduce a travelling wave solution whose position coincides with the approximation (5.24).

■ **Experiment 5.13 — Fisher-KPP benchmark.** Let $\Delta x_0 := \frac{1}{100}$ and $DSC_0 = 0.2$, which gives the time step $\Delta t_0 = DSC_0 \frac{\Delta x_0^2}{2k} = 9.38 \times 10^{-3}$. We compute the $P_1^{(E+)}$ solution for the parameters given in Table 5.2 with both second-order schemes MM_{2m} and MM_{2i} for each of the following resolutions:

1. Coarse grid Δx_0 , intermediate time step DSC_0
2. Coarse grid Δx_0 , small time step $\frac{1}{4}DSC_0$
3. Medium grid $\frac{1}{2}\Delta x_0$, intermediate time step DSC_0
4. Medium grid $\frac{1}{2}\Delta x_0$, small time step $\frac{1}{4}DSC_0$
5. Fine grid $\frac{1}{4}\Delta x_0$, intermediate time step DSC_0
6. fine grid $\frac{1}{4}\Delta x_0$, small time step $\frac{1}{4}DSC_0$

For the intermediate resolution $\frac{1}{2}\Delta x_0$, DSC_0 we also compute the solution with the MM_{1m} and MM_{1i} schemes.

We display the results of Experiment 5.13 in Figure 5.14. In contrast to the analytic travelling wave solution, the numerical solutions at $t = 1$ are not rotationally symmetric. As an artifact of the regular grid, the wave travels faster along the coordinate directions than diagonal to them. The

speed difference is independent of the time step and the temporal discretization of the reaction terms. It is proportional to the grid resolution, thus with finer grids, the solution becomes more symmetric. The profile of the travelling wave is always the same, no matter which scheme or resolution is used. For the second-order schemes, the difference between explicit and implicit temporal discretization of the reaction terms (MM_{2m} or MM_{2i}) becomes negligible for time steps smaller than $\frac{1}{4}\Delta t_0$. The MM_{1i} solution, however, benefits from the implicit discretization compared to the MM_{1m} solution (see Figure 5.14g). To capture the correct speed of the travelling wave, a small time step has to be used, otherwise the speed is underestimated.

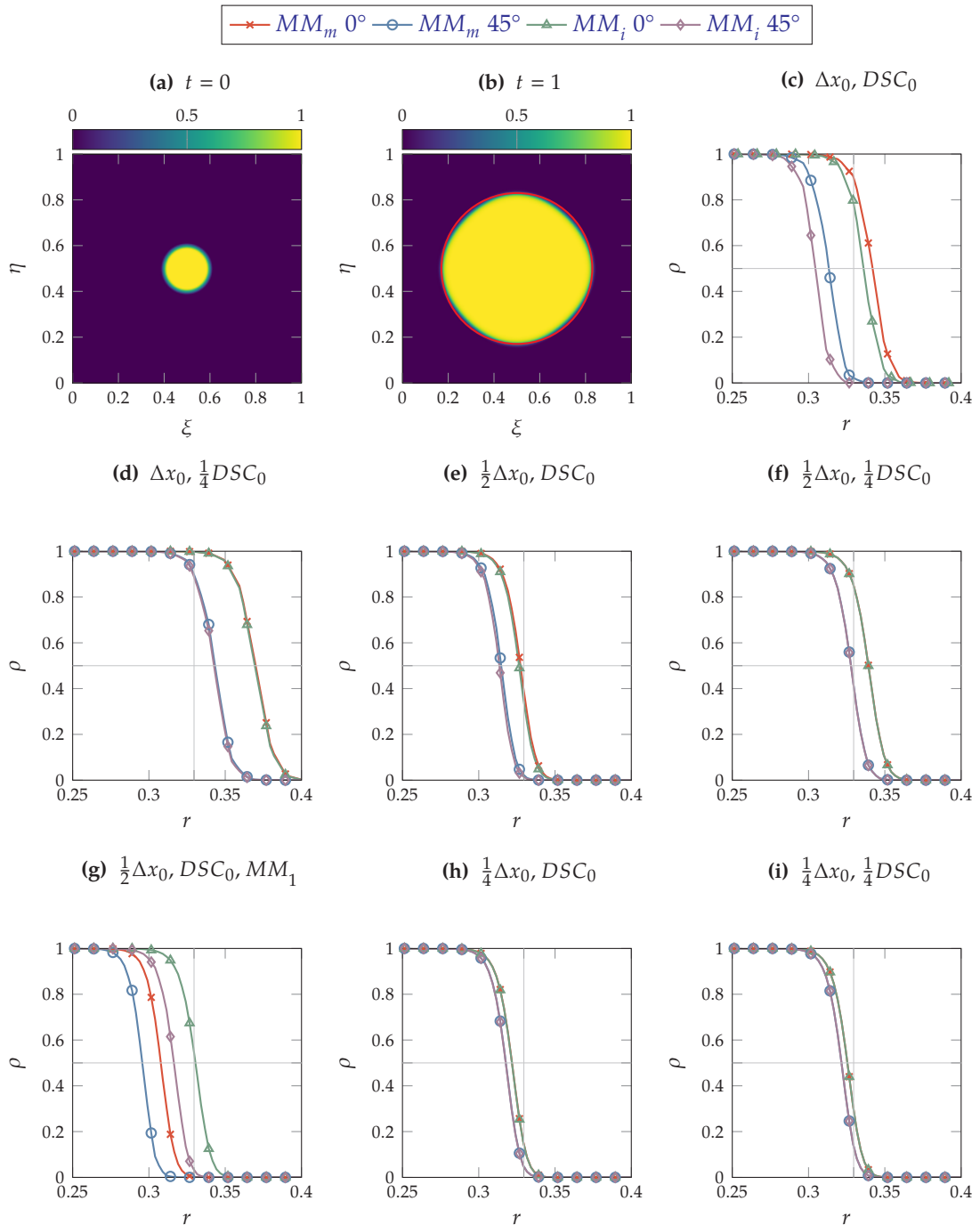


Figure 5.14: Results of Experiment 5.13—Fisher-KPP benchmark. Figure 5.14a: Initial condition, Figure 5.14b: Solution at time $t = 1$ for the MM_{2m} at $\frac{1}{2}\Delta x_0$ and $\frac{1}{4}\Delta t_0$. The red circle indicates the front position of the analytical approximation. Figures 5.14c–5.14i: Line plots of the density. One line is along the ξ -axis and the other at a 45° angle. The plots are zoomed in on the wave position. The gray cross indicates the front position from (5.24). Figure 5.14g: first-order schemes MM_1 .

5.4.6 Stroock's model

We consider the model from Section 3.4.3 with the isotropic kernel $K(v, v') = E(v) = \frac{1}{\langle v \rangle}$. Stroock raised the question, whether the dependence of λ on x or v provides the bacterium with the more 'efficient' means of directed migration. He hypothesized that the v -dependence is the 'better' mechanism, but couldn't prove this conclusively. The following numerical simulations provide some evidence for this intuition.

We take inspiration from an experiment shown in [16]. In the original experiment, *E. coli* are placed on a Petri plate, which contains some uniformly distributed nutrients. Chemotactic interaction between bacteria and nutrients leads to the ring patterns seen in Figure 5.15. The small white spot on the left of the Petri plate in Figure 5.15 is a bacteria population that is insensitive to the nutrients. It therefore serves as a reference to our model computations. The other results are not directly comparable to this setting, in which we prescribe the gradient of a stationary stimulus. Berg [16] mentions that *E. coli* react to non-chemical stimuli, such as temperature or light. In Table 5.3 we list the parameters for the experiment.

On the domain $\Omega_x = [-40 \text{ mm}, 40 \text{ mm}]$, the stimulus is given by $Q(\xi) = 1 + \frac{1}{80 \text{ mm}} \xi$, i.e., its magnitude is one at the center and $\frac{\|\nabla_x Q\|}{X}$ is one. Therefore, we have $\delta = \nu = \frac{c^2 T}{\lambda_0 X^2}$. The scaling number $\varepsilon = 2.65 \times 10^{-4}$ indicates that this situation is already close to the diffusion limit.

The diffusion limit (3.32) for Stroock's model is

$$\partial_t \rho_0 - \nabla_x \cdot \left(\frac{\delta}{3\alpha_x(Q)} \nabla_x \rho_0 - \frac{\nu \beta_v}{3\alpha_x(Q)} \nabla_x \hat{Q} \rho_0 \right) = 0.$$

The advection term in the bracket is a result of the v -dependence of λ . Through the chain rule, the x -dependence introduces effectively another drift vector $\frac{\delta}{3} \nabla_x \frac{1}{\alpha_x(Q)}$.

We compare two different strategies for the bacterium to move in the presence of a stimulus $Q = Q_0 + \nabla_x Q \cdot x$ with constant gradient $\nabla_x Q$:

1. The bacterium adjusts its turning rate according to the activation function $\alpha_x = \frac{1}{Q^p}$. It does not react to the gradient: $\beta_v = 0$. This choice leads to the drift vector $\frac{\delta}{3} \nabla_x \frac{1}{\alpha_x(Q)} = \frac{\delta}{3} p Q^{p-1} \nabla_x Q$ opposite to the gradient.
2. The bacterium detects the gradient, but does not react to stimulus magnitude: $\alpha_v(Q) = 1, \beta_v > 0$.

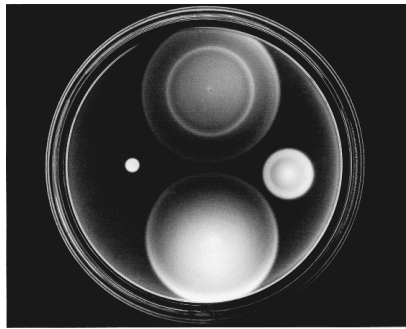


Figure 5.15: A chemotaxis experiment with *E. coli* on a Petri plate. Taken from [16]. For full credits, see the Image Credits at the end of the document.

λ_0	1 s^{-1}	base turning rate
c	2.12 mm s^{-1}	speed
X	80 mm	diameter of the Petri plate
T	28 800 s	eight hours
ε	0.000 265	parabolic scaling number
δ	0.002	diffusion time ratio
ν	0.002	advection time ratio

Table 5.3: Parameters for the Petri plate experiment from [16].

■ **Experiment 5.14 — Stroock’s model.** Using the parameters from Table 5.3, we compute the $P_1^{(E+)}$ solution of Stroock’s model in one space dimension on a grid with 160 cells. The initial condition is a rectangle of width 2 mm in the center of the domain:

$$f(0, \xi, v) = \frac{1}{\langle 1 \rangle} \begin{cases} 1, & |\xi| \leq 1 \text{ mm}, \\ 0, & |\xi| > 1 \text{ mm}. \end{cases}$$

For the first strategy, we compute the model with activation functions $\alpha_x(Q) = \frac{1}{Q}$, $\alpha_x(Q) = \frac{1}{Q^5}$, and $\alpha_x(Q) = \frac{1}{Q^{10}}$. For the second strategy, we compute solutions with $\beta_v = 1$, $\beta_v = 10$, and $\beta_v = 40$. Additionally, the model solution in absence of any stimuli serves as a reference ($\alpha_x(Q) = 1, \beta_v = 0$).

Figure 5.16 shows the results for Experiment 5.14. In absence of any stimulus, the model bacteria only diffuse due to their random changes in direction and the resulting solution is symmetric. Unfortunately, the model does not match with the Petri plate experiment, in which the cell population has a much sharper front. From Figure 5.15, we estimate that the radius of the cluster is about 0.25 cm, at which ρ_0 in the model computation is roughly half of the peak value. In reality, the bacterias’ behavior seems to be governed by more than random tumbling.

The first strategy causes a small drift opposite to the gradient. At the center of the domain, where $Q = 1$, this drift is proportional to the exponent p . Also, the diffusion constant increases along the ξ -axis, thus the right flank of the solution is flatter than the left. The diffusion coefficient at the center is the same for all exponents. At $p = 1$ the drift magnitude is too small to have any visible effect, but we see the increased diffusion to the right. To achieve a visible drift, we have to increase p to 10, which also means the right flank is much flatter. Concerning directed motion, this strategy is ambiguous. Although the right flank diffuses faster, the bulk of cells moves slowly to the left. As Stroock [127] already remarked, to increase directed motion in this way, one has to allow the turning rate λ to become large in negative ξ -direction.

In contrast, a dependence of λ on orientation introduces a drift term which scales linearly with β_v . With $\beta_v = p$, the second strategy achieves the same drift magnitude as the first strategy, but in opposite direction. The second strategy enables the bacteria population to move up the stimulus gradient. Note that due to the first-order discretization of the drift and the relatively coarse grid,

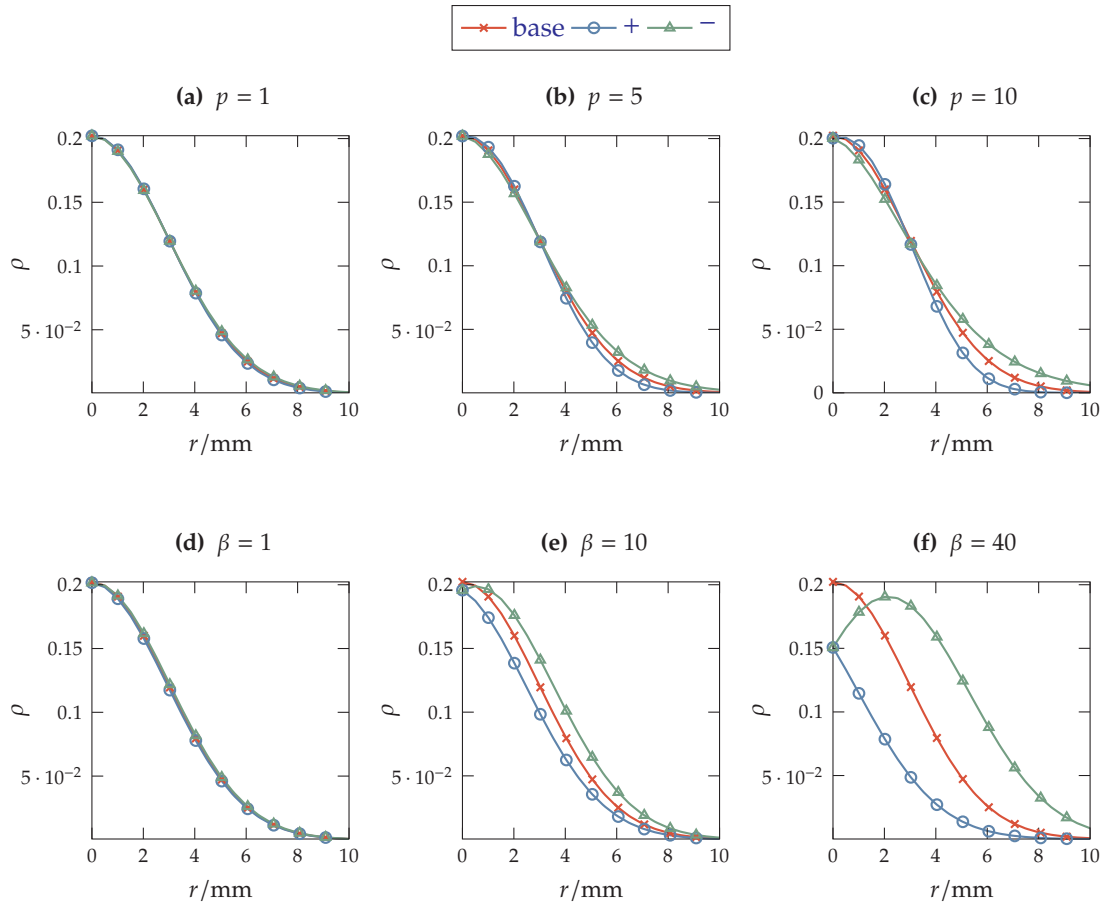


Figure 5.16: Results of Experiment 5.14—Stroock’s model. Top row: strategy 1. Bottom row: strategy 2. In each figure, the solution in the positive half (+), the solution in the negative half (−) and the symmetric solution without stimuli (base) are plotted.

there is some numerical diffusion visible in the solution with $\beta_v = 40$.

5.4.7 The glioma model with DTI data from a human brain

To demonstrate the full capabilities of the scheme, we compute the [EHKS model](#) of glioma invasion in the human brain (see Section 3.4.2).

The water diffusion tensors $D_W(x)$ for all computations come from the open source Camino [DTI data set](#) [30]. The data set has $112 \times 112 \times 50$ cubic voxels with side length 2 mm, therefore the three-dimensional domain is $\Omega_x = [0 \text{ mm}, 224 \text{ mm}] \times [0 \text{ mm}, 224 \text{ mm}] \times [0 \text{ mm}, 100 \text{ mm}]$. To avoid interpolation artifacts, we align the spatial discretization with the data mesh. With one exception, all computations are performed with the reduced two-dimensional version (see Section 1.1.2) of the glioma model on the slice of the Camino data visualized in Figure 2.3.

In the previous experiments, we chose a constant λ_H . Recall the derivation of the glioma model

	set A [47]	set B [35]	
c	$2.1 \times 10^{-4} \text{ mm s}^{-1}$	$1.39 \times 10^{-5} \text{ mm s}^{-1}$	cell speed
λ_0	0.8 s^{-1}	0.1 s^{-1}	base turning rate
λ_1	10 s^{-1ab}	10 s^{-1}	slope of turning rate
k^+	0.1 s^{-1}	0.0342 s^{-1}	cell-ECM binding rate
k^-	0.1 s^{-1}	0.01 s^{-1}	cell-ECM unbinding rate
μ	$8.44 \times 10^{-7} \text{ s}^{-1}$	$2.6 \times 10^{-7} \text{ s}^{-1}$	net growth rate
ε	1.2×10^{-6}	6.2×10^{-7}	parabolic scaling number
δ	6.9×10^{-5}	2.4×10^{-6}	diffusion time ratio
ν	8.7×10^{-4}	2.4×10^{-4}	advection time ratio
θ	53	16.4	growth time ratio
Ξ	0.7	0.9	parabolic-hyperbolic blending

^aOur λ_1 corresponds to the product $R_0\lambda_1$ in [47], with R_0 the number of receptors per cell. Because R_0 only occurs as a weight for the advection, we include it directly in λ_1 .

^bIn [47], λ_1 (including R_0) has been estimated as 1000 s^{-1} .

Table 5.4: The reference parameters and the resulting characteristic numbers used in the simulations of glioma invasion in the human brain.

in Section 3.3.2 and the equation (3.19) for λ_H . Here, we choose

$$\lambda_H = \frac{\lambda_1}{\alpha + \lambda_0} \frac{\partial y^*}{\partial Q} = \frac{\lambda_1}{k^+Q + k^- + \lambda_0} \frac{k^-}{(k^+Q + k^-)^2}$$

in accordance with the EHKS model [36, 44]. Note that equation (3.19) contains the additional summand μ in the first denominator, which we neglect here. In the considered parameter sets, however, μ is negligible in comparison to k^+ and k^- . We estimate the volume fraction of fibers Q with the FA index (2.1):

$$Q(x) = FA(D_W(x)).$$

In all following experiments, we simulate the tumor growth over the time span T of two years. The initial tumor mass at position $x_0 = (90 \text{ mm}, 90 \text{ mm}, 60 \text{ mm})^\top$ is given by a Gaussian with standard deviation $\sigma = 1.4 \text{ mm}$, which is normalized to $\rho(x_0) = 0.1$. The tumor starts in equilibrium, i.e., $g(0, x) = 0$ everywhere. We are not interested in absolute values of ρ but rather in the ratio $\frac{\rho}{\rho_{cc}}$ and therefore set the carrying capacity for logistic growth to one in the computations.

Estimates for the parameters in this model vary wildly in the literature. In Table 5.4 we show the parameters from [47] and [35] side by side. With the currently available clinical data it is not possible to validate any set of parameters.

In the next experiment we investigate the influence of model parameters on the predicted tumor shape qualitatively.

■ **Experiment 5.15 — Glioma parameter study.** We compute the $P_1^{(E+)}$ solution of the glioma model with the MM_{1m}^+ scheme for these parameter sets (see Table 5.4):

I: set A,

II: set B,

III: set A, but with μ from set B,

IV: set B, but with c from set A,

V: set B, but with c, k^+, k^- from set A.

Additionally, we compute the Fisher approximation (5.24) for each parameter set.

In Figure 5.17 we display the tumor densities for the computations from Experiment 5.15 together with the Fisher approximation. With the parameters from sets A and B, the tumor essentially evolves like a traveling wave in the fisher equation. The cell density ρ inside the tumor is almost stationary. It fluctuates slightly around the carrying capacity $\rho_{cc} = 1$ of the logistic growth due to advection. The set A parameters result in an almost isotropic spread, because the relatively large growth term evens out the anisotropic diffusion and drift. The discretization is coarse: the 60 mm by 60 mm section of the domain shown in Figure 5.17 has only 30×30 grid cells. As seen in Experiment 5.13, the scheme has trouble to approximate the travelling waves correctly. The wave speed is larger parallel to the axis directions, which results in an artificial anisotropy. Further, in this situation, the scheme overestimates the Fisher speed generally. Both problems could be cured with a finer spatial resolution, which comes at the cost of interpolation artifacts in the diffusion tensors (see Experiment 5.18). When the growth constant is reduced (set III), the tumor spread is slower and more irregular. The tumor front is also flatter, thus the numerical scheme has no problems to produce the correct front speed in this situation. In set B, the drift is faster (due to decreased k^+, k^-), but growth and diffusion are slower compared to set A. We observe a preferred tumor growth along the central vertical fiber tract. When we increase the speed in set B, we are in a situation with fast diffusion and drift, but relatively slow growth. Thus, in the results for set IV, we observe a highly anisotropic tumor with a strong preference to grow along the white matter tracts. Due to the drift, the cell density ρ exceeds the carrying capacity ρ_{cc} by a large margin. It is unclear how to interpret cell densities above the carrying capacity. On the one hand, we could interpret the carrying capacity as the maximum number of cells that physically fit into a given volume. Then, a density above ρ is clearly unphysical. We would have to limit the drift velocity in the model to prevent cells from moving into already full regions. On the other hand, we could argue that cell proliferation stops well before the volume is filled to capacity. In this case, $\rho > \rho_{cc}$ is allowed, and ρ_{cc} is just an arbitrary reference scale for the cell density. We see the effect of the receptor dynamics by comparing results for sets IV and V. The difference between these situations is the choice of binding and unbinding rate k^+, k^- . In set V, the resulting λ_H is smaller compared to set IV. As a result, the tumor is shaped more regularly and does not exceed the carrying capacity as much.

In light of the considerations in Chapter 2, the glioma model that we consider here is very simple.

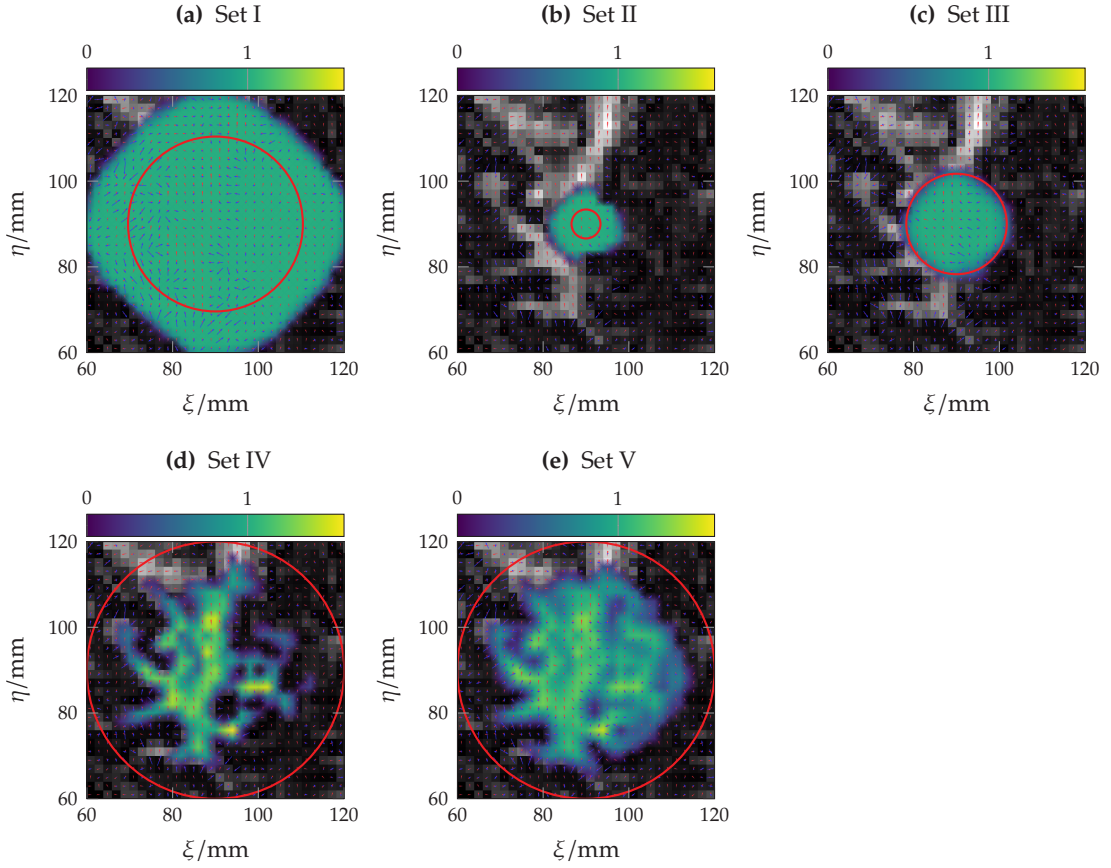


Figure 5.17: Tumor density ρ in the glioma model with the parameter sets from Experiment 5.15—glioma parameter study. Red contour: The Fisher approximation. Grayscale image: Fractional anisotropy $FA(D_W)$. Red arrows: Main axis of D_W . Blue arrows: Drift vector a in the limit equation.

Nevertheless, we observe a wide range of predicted tumor shapes, which depend strongly on the model parameters. To formulate mathematical models that are useful in patient-specific therapy, future efforts should be concentrated on parameter identification and model validation. Important open questions are: How much do the parameters vary from patient to patient? If the parameters vary, how can we estimate them from the medical data? How can we obtain enough data for model validation?

The values of ε in Table 5.4 indicate that the situation is close to the diffusion limit. We show the influence of ε on the solution in the next experiment.

■ **Experiment 5.16 — Parabolic scaling.** We compute the $P_1^{(E+)}$ solution of the glioma model with the MM_{1m}^+ scheme, using parameter set III from Experiment 5.15. We perform the same computation with artificially changed values for $\varepsilon = 10^{-3}, 10^{-4}, 10^{-5}, 10^{-10}$. The physical parameters in these computations are chosen according to (3.30) such that the remaining parabolic scaling parameters δ, ν, θ are constant.

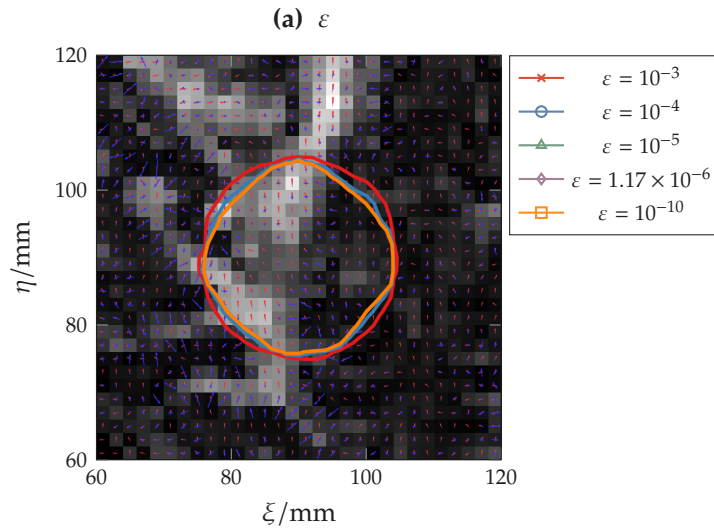


Figure 5.18: Results for Experiment 5.16—parabolic scaling: influence of ε . Shown are the 10% contour lines of the tumor density ρ . Grayscale image: fractional anisotropy $FA(D_W)$. Red arrows: main axis of D_W . Blue arrows: drift vector a in the limit equation.

In Figure 5.18 we show the 10% contours of the tumor density ρ for the results of Experiment 5.16. The contours for the $\varepsilon = 10^{-10}$, $\varepsilon = 1.17 \times 10^{-6}$, and $\varepsilon = 10^{-5}$ solutions lie on top of each other. Thus, the parameters describe a situation well within the diffusive regime. For practical purposes, the meso-scale description does not add any useful information to the macroscopic model. At $\varepsilon = 10^{-4}$, two orders of magnitude larger than the natural value, small deviations from the diffusion limit are visible. This value of ε corresponds to the cell speed $c \approx 2.4 \times 10^{-6} \text{ mm s}^{-1}$, which is about a hundredth of the original value, and turning rates $\lambda_0 \approx 1.1 \times 10^{-4} \text{ s}^{-1}$, $\lambda_1 \approx 1.4 \times 10^{-3} \text{ s}^{-1}$ approximately one thousandth of the original rates. Thus, the kinetic model could be relevant for cell species that migrate slowly and change their orientation rarely (in this example once every 150 minutes). At $\varepsilon = 1 \times 10^{-3}$, the contour distance to the diffusive model is roughly the length of one voxel. Further away from the diffusion limit, the invasion front is faster because individual cells have a higher chance of overtaking the diffusive invasion front.

Finally, we investigate the influence of the moment order, the numerical scheme and the space dimension onto the solution.

■ **Experiment 5.17 — Choice of moment order, scheme, and space dimension.** We start with the parameters from set III in Experiment 5.15 and compute

1. the $P_1^{(E+)}$ and $P_3^{(E+)}$ approximations of the glioma model with the MM_{1m}^+ scheme,
2. the $P_1^{(E+)}$ and $P_3^{(E+)}$ approximations of the glioma model with artificially increased $\varepsilon = 10^{-3}$ with the MM_{1m}^+ scheme,
3. the $P_1^{(E+)}$ glioma model with the MM_{1m}^+ , MM_{1i}^+ , MM_{2m}^+ , and MM_{2i}^+ schemes,
4. the $P_1^{(E+)}$ glioma model with the MM_{1m}^+ scheme on the full three-dimensional domain.

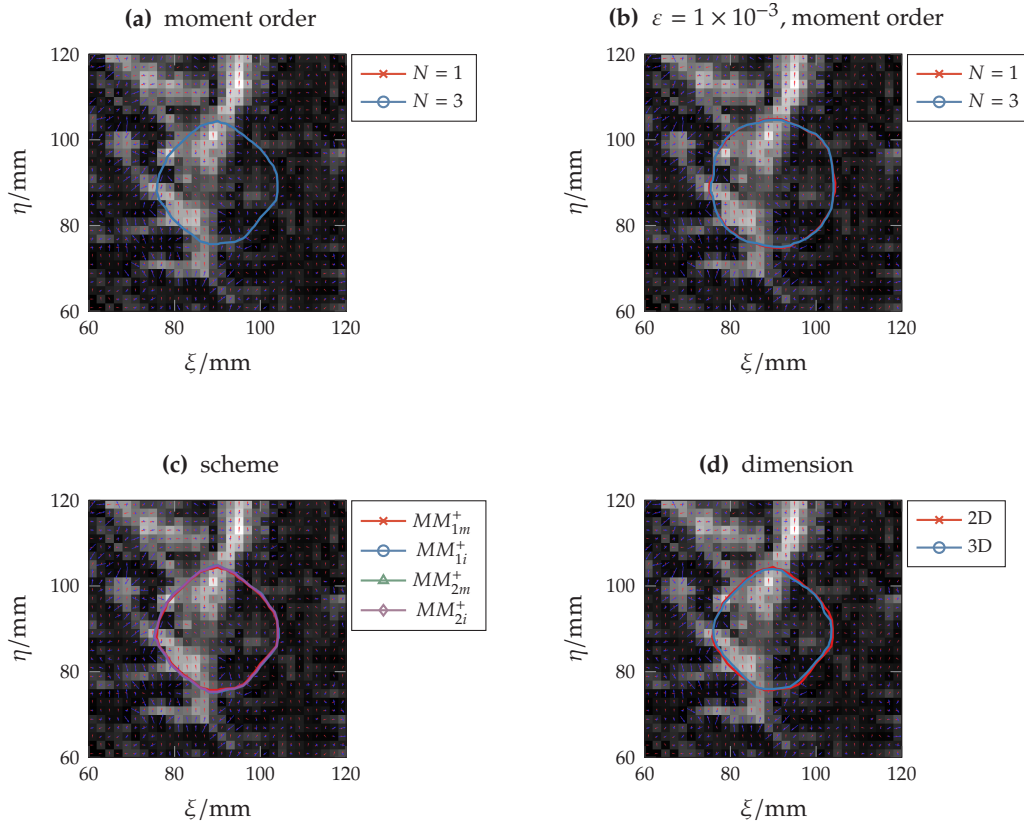


Figure 5.19: Results for Experiment 5.17—choice of moment order, scheme, and space dimension. Shown are the 10% contour lines of the tumor density ρ . Grayscale image: fractional anisotropy $FA(D_W)$. Red arrows: main axis of D_W . Blue arrows: drift vector a in the limit equation.

Results for Experiment 5.17 are displayed in Figure 5.19. The moment models of any order converge to the diffusion limit, thus for the chosen parameters, the first-order model $P_1^{(E+)}$ is sufficient. Even if we artificially set $\varepsilon = 10^{-3}$, the $P_3^{(E+)}$ solution deviates from the $P_1^{(E+)}$ solution by much less than a millimeter. The choice of scheme only has a minuscule impact on the solution. Finally, we compare the solution of the two-dimensional model with a slice of the three-dimensional model. The contour distance is less than a voxel everywhere. Thus, the reduced two-dimensional model, which needs less resources to compute, is accurate enough to explore the parameter space. We repeated Experiment 5.17 with parameter set V, without observing anything new.

In Experiment 5.15 the grid resolution Δx is chosen to match the data resolution Δx_{DTI} . Due to the coarse discretization, for some parameters (set I, set II) the scheme introduces artificial anisotropy and overestimates the speed of travelling waves. In the next experiment we choose a finer grid to overcome these problems.

■ **Experiment 5.18 — Grid refinement and interpolation artifacts.** We refine the grid such that each voxel of the Camino data set is discretized with 4×4 grid cells. The grid resolution is thus $\Delta x = 0.5$ mm. We map the water diffusion tensors D_W , which are piece-wise constant in the

Camino data, onto the fine grid. The mapping is done for each tensor component individually. We consider two choices:

1. A smoothed mapping $D_W(x) = \sum_i w(x - x_i)D_W(x_i)$ with a Gaussian kernel w with standard deviation $\sigma = 1.2\Delta x_{DTI}$.
2. A linear interpolation by first-order B-splines.

We compute the MM_{1m}^+ solution of the $P_1^{(E+)}$ glioma model with parameter sets I and V (see Experiment 5.15) for each mapping.

We show the results of Experiment 5.18 in Figure 5.20. The 60 mm by 60 mm section of the domain shown in Figure 5.20 is now discretized with 120×120 grid cells. In the computation with the set I parameters, the artificial anisotropy is greatly reduced compared to the computation on the coarse grid. The speed of the travelling wave is captured adequately. The set I parameters correspond to an almost isotropic growth with little drift. Therefore, the choice of mapping does not influence the tumor shape much. However, in the 100 % contours, the mapping artifacts are visible. The parameter set V corresponds to an anisotropic finger-like spread, in which the drift plays a large role. Because the drift depends on $\nabla_x Q$, which depends on D_W , the mapping has a significant impact on the tumor shape. To find a natural mapping procedure for diffusion tensors is an interesting problem in its own right, which we do not discuss further. But note that both mappings considered in this experiment are chosen arbitrarily. Especially the component wise interpolation of tensors is questionable.

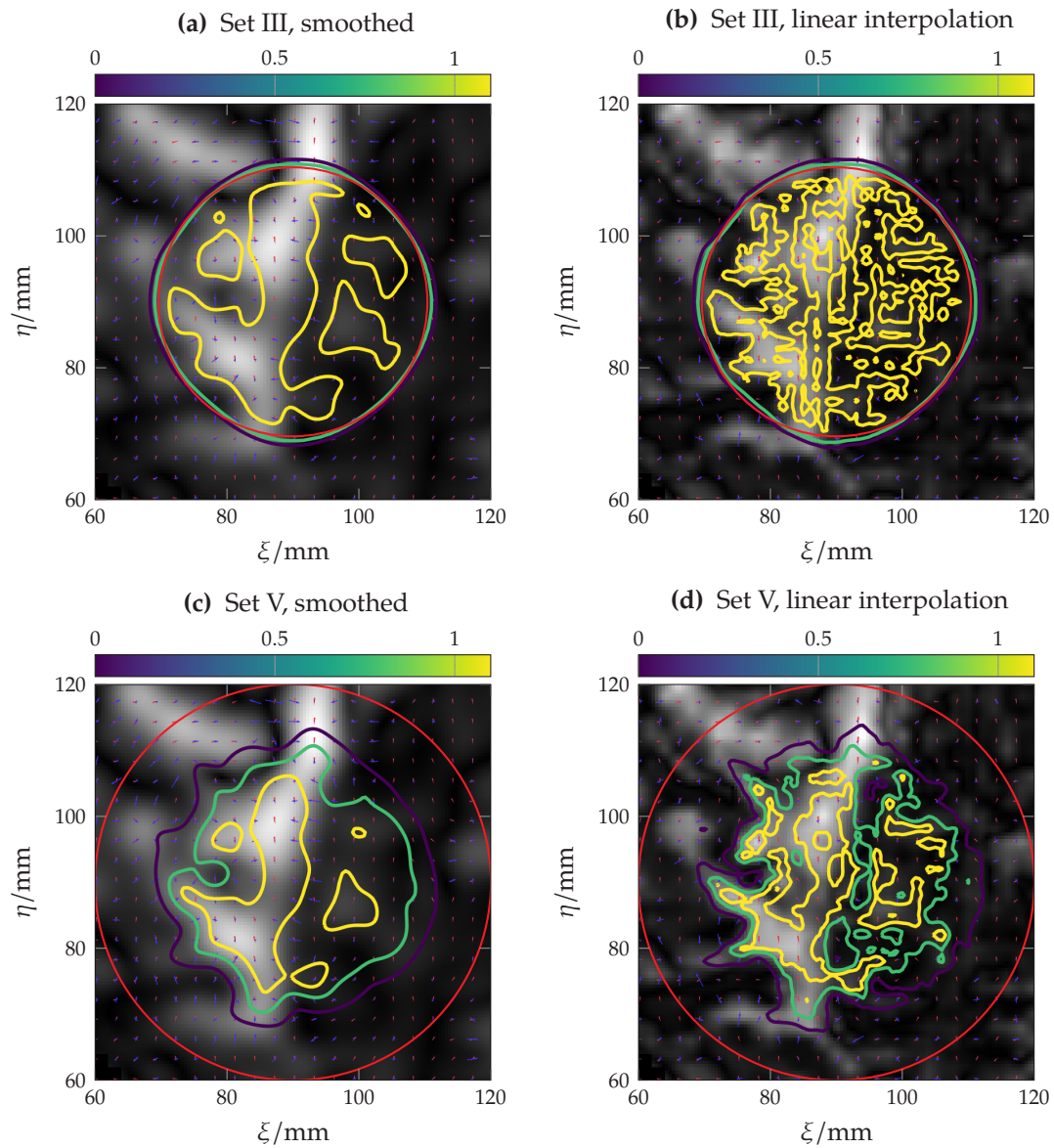


Figure 5.20: Results for Experiment 5.18—grid refinement and interpolation artifacts. Top row: set I. Bottom row: set V. Left column: gaussian smoothing. Right column: linear interpolation. Shown are the 10%, 50%, and 100% contour lines of the tumor density ρ . Red contour: The Fisher approximation. Grayscale image: Fractional anisotropy $FA(D_W)$. Red arrows: Main axis of D_W . Blue arrows: Drift vector a in the limit equation.

6

Conclusions

To improve cancer therapy by predictive mathematical models is a task that requires insights from many disciplines to be brought together, including biology, medicine, and theoretical and applied mathematics. Although the focus of this thesis lies on the development of numerical methods for meso-scale glioma models, we did not ignore the wider context.

Two fundamentally different levels of description for glioma invasion have to be taken into account: The macroscopic shapes and growth patterns observed in clinical practice are caused by microscopic interactions of glioma cells with their environment. Ultimately, a prediction of the macroscopic shape of the tumor invasion margin is needed in therapy. A multi-scale model carries averaged information about the small-scale behavior of individual cells to a macroscopic description. In Chapter 2 we gave an overview on the intricate microscopic processes involved in tumor growth. Compared to the complexity of tumor cells the reviewed mathematical models are incredibly simple. However, patient specific models are only useful if the required input data is readily available. The [EHKS model](#) at the center of this thesis [44, 46] concentrates on the interaction of individual cells with the [ECM](#) fibers in white matter. Coarse estimates for this directed structure can be obtained from routinely performed [DTI](#), which yields a water diffusion tensor in each voxel of the three-dimensional image. It is tempting to include further effects into the model, though even for the presented model there is not enough clinical data for validation and parameter identification. We demonstrated that the uncertainties of parameters in the literature lead to widely differing predictions for the tumor shapes. Beyond that, we did not make further attempts at parameter identification.

In Chapter 3 we reviewed the [EHKS model](#) [44] in detail and made all model assumptions explicit. The subcellular and particle level descriptions of cell-[ECM](#) interactions are constructed with the resulting macroscopic model in mind. For example, the receptor binding dynamics are approximated by simple mass action kinetics. Many assumptions on the particle level are coarse from the perspective of a single cell. Especially the assumption of free linear movement interspersed with random and uncorrelated turning events is better suited to describe movement of bacteria than glioma cells. A much more detailed description of a glioma cell's internal structure and the resulting forces is provided by Uatay [133]. However, in the limit, both approaches lead to an advection-diffusion type equation. Thus, we justified most assumptions in the [EHKS model](#) by their simplicity and incorporated important experimentally observed phenomena phenomenologically. Indeed, contact guidance, the cells' preference to move along directed fibers, and gradient detection, are explicitly built into the turning operator on the meso-scale. A modeling choice appropriate for the diffuse invasion margin of the tumor, but not so much for the dense tumor center, is to neglect cell-cell interactions completely.

From the full mesoscopic description including the cell's receptor state, one can pass directly to a macroscopic limit, as in [44]. Alternatively, one can make an intermediate step and derive a simplified kinetic equation by averaging over the receptor state. In this thesis we concentrated on the simplified meso-scale model and its generalizations. In any case, the crucial assumption is that the receptor state equilibrates rapidly compared to the other effects, such that the moments with respect to activity decay rapidly. We showed that the decay of moments, and therefore the validity of the assumption, depends on the choice of parameters and on the proliferation model. For typical glioma parameters and an appropriate proliferation kernel, the activity moments decay fast enough to justify the zeroth-order approximation.

With the simplified meso-scale glioma model as a prototype, we derived a general class of kinetic equations: the so-called haptotaxis equation. Stroock's model for directed movement of *E. coli* [127] is another example that fits into this structure. In contrast to the classical kinetic equations from radiative transfer, the turning operator has an anisotropic equilibrium. Additionally, there is another kernel-integral operator that acts as a perturbation on the turning operator. We identified the necessary structure for this equation such that it converges to a reaction-diffusion-advection equation in the parabolic limit. As some assumptions were made purely for convenience, further generalizations may be possible.

In a moment model, the angular variable in the particle distribution is approximated by a system of equations for the moments. The quality of this approximation depends on the specific parameters and setting, the number of moments and the choice of moment closure. Generally speaking, in more diffusive settings, fewer moments are needed than in free-streaming situations. Therefore, even the first-order moment methods should at least be able to approximate the correct diffusion limit. We demonstrated that the classical first-order moment models, however, fail to capture any information about the anisotropic equilibrium in the haptotaxis equation. Hence, they do not converge to the same diffusion limit as the kinetic equation.

The turning operator in the kinetic equation relaxes the particle distribution onto its equilibrium state. This relaxation is controlled by the dissipation of entropy. In the classical kinetic theory, the isotropic equilibrium minimizes the classical entropy. When the equilibrium is anisotropic, it makes sense to consider another entropy which is minimized by this anisotropic equilibrium. We constructed a modified entropy based on the concept of relative entropy [132], which was originally introduced to study the limit of hyperbolic relaxation systems. For the Maxwell-Boltzmann entropy relative to the equilibrium, we proved a local entropy dissipation law for the haptotaxis equation.

Minimum entropy closures carry the entropy dissipation law for the kinetic equation over to the moment system. We adapted this theory for the modified entropy and derived modified linear and exponential minimum-entropy models in analogy to their classical counterparts. The physical relevance of the Maxwell-Boltzmann entropy for glioma is unclear, but the resulting ansatz function is at least always positive. We also included the modified additive linear moment closure in this framework, although it is based on a quadratic entropy function, for which we did not prove the entropy dissipation law. In contrast, the multiplicative linear closure, which was originally proposed in [36] as an ad hoc modification, does not fit in this minimum-entropy theory.

To investigate the moment methods numerically, we implemented a second-order scheme with

splitting between fluxes and reactions. The fluxes are discretized by a standard finite-volume method with minmod limited second-order reconstruction in characteristic variables, and updated with a second-order Runge-Kutta method in time. The reactions reduce to an ODE for the evolution of the cell mean over time in each grid cell, which is solved by a stiffly accurate DG¹ method. The scheme is well-suited for a kinetic to intermediate regime, but in the diffusive regime it suffers from severe restrictions on the spatial and temporal resolution. For an optically thick discretization, the scheme is dominated by numerical diffusion. Thus, to approach the diffusion limit, one would have to refine the grid indefinitely. The computation with typical glioma parameters is entirely infeasible with this direct scheme. We therefore considered kinetic to intermediate transport regimes in our numerical experiments to compare modified and classical moment methods for the haptotaxis equation. Although no analytic solution exists for the anisotropic version of the line source test, it still unveils the structure of the moment methods nicely. The structural difference between the modified moment methods and their classical counterparts becomes most apparent for low moment orders. The modified models encode the equilibrium distribution directly into the fluxes. Thus, with the peanut distribution, the resulting waves in the line source test have an ellipsoidal form. In the lower-order moment methods this modification is the most pronounced. In the higher-order models, the slower waves are modified the most, whereas the fastest waves are barely modified at all. The classical higher-order moment models can reproduce the anisotropic equilibrium, even though it is not explicitly included. The peanut distribution is essentially a second-order polynomial, therefore the third-order classical ansatz should be able to reproduce the correct diffusion limit. In this case, the benefit of the modified ansatz compared to the classical ansatz vanishes. It would be interesting to see how the modified methods perform compared to the classical methods if the equilibrium cannot be approximated by a low-order polynomial.

As a small model extension, we implemented a model for proteolytic degradation of tissue. Because the fiber layout changes over time, so does the equilibrium distribution. The peanut distribution can be interpreted as a second-order polynomial ansatz for the fiber distribution, hence a second-order linear moment model for the fiber dynamics is natural. The result is a coupled system for the particle moments and fiber moments.

To compute the kinetic glioma model with realistic parameters, we developed an asymptotic-preserving scheme for the haptotaxis equation. As a starting point for our scheme, we used the method developed by Lemou and Mieussens [96]. This scheme employs a micro-macro decomposition and discretizes the microscopic and macroscopic components on different parts of a staggered grid. Here, we generalized the method to an asymptotic preserving finite-volume formulation on primal-dual mesh pairs that works in two and three space dimensions. In the description of the method, we used a mostly mesh-agnostic notation because we are confident that it is also applicable on unstructured meshes. Most parts of the implementation in DUNE [7] are already written mesh-independently, but a complete implementation exists only for tensor-product grids. Development and testing of the unstructured implementation are left for the future.

To discretize the velocity space in the micro equation, we employed the method of moments. More specifically, we used spherical harmonic basis functions and a linear reconstruction ansatz.

¹discontinuous-Galerkin

The resulting moment system is equivalent to the linear additive minimum-entropy method. In the diffusive regime, first-order basis polynomials are accurate enough, which means that only one degree of freedom per space dimension is needed. Compare this to the discrete ordinates method, that needs at least two degrees of freedom per space dimension to maintain symmetry. For successively less diffusive regimes, higher moment orders can be added as needed. Of course, in the kinetic regime the linear moment method has the usual drawback of producing unphysical Gibb's phenomena. But this is not a problem in the diffusive regime.

For asymptotic preserving methods, one special point of interest is the resulting discretization in the parabolic limit. Analytically, we computed the limit diffusion and drift approximations for a simplified setting, a regular grid with constant and isotropic coefficients, and identified two drawbacks of the basic method. First, the limit diffusion approximation is a five-point diagonal stencil that leads to a decoupling of grids and spurious oscillations. The same effect is also described in [22] and seems to be a general problem for primal-dual discretizations. We altered the basic method and modified the limiting discretization of the diffusion and drift terms. In effect, this led to the classical five-point stencil for the diffusion and an upwind approximation of the drift. However, the drift discretization comes at the price of being inherently first-order accurate.

The implementation was developed specifically for the [EHKS model](#), and we took advantage of the simplifications it offers compared to the general haptotaxis equation, for example that the turning operator is explicitly invertible or that the equilibrium distribution is a quadratic form. But probably the most significant factor in the method's development were the associated data. [DTI](#) data are measured and delivered on regular grids with fixed spatial resolution. On each grid cell, the water diffusion tensor is assumed constant, because there is no natural way to interpolate between those tensors. To avoid interpolation artifacts in the solution, the space discretization has to use the same grid as the original data. As a consequence, we implemented the method for tensor-product grids only. In the method's development we had to respect the strong heterogeneities and discontinuities in the [DTI](#) data.

Instead of further analysis of the scheme on paper, we investigated the method's properties numerically in a wide range of benchmarks. The fundamental solution test demonstrates that the method indeed is asymptotic preserving and in the limit converges with the correct order to the fundamental solution. Moreover, we used this benchmark to estimate properties of the modified equation of the scheme. Of special interest is the behavior of the method in presence of strong discontinuities as encountered in the [DTI](#) data. For this, we adapted two stationary benchmark tests from the porous media community. The scheme deals well with strong jumps in permeability and accurately resolves interfaces with an abrupt change in the diffusion direction. An approximate circular travelling wave solution to the Fisher-KPP equation served as a benchmark for the instationary part of the scheme. We saw that the scheme resolves the travelling waves with increasing accuracy for refined grids. On coarse grids, however, an artifact of the regular grid becomes apparent as the numerical solution is not rotationally symmetric and travelling waves move faster along the coordinate axes.

We applied the [AP](#) scheme to Stroock's *E. coli* model in one dimension. Stroock posed the question, whether klinokinesis or klinotaxis provide the bacteria with the more efficient means to detect stimulus gradients. The simulations support Stroock's hypothesis that klinotaxis, i.e.,

the dependency of the turning rate on direction, is the better mechanism.

Last but not least we demonstrated the capabilities of the [AP](#) method on the [EHKS model](#) for glioma invasion. Although the parameters are rough estimates, the overall situation is similar to the application. The method performs mostly well on the coarse and heterogeneous real-world [DTI](#) data. However, for some parameter sets the approximation quality of travelling waves suffers from the coarse spatial discretization dictated by the [DTI](#) data.

The parameters in both application contexts are in a diffusive regime. We showed experimentally that the kinetic model does not add useful information compared to the limit equation. In practice, we recommend using a dedicated numerical scheme for the limit equation instead. Let us just mention the [MPFA](#) method here as one example. Due to its origins in porous media applications, it is designed to work with highly anisotropic and heterogeneous coefficients.

A

Calculation details

A.1 Notation for vector and matrix calculus

By default, all vectors are column vectors. Given two vectors $v, w \in \mathbb{R}^n$, the dot product is to be understood as

$$v \cdot w := v^\top w = \sum_{i=1}^n v_i w_i.$$

The tensor product vw^\top of two vectors $v \in \mathbb{R}^n, w \in \mathbb{R}^m$ is an $\mathbb{R}^{n \times m}$ matrix with entries $v_i w_j$. For a function $f : \mathbb{R}^d \mapsto \mathbb{R}$, the gradient

$$\nabla_x f(x) = \begin{pmatrix} \frac{\partial f}{\partial x_1} \\ \vdots \\ \frac{\partial f}{\partial x_d} \end{pmatrix} \in \mathbb{R}^d$$

is a column vector but the derivative

$$\frac{\partial f}{\partial x} = \left(\frac{\partial f}{\partial x_1} \quad \dots \quad \frac{\partial f}{\partial x_d} \right) \in \mathbb{R}^{1 \times d}$$

is a row vector. The divergence of a vector field $v : \mathbb{R}^d \mapsto \mathbb{R}^d$ is denoted

$$\nabla_x \cdot v(x) = \sum_{i=1}^d \frac{\partial v_i}{\partial x_i} \in \mathbb{R}.$$

For the divergence of tensor field $A : \mathbb{R}^d \mapsto \mathbb{R}^{d \times n}$, we write

$$\nabla_x \cdot A(x) = \begin{pmatrix} \sum_{i=1}^d \frac{\partial A_{i1}}{\partial x_i} \\ \vdots \\ \sum_{i=1}^d \frac{\partial A_{id}}{\partial x_i} \end{pmatrix} \in \mathbb{R}^n.$$

The divergence contracts components of ∇_x with the columns of A and produces a column vector. This is a slight abuse of notation, because the left-multiplication of ∇_x^\top to A should yield a row vector. We define the tensor divergence in this way to avoid transpose signs in the moment systems.

A.2 Monomial integrals

With \mathbb{S}^n we denote the boundary of the unit ball in $d = n + 1$ dimensions. Thus, \mathbb{S}^1 is the unit circle and \mathbb{S}^2 the unit sphere. For integrals over \mathbb{S}^n , we write

$$\langle \cdot \rangle_{\mathbb{S}^n} := \int_{\mathbb{S}^n} \cdot dS(v).$$

Each multiindex $\mathbf{i} = (i_1, \dots, i_d) \in \mathbb{N}_+^d$ identifies a monomial $v^{\mathbf{i}} := v_1^{i_1} v_2^{i_2} \dots v_d^{i_d}$. Because the sphere is symmetric, the integral over a monomial does not change when indices are swapped. For example, the integrals $\langle v_\xi v_\eta^2 \rangle_{\mathbb{S}^2} = \langle v_\xi^2 v_\eta \rangle_{\mathbb{S}^2}$ are the same. Therefore we introduce the notation for monomial integrals:

$$\begin{aligned} \mathcal{M}_n &= \langle 1 \rangle_{\mathbb{S}^n}, \\ \mathcal{M}_n^k &= \langle v_1^k \rangle_{\mathbb{S}^n} = \dots = \langle v_d^k \rangle_{\mathbb{S}^n}, \\ \mathcal{M}_n^{k,l} &= \langle v_1^k v_2^l \rangle_{\mathbb{S}^n} = \langle v_1^k v_3^l \rangle_{\mathbb{S}^n} = \dots, \\ \mathcal{M}_n^{k,l,\dots,s} &= \langle v_1^k \dots v_q^s \rangle_{\mathbb{S}^n} = \dots \end{aligned} \quad q \leq d, \text{ indices } k, l, \dots, s.$$

The symbol $\mathcal{M}_n^{k,l,\dots,s}$ denotes all monomial integrals $\langle v^{\mathbf{i}} \rangle_{\mathbb{S}^n}$, where one arbitrary component of \mathbf{i} is equal k , a different component is equal l , and so on; and the remaining $d - q$ components are zero. When the monomial contains an odd power, i.e., at least one of k, l, \dots, s is an odd integer, the integral is zero due to symmetry of the sphere.

Monomial Integrals over the unit circle

The non-zero monomial integrals over the circle \mathbb{S}^1 up to order four are

$$\begin{aligned} \mathcal{M}_1 &= \langle 1 \rangle_{\mathbb{S}^1} = 2\pi, \\ \mathcal{M}_1^2 &= \langle v_\xi^2 \rangle_{\mathbb{S}^1} = \pi, \\ \mathcal{M}_1^4 &= \langle v_\xi^4 \rangle_{\mathbb{S}^1} = \frac{3}{4}\pi, \\ \mathcal{M}_1^{2,2} &= \langle v_\xi^2 v_\eta^2 \rangle_{\mathbb{S}^1} = \frac{1}{4}\pi. \end{aligned}$$

We have $\mathcal{M}_1^4 = 3\mathcal{M}_1^{2,2}$.

Monomial Integrals over the unit sphere

The first monomial integrals over the sphere \mathbb{S}^2 are

$$\begin{aligned} \mathcal{M}_2 &= \langle 1 \rangle_{\mathbb{S}^2} = 4\pi, \\ \mathcal{M}_2^2 &= \langle v_\xi^2 \rangle_{\mathbb{S}^2} = \frac{4}{3}\pi, \\ \mathcal{M}_2^4 &= \langle v_\xi^4 \rangle_{\mathbb{S}^2} = \frac{4}{5}\pi, \\ \mathcal{M}_2^{2p} &= \langle v_\xi^p \rangle_{\mathbb{S}^2} = \frac{4}{2p+1}\pi, \\ \mathcal{M}_2^{2,2} &= \langle v_\xi^2 v_\eta^2 \rangle_{\mathbb{S}^2} = \frac{4}{15}\pi. \end{aligned}$$

We have again $\mathcal{M}_2^4 = 3\mathcal{M}_2^{2,2}$.

A.3 The tumor diffusion tensor for a peanut ansatz

Moments of the Quadratic Form

For a matrix $D \in \mathbb{R}^{d \times d}$, and vector $v \in \mathbb{R}^d$, define the quadratic form $v^\top D v$. We compute the moments up to order two of $v^\top D v$ on the sphere \mathbb{S}^n . The zeroth moment is

$$\begin{aligned} \langle v^\top D v \rangle_{\mathbb{S}^d} &= \sum_{i=0}^n \sum_{j=0}^n D_{ij} \langle v_i v_j \rangle_{\mathbb{S}^d} \\ &= \sum_{i=0}^n \sum_{j \neq i} D_{ij} \langle v_i v_j \rangle_{\mathbb{S}^d} + \sum_{i=0}^n D_{ii} \langle v_i^2 \rangle_{\mathbb{S}^d} \\ &= \mathcal{M}_d^2 \operatorname{tr}(D). \end{aligned}$$

The vector of first moments contains exclusively odd monomial integrals and is therefore identical zero:

$$\langle (v^\top D v) v \rangle_{\mathbb{S}^d} = 0.$$

The tensor of second moments is

$$\begin{aligned} \langle (v^\top D v) v v^\top \rangle_{\mathbb{S}^d} &= \sum_{i=0}^n \sum_{j=0}^n D_{ij} \langle v_i v_j v_k v_l \rangle_{\mathbb{S}^d} \\ &= \sum_{i=0}^n \sum_{j \neq i} D_{ij} \langle v_i v_j v_k v_l \rangle_{\mathbb{S}^d} + \sum_{i=0}^n D_{ii} \langle v_i^2 v_k v_l \rangle_{\mathbb{S}^d}. \end{aligned}$$

Note that in the first sum the integral $\langle v_i v_j v_k v_l \rangle_{\mathbb{S}^d}$ is only non-zero, if $(i = k \wedge j = l)$ or $(i = l \wedge j = k)$. This sum reduces to

$$\sum_{i=0}^n \sum_{j \neq i} D_{ij} \langle v_i v_j v_k v_l \rangle_{\mathbb{S}^d} = \mathcal{M}_d^{2,2} (D_{kl} + D_{lk}) (1 - \delta_{kl}).$$

In the second sum, the integral is only non-zero, if $k = l$ and thus we write

$$\begin{aligned} \sum_{i=0}^n D_{ii} \langle v_i^2 v_k v_l \rangle_{\mathbb{S}^d} &= \sum_{i=0}^n D_{ii} \langle v_i^2 v_k^2 \rangle_{\mathbb{S}^d} \delta_{kl} \\ &= \left(\sum_{i \neq k} D_{ii} \langle v_i^2 v_k^2 \rangle_{\mathbb{S}^d} + \langle v_k^4 \rangle_{\mathbb{S}^d} D_{kk} \right) \delta_{kl} \\ &= \left(\mathcal{M}_d^{2,2} \sum_{i \neq k} D_{ii} + \mathcal{M}_d^4 D_{kk} \right) \delta_{kl} \\ &= \left(\sum_{i \neq k} D_{ii} + 3D_{kk} \right) \mathcal{M}_d^{2,2} \delta_{kl} \\ &= \left(\sum_{i=0}^n D_{ii} + D_{kl} + D_{lk} \right) \mathcal{M}_d^{2,2} \delta_{kl}. \end{aligned}$$

In the second last step we used that $\mathcal{M}_d^4 = 3\mathcal{M}_d^{2,2}$. Finally, the second moments are given by

$$\begin{aligned} \langle (v^\top D v) v v^\top \rangle_{\mathbb{S}^d} &= \mathcal{M}_d^{2,2} (D_{kl} + D_{lk}) (1 - \delta_{kl}) + \left(\sum_{i=0}^n D_{ii} + D_{kl} + D_{lk} \right) \mathcal{M}_d^{2,2} \delta_{kl}, \\ &= \mathcal{M}_d^{2,2} (\text{tr}(D) I_n + D + D^\top). \end{aligned}$$

The tumor diffusion tensor in three space dimensions

Measurements of the water diffusion tensor D_W are given for $d = 3$. Using the normalized quadratic ansatz

$$E(v) = \frac{1}{\langle v^\top D_W v \rangle_{\mathbb{S}^2}} v^\top D_W v$$

for the fiber distribution, we can use the integrals from the previous part to compute the tumor diffusion tensor $D_{T,3}$ as

$$\begin{aligned} D_{T,3} &= \langle E(v) v v^\top \rangle_{\mathbb{S}^2} = \frac{\mathcal{M}_2^{2,2}}{\mathcal{M}_2^2} \left(I_3 + \frac{D_W + D_W^\top}{\text{tr}(D_W)} \right) \\ &= \frac{1}{5} \left(I_3 + \frac{D_W + D_W^\top}{\text{tr}(D_W)} \right). \end{aligned} \tag{A.1}$$

For an isotropic water diffusion tensor $D_W = I$, we have

$$D_{T,3} = \frac{1}{5} \left(I_3 + \frac{2}{3} I_3 \right) = \frac{1}{3} I_3.$$

Even for completely degenerate water diffusion

$$D_W = \begin{pmatrix} 1 & 0 & 0 \\ 0 & 0 & 0 \\ 0 & 0 & 0 \end{pmatrix}$$

we have a non-degenerate tumor diffusion tensor

$$D_{T,3} = \frac{1}{5} \begin{pmatrix} 3 & 0 & 0 \\ 0 & 1 & 0 \\ 0 & 0 & 1 \end{pmatrix}.$$

This limits the amount of anisotropy we can get from the quadratic model. If we want more anisotropy for the tumor diffusion, we can use for example a bimodal Fisher ansatz.

The tumor diffusion tensor in two space dimensions

We have two options when computing the tumor diffusion tensor in two space dimensions. The first option is to start from a truly two-dimensional kinetic model, i.e., $v \in \mathbb{S}^1$. Then it is natural to estimate the fiber distribution from the reduced water diffusion tensor $D_{W,2}$, which consists of the upper left corner of D_W :

$$E_2(v) = \frac{1}{\langle v^\top D_{W,2} v \rangle_{\mathbb{S}^1}} v^\top D_{W,2} v.$$

The moment formulas then give

$$\begin{aligned} D_{T,2} &= \left\langle E(v)vv^\top \right\rangle_{\mathbb{S}^1} = \frac{\mathcal{M}_1^{2,2}}{\mathcal{M}_1^2} \left(I_2 + \frac{D_{W,2} + D_{W,2}^\top}{\text{tr}(D_{W,2})} \right) \\ &= \frac{1}{4} \left(I_2 + \frac{D_{W,2} + D_{W,2}^\top}{\text{tr}(D_{W,2})} \right) \end{aligned}$$

for the tumor diffusion tensor. The second option is to start from a three-dimensional kinetic model which is constant and extended infinitely along the ζ -axis. Then the velocity space remains $v \in \mathbb{S}^2$. This means that the formulas for the $d = 3$ case are used to compute $D_{T,3}$ and then only the upper left corner of this tensor is the two-dimensional tumor diffusion tensor $\tilde{D}_{T,2}$:

$$\tilde{D}_{T,2} = \frac{1}{5} \left(I_2 + \frac{D_{W,2} + D_{W,2}^\top}{\text{tr}(D_{W,3})} \right).$$

Comparing these two approaches for an isotropic water diffusion tensor $D_{W,3} = I_3$ gives

$$\begin{aligned} D_{T,2} &= \frac{1}{4} \left(I_2 + \frac{2I_2}{2} \right) = \frac{1}{2} I_2, \\ \tilde{D}_{T,2} &= \frac{1}{5} \left(I_2 + \frac{2I_2}{3} \right) = \frac{1}{3} I_2. \end{aligned}$$

Intuitively, it makes sense that the overall diffusion is faster in the truly two-dimensional model, because here the cells always move with unit speed in the (ξ, η) -plane. In the reduced three-dimensional model, cells still have a velocity in \mathbb{S}^2 which means that their speed projected onto the (ξ, η) -plane is less than one.

A.4 Real valued spherical harmonics

We parametrize the unit sphere with

$$\begin{pmatrix} v_\xi \\ v_\eta \\ v_\zeta \end{pmatrix} = \begin{pmatrix} \sqrt{1-\mu^2} \cos(\phi) \\ \sqrt{1-\mu^2} \sin(\phi) \\ \mu \end{pmatrix}.$$

The complex spherical harmonics $Y_l^m, 0 \leq l, -l \leq m \leq l$ are defined as

$$Y_l^m(\mu, \phi) = \sqrt{\frac{2l+1}{4\pi} \frac{(l-m)!}{(l+m)!}} P_l^m(\mu) \exp(im\phi),$$

with the associated legendre polynomials

$$P_l^m(\mu) = (-1)^m (1-\mu^2)^{\frac{m}{2}} \frac{d^m P_l(\mu)}{d\mu^m},$$

and

$$P_l(\mu) = \frac{1}{2^l l!} \frac{d^l}{d\mu^l} (\mu^2 - 1)^l.$$

This is the same definition as in the Boost library [40]. We define the real valued spherical harmonics in the same way as the StarMAP paper [123]: For $0 \leq l, 0 \leq m$, we have

$$Y_{l,m} = \begin{cases} -\frac{i(-1)^m}{\sqrt{2}} (Y_l^{-m} - (-1)^m Y_l^m), & m < 0, \\ Y_l^0, & m = 0, \\ \frac{(-1)^m}{\sqrt{2}} (Y_l^m + (-1)^m Y_l^{-m}), & m > 0, \end{cases}$$

$$= \begin{cases} \sqrt{2}(-1)^m \operatorname{Im}(Y_l^{-m}), & m < 0, \\ Y_l^0, & m = 0, \\ \sqrt{2}(-1)^m \operatorname{Re}(Y_l^m), & m > 0. \end{cases}$$

Note that in the StarMAP paper, there is a minus sign missing in the definition of $Y_{l,m}$, $m < 0$. With this definition, the first basis functions are

$$\begin{pmatrix} Y_{0,0} \\ Y_{1,1} \\ Y_{1,-1} \\ Y_{1,0} \\ Y_{2,2} \\ Y_{2,-2} \\ Y_{2,1} \\ \vdots \end{pmatrix} = \sqrt{\frac{1}{4\pi}} \begin{pmatrix} 1 \\ \sqrt{3}v_\xi \\ \sqrt{3}v_\eta \\ \sqrt{3}v_\zeta \\ \frac{\sqrt{15}}{2}(v_\xi^2 - v_\eta^2) \\ \sqrt{15}v_\xi v_\eta \\ \sqrt{15}v_\xi v_\zeta \\ \vdots \end{pmatrix}.$$

With this ordering, which corresponds to the ordering in [123], we obtain the density ρ and flux q from the moments $\mathbf{u} = \langle f \mathbf{a} \rangle$ via

$$\rho = \langle f \rangle = \sqrt{4\pi} \langle f Y_{0,0} \rangle = \sqrt{4\pi} \mathbf{u}^{(0)},$$

$$q = \langle f \mathbf{v} \rangle = \begin{pmatrix} \langle f v_\xi \rangle \\ \langle f v_\eta \rangle \\ \langle f v_\zeta \rangle \end{pmatrix} = \sqrt{\frac{4\pi}{3}} \begin{pmatrix} \langle f Y_{1,1} \rangle \\ \langle f Y_{1,-1} \rangle \\ \langle f Y_{1,0} \rangle \end{pmatrix} = \sqrt{\frac{4\pi}{3}} \mathbf{u}^{(1)}.$$

A.5 The eigenstructure of the Kershaw moment system

We compute the eigenvalues and eigenvectors of the flux Jacobian for the modified Kershaw moment system from Section 4.2.2. The calculation is similar to that in Kershaw's original paper [86] and is based on rotations into a suitable reference frame. It has been published originally in [36].

Recall the formula (1.14) for the flux Jacobian $J\mathcal{F}_n$

$$J\mathcal{F}_n = \begin{pmatrix} 0 & n^\top \\ \hat{P}n - \frac{\partial \hat{P}n}{\partial \hat{q}} \hat{q} & \frac{\partial \hat{P}n}{\partial \hat{q}} \end{pmatrix}.$$

With $\hat{P} = \hat{P}^{(K)}$ from (4.6), and writing $P_E = \langle v v^\top E \rangle$, we have

$$\frac{\partial \hat{P}n}{\partial \hat{q}} = -2(P_E n) \hat{q}^\top + I(\hat{q}^\top n) + \hat{q} n^\top,$$

$$\frac{\partial \hat{P}n}{\partial \hat{q}} \hat{q} = -2(P_E n) \hat{q}^\top \hat{q} + 2(\hat{q}^\top n) \hat{q}.$$

The Jacobian becomes

$$\begin{aligned} J\mathcal{F}_n &= \begin{pmatrix} 0 & n^\top \\ (1 + |\hat{q}|^2)(P_E n) - (\hat{q}^\top n)\hat{q} & -2(P_E n)\hat{q}^\top + I(\hat{q}^\top n) + \hat{q}n^\top \end{pmatrix} \\ &= \begin{pmatrix} 0 & n^\top \\ (1 + |\hat{q}|^2)(P_E n) - |\hat{q}|^2(q^{*\top} n)q^* & |\hat{q}|(-2(P_E n)q^{*\top} + I(q^{*\top} n) + q^*n^\top) \end{pmatrix}, \end{aligned}$$

where $q^* = \frac{\hat{q}}{|\hat{q}|}$ is the free-streaming first moment. Define the rotation matrix \hat{R} that rotates q^* onto the first unit vector e_1

$$\hat{R}q^* = e_1,$$

and a compatible extension

$$R := \begin{pmatrix} 1 & 0 \\ 0 & \hat{R} \end{pmatrix}$$

to the full Jacobian. Under the similarity transform R the Jacobian becomes

$$RJ\mathcal{F}_n R^\top = \begin{pmatrix} 0 & n^\top \hat{R}^\top \\ (1 + |\hat{q}|^2)\hat{R}(P_E n) - |\hat{q}|^2(e_1^\top \hat{R}n)e_1 & |\hat{q}|(-2(\hat{R}P_E n)e_1^\top + I(e_1^\top \hat{R}n) + e_1 n^\top \hat{R}^\top) \end{pmatrix}.$$

Let n_j such that $\hat{R}n_j = e_j$, $j = 1, 2, 3$. That is, n_1 is parallel to q^* and n_2, n_3 are orthogonal to the free-streaming direction. We compute the eigenvectors and eigenvalues of $RJ\mathcal{F}_n R^\top$ for these basis vectors. The Jacobians become

$$RJ\mathcal{F}_{n_j} R^\top = \begin{pmatrix} 0 & e_j^\top \\ (1 + |\hat{q}|^2)S e_j - |\hat{q}|^2 \delta_{1j} e_1 & |\hat{q}|(-2S e_j e_1^\top + I \delta_{1j} + e_1 e_j^\top) \end{pmatrix},$$

where S is the similarity transform of P_E :

$$S := \hat{R}P_E \hat{R}^\top.$$

For $j = 1$, we have

$$RJ\mathcal{F}_{n_1} R^\top = \begin{pmatrix} 0 & 1 & 0 & 0 \\ (1 + |\hat{q}|^2)S_{11} - |\hat{q}|^2 & |\hat{q}|(-2S_{11} + 2) & 0 & 0 \\ (1 + |\hat{q}|^2)S_{21} & |\hat{q}|(-2S_{21}) & |\hat{q}| & 0 \\ (1 + |\hat{q}|^2)S_{31} & |\hat{q}|(-2S_{31}) & 0 & |\hat{q}| \end{pmatrix},$$

with characteristic polynomial

$$\det(RJ\mathcal{F}_{n_1} R^\top - \lambda I) = (|\hat{q}| - \lambda)^2 [\lambda^2 - 2\lambda|\hat{q}|(1 - S_{11}) + |\hat{q}|^2 - (1 + |\hat{q}|^2)S_{11}]$$

and eigenvalues

$$\begin{aligned} \lambda_{2,3} &= |\hat{q}|, \\ \lambda_{1,4} &= (1 - S_{11})|\hat{q}| \pm \sqrt{g(|\hat{q}|, S_{11})}. \end{aligned}$$

In a hyperbolic system, all eigenvalues must be real, which is the case if the term under the square root

$$g(|\hat{q}|, S_{11}) = S_{11}^2 |\hat{q}|^2 + S_{11}(1 - |\hat{q}|^2)$$

is greater than or equal to zero. The matrix component

$$S_{11} = e_1^\top \hat{R} \langle v v^\top E \rangle \hat{R}^\top e_1 = \langle (e_1^\top \hat{R} v)^2 E \rangle > 0,$$

is positive because E is positive. Since $|\hat{q}| \in [0, 1]$, we have indeed

$$g(|\hat{q}|, S_{11}) > 0.$$

Because $g > 0$, the eigenvalues $\lambda_1 \neq \lambda_4$ are distinct.

The Jacobian is diagonalizable if there are four linearly independent eigenvalues. We see immediately that the dimension of the nullspace of $RJ(F \cdot n_1)R^\top - |\hat{q}|I$ is two. Thus, two independent eigenvectors exist for the eigenvalue $\lambda_{1,2} = |\hat{q}|$. They are given by $V_2 = (0, e_2)$ and $V_3 = (0, e_3)$, and therefore are the characteristic speeds of transversal waves. Because $S_{11} > 0$, the eigenvalues $\lambda_{1,4}$ are distinct and a complete basis of eigenvectors exists. The eigenvectors V_1, V_4 to eigenvalues λ_1, λ_4 have the form $(1, \lambda_{1,4}, r, s)$. Unfortunately, the last two components r, s are in general not zero, hence the characteristic waves are not longitudinal. But if S is diagonal, which happens if n_1 is along an eigenvector of P_E , we have $V_{1,4} = (1, \lambda_{1,4}, 0, 0)$.

In the free-streaming situation, the characteristic speeds are $\lambda_1 = 1$ and $\lambda_4 = 1 - 2S_{11}$. Additionally the eigenvector to the main eigenvalue is $V_1 = (1, e_1)$.

For $j = 2$ the Jacobian is

$$RJ\mathcal{F}_{n_2}R^\top = \begin{pmatrix} 0 & 0 & 1 & 0 \\ (1 + |\hat{q}|^2)S_{12} & |\hat{q}|(-2S_{12}) & |\hat{q}| & 0 \\ (1 + |\hat{q}|^2)S_{22} & |\hat{q}|(-2S_{22}) & 0 & 0 \\ (1 + |\hat{q}|^2)S_{32} & |\hat{q}|(-2S_{32}) & 0 & 0 \end{pmatrix},$$

with characteristic polynomial

$$\det(RJ\mathcal{F}_{n_2}R^\top - \lambda I) = \lambda^2 \left[\lambda^2 + 2|\hat{q}|S_{12}\lambda + S_{22}(|\hat{q}|^2 - 1) \right]$$

and eigenvalues

$$\begin{aligned} \lambda_{2,3} &= 0, \\ \lambda_{1,4} &= -|\hat{q}|S_{12} \pm \sqrt{h}, \end{aligned}$$

where

$$h = S_{12}^2 |\hat{q}|^2 + S_{22}(1 - |\hat{q}|^2) \geq 0$$

is non-negative by the same arguments as before.

This matrix cannot be diagonalized when the first moment is on the surface of the realizable set $|\hat{q}| = 1$. In this situation, the three eigenvalues $\lambda_{1,2,3} = 0$ are zero. But the matrix

$$RJ\mathcal{F}_{n_2}R^\top - 0I = \begin{pmatrix} 0 & 0 & 1 & 0 \\ 2S_{12} & -2S_{12} & 1 & 0 \\ 2S_{22} & -2S_{22} & 0 & 0 \\ 2S_{32} & -2S_{32} & 0 & 0 \end{pmatrix}$$

has rank two, thus there are only two linearly independent eigenvectors to the eigenvalue zero. The case $j = 3$ is completely analogous to $j = 2$.

A.6 A second-order time stepping

The stiffly accurate IMEX scheme ARS(2,2,2) [4] applied to the system (5.10) reads:

$$\begin{array}{l}
 (\bar{\Phi}^\rho)^{(1)} = \bar{\Phi}^\rho(\bar{\rho}^n, \bar{g}^n) \\
 (\bar{\Phi}_E^g)^{(1)} = \bar{\Phi}_E^g(\bar{\rho}^n, \bar{g}^n) \\
 (\bar{\Phi}^g)^{(1)} = \bar{\Phi}^g(\bar{\rho}^n, \bar{g}^n) \\
 \bar{\rho}^* = \bar{\rho}^n + \tau\Delta t(\bar{\Phi}^\rho)^{(1)} \\
 \bar{g}^* = \bar{g}^n + \tau\Delta t \left((\bar{\Phi}_E^g)^{(1)} + (\bar{\Phi}^g)^{(1)} \right) \\
 \bar{\rho}^{(n,1)} = \bar{\rho}^* + \tau\Delta t\bar{\Gamma}^\rho(\bar{\rho}^{(n,1)}, \bar{g}^*) \\
 \bar{g}^{(n,1)} = \bar{g}^* + \tau\Delta t\bar{\Gamma}^g(\bar{\rho}^*, \bar{g}^{(n,1)}) \\
 (\bar{\Phi}^\rho)^{(2)} = \bar{\Phi}^\rho(\bar{\rho}^{(n,1)}, \bar{g}^{(n,1)}) \\
 (\bar{\Phi}_E^g)^{(2)} = \bar{\Phi}_E^g(\bar{\rho}^{(n,1)}, \bar{g}^{(n,1)}) \\
 (\bar{\Phi}^g)^{(2)} = \bar{\Phi}^g(\bar{\rho}^{(n,1)}, \bar{g}^{(n,1)}) \\
 (\bar{\Gamma}^\rho)^{(2)} = \bar{\Gamma}^\rho(\bar{\rho}^{(n,1)}, \bar{g}^{(n,1)}) \\
 (\bar{\Gamma}^g)^{(2)} = \bar{\Gamma}^g(\bar{\rho}^{(n,1)}, \bar{g}^{(n,1)}) \\
 \bar{\rho}^{**} = \bar{\rho}^n + (1 - \tau)\Delta t(\bar{\Gamma}^\rho)^{(2)} \\
 \quad + \Delta t(\sigma(\bar{\Phi}^\rho)^{(1)} + (1 - \sigma)(\bar{\Phi}^\rho)^{(2)}) \\
 \bar{g}^{**} = \bar{g}^n + (1 - \tau)\Delta t(\bar{\Gamma}^g)^{(2)} \\
 \quad + \Delta t(\sigma(\bar{\Phi}_E^g + \bar{\Phi}^g)^{(1)} + (1 - \sigma)(\bar{\Phi}_E^g + \bar{\Phi}^g)^{(2)}) \\
 \bar{\rho}^{n+1} = \bar{\rho}^{**} + \tau\Delta t\bar{\Gamma}^\rho(\bar{\rho}^{n+1}, \bar{g}^{**}) \\
 \bar{g}^{n+1} = \bar{g}^{**} + \tau\Delta t\bar{\Gamma}^g(\bar{\rho}^{**}, \bar{g}^{n+1})
 \end{array}
 \begin{array}{l}
 \left. \begin{array}{l} \\ \\ \\ \end{array} \right\} \begin{array}{l} \text{compute operators} \\ \text{at time } t \end{array} \\
 \left. \begin{array}{l} \\ \\ \end{array} \right\} \begin{array}{l} \text{intermediate explicit} \\ \text{step to } t + \tau\Delta t \end{array} \\
 \left. \begin{array}{l} \\ \\ \\ \\ \\ \end{array} \right\} \begin{array}{l} \text{intermediate implicit} \\ \text{step} \end{array} \\
 \left. \begin{array}{l} \\ \\ \\ \\ \\ \end{array} \right\} \begin{array}{l} \text{compute operators} \\ \text{at time } t + \tau\Delta t \end{array} \\
 \left. \begin{array}{l} \\ \\ \end{array} \right\} \begin{array}{l} \text{explicit step to } t + \Delta t \end{array} \\
 \left. \begin{array}{l} \\ \end{array} \right\} \text{implicit step}
 \end{array}$$

with the constants

$$\begin{aligned}
 \tau &= \frac{2 - \sqrt{2}}{2}, \\
 \sigma &= 1 - \frac{1}{2\tau}.
 \end{aligned}$$

B

Software and data

The complete source code and data for this thesis is publicly available online [34] under the doi <https://doi.org/10.26204/data/2>. This includes the source of the implementation of the numerical schemes, as well as the scripts for plotting the results and the source code for this document. Furthermore, the computations for the experiments in this thesis are documented in this archive, including precise settings and output data. In Section B.2, we describe the archiving tool we developed for this purpose.

B.1 Used software

The implementation of the numerical schemes from Section 4.3.1 and Section 5.3 is built upon the DUNE [7–9] and DUNE PDELAB [10] environments. These are C++ toolboxes that provide core functionality to discretize PDEs with standard grid based methods. DUNE is organized in so-called modules. We provide three such modules: `KERSHAW-KINETIC` implements the scheme from Section 4.3.1, `KERSHAW-AP` implements the `AP` scheme from Section 5.3, and `KERSHAW-COMMON` holds common functionality, e.g., code related to moment methods or IO.

The code depends on the `EIGEN` library [67] to perform the necessary linear algebra computations in the context of moment methods, and the `BOOST` library [40] to evaluate spherical harmonic functions. To read the `DTI` data, `NETCDF` [134] is required, but this dependency is optional if only synthetic data are used.

The `KERSHAW-KINETIC` and `KERSHAW-AP` programs produce outputs in the `VTK` format [122], which is supported by DUNE. Postprocessing of the simulation outputs is done with `PYTHON` [52]. The figures in this thesis have been generated with the python library `MATPLOTLIB` [77].

Table B.1 summarizes the dependencies.

B.2 Computational experiments

When investigating mathematical models and numerical methods computationally, as we do in Section 4.3 and Section 5.4, one cannot avoid the concept of computational experiments. Fundamentally, computation is experimentation:

So science is still carried out as an ongoing interplay between theory and experimentation. The complexity of both, however, has increased to such a degree that they cannot be carried out without computation. There is no need, therefore, to attach new legs to science. ([135])

Software	Version	Use
G++	7.5.0 ^a	compiler
DUNE ^b	2.6	PDE discretization
EIGEN	3	Linear algebra for moment methods
BOOST	1.66.0	Spherical harmonics
NETCDF ^c	4	reading DTI input
MPI ^d	2	parallelization
PYTHON ^e	2.7	postprocessing + visualization
VTK	5.10	visualization

^aC++17 standard
^brequired modules: dune-common, dune-geometry, dune-grid, dune-typetree, dune-multidomaingrid, dune-istl, dune-localfunctions, dune-functions, dune-pdelab
^coptional
^doptional
^enotable modules: vtk, matplotlib, numpy

Table B.1: Dependencies for the KERSHAW modules.

Thus, computational experiments should be subject to the same established practices as traditionally executed experiments:

We believe that software is just another kind of experimental apparatus [135] and should be built, checked, and used as carefully as any physical apparatus. ([139])

But what is an experiment? Here is our presumptuous attempt to summarize several centuries of scientific practice in a single sentence:

Definition B.1 — Experiment. A carefully planned, executed and documented observation of a system in a controlled environment, in order to support or reject a theory.

For example, let us see, how this definition applies to Experiment 5.7. We want to investigate whether the modified $P_1^{(E+)}$ moment model (system) converges to the correct diffusion limit (theory). Therefore, we compute (execution) this model with a numerical scheme (environment) with several small values for ε (planning) and compute the difference to the analytic solution (observation). The observations (see Figure 5.7b) support the theory (evaluation). The classification above is not as clear cut as it might seem. We can look at the same experiment in a different way: Having gathered strong theoretical evidence (see Lemma 4.2), that the first-order modified moment model converges to the correct diffusion limit, we want to verify this convergence (theory) for the numerical schemes, e.g. MM_{1m}^+ (system). We run computations (execution) of this scheme, using the current version of its implementation (environment), with several small values for ε (planning) and compute the difference to the analytic solution (observation). Again, our observations support the theory (evaluation).

There are too many aspects to the proper conduct of experiments to list them all. Let us point to [109, 139] for guides on best practices. One major recommendation is the use of standardized and thoroughly tested equipment. In the context of this thesis, DUNE [7–9] and DUNE PDELAB [10] as standard toolboxes for numerical solution of PDEs are part of this equipment.

For someone to benefit from the hard work put into an experiment, all the steps have to be documented. Noble summarizes the possible use cases in his guide to best practices in computational biology nicely:

This “someone” could be any of a variety of people: someone who read your published article and wants to try to reproduce your work, a collaborator who wants to understand the details of your experiments, a future student working in your lab who wants to extend your work after you have moved on to a new job, your research advisor, who may be interested in understanding your work or who may be evaluating your research skills. Most commonly, however, that “someone” is you. ([109])

Ideally, as many people as possible should benefit from the documentation of an experiment. However, the scope and purpose of documentation differs too much between audiences to address all concerns at once. We focus on a single aspect:

This leads to the second principle, which is actually more like a version of Murphy’s Law: Everything you do, you will probably have to do over again. ([109])

The ARCHIVIST—the archiving tool that we describe in the following—is a direct consequence of too many first-hand experiences with this principle.

Many researchers have approached the issue of documentation from different angles. The major concern in reproducible research [39, 99, 126] is, as the name suggests, to enable oneself and other researchers to reproduce experiments independently, i.e., using different source code. This goes beyond simple replication, i.e., rerunning the same computation using the same code (in the same environment) again. Although one functionality of the ARCHIVIST is the replication of previous experiments, this is not enough to ensure the research is reproducible in this sense. Therefore, we avoid the phrase ‘reproducible research’ in the following. Another purpose of documentation is to prove the provenance of data, such as experiment results. Verifiable Result Identifiers [60] have been proposed as an automatic and cheat-proof tool to document how each piece of data in the chain of computations from raw data to results came into existence. The ARCHIVIST provides only a few links in this chain and leaves much room for human error or manipulation. Source code is also documentation [104]. Although automation software can do the bookkeeping task to remember, for example commit numbers, no piece of software can ensure that the source code itself is understandable. Therefore, good coding practices [82, 104] are always important.

Rather than a fully automated solution to all issues of documentation, the ARCHIVIST should be understood as an electronic lab journal. It does not guarantee a clean and seamless documentation; but used properly, it enables it. Many other pieces of software with similar functionality exist [39, 99, 115].

B.2.1 The ARCHIVIST

The ARCHIVIST has been presented at the Dune User and Developer Meeting 2018 [33] and is available online [31]. It is a PYTHON tool that aims to automate error-prone and tedious bookkeeping tasks essential to the proper conduct of computational experiments.

Figure B.1 gives an overview of the environment of a computational experiment, from the perspective of the ARCHIVIST. An experiment requires to run an executable to produce output.

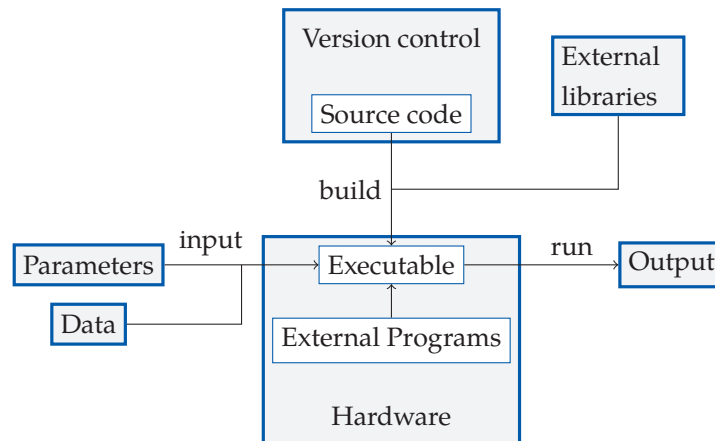


Figure B.1: The environment of a computational experiment.

This can be anything from a compiled stand-alone application to a shell script that calls other programs in some order. To produce the desired result, the executable usually consumes input. As far as the ARCHIVIST is concerned, there are two types of input—parameters and data—which are treated differently. Parameters are usually inputs that are human readable and writable, and most importantly, small enough to store plain copies every time an experiment is archived. This could be command line inputs or configuration files. Data are typically generated by measurements or other software, they could be in raw binary format, and they are too large to store as copies. An example from this work is the DTI data set used in Experiment ???. The ARCHIVIST assumes that the executable can be built by a single command. It does not matter whether this is a plain shell script, a makefile, an entire build system, e.g. CMAKE, or nothing at all. Most importantly, the source code for the executable must be under version control¹. This restriction is built in on purpose to enforce the use of version control. Of course, any external dependencies, such as libraries or other executables, as well as the hardware, belong also to the environment.

The ARCHIVIST performs these functions:

- Archive the inputs, source code, and outputs of an experiment.
- Restore the inputs, source code, and executable to match an archived experiment, and optionally run it again.
- Organize experiments into so-called file cabinets, attach descriptions and tags to experiments.

It does not

- manage external dependencies,
- record versions for external dependencies,
- record hardware details,

¹Currently, only Git is supported.

aspect	archiving	restoring
environment	-	-
source code	store commit hash	checkout commit
parameters	copy to archive	copy to project
data	store hashes	verify hashes
executable	store command line arguments	build and run
output	copy	-
description	query user input	-

Table B.2: The actions the ARCHIVIST performs on components of the environment.

- manage data inputs.

Table B.2 lists the actions that the ARCHIVIST takes for each component of the environment to archive and restore experiments. Managing external dependencies is a complicated task that is addressed by other tools, e.g. CDE [126] or CONDA. As far as the ARCHIVIST is concerned, it is the user's responsibility to install the required dependencies. Note the distinction between parameters and data. Parameters are stored as plain copies, whereas for data only the hashes are stored. The user has to ensure that data are archived separately. If input data are corrupted or missing, the ARCHIVIST will report an error when trying to restore an experiment. It should go without saying that the ARCHIVIST cannot force the user to provide sensible descriptions. Because the experiment archive should serve as documentation, everything is stored in the human readable JSON format in plain text files.

Bibliography

- [1] G. W. Alldredge, C. D. Hauck, and A. L. Tits. *High-order entropy-based closures for linear transport in slab geometry II: A computational study of the optimization problem*. *SIAM Journal on Scientific Computing*, 34: B361–B391, 2012. (see pp. 16, 78)
- [2] H. W. Alt. *Lineare Funktionalanalysis*. 6th ed. Springer, 2012. 353, 387–395, 407 (see pp. 43, 46, 50)
- [3] A. R. Anderson. *A hybrid mathematical model of solid tumour invasion: the importance of cell adhesion*. *Mathematical medicine and biology: a journal of the IMA*, 22: 163–186, 2005. (see p. 28)
- [4] U. M. Ascher, S. J. Ruuth, and R. J. Spiteri. *Implicit-explicit Runge-Kutta methods for time-dependent partial differential equations*. *Applied Numerical Mathematics*, 25: 151–167, 1997. (see pp. 108, 109, 159)
- [5] H. Babovsky. *Die Boltzmann-Gleichung: Modellbildung-Numerik-Anwendungen*. Springer, 1998. (see pp. 5, 6, 8)
- [6] C. Bardos, R. Santos, and R. Sentis. *Diffusion approximation and computation of the critical size*. *Transactions of the american mathematical society*, 284: 617–649, 1984. (see p. 3)
- [7] P. Bastian *DUNE Web page 2011* URL: <http://www.dune-project.org> (visited on 06/23/2020) (see pp. 103, 147, 161, 162)
- [8] P. Bastian, M. Blatt, A. Dedner, C. Engwer, R. Klöfkorn, R. Kornhuber, M. Ohlberger, and O. Sander. *A generic grid interface for parallel and adaptive scientific computing. Part II: implementation and tests in DUNE*. *Computing*, 82: 121–138, 2008. (see pp. 161, 162)
- [9] P. Bastian, M. Blatt, A. Dedner, C. Engwer, R. Klöfkorn, M. Ohlberger, and O. Sander. *A generic grid interface for parallel and adaptive scientific computing. Part I: abstract framework*. *Computing*, 82: 103–119, 2008. (see pp. 161, 162)
- [10] P. Bastian, F. Heimann, and S. Marnach. *Generic implementation of finite element methods in the distributed and unified numerics environment (DUNE)*. *Kybernetika*, 46: 294–315, 2010. (see pp. 161, 162)
- [11] R. Bauer. *Discontinuous Galerkin Methods for ordinary differential equations*. Master thesis. University of Colorado at Denver, 1995. (see p. 74)
- [12] C. Beadle, M. C. Assanah, P. Monzo, R. Vallee, S. S. Rosenfeld, and P. Canoll. *The role of myosin II in glioma invasion of the brain*. *Molecular biology of the cell*, 19: 3357–3368, 2008. (see pp. 2, 27)

- [13] N. Bellomo, A. Bellouquid, J. Nieto, and J. Soler. *Complexity and mathematical tools toward the modelling of multicellular growing systems*. *Mathematical and Computer Modelling*, 51: 441–451, 2010. (see pp. 29, 41)
- [14] N. Bellomo, C. Bianca, and M. Delitala. *Complexity analysis and mathematical tools towards the modelling of living systems*. *Physics of Life Reviews*, 6: 144–175, 2009. (see pp. 3, 29, 41)
- [15] N. Bellomo, E. De Angelis, and L. Preziosi. *Multiscale modeling and mathematical problems related to tumor evolution and medical therapy*. *Computational and Mathematical Methods in Medicine*, 5: 111–136, 2003. (see pp. 28, 29)
- [16] H. C. Berg. *E. coli in Motion*. Springer Science & Business Media, 2008. 19–22, 26 (see pp. 135, 136, 181)
- [17] H. C. Berg and D. A. Brown. *Chemotaxis in Escherichia coli analysed by three-dimensional tracking*. *Nature*, 239: 500–504, 1972. (see p. 4)
- [18] F. Berthelin and A. Vasseur. *From kinetic equations to multidimensional isentropic gas dynamics before shocks*. *SIAM Journal on Mathematical Analysis*, 36: 1807–1835, 2005. DOI: [10.1137/S0036141003431554](https://doi.org/10.1137/S0036141003431554) (see p. 62)
- [19] L. Boltzmann. *Weitere Studien über das Wärmegleichgewicht unter Gasmolekülen*. in: *Kinetische Theorie II*. Springer, 1970. 115–225 (see pp. 2, 8)
- [20] S. Boscarino, L. Pareschi, and G. Russo. *A unified IMEX Runge–Kutta approach for hyperbolic systems with multiscale relaxation*. *SIAM Journal on Numerical Analysis*, 55: 2085–2109, 2017. (see p. 101)
- [21] T. A. Brunner and J. P. Holloway. *Two-dimensional time dependent Riemann solvers for neutron transport*. *Journal of Computational Physics*, 210: 386–399, 2005. (see pp. 18, 117)
- [22] C. Buet, B. Després, and E. Franck. *Design of asymptotic preserving finite volume schemes for the hyperbolic heat equation on unstructured meshes*. *Numerische Mathematik*, 122: 227–278, 2012. (see pp. 3, 101, 103, 104, 110, 148)
- [23] P. K. Burgess, P. M. Kulesa, J. D. Murray, and E. C. Alvord Jr. *The interaction of growth rates and diffusion coefficients in a three-dimensional mathematical model of gliomas*. *Journal of Neuropathology & Experimental Neurology*, 56: 704–713, 1997. (see pp. 2, 25, 28)
- [24] D. Burini and N. Chouhad. *Hilbert method toward a multiscale analysis from kinetic to macroscopic models for active particles*. *Mathematical Models and Methods in Applied Sciences*, 27: 1327–1353, 2017. (see pp. 3, 52)
- [25] J. A. Carrillo and B. Yan. *An asymptotic preserving scheme for the diffusive limit of kinetic systems for chemotaxis*. *Multiscale Modeling & Simulation*, 11: 336–361, 2013. (see p. 100)
- [26] S. B. Carter. *Haptotaxis and the mechanism of cell motility*. *Nature*, 213: 256, 1967. (see p. 28)
- [27] G. Q. Chen, C. D. Levermore, and T.-P. Liu. *Hyperbolic conservation laws with stiff relaxation terms and entropy*. *Communications on Pure and Applied Mathematics*, 47: 787–830, 1994. DOI: [10.1002/cpa.3160470602](https://doi.org/10.1002/cpa.3160470602) (see pp. 8, 58)
- [28] P. Chidyagwai, M. Frank, F. Schneider, and B. Seibold. *A Comparative Study of Limiting Strategies in Discontinuous Galerkin Schemes for the M1 Model of Radiation Transport*. 1–24, 2017. arXiv: [1706.10174](https://arxiv.org/abs/1706.10174) (see p. 73)

- [29] A. Claes, A. J. Idema, and P. Wesseling. *Diffuse glioma growth: a guerilla war*. *Acta neuropathologica*, 114: 443–458, 2007. (see pp. 1, 2)
- [30] P. Cook, Y. Bai, S. Nedjati-Gilani, K. Seunarine, M. Hall, G. Parker, and D. C. Alexander. *Camino: open-source diffusion-MRI reconstruction and processing*. in: *14th scientific meeting of the international society for magnetic resonance in medicine*. ISMRM Seattle WA, USA, 2006. 2759 (see pp. 31, 33, 137)
- [31] G. Corbin *Archive computational experiments* 2018 URL: <https://github.com/gcorbin/archive-computational-experiments> (visited on 06/23/2020) (see p. 163)
- [32] G. Corbin *Asymptotic preserving P_N methods for haptotaxis equations* 2019 arXiv: [1909.08514 \[math.NA\]](https://arxiv.org/abs/1909.08514) (see p. 99)
- [33] G. Corbin. *Making numerical experiments in Dune reproducible*. in: *Dune User and Developer Meeting 2018*. URL: <https://www.ians.uni-stuttgart.de/institute/news/events/Dune-User-and-Developer-Meeting-2018/> University of Stuttgart Nov. 5, 2018. (see p. 163)
- [34] G. Corbin *Numerical methods for multi-scale cell migration models: source code and data* 2020 doi: <https://doi.org/10.26204/data/2> (see p. 161)
- [35] G. Corbin, C. Engwer, A. Klar, J. Nieto, J. Soler, C. Surulescu, and M. Wenske *Modeling glioma invasion with anisotropy- and hypoxia-triggered motility enhancement: from subcellular dynamics to macroscopic PDEs with multiple taxis* 2020 arXiv: [2006.12322 \[q-bio.TO\]](https://arxiv.org/abs/2006.12322) (see pp. 30, 90, 138)
- [36] G. Corbin, A. Hunt, A. Klar, F. Schneider, and C. Surulescu. *Higher-order models for glioma invasion: from a two-scale description to effective equations for mass density and momentum*. *Mathematical Models and Methods in Applied Sciences*, 2018. (see pp. 36, 52, 67, 68, 70, 72, 138, 146, 156)
- [37] J.-F. Coulombel, F. Golse, and T. Goudon. *Diffusion approximation and entropy-based moment closure for kinetic equations*. *Asymptotic Analysis*, 45: 1–39, 2005. (see pp. 8, 20, 21)
- [38] R. Dautray and J.-L. Lions. *Mathematical Analysis and Numerical Methods for Science and Technology: Volume 6 Evolution Problems II*. Springer, 1988. 372–379 (see p. 11)
- [39] A. P. Davison. *Automated capture of experiment context for easier reproducibility in computational research*. *Computing in Science & Engineering*, 14: 48–56, 2012. (see p. 163)
- [40] B. Dawes, D. Abrahams, and R. Rivera *boost c++ libraries* 2020 URL: <https://www.boost.org/> (visited on 06/09/2020) (see pp. 156, 161)
- [41] R. B. Dickinson and R. T. Tranquillo. *A stochastic model for adhesion-mediated cell random motility and haptotaxis*. *Journal of mathematical biology*, 31: 563–600, 1993. (see pp. 28, 37, 40)
- [42] B. Dubroca and J.-L. Feugeas. *Etude théorique et numérique d’une hiérarchie de modèles aux moments pour le transfert radiatif*. *Comptes Rendus de l’Académie des Sciences-Series I-Mathematics*, 329: 915–920, 1999. (see p. 17)
- [43] G. Eigestad and R. Klausen. *On the convergence of the multi-point flux approximation O-method: Numerical experiments for discontinuous permeability*. *Numerical Methods for Partial Differential Equations: An International Journal*, 21: 1079–1098, 2005. (see pp. 99, 128–130)

- [44] C. Engwer, T. Hillen, M. Knappitsch, and C. Surulescu. *Glioma follow white matter tracts: a multiscale DTI-based model*. *J. Math Biol.*, 71: 551–582, 2015. (see pp. 3, 4, 30, 33, 36, 37, 39, 52, 138, 145, 146)
- [45] C. Engwer, A. Hunt, and C. Surulescu. *Effective equations for anisotropic glioma spread with proliferation: a multiscale approach*. *Mathematical Medicine and Biology. A Journal of the IMA*, 33: 435–459, 2016. (see p. 31)
- [46] C. Engwer, M. Knappitsch, and C. Surulescu. *A multiscale model for glioma spread including cell-tissue interactions and proliferation*. *Journal of Mathematical Engineering*, 13: 443–460, 2016. (see pp. 3, 4, 30, 33, 145)
- [47] C. Engwer, A. Hunt, and C. Surulescu. *Effective equations for anisotropic glioma spread with proliferation: a multiscale approach and comparisons with previous settings*. *Mathematical medicine and biology: a journal of the IMA*, 33: 435–459, 2016. (see p. 138)
- [48] C. Engwer and M. Wenske *Estimating the extent of glioblastoma invasion* 2020 arXiv: 2001.05369 [q-bio.CB] (see p. 3)
- [49] R. Erban and H. G. Othmer. *From individual to collective behavior in bacterial chemotaxis*. *SIAM Journal on Applied Mathematics*, 65: 361–391, 2004. (see pp. 37, 40)
- [50] R. Erban and H. G. Othmer. *From signal transduction to spatial pattern formation in E. coli: a paradigm for multiscale modeling in biology*. *Multiscale Modeling & Simulation*, 3: 362–394, 2005. (see pp. 37, 40, 52)
- [51] R. Faguer, J.-Y. Tanguy, A. Rousseau, A. Clavreul, and P. Menei. *Early presentation of primary glioblastoma*. *Neurochirurgie*, 60: 188–193, 2014. (see p. 25)
- [52] T. P. S. Foundation *Python* URL: <https://www.python.org/> (visited on 06/09/2020) (see p. 161)
- [53] P. Friedl and E.-B. Bröcker. *The biology of cell locomotion within three-dimensional extracellular matrix*. *Cellular and molecular life sciences CMLS*, 57: 41–64, 2000. (see pp. 27, 90)
- [54] P. Friedl and K. Wolf. *Plasticity of cell migration: a multiscale tuning model*. *The Journal of cell biology*, 188: 11–19, 2010. (see p. 27)
- [55] P. G. Gritsenko, O. Ilina, and P. Friedl. *Interstitial guidance of cancer invasion*. *The Journal of pathology*, 226: 185–199, 2012. (see pp. 2, 27)
- [56] A. F. Gaillard and J. Jones *Radiopaedia: MRI* 2019 URL: <https://radiopaedia.org/articles/mri-2> (visited on 07/24/2019) (see pp. 27, 30)
- [57] A. F. Gaillard and J. Jones *Radiopaedia: WHO Classification of CNS tumors* 2019 URL: <https://radiopaedia.org/articles/who-classification-of-cns-tumours-1?lang=us> (visited on 07/24/2019) (see p. 1)
- [58] B. Ganapol, R. S. Baker, J. A. Dahl, and R. E. Alcouffe *Homogeneous infinite media time-dependent analytical benchmarks* tech. rep. Los Alamos National Laboratory, 2001 (see pp. 72, 75)
- [59] C. K. Garrett and C. D. Hauck. *A comparison of moment closures for linear kinetic transport equations: The line source benchmark*. *Transport Theory and Statistical Physics*, 42: 203–235, 2013. (see pp. 16, 75, 117, 119, 124)

- [60] M. Gavish and D. Donoho. *A universal identifier for computational results*. *Procedia Computer Science*, 4: 637–647, 2011. (see p. 163)
- [61] K. Gellrich. *Stability Preserving Runge-Kutta and Discontinuous-Galerkin Methods for Hyperbolic Conservation Laws*. Bachelor thesis. TU Kaiserslautern, 2017. (see p. 74)
- [62] F. Golse. *Recent results on the periodic Lorentz gas*. in: *Nonlinear partial differential equations*. Springer, 2012. chap. 0.1, 0.2, 7–17 (see pp. 2, 3, 5, 6, 40)
- [63] L. Gosse and G. Toscani. *An asymptotic-preserving well-balanced scheme for the hyperbolic heat equations*. *Comptes Rendus Mathématique*, 334: 337–342, 2002. (see p. 3)
- [64] S. Gottlieb. *On high order strong stability preserving Runge-Kutta and multi step time discretizations*. *Journal of Scientific Computing*, 25: 105–128, 2005. (see p. 73)
- [65] S. Gottlieb *Strong Stability Preserving Methods 2020* URL: <http://www.cfm.brown.edu/people/sg/SSPpage/sspsite/> (visited on 06/16/2020) (see p. 73)
- [66] H. Grad. *Principles of the kinetic theory of gases*. in: *Thermodynamik der Gase/Thermodynamics of Gases*. Springer, 1958. 205–294 (see p. 2)
- [67] G. Guennebaud, B. Jacob, et al. *Eigen v3* 2010 URL: <http://eigen.tuxfamily.org> (visited on 06/09/2020) (see p. 161)
- [68] C. Hancock, B. Bernal, C. Medina, and S. Medina. *Cost analysis of Diffusion Tensor Imaging and MR tractography of the brain*. *Open Journal of Radiology*, 2014: 2014. (see p. 31)
- [69] H. L. Harpold, E. C. Alvord Jr, and K. R. Swanson. *The evolution of mathematical modeling of glioma proliferation and invasion*. *Journal of Neuropathology & Experimental Neurology*, 66: 1–9, 2007. (see pp. 1, 28, 29)
- [70] T. E. Harris. *The theory of branching process*. 1st ed. vol. 119 Berlin: Springer Verlag, 1964. 67 (see pp. 43, 46)
- [71] C. D. Hauck. *High-order entropy-based closures for linear transport in slab geometry*. *Communications in Mathematical Sciences*, 9: 187–205, 2011. (see p. 15)
- [72] C. Hauck and R. McClarren. *Positive P_N closures*. *SIAM Journal on Scientific Computing*, 32: 2603–2626, 2010. (see pp. 18, 78)
- [73] T. Hillen. *M 5 mesoscopic and macroscopic models for mesenchymal motion*. *Journal of mathematical biology*, 53: 585–616, 2006. (see pp. 52, 90)
- [74] T. Hillen, K. J. Painter, A. C. Swan, and A. D. Murtha. *Moments of von Mises and Fisher distributions and applications*. *Mathematical Biosciences & Engineering*, 14: 673–694, 2017. (see p. 34)
- [75] C. Hogue, C. Davatzikos, and G. Biros. *Modeling glioma growth and mass effect in 3D MR images of the brain*. in: *International Conference on Medical Image Computing and Computer-Assisted Intervention*. Springer 2007. 642–650 (see p. 29)
- [76] A. Hunt. *DTI-Based Multiscale Models for Glioma Invasion*. PhD thesis. Technische Universität Kaiserslautern, 2018. (see pp. 3, 33, 34)
- [77] J. D. Hunter. *Matplotlib: A 2D graphics environment*. *Computing in Science & Engineering*, 9: 90–95, 2007. DOI: [10.1109/MCSE.2007.55](https://doi.org/10.1109/MCSE.2007.55) (see p. 161)

- [78] S. Jbabdi, E. Mandonnet, H. Duffau, L. Capelle, K. R. Swanson, M. Pélégriani-Issac, R. Guillevin, and H. Benali. *Simulation of anisotropic growth of low-grade gliomas using diffusion tensor imaging*. *Magnetic Resonance in Medicine: An Official Journal of the International Society for Magnetic Resonance in Medicine*, 54: 616–624, 2005. (see pp. 29, 31)
- [79] S. Jin and C. D. Levermore. *Numerical schemes for hyperbolic conservation laws with stiff relaxation terms*. *Journal of computational physics*, 126: 449–467, 1996. (see pp. 3, 53, 55, 58, 96, 100)
- [80] S. Jin and L. Pareschi. *Discretization of the multiscale semiconductor Boltzmann equation by diffusive relaxation schemes*. *Journal of Computational Physics*, 161: 312–330, 2000. (see p. 100)
- [81] S. Jin, L. Pareschi, and G. Toscani. *Uniformly accurate diffusive relaxation schemes for multiscale transport equations*. *SIAM Journal on Numerical Analysis*, 38: 913–936, 2000. (see pp. 3, 99, 100)
- [82] J. R. Johansson *Lectures in scientific python* 2018 URL: <https://github.com/jrjohansson/scientific-python-lectures/blob/master> (visited on 12/05/2018) (see p. 163)
- [83] M. Junk. *Maximum entropy for reduced moment problems*. *Mathematical Models and Methods in Applied Sciences*, 10: 1001–1025, 2000. DOI: [10.1142/S0218202500000513](https://doi.org/10.1142/S0218202500000513) (see pp. 17, 64)
- [84] H. Keller, A. Zimmermann, and H. Cottier. *Crawling-like movements, adhesion to solid substrata and chemokinesis of neutrophil granulocytes*. *Journal of cell science*, 64: 89–106, 1983. (see p. 38)
- [85] P. J. Kelly and C. Hunt. *The limited value of cytoreductive surgery in elderly patients with malignant gliomas*. *Neurosurgery*, 34: 62–67, 1994. (see p. 1)
- [86] D. Kershaw *Flux limiting nature’s own way* tech. rep. UCRL-78378 Lawrence Livermore National Laboratory, 1976 DOI: [10.2172/104974](https://doi.org/10.2172/104974) (see pp. 19, 69, 70, 156)
- [87] A. Klar. *An asymptotic-induced scheme for nonstationary transport equations in the diffusive limit*. *SIAM journal on numerical analysis*, 35: 1073–1094, 1998. (see pp. 3, 100)
- [88] K. Kono, Y. Inoue, K. Nakayama, M. Shakudo, M. Morino, K. Ohata, K. Wakasa, and R. Yamada. *The role of diffusion-weighted imaging in patients with brain tumors*. *American journal of neuroradiology*, 22: 1081–1088, 2001. (see pp. 31, 33)
- [89] W. H. Koppenol and P. L. Bounds. *The Warburg effect and metabolic efficiency: re-crunching the numbers*. *Science*, 324: 1029–1033, 2009. (see p. 28)
- [90] D. Lane. *The regulation of p53 function: Steiner award lecture*. *International journal of cancer*, 57: 623–627, 1994. (see p. 27)
- [91] N. Laperriere, L. Zuraw, G. Cairncross, et al. *Radiotherapy for newly diagnosed malignant glioma in adults: a systematic review*. *Radiotherapy and Oncology*, 64: 259–273, 2002. (see p. 1)
- [92] E. W. Larsen and J. E. Morel. *Advances in discrete-ordinates methodology*. in: *Nuclear Computational Science*. Springer, 2010. 1–84 (see p. 119)
- [93] E. W. Larsen, J. E. Morel, and W. F. Miller Jr. *Asymptotic solutions of numerical transport problems in optically thick, diffusive regimes*. *Journal of Computational Physics*, 69: 283–324, 1987. (see pp. 3, 96, 99)

- [94] E. Larsen and J. Keller. *Asymptotic Solution of Neutron Transport Problems for Small Mean Free Path*. *Journal of Mathematical Physics*, 15: 75, 1974. (see p. 3)
- [95] D. Le Bihan, J.-F. Mangin, C. Poupon, C. A. Clark, S. Pappata, N. Molko, and H. Chabriat. *Diffusion tensor imaging: concepts and applications*. *Journal of Magnetic Resonance Imaging: An Official Journal of the International Society for Magnetic Resonance in Medicine*, 13: 534–546, 2001. (see pp. 30, 31)
- [96] M. Lemou and L. Mieussens. *A new asymptotic preserving scheme based on micro-macro formulation for linear kinetic equations in the diffusion limit*. *SIAM Journal on Scientific Computing*, 31: 334–368, 2008. (see pp. 3, 99, 101–103, 108, 147)
- [97] R. J. LeVeque. *Finite Volume Methods for Hyperbolic Problems*. 1st ed. Cambridge University Press, 2002. 171–181, 476–477 (see pp. 74, 88)
- [98] R. J. LeVeque. *Finite-volume methods for non-linear elasticity in heterogeneous media*. *International Journal for Numerical Methods in Fluids*, 40: 93–104, 2002. (see pp. 74, 107)
- [99] R. J. LeVeque. *Python tools for reproducible research on hyperbolic problems*. *Computing in Science & Engineering*, 11: 19–27, 2009. (see p. 163)
- [100] C. D. Levermore. *Entropy-based moment closures for kinetic equations*. *Transport Theory and Statistical Physics*, 26: 591–606, 1997. DOI: [10.1080/00411459708017931](https://doi.org/10.1080/00411459708017931) (see p. 15)
- [101] C. D. Levermore. *Moment closure hierarchies for kinetic theories*. *Journal of statistical Physics*, 83: 1021–1065, 1996. (see p. 16)
- [102] C. D. Levermore. *Moment closure hierarchies for the Boltzmann-Poisson equation*. *VLSI Design*, 6: 97–101, 1998. (see p. 15)
- [103] E. A. Maher, F. B. Furnari, R. M. Bachoo, D. H. Rowitch, D. N. Louis, W. K. Cavenee, and R. A. DePinho. *Malignant glioma: genetics and biology of a grave matter*. *Genes & development*, 15: 1311–1333, 2001. (see pp. 1, 2)
- [104] R. C. Martin. *Clean code: a handbook of agile software craftsmanship*. Pearson Education, 2009. (see p. 163)
- [105] J. B. McCARTHY and L. T. Furcht. *Laminin and fibronectin promote the haptotactic migration of B16 mouse melanoma cells in vitro*. *The Journal of cell biology*, 98: 1474–1480, 1984. (see p. 38)
- [106] R. G. McClarren, J. P. Holloway, and T. A. Brunner. *On solutions to the Pn equations for thermal radiative transfer*. *Journal of Computational Physics*, 227: 2864–2885, 2008. (see p. 18)
- [107] J. Metzcar, Y. Wang, R. Heiland, and P. Macklin. *A review of cell-based computational modeling in cancer biology*. *JCO clinical cancer informatics*, 2: 1–13, 2019. (see p. 28)
- [108] P. Mosayebi, D. Cobzas, A. Murtha, and M. Jagersand. *Tumor invasion margin on the Riemannian space of brain fibers*. *Medical image analysis*, 16: 361–373, 2012. (see pp. 3, 29)
- [109] W. S. Noble. *A quick guide to organizing computational biology projects*. *PLoS Computational Biology*, 5: 2009. DOI: [10.1371/journal.pcbi.1000424](https://doi.org/10.1371/journal.pcbi.1000424) (see pp. 162, 163)
- [110] E. Olbrant, C. Hauck, and M. Frank. *A realizability-preserving discontinuous Galerkin method for the M1 model of radiative transfer*. *Journal of Computational Physics*, 231: 5612–5639, 2012. DOI: [10.1016/j.jcp.2012.03.002](https://doi.org/10.1016/j.jcp.2012.03.002) (see p. 73)

- [111] H. G. Othmer and T. Hillen. *The diffusion limit of transport equations derived from velocity-jump processes*. *SIAM Journal on Applied Mathematics*, 61: 751–775, 2000. (see pp. 3, 43, 52)
- [112] K. Painter and T. Hillen. *Mathematical modelling of glioma growth: the use of diffusion tensor imaging (DTI) data to predict the anisotropic pathways of cancer invasion*. *Journal of theoretical biology*, 323: 25–39, 2013. (see pp. 29, 33)
- [113] K. Pavnkova, D. Rosel, M. Novotny, and J. Brabek. *The molecular mechanisms of transition between mesenchymal and amoeboid invasiveness in tumor cells*. *Cellular and molecular life sciences*, 67: 63–71, 2010. (see p. 27)
- [114] G. Pomraning. *The Equations of Radiation Hydrodynamics*. Dover books on physics Dover Publications, 2005. 1–5 (see pp. 14, 18)
- [115] P. Ramachandran. *automan: A Python-Based Automation Framework for Numerical Computing*. *Computing in Science & Engineering*, 20: 81–97, 2018. (see p. 163)
- [116] G. Ramirez-San Juan, P. Oakes, and M. Gardel. *Contact guidance requires spatial control of leading-edge protrusion*. *Molecular biology of the cell*, 28: 1043–1053, 2017. (see p. 38)
- [117] J. S. Rao. *Molecular mechanisms of glioma invasiveness: the role of proteases*. *Nature Reviews Cancer*, 3: 489–501, 2003. (see pp. 2, 27)
- [118] B. Riviè, M. F. Wheeler, K. Banaś, et al. *Part II. Discontinuous Galerkin method applied to a single phase flow in porous media*. *Computational Geosciences*, 4: 337–349, 2000. (see p. 128)
- [119] K. Salari and P. Knupp *Code verification by the method of manufactured solutions* tech. rep. SAND2000-1444 Sandia National Labs., Albuquerque, NM (US); Sandia National Labs., Livermore, CA (US), 2000 doi: [10.2172/759450](https://doi.org/10.2172/759450) (see p. 125)
- [120] N. Sanai, A. Alvarez Buylla, and M. S. Berger. *Neural stem cells and the origin of gliomas*. *New England Journal of Medicine*, 353: 811–822, 2005. (see pp. 2, 27)
- [121] F. Schneider. *Moment models in radiation transport equations*. Verlag Dr. Hut, 2016. (see pp. 12, 15, 16, 73, 78)
- [122] W. Schroeder, K. Martin, and B. Lorensen. *The Visualization Toolkit*. 4th ed. ISBN 978-1-930934-19-1 Kitware, 2006. (see p. 161)
- [123] B. Seibold and M. Frank. *StaRMAP—A Second Order Staggered Grid Method for Spherical Harmonics Moment Equations of Radiative Transfer*. *ACM Transactions on Mathematical Software*, 41: 4, 2014. (see pp. 75, 117, 118, 156)
- [124] D. L. Silbergeld and M. R. Chicoine. *Isolation and characterization of human malignant glioma cells from histologically normal brain*. *Journal of neurosurgery*, 86: 525–531, 1997. (see p. 1)
- [125] W. G. Stetler-Stevenson, S. Aznavoorian, and L. A. Liotta. *Tumor cell interactions with the extracellular matrix during invasion and metastasis*. *Annual review of cell biology*, 9: 541–573, 1993. (see p. 27)
- [126] V. Stodden *AMP Workshop on Reproducible Research 2011* URL: <http://www.stodden.net/AMP2011/> (visited on 06/23/2020) (see pp. 163, 165)
- [127] D. W. Stroock. *Some stochastic processes which arise from a model of the motion of a bacterium*. *Probability Theory and Related Fields*, 28: 305–315, 1974. (see pp. 3, 4, 6, 37, 40, 51, 136, 146)

- [128] P. Sundgren, Q. Dong, D. Gomez-Hassan, S. Mukherji, P. Maly, and R. Welsh. *Diffusion tensor imaging of the brain: review of clinical applications*. *Neuroradiology*, 46: 339–350, 2004. (see pp. 31, 33)
- [129] A. Swan, T. Hillen, J. C. Bowman, and A. D. Murtha. *A patient-specific anisotropic diffusion model for brain tumour spread*. *Bulletin of mathematical biology*, 80: 1259–1291, 2018. (see pp. 3, 29)
- [130] K. R. Swanson, E. C. Alvord Jr, and J. Murray. *A quantitative model for differential motility of gliomas in grey and white matter*. *Cell proliferation*, 33: 317–329, 2000. (see pp. 25, 29)
- [131] D. S. Tuch. *Q-ball imaging*. *Magnetic Resonance in Medicine: An Official Journal of the International Society for Magnetic Resonance in Medicine*, 52: 1358–1372, 2004. (see pp. 2, 33)
- [132] A. E. Tzavaras. *Relative entropy in hyperbolic relaxation*. *Communications in Mathematical Sciences*, 3: 119–132, 2005. (see pp. 62, 146)
- [133] A. Uatay. *Multiscale Mathematical Modeling of Cell Migration: From Single Cells to Populations*. <http://nbn-resolving.de/urn:nbn:de:hbz:386-kluedo-56252> PhD thesis. Technische Universität Kaiserslautern, 2019. (see pp. 4, 28, 30, 36, 37, 145)
- [134] Unidata *NetCDF 4.7 2020* URL: <https://doi.org/10.5065/D6H70CW6> (visited on 06/23/2020) (see p. 161)
- [135] M. Y. Vardi. *Science has only two legs*. *Communications of the ACM*, 53: 5–5, 2010. (see pp. 161, 162)
- [136] C. Villani *H-Theorem and beyond: Boltzmann’s entropy in today’s mathematics* 2008 (see p. 8)
- [137] V. Volpert and S. Petrovskii. *Reaction–diffusion waves in biology*. *Physics of life reviews*, 6: 267–310, 2009. (see p. 131)
- [138] K. Weiss, F. Iuricich, R. Fellegara, and L. De Florian. *A primal/dual representation for discrete Morse complexes on tetrahedral meshes*. in: *Computer Graphics Forum*. vol. 32 Wiley Online Library 2013. 361–370 (see p. 104)
- [139] G. Wilson et al. *Best practices for scientific computing*. *PLoS biology*, 12: e1001745, 2014. doi: [10.1371/journal.pbio.1001745](https://doi.org/10.1371/journal.pbio.1001745) (see p. 162)

List of Figures

2.1	Growth patterns of GBM as seen on MRI	26
2.2	Tensor ellipsoids and peanuts.	32
2.3	Visualization of the Camino [30] DTI data set.	33
4.1	The construction of the atomic representing density.	71
4.2	Results of Experiment 4.6—kinetic regime: $P_N^{(E)}$ and P_N with $N = 1, 3, 5$	79
4.3	Results of Experiment 4.6—kinetic regime: $P_N^{(E)}$ and P_N with $N = 7, 9$	80
4.4	Results of Experiment 4.6—kinetic regime: lineouts of $P_N^{(E)}$ and P_N with $N = 1, 3, 5, 7$	81
4.5	Results of Experiment 4.6—kinetic regime: $M_N^{(E)}$ and M_N with $N = 1, 2$	82
4.6	Results of Experiment 4.6—kinetic regime: lineouts of $M_N^{(E)}$ and M_N with $N = 1, 2$	83
4.7	Results of Experiment 4.6—kinetic regime: $K_1^{(E)}$, $M_1^{(E)}$, $P_1^{(E)}$	83
4.8	Results of Experiment 4.7—intermediate regime: $K_1^{(E)}$, $M_1^{(E)}$, and $P_1^{(E)}$	84
4.9	Results of Experiment 4.7—intermediate regime: $P_N^{(E)}$ and P_N with $N = 1, 3, 5$	85
4.10	Results of Experiment 4.8—drift.	86
4.11	Results of Experiment 4.8—drift: lineouts.	87
4.12	Results of Experiment 4.9—Lax-Friedrichs vs. Godunov.	89
4.13	Results of Experiment 4.10—Lax-Friedrichs vs. Kershaw-kinetic.	90
4.14	Results of Experiment 4.11—proteolysis, kinetic regime.	93
4.15	Results of Experiment 4.12—proteolysis, intermediate regime.	94
4.16	Results of Experiment 4.13—extreme remodeling.	95
4.17	Results of Experiment 4.14—numerical diffusion.	97
5.1	The primal-dual mesh pair in two dimensions.	104
5.2	The primal-dual mesh pair in three dimensions.	105
5.3	The diffusion stencil with midpoint flux evaluations.	112
5.4	The diffusion stencil with shifted flux evaluations.	113
5.5	A second-order accurate shifted update variant.	115
5.6	Drift discretizations: central and upwind scheme.	115

5.7	Results of Experiment 5.6—grid refinement—and Experiment 5.7—convergence to diffusion limit.	121
5.8	Results of Experiment 5.7—convergence to diffusion limit: kinetic to intermediate regime. .	122
5.9	Results of Experiment 5.7—convergence to diffusion limit: intermediate to diffusive regime.	123
5.10	Results of Experiment 5.8—numerical diffusion.	125
5.11	Results of Experiment 5.9—order of convergence.	127
5.12	Results of Experiment 5.10—improved stencil.	128
5.13	Results of Experiment 5.11—quadrants benchmark.	130
5.14	Results of Experiment 5.13—Fisher-KPP benchmark.	134
5.15	A chemotaxis experiment with E.coli on a Petri plate [16].	135
5.16	Results of Experiment 5.14—Stroock’s model.	137
5.17	Results of Experiment 5.15—glioma parameter study.	140
5.18	Results for Experiment 5.16—parabolic scaling: influence of ε	141
5.19	Results for Experiment 5.17—choice of moment order, scheme, and space dimension. .	142
5.20	Results for Experiment 5.18—grid refinement and interpolation artifacts.	144
B.1	The environment of a computational experiment.	164

List of Tables

4.1	Base parameters for the line source benchmark.	77
4.2	Base parameters for the stripes benchmark.	88
4.3	Base parameters for the proteolysis computations.	92
5.1	Coefficients for the exact solution (5.22) of the quadrants test.	131
5.2	Parameters for the Fisher-KPP benchmark.	132
5.3	Parameters for the Petri plate experiment from [16].	136
5.4	Two parameter sets for the glioma model.	138
B.1	Dependencies for the KERSHAW modules.	162
B.2	The actions the ARCHIVIST performs on components of the environment.	165

Image Credits

Figure 2.1b

License: CC BY-NC-SA 3.0, Case courtesy of Assoc. Prof. Frank Gaillard, [Radiopaedia.org](https://radiopaedia.org), rID: 5565. 26

Figure 2.1c

License: CC BY-NC-SA 3.0, Case courtesy of Assoc. Prof. Frank Gaillard, [Radiopaedia.org](https://radiopaedia.org), rID: 2589. 26

Figure 2.1f

License: CC BY-NC-SA 3.0, Case courtesy of Dr Ahmed Abdrabou, [Radiopaedia.org](https://radiopaedia.org), rID: 24489. 26

Figure 2.1e

License: CC BY-NC-SA 3.0, Case courtesy of Assoc. Prof. Frank Gaillard, [Radiopaedia.org](https://radiopaedia.org), rID: 14564. 26

Figure 2.1d

License: CC BY-NC-SA 3.0, Case courtesy of Dr Hani Salam, [Radiopaedia.org](https://radiopaedia.org), rID: 8576. 26

Figure 2.1a

License: CC BY-NC-SA 3.0, Case courtesy of Dr Nick Tarasov, [Radiopaedia.org](https://radiopaedia.org), rID: 39177. 26

Figure 5.15

[16]: H.C.Berg. E. coli in Motion. Springer Science & Business Media, 2008, p.22. Photograph by J.S. Parkinson, University of Utah. 135

Glossary

apparent diffusion coefficient (ADC)

The isotropic component of the diffusion tensor. [31](#), [33](#)

asymptotic preserving (AP)

A numerical scheme that converges to a valid scheme for a scaling limit. [3](#), [4](#), [65](#), [99](#), [101](#), [102](#), [148](#), [149](#), [161](#)

characteristic length estimate (CL)

An estimate for the volume fraction of fibers, based on a characteristic diffusion length. [31](#), [33](#)

computed tomography (CT)

A noninvasive 3D imaging technique based on absorption of x-rays in tissue. [30](#)

diffusion tensor imaging (DTI)

A series of MRI images that can be used to measure diffusion speed of water molecules. [2](#), [29–31](#), [33](#), [39](#), [42](#), [45](#), [120](#), [137](#), [145](#), [148](#), [149](#), [161](#), [162](#), [164](#), [177](#)

Engwer-Hillen-Knappitsch-Surulescu model (EHKS model)

The glioma model proposed by Engwer, Hillen, Knappitsch, and Surulescu. [36](#), [137](#), [138](#), [145](#), [148](#), [149](#)

extracellular matrix (ECM)

The fibrous protein structure outside of cells that provides stability to the tissue and is used by cells to attach to. [2](#), [27](#), [28](#), [30](#), [31](#), [36](#), [37](#), [90](#), [145](#)

fractional anisotropy (FA)

A measure of anisotropy of a diffusion tensor. [31](#), [33](#), [138](#)

glioblastoma multiforme (GBM)

The most aggressive type of glioma; grade IV astrocytoma. [1](#), [2](#), [25](#), [26](#), [177](#)

implicit-explicit (IMEX)

A mixture of implicit and explicit time stepping. [101](#), [108](#), [109](#), [159](#)

kinetic theory of active particles (KTAP)

A mathematical structure to model living systems with kinetic equations. [3](#), [29](#), [30](#), [41](#)

magnetic resonance imaging (MRI)

A noninvasive imaging technique based on the interaction of magnetic fields with hydrogen atoms. [2](#), [4](#), [25](#), [26](#), [30](#), [31](#), [177](#)

multi-point flux approximation (MPFA)

A numerical scheme for flow through porous media. [99](#), [149](#)

Academic curriculum vitae

- 2016 Accepted as postgraduate of Prof. Dr. Axel Klar at the department of mathematics at the university of Kaiserslautern.
- 2016 Master degree in Computational Engineering Science with specialization mathematics at the RWTH Aachen.
Title of the master thesis: *An entropy closure for linear transport using piecewise quadratic basis functions.*
- 2014 Bachelor degree in Computational Engineering Science with specialization in fluid dynamics at the RWTH Aachen.
Title of the bachelor thesis: *Application of the PN method on staggered grids to the Boltzmann Continuous Slowing Down equation for electron transport in media with spatially varying density.*
- 2010 Matriculation at the RWTH Aachen University.
- 2010 General higher education entrance qualification at the Kaiser-Karls-Gymnasium, Aachen.

Akademischer Lebenslauf

- 2016 Annahme als Doktorand am Fachbereich Mathematik an der Technischen Universität Kaiserslautern unter Prof. Dr. Axel Klar.
- 2016 Master-Abschluss in Computational Engineering Science mit Schwerpunkt Mathematik an der Fakultät für Maschinenwesen der RWTH Aachen.
Thema der Master-Arbeit: *Stückweise quadratische Basisfunktionen für die Entropie-Schließung in linearen kinetischen Gleichungen.*
- 2014 Bachelor-Abschluss in Computational Engineering Science mit Schwerpunkt Strömung und technische Verbrennung an der Fakultät für Maschinenwesen der RWTH Aachen.
Thema der Bachelor-Arbeit: *Anwendung der PN Methode auf versetzten Gittern auf die Boltzmann Continuous Slowing Down Gleichung für elektronentransport in Medien mit örtlich veränderlicher Dichte.*
- 2010 Immatrikulation an der Rheinisch-Westfälischen Technischen Hochschule (RWTH) Aachen.
- 2010 Allgemeine Hochschulreife am Kaiser-Karls-Gymnasium, Aachen.

